

# **Synthesis, characterisation and corrosion studies of CoCrMo nanoparticles for hip implants**

**Thiago Araujo Simões**

Submitted in accordance with the requirements for the degree of  
Doctor of Philosophy

The University of Leeds  
Institute for Materials Research - IMR  
School of Chemical & Process Engineering - SCAPE

**September, 2015**

The candidate confirms that the work submitted is his own, except where work which has formed part of jointly-authored publications has been included. The contribution of the candidate and the other authors to this work has been explicitly indicated below. The candidate confirms that appropriate credit has been given within the thesis where reference has been made to the work of others.

1. **T. A. Simoes**, A.P. Brown, S. J. Milne and R. M. D. Brydson ( 2014). *CoCrMo nanoparticles produced by mechanochemical milling: a route to simulate wear debris from hip implants*, proceedings of XIII Brazilian Materials Research Society.
2. **TA Simoes**, AE Goode, AE Porter, MP Ryan, SJ Milne, AP Brown, RMD Brydson (2014). *Microstructural characterization of low and high carbon CoCrMo alloy nanoparticles produced by mechanical milling*, Journal of Physics: Conference Series, 522, 012059. Doi 10.1088/1742-6596/522/1/012059
3. **TA Simoes**, AP Brown, SJ Milne and RMD Brydson (2015). *Bovine Serum Albumin binding to CoCrMo nanoparticles and the influence on dissolution*, Journal of Physics: Conference Series. [in press]
4. **Simoes T**, Bryant M, Brown A, Milne S J, Ryan M, Neville A and Brydson R (2015). *Quantitative assessment of metal dissolution from CoCrMo alloys during Tribocorrosion*. [Manuscript submitted for publication]
5. Andrea L. Armstead, **Thiago A. Simoes**, Xianfeng Wang, Rik Brydson, Bing-Hua Jiang, Yon Rojanasakul, and Bingyun Li (2015). *Toxicity and oxidative stress response induced by nano- and micro-CoCrMo particles in human cells are cell specific*. [In Preparation]

All of the work contained within publication 1, 2, 3 and 4 is directly attributable to T. A. Simoes under the guidance of academic supervisors R. Brydson, A.P. Brown and S.J. Milne, and is discussed in Chapters 4 and 5. For publications 5, T. A. Simoes provided the CoCrMo nanoparticles and size characterisation data presented in the paper used in the investigation.

This copy has been supplied on the understanding that it is copyright material and that no quotation from the thesis may be published without proper acknowledgement.

## **Acknowledgements**

I would like to express my gratitude to all my supervisors, Prof. Rik Brydson and Dr Andy Brown, as well as Dr Steven Milne. Prof. Brydson's advice was invaluable throughout the project, his patience and knowledge of many aspects of science contributed immensely towards the investigation. Dr Andy Brown's guidance helped me throughout the research and writing of this thesis. Dr Steven Milne who was a good source of information and always agreed to proof read drafts of my work. I could not have imagined having a better advisors and mentors for my Ph.D.

Thank you to SCAPE staff who provided me with experimental training and assistance throughout the course of this study, most notably Dr Mike Ward, Mr Stuart Micklethwaite, Mr John Harrington, Dr Tim Comyn, Dr Adrian Cunliffe, Dr Nicole Hondow and Mr Robert Simpson for their assistance.

I would like to special thank for all the co-workers from different universities and institutes for the stimulating discussions as: Dr M Bryant and Prof A Neville (Institute of Functional Surfaces/ University of Leeds), Dr A Goode, Dr A Porter, Prof M Ryan (Imperial College) and Prof B Li (West Virginia University).

I also thank my fellow lab and office mates for the sleepless nights we were worked together before deadlines, and for all the fun we have had in the last four years, especially Dr Mathew Bilton and Dr Rachel Wallace as well as (soon-to-be Dr) Mr Yothin Chimupala, Mr Faith Bamiduro, Mr Omar Matar and the many past and present friends of room 1.19.

I would also like to thank my family for the support they provided me through my entire life and in particular I must acknowledge Vanessa because without her love, encouragement and editing assistance, I would not have finished this thesis.

Thanks to all of you for making my academic life at Leeds a wonderful place to learn and thanks to my family for making home a wonderful place to come back to.

Finally, the author gratefully acknowledges funding from the Capes Foundation (Ministry of Education of Brazil): BEX-5515/10-6 for the financial support through the PhD life in UK.

## **Abstract**

CoCrMo Metal on Metal (MoM) hip implants were designed to be durable, targeting a better quality of life for young, active patients. However, evidence suggests that such implants can release wear particles and metal ions due to a bio-tribocorrosion process. Metallic particles, produced by wear, at articulating interfaces of the joint surface have been linked with the formation of pseudotumors and lymphatic circulation. Whilst the ion release mechanism from the bulk alloy is the focus of many studies, it is not unreasonable to expect further corrosion of particles once they become detached from the surface of the implant. Wear debris is inherent to the process because it is an inevitable consequence of the relative motion between two opposite surfaces in contact. By this means, the removal of material due to mechanical action can generate millions of nanoparticles for each cycle of movement, which can then migrate into the tissues surrounding the implant. Several studies have indicated that metal ion levels rise after surgery and persist. Specifically metal particles spread by lymphatic circulation can continue to release ions even after removal of the source of wear. The mechanisms of ion release at this scale are still unclear along with the subsequent interaction between metal-ions and biological media (e.g. bovine serum albumin (BSA) proteins).

Statistically significant toxicological studies require relatively large amounts of wear debris because most studies are based on the dose-response of triplicate assays, which could require more than a hundred milligrams of nanoparticles. However, producing large volumes of wear debris particles which match the composition, size and morphology of those generated in actual hip replacements remains extremely difficult. This study focuses on the synthesis and characterization of CoCrMo nanoparticles, which mimic metal-on-metal (MoM) wear debris from hip implants. For the synthesis process, we have used a hitherto unexplored approach employing mechanochemical milling to produce a large amount of CoCrMo mimetic wear debris over short time scales. The nanoparticles produced were found to be similar in size, shape and composition to real implant wear debris from CoCrMo hip implants. In addition, pure metals that compose the alloy were compared in terms of their electrochemical corrosion, static corrosion and protein binding.

Dissolution studies indicated a much lower dissolution of cobalt than previously reported. This was attributed to the efficient separation of nanoparticles prior to solute analysis through the use of centrifugation

combined with ultrafiltration. The data suggest that the previously accepted route for the release of cobalt ions may need revision. The study showed that after tribocorrosion of the CoCrMo alloy in BSA, the level of Co and Mo ions in solution increased dramatically. The increase in Mo ions could be linked with the preferential binding of Mo to the BSA proteins which results in the formation of a hard protein corona on CoCrMo and Mo particles and does not readily desorb even after washing. These findings are important as it highlighted the interaction of Mo-rich surfaces with amide groups in serum proteins and the possible formation of metal carbonyl complexes both of which can modify biological molecules, altering their ability to function properly.

Electrochemical corrosion in the presence of a realistic concentration of BSA suggested that proteins play an important role in Mo dissolution from CoCrMo. Mo presumably reacts with amino acid residues present in protein molecules, initiating preferential dissolution even at low potentials, where there is no disruption of the Cr passivation layer on the CoCrMo alloy. Co and Mo samples showed active dissolution in all electrolyte solutions, whereas degradation of CoCrMo and Cr samples were controlled by a passivating oxide layer. The use of PBS accelerated the corrosion for all samples, increasing the metal ion concentration in the electrolyte and there was a high incidence and growth of pitting corrosion on Co samples.

This work suggests that the role of Mo as well as Co ions should be accounted for in the tribocorrosion of CoCrMo implant alloys, particularly in terms of inflammatory and toxicological responses.

## Table of Contents

|  |               |
|--|---------------|
| <b>Acknowledgements</b> .....  | <b>iii</b>    |
| <b>Abstract</b> .....  | <b>iv</b>     |
| <b>Table of Contents</b> .....   | <b>vi</b>     |
| <b>List of Tables</b> .....  | <b>xi</b>     |
| <b>List of Figures</b> .....   | <b>xiii</b>   |
| <b>List of Abbreviations</b> .....   | <b>xxii</b>   |
| <b>Chapter 1 - Introduction</b> .....  | <b>- 1 -</b>  |
| 1.1 Hip Replacement: A short overview .....  | - 1 -         |
| 1.2 The Aims .....   | - 6 -         |
| 1.3 Objectives .....   | - 6 -         |
| 1.4 Chapter overview .....   | - 7 -         |
| 1.5 Publications.....  | - 8 -         |
| <b>Chapter 2 - Literature Review</b> .....   | <b>- 10 -</b> |
| 2.1 Metal-on-Metal hip replacements .....  | - 10 -        |
| 2.1.1- Cellular reaction to the implant.....   | - 11 -        |
| 2.2 CoCrMo alloy .....   | - 12 -        |
| 2.2.1- Production of CoCrMo Alloys .....   | - 13 -        |
| 2.2.2- The effect of carbon in CoCrMo alloys.....  | - 14 -        |
| 2.2.3- Crystallography .....   | - 15 -        |
| 2.3 Hip implant degradation and failure.....   | - 17 -        |
| 2.4 Specification of wear debris and metal ions collected from<br>patients with MoM hip implants ..... | - 21 -        |
| 2.4.1- CoCrMo alloy wear debris.....   | - 22 -        |
| 2.4.2- Metal ions.....   | - 25 -        |
| 2.5 Biological responses to CoCrMo wear debris and ions .....  | - 28 -        |
| 2.5.1- Toxicity of particles .....   | - 29 -        |
| 2.5.2- Toxicity of ions .....  | - 30 -        |
| 2.6 Synthetic approaches to generating wear debris and metal<br>ions.....                              | - 30 -        |
| 2.6.1- Body fluid simulation .....   | - 32 -        |
| 2.6.1.1 - Serum Albumin .....  | - 33 -        |
| 2.6.1.2 - CoCrMo corrosion under incubation in<br>Simulation Body Fluid .....                          | - 35 -        |
| 2.6.2- Hip Simulators.....   | - 37 -        |

|  |               |
|--|---------------|
| 2.6.3- Pin-on-plate.....   | - 41 -        |
| 2.6.4- Mechanochemical Milling.....  | - 42 -        |
| 2.7 - Electrochemical corrosion of hip implant alloys.....                                   | - 46 -        |
| 2.8 Summary.....   | - 50 -        |
| <b>Chapter 3 - Materials and Methods .....</b>   | <b>- 52 -</b> |
| 3.1 Wear debris simulation.....  | - 52 -        |
| 3.1.1- Simulated Body Fluids .....   | - 52 -        |
| 3.1.2- Hip Simulators.....   | - 52 -        |
| 3.1.3- Pin-on-plate.....   | - 53 -        |
| 3.1.4- Ball Milling.....   | - 54 -        |
| 3.2 Reference materials for studies of corrosion during incubation and protein binding ..... | - 56 -        |
| 3.3 Electrochemical corrosion by cyclic polarization .....                                   | - 56 -        |
| 3.4 Materials characterization techniques .....  | - 57 -        |
| 3.4.1- X-ray diffraction.....  | - 58 -        |
| 3.4.1- Scanning electron microscopy .....  | - 59 -        |
| 3.4.1.1 - Secondary electrons .....  | - 60 -        |
| 3.4.1.2 - Backscattered electrons.....   | - 60 -        |
| 3.4.1.3 - Energy dispersive X-ray spectroscopy.....  | - 60 -        |
| 3.4.2- Transmission electron microscopy.....   | - 61 -        |
| 3.4.2.1 - Scanning transmission electron microscope .-                                       | - 64 -        |
| 3.4.2.2 - Energy-filtered transmission electron microscopy.....                              | - 64 -        |
| 3.4.3- Inductively coupled plasma mass spectrometry.....                                     | - 65 -        |
| 3.4.4- X-ray photoelectron spectroscopy.....   | - 67 -        |
| 3.4.5- Dynamic light scattering .....  | - 68 -        |
| 3.4.6- Zeta Potential.....   | - 70 -        |
| 3.4.7- Fourier transform infrared spectroscopy .....   | - 71 -        |
| 3.4.8- Ultraviolet-visible spectroscopy.....   | - 72 -        |
| 3.4.9- Thermogravimetric analysis .....  | - 72 -        |
| 3.4.10 - Centrifugal Particle Sizing (CPS).....  | - 73 -        |
| 3.5 Characterization of as-Received Materials.....   | - 74 -        |
| 3.5.1- CoCrMo powder alloy .....   | - 74 -        |
| 3.5.2- CoCrMo bulk alloy.....  | - 76 -        |
| 3.6 Materials Sample Preparation.....  | - 79 -        |

|   |                |
|---|----------------|
| 3.6.1- Mechanochemical milling using 440C Hardened Steel vial/ beads (Section 4.2.1).....   | - 79 -         |
| 3.6.2- Mechanochemical milling using Zirconium Oxide Vial/Beads (Section 4.2.2).....  | - 80 -         |
| 3.6.3- Mechanochemical milling Optimization (Section 4.3.1).-   | 80 -           |
| 3.6.4- Simulating wear debris from hip implants (Section 4.3.4).....  | - 81 -         |
| 3.6.5- Accurate ICP-MS measurement (Section 5.1) .....  | - 81 -         |
| 3.6.6- Microstructural characterization of low and high carbon CoCrMo alloy nanoparticles produced by mechanical milling (Section 5.2)..... | - 82 -         |
| 3.6.7- Corrosion of CoCrMo alloy in relevant media (Section 5.3).....   | - 82 -         |
| 3.6.8- Bovine Serum Albumin binding to CoCrMo nanoparticles and the influence on dissolution (Section 5.4).....                             | - 83 -         |
| <b>Chapter 4 - Production of synthetic CoCrMo wear debris .....</b>   | <b>- 84 -</b>  |
| 4.1 Introduction .....  | - 84 -         |
| 4.2 Mechanochemical Milling .....   | - 85 -         |
| 4.2.1- 440C Hardened Steel Vial/beads.....  | - 85 -         |
| 4.2.2- Zirconium Oxide Vial/Beads.....  | - 88 -         |
| 4.3 Optimization of the Milling Process .....   | - 93 -         |
| 4.3.1- Characterization of the milled particles from factorial design .....   | - 94 -         |
| 4.3.2- Analysing the effects of variables and the interactions .-   | 96 -           |
| 4.3.3- Isolating Nanoparticles.....   | - 100 -        |
| 4.3.4- Simulating wear debris from hip implants .....   | - 102 -        |
| 4.4 Validation of CoCrMo milled particles with hip wear debris from literature .....  | - 105 -        |
| 4.4.1.1 - Size .....  | - 105 -        |
| 4.4.1.2 - Morphology .....  | - 106 -        |
| 4.4.1.3 - Chemical Composition .....  | - 106 -        |
| 4.4.1.4 - Brief Summary .....   | - 106 -        |
| 4.5 Pin-on-plate Method for Production of Synthetic Wear Debris-  | 107 -          |
| 4.6 Summary.....  | - 110 -        |
| <b>Chapter 5 - Tribocorrosion of Nanoparticulate and Wear Debris....</b>  | <b>- 112 -</b> |
| 5.1 Accurate ICP-MS measurement: the influence of sample preparation .....  | - 112 -        |

|  |  |       |
|--|--|-------|
| 5.1.1-   | TEM/ EDX analysis of wear debris from hip simulator prior to ICP-MS measurements.....                              | 113 - |
| 5.1.2-   | TEM/ EDX analysis of supernatant from hip simulator samples after ultracentrifugation .....                        | 116 - |
| 5.1.3-   | Ionic release after hip simulator test in FBS+PBS with different ICP-MS sample preparation procedures .....        | 117 - |
| 5.1.4-   | Co, Cr and Mo ionic standards through ultrafilters .....   | 118 - |
| 5.1.5-   | Brief Summary .....  | 119 - |
| 5.2  | Microstructural characterization of low and high carbon CoCrMo alloy nanoparticles produced by mechanical milling- | 120 - |
| 5.2.1-   | Particle size and shape.....   | 120 - |
| 5.2.2-   | Phase analysis.....  | 122 - |
| 5.2.3-   | Composition.....   | 124 - |
| 5.2.4-   | Brief Summary .....  | 126 - |
| 5.3  | Corrosion of the CoCrMo alloy in relevant media.....   | 126 - |
| 5.3.1-   | Fourier Transform Infrared Spectroscopy (FTIR).....  | 129 - |
| 5.3.2-   | Brief Summary .....  | 130 - |
| 5.4  | Bovine Serum Albumin binding to CoCrMo nanoparticles and the influence on dissolution .....                        | 131 - |
| 5.4.1-   | TEM/EDX on milled particles and reference materials immersed in BSA .....  | 132 - |
| 5.4.2-   | Static dissolution of the reference materials.....   | 134 - |
| 5.4.3-   | Zeta Potential to measure protein binding between metal particles and BSA.....                                     | 134 - |
| 5.4.1-   | Brief Summary .....  | 136 - |
| 5.5  | Discussion.....  | 137 - |
| 5.6  | Conclusion .....   | 141 - |
| <b>Chapter 6 - Electrochemical Corrosion Studies of Bulk Materials Immersed in Biological Media.....</b> |  |       |
| 6.1  | Introduction .....   | 143 - |
| 6.2  | Pourbaix diagram for Co, Cr and Mo.....  | 144 - |
| 6.3  | Polarization Curves .....  | 147 - |
| 6.4  | Surface analysis.....  | 151 - |
| 6.4.1-   | Scanning Electron Microscopy.....  | 151 - |
| 6.4.2-   | X-ray Photoelectron Spectroscopy.....  | 157 - |
| 6.4.2.1  | - Nitrogen (1s), Carbon (1s) and Phosphorous P (2p) Photoelectron Lines.....                                       | 158 - |

|   |                |
|---|----------------|
| 6.4.2.2 - Cobalt (2p), Chromium (2p) and Molybdenum (3d) .....      | - 163 -        |
| 6.5 Analysis of the Electrolyte Following Anodic Polarization ..... | - 170 -        |
| 6.5.1- Inductively Coupled Plasma Mass Spectrometry .....           | - 170 -        |
| 6.5.2- Ultraviolet-visible Spectroscopy .....                       | - 172 -        |
| 6.6 Discussion .....  | - 173 -        |
| 6.7 Conclusion .....  | - 176 -        |
| <b>Chapter 7 - Conclusions .....</b>                                | <b>- 177 -</b> |
| 7.1 Limitations of this Study and Future Work.....                  | - 180 -        |
| <b>References .....</b>   | <b>- 182 -</b> |
| <b>Appendix A .....</b>   | <b>- 207 -</b> |

## List of Tables

|  |       |
|--|-------|
| Table 2.1 - ASTM F75 specifications for chemical composition of cast CoCrMo for surgical implants [57] .....   | 13 -  |
| Table 2.2 - Characteristics of Calf Sera from HyClone used for synovial fluid simulation [119] .....   | 32 -  |
| Table 2.3 - Properties of the main amino acids present in BSA. Values collected from [127–129]. $pK_a$ is the negative logarithm of the dissociation constant for the $-\text{COOH}$ group, and $pK_b$ for the $-\text{NH}_3^+$ group. ....  | 34 -  |
| Table 2.4 - Main vials and balls materials used in high-energy milling [163] .....   | 44 -  |
| Table 2.5 - Co, Cr and Mo aqueous reaction .....   | 46 -  |
| Table 3.1 - Elemental composition (wt%) of CoCrMo from powder suppliers.....   | 55 -  |
| Table 3.2 - Reference XRD pattern from ICDD corresponding to the sample peaks .....  | 77 -  |
| Table 3.3 - TEM/EDX on CoCrMo low carbon standard showing the average weight composition in 30 different areas of the sample.....  | 79 -  |
| Table 3.4 - Description of the milling parameters in the factorial design experiment. ....   | 80 -  |
| Table 4.1 - Description of the milling parameters in the factorial design experiment plus the size reduction and contamination level in wt% relative to Co, Cr and Mo. ....  | 95 -  |
| Table 5.1 - Classification of CoCrMo high carbon wear particle's shape and length generated by hip simulator over 30,000 cycles. ....  | 114 - |
| Table 5.2 - Metallic elemental levels in supernatant samples following centrifugation plus ultrafiltration and ICP-MS of CoCrMo powders milled in different environments (diluted 20x). Results are given in both absolute terms ( $\mu\text{g/L}$ ) and also relative terms (%). .... | 127 - |
| Table 6.1- Corrosion data extracted from polarization curves. ....   | 150 - |
| Table 6.2 - Co 2p XPS quantification for elemental Co sample after anodic polarization in BSA, PBS and BSA+PBS. Co (+2) included oxides and hydroxides. ....   | 164 - |
| Table 6.3 - Co 2p XPS quantification for CoCrMo alloy after anodic polarization in BSA, PBS and BSA+PBS. ....  | 165 - |
| Table 6.4 - Cr 2p XPS quantification for elemental Cr sample after anodic polarization in BSA, PBS and BSA+PBS.....  | 166 - |
| Table 6.5 - Cr 2p XPS quantification for CoCrMo alloy after anodic polarization in BSA, PBS and BSA+PBS. ....  | 167 - |

Table 6.6 - Mo 3d XPS quantification for elemental Mo sample after anodic polarization in BSA, PBS and BSA+PBS..... - 168 -

Table 6.7 - Mo 3d XPS quantification for CoCrMo alloy after anodic polarization in BSA, PBS and BSA+PBS. .... - 169 -

## List of Figures

|  |        |
|--|--------|
| Figure 1.1 - X-ray of an artificial total hip replacement [6].   | - 2 -  |
| Figure 1.2 - Wear rate comparison among different hip implants materials [10].   | - 3 -  |
| Figure 2.1 - Market share in USA for MoM hip implants from [34].   | - 10 - |
| Figure 2.2 - Scanning electron micrograph of (a) low carbon (3300x), forged alloy showing small grains ( $< 10 \mu\text{m}$ ), (b) high carbon (3300x), forged alloy showing small grain sizes ( $< 10 \mu\text{m}$ ) and small carbides at the grain boundaries and (c) high carbon, cast alloy showing larger grain sizes (30-100 $\mu\text{m}$ ) and larger carbides at the grain boundaries [55].  | - 15 - |
| Figure 2.3 - The binary Co-Cr phase diagram system [58], with the 27-30% Cr phase field highlighted in red.  | - 16 - |
| Figure 2.4 - Schematic wear process: (a) generation of wear particles; (b) a metal alloy (gray scaffold) with an oxidized surface film on the upper surface (molecules marked in red); (c) damage to the passive surface film (e.g. by scratching or pounding); (d) occurrence of corrosion due to the lack of a protective layer; (e) liberation of soluble compounds and wear particles; and (f) repassivation of the surfaces including wear particles (arrows) [70]. | - 19 - |
| Figure 2.5 - Components of volume loss for CoCrMo high (a) and low (b) carbon in 50% serum, DMEM (Dulbecco's Modified Eagle's Medium, a common cell culture media) and 0.3% NaCl [27]. W is the wear in the absence of corrosion, C represents the corrosion in the absence of wear, and S is the interaction between this two components.   | - 21 - |
| Figure 2.6 - TEM image of a capsular tissue section fixed with osmic acid. The area imaged is the dense macrophage zone, just below the surface of the joint lining. The EDX analysis from region 1 shows an abundance of Cr in comparison with the background spectrum from region 2. There is a suspicion that the iron peaks, in region 3, are due to ferritin. No Co was detected [90].  | - 23 - |
| Figure 2.7 - Examples of particles found within CoCrMo hip joint synovial fluid. Particle A (crystalline) is composed of the raw material, particle B (amorphous) is richer in Cr and Mo and particles C (amorphous) appear to be composed mainly of Cr and O [14].  | - 24 - |
| Figure 2.8 - Transmission electron micrographs of macrophages containing wear debris (a-b) Bright field TEM images show electron dense debris (dark particles) and damaged mitochondria (arrows), (c) HAADF-STEM imaging reveals abnormal nuclear membrane structure (arrows) (d) 3D reconstruction of a volume within a cell, where wear debris appears green [13].   | - 25 - |

- Figure 2.9 - Average concentration and range, calculated from medians, in blood (red) and serum (blue) following various types of MoM hip arthroplasty for (A) Cobalt and (B) Chromium [112] ..... - 27 -
- Figure 2.10 - Amount of (a) Co, (b) Cr, and (c) Mo released from a Co–28Cr–6Mo alloy into PBS solutions containing various BSA concentrations (0–4 g/L) at 37°C following incubation for 8, 14 and 22 weeks in the media. The dashed line shows the analytical detection limit [118]. ..... - 36 -
- Figure 2.11 - TEM bright field image of particles generated by a hip simulator testing of the MoM implant pair in 95% bovine serum for different test periods. (A,B\*) cast alloy after the 0.25 Mc and 1.75–2 Mc test periods, respectively; (C,D\*) micrographs obtained with the high carbon wrought alloy after the 0.25 Mc and 1.75–2 Mc, respectively; and (E,F) low carbon wrought alloy after the 0.25 Mc and 1.75–2 Mc test periods, respectively. \*Due to the smaller number of particles, (B) and (D) show the two areas of a representative micrograph that contained the most particles [135]. - 38 -
- Figure 2.12 - EDX of particles obtained from hip simulator testing of the metal-on-metal implants immersed in 95% serum after the 0.25 Mc test period. (A) representative spectrum with Cr, O, and P (chromium oxide particles most likely from the passivation layer); (B) spectrum with Co, Cr, Mo, and P, C with a higher Cr intensity peak than Co (CoCrMo particles most likely from the carbides); and (C) spectrum with Co, Cr, and Mo, with a higher Co intensity peak than Cr (CoCrMo particles most likely from the matrix material - below the passivation layer and away from the carbides) [135]. C and Cu background noise from the carbon TEM grid. .... - 39 -
- Figure 2.13 - Levels of Co, Cr, and Mo in lubricant from 0.13, 0.5, 3.6, and 11.4 Mc (bottom), levels of Co, Cr, and Mo from 3.6 and 11.4 Mc only (top right) for 39 and 55 mm head size bearing [136] ..... - 40 -
- Figure 2.14 - CoCrMo nanoparticles produced by pin-on-plate test after filtration of immersion fluid onto a 100 nm pore sized membrane filter in a sonic bath for 1 h [109]. ..... - 42 -
- Figure 2.15 - Main stress types in mills, R1 – compression, R2 – shear (attrition), R3 – impact (stroke), R4 – impact (collision), circle – mass of milling media, square – mass of material charge, rectangle – mass of mill wall [140] ..... - 42 -
- Figure 2.16 - TEM images of nanoparticles produced by Milling Fe powders for: (a) 1 hr and (b) 5 hrs, and by milling SmCo5-based powders for (c) 5 hrs and (d) 25 hrs [144] ..... - 45 -
- Figure 2.17 - Cyclic polarization in a typically Evans Diagram for a passive material. .... - 48 -

Figure 2.18 - Cyclic polarization curve for the CoCrMo alloy in aerated PBS at room temperature (pH = 7.4), scan rate of 10 mV/min, with marked potential value applied to the sample during the potentiostatic polarization measurement followed by metal ion release analyses [154]. ..... - 49 -

Figure 2.19 - Composition of the passive layer after oxidation of CoCrMo alloy immersed in Hank's solution as a function of oxidation potential estimated by deconvolution of the peaks in X-ray photoelectron spectroscopy. Thin lines denote the atomic fractions for Co, Cr and Mo in the bulk alloy [50]..... - 49 -

Figure 2.20 - Potentiodynamic polarization curves of CoCrMo in PBS solutions at various BSA concentrations from 0.25 V (OCP) to 1 V (Ag/AgCl) with a scan rate of 0.167 mV/s in aerated conditions at 37°C and pH of 7.4 [131]...... - 50 -

Figure 3.1 - Prosim hip simulator ..... - 53 -

Figure 3.2 - Pin-on-plate experimental scheme..... - 54 -

Figure 3.3 - Spex milling machine used in the experiments ..... - 55 -

Figure 3.4 - Experimental setup to induce electrochemical corrosion ..... - 57 -

Figure 3.5 - X-ray diffraction and Bragg's law..... - 58 -

Figure 3.6 - Electron movement after the incidence of an electron beam ..... - 61 -

Figure 3.7 - Schematic of a TEM..... - 62 -

Figure 3.8 - Relation between MWCO of filters/ ultrafilters and equivalent pore size [179] ..... - 66 -

Figure 3.9 - Schematic diagram of the XPS process..... - 68 -

Figure 3.10 - Particle migration in Zeta Potential ..... - 70 -

Figure 3.11 - CPS disk centrifuge scheme..... - 73 -

Figure 3.12 - XRD of starting CoCrMo ASTM75 powder: (a) low carbon and (b) high carbon. .... - 74 -

Figure 3.13 - SEM of the CoCrMo ASTM75 gas atomized raw material: (a) low carbon and (b) high carbon powder..... - 75 -

Figure 3.14 - SEM/EDX of the CoCrMo ASTM75 gas atomized raw material: (a) low carbon and (b) high carbon powder. .... - 76 -

Figure 3.15 - XRD of the polished surfaces of Co, Cr, Mo and CoCrMo rods. .... - 77 -

Figure 3.16- SEM backscattered electron imaging and EDX mapping of a selected area of the surface of CoCrMo ASTM75 raw material. Image with a scale bar of 2 µm. .... - 78 -

|  |      |
|--|------|
| Figure 3.17 – (a) TEM bright field of a thin section of CoCrMo low carbon standard showing the presence of a mixed phase of CoCrMo (fcc) and Cr <sub>2</sub> O <sub>3</sub> (orthorhombic) (b) on the surface identified by electron diffraction (c) according to ICDD 04-016-6869 and 04-002-5942, respectively. .... | 78 - |
| Figure 4.1 - DLS of ASTM75 CoCrMo low carbon milled for 4h in heptane with 10% oleylamine showing size distribution by: (a) number, (b) intensity and (c) volume. ....   | 86 - |
| Figure 4.2 - Bright field image and EDX of ASTM75 CoCrMo low carbon alloy powder milled for 4h using heptane with 10% oleylamine in steel vial/ beads. ....  | 87 - |
| Figure 4.3 - EFTEM of ASTM75 CoCrMo low carbon alloy powder milled for 4h in heptane with 10% oleylamine in steel vials/ beads: (a) Zero loss filtered image; (b) Cr L <sub>2,3</sub> – edge elemental map. ....   | 88 - |
| Figure 4.4 - Liquid dispersion of CoCrMo particles following wet milling in heptane with 10% oleylamine for (a) 15 min, (b) 30 min, (c) 60 min and (d) 120 min. ....   | 89 - |
| Figure 4.5 - DLS intensity plot of the milled CoCrMo particles at different times. ....  | 89 - |
| Figure 4.6 - SEM secondary electron image of CoCrMo milled for: (a) 15 min, (b) 30 min, (c) 60 min and (d) 120 min. ....   | 90 - |
| Figure 4.7 - SEM-EDX of the micron-sized milled particles: (a) typical CoCrMo with ASTM75 composition, (b) CoCrMo with traces of Zr and (c) Cr-rich particles with traces of Zr. ....  | 91 - |
| Figure 4.8 – TEM bright field images and EDX analysis (wt%) of CoCrMo powder milled for 120 min. ....  | 91 - |
| Figure 4.9 – TEM bright field (a) and dark field (b) images of a CoCrMo particle milled for 60 min. ....   | 92 - |
| Figure 4.10 - TEM bright field image (a) and selected area electron diffraction pattern (b) of CoCrMo particle milled for 60 min. ....   | 92 - |
| Figure 4.11 - Average size of the particles produced during factorial design study as measured by DLS. ....  | 96 - |
| Figure 4.12 – Contamination for samples produced in factorial design study measured by SEM/EDX. ....   | 96 - |
| Figure 4.13 - ANOVA of the effect of variables during milling using size reduction as the response: (a) Normal plot of the effects and (b) Pareto chart of the effects. ....   | 97 - |
| Figure 4.14 - Contour plot of size average for number of balls versus milling time. ....   | 98 - |
| Figure 4.15 - ANOVA of the variables effects of the factorial design 2 <sup>4</sup> during milling using contamination as response: (a) Normal plot of the effects and (b) Pareto chart of the effects. ....   | 99 - |
| Figure 4.16 - Contour plot of Zr contamination for Ball-to-Powder weight ratio versus Milling Time. ....   | 99 - |

|   |       |
|---|-------|
| Figure 4.17 - Optimization plot for the factorial design. ....  | 100 - |
| Figure 4.18 - CPS of milled CoCrMo particles centrifuged for 10 min at 14000 rpm. ....  | 100 - |
| Figure 4.19 - CPS of milled CoCrMo and centrifuged particles for 7 min. ....  | 101 - |
| Figure 4.20 - XRD of CoCrMo particles: (a) after milling and (b) after milling and centrifuged. ....  | 101 - |
| Figure 4.21 - CoCrMo low carbon milled particles in BSA for 2h30, using 3:2 ball-to-powder weight ratio and 3 balls: (a) TEM bright field image; (b) size distribution by TEM image analysis. ....  | 103 - |
| Figure 4.22 - CoCrMo low carbon milled particles in BSA for 2h30, using 3:2 ball-to-powder weight ratio and 3 balls, following centrifugation for 10 min at 14 000 rpm: (a) TEM bright field image; (b) size distribution, by TEM image analysis with an expanded view of the small size region. .... | 103 - |
| Figure 4.23 - Energy Dispersive X-ray Spectroscopy (EDX) of two representative types of CoCrMo ASTM F75 low carbon alloy milled particles: (a) CoCrMo, similar to the raw material and (b) Co and Chromium rich. ....   | 104 - |
| Figure 4.24 - Thermogravimetric analysis of the centrifuged supernatant of CoCrMo milled in BSA for 2h30, using a 3:2 ball-to-powder weight ratio and 3 balls. ....   | 105 - |
| Figure 4.25 - Size distribution of CoCrMo particles generated by Pin-on-Plate for 4 h immersed in BSA using contact pressure of: 5 and 20 MPa. ....   | 107 - |
| Figure 4.26 - TEM bright field image of CoCrMo low carbon wear debris generated from pin-on-plate for 4 h at different contact pressure: (a) 5 and (b) 20 MPa. ....   | 108 - |
| Figure 4.27 – Elemental composition measured by TEM/EDX of pin-on-plate CoCrMo wear debris particles using different loads. ....  | 108 - |
| Figure 4.28 - TEM-EDX of pin-on-plate particles: (a) particles exhibit composition similar to raw material, Cr-rich particles with (b) and without (c) the presence of Mo. ....   | 109 - |
| Figure 4.29 - Thermogravimetric analysis of the solution of CoCrMo low carbon alloy immersed in 20 g/L of BSA diluted in MilliQ water for 4 h during pin-and-plate experiment using 20 MPa load. ....   | 109 - |
| Figure 5.1 - Flow chart with overall tests and analysis undertaken in this section. ....  | 113 - |
| Figure 5.2 - A and B, bright field TEM images of: different types of wear particles from the hip simulator test with Foetal Bovine Serum (FBS) in Phosphate-Buffered Saline solution (PBS) used as the lubricant. ....  | 114 - |
| Figure 5.3 - EDX of the particles generated by hip simulator shown and labelled in Figure 5.2. ....   | 115 - |

|   |       |
|---|-------|
| Figure 5.4 - A and B, bright field TEM images of: different particles in the supernatant of the lubricant following ultracentrifugation at 60,000 rpm for 60 min. ....  | 116 - |
| Figure 5.5 - EDX of particles found on supernatant after ultracentrifugation (60,000 rpm for 60 min) shown are labelled in Figure 5.4: (A) Cr rich particles, (B) Co rich particle. ....  | 117 - |
| Figure 5.6 - Metallic elemental levels in supernatants (8x diluted in MilliQ water) by ICP-MS after different sample preparation procedures, given as the average of duplicate assays, with the error bar indicating standard deviation. The percentage values refer to the relative elemental composition for comparison with the bulk alloy (Co-60%, Cr-29%, Mo-7%). .... | 117 - |
| Figure 5.7 - ICP-MS of Co, Cr and Mo ionic standards in three conditions: only mixed, mixed and passed through ultrafilter (2 kDa MWCO) and finally mixed with BSA+PBS and passed through ultrafilter (2 kDa MWCO). ....  | 119 - |
| Figure 5.8 - CoCrMo high carbon particles after ball milling for 150 min in BSA diluted in deionized water, presenting surface degradation (shear bands) as a consequence of mechanical interactions. ....  | 121 - |
| Figure 5.9 - DLS particle size distributions by number for the high and low after ball milling for 150 min in BSA diluted in deionized water. ....  | 122 - |
| Figure 5.10 - TEM particle size distributions for the high and low carbon alloys after ball milling for 150 min in BSA diluted in deionized water. ....   | 122 - |
| Figure 5.11 – Phase identification by XRD: (a) high carbon raw material, (b) low carbon raw material, (c) high carbon milled material and (d) low carbon milled material, after ball milling for 150 min in BSA diluted in deionized water ....   | 123 - |
| Figure 5.12 - Phase identification in post milled CoCrMo particles by measuring distances between atomic planes in high resolution transmission electron microscopy: (a) hcp phase on high carbon (102), $1.49 \text{ \AA} \pm 0.27 \text{ \AA}$ ; (b) fcc phase on low carbon (102), $2.04 \text{ \AA} \pm 0.27 \text{ \AA}$ . ....  | 124 - |
| Figure 5.13 - Boxplot of TEM/SEM EDX of high and low carbon, raw and milled material. ....  | 125 - |
| Figure 5.14 - ICP-MS of low and high carbon post milled material. ....  | 126 - |
| Figure 5.15 - Ionic release of CoCrMo milled in BSA particles over time, as measured by ICP-MS with centrifugation plus ultrafiltration procedure. ....   | 128 - |
| Figure 5.16 - Ionic release of CoCrMo milled in PBS particles over time, as measured by ICP-MS with centrifugation plus ultrafiltration procedure. ....   | 128 - |
| Figure 5.17 - Ionic release of CoCrMo milled in SSF particles over time, as measured by ICP-MS with centrifugation plus ultrafiltration procedure. ....   | 128 - |

- Figure 5.18 - FTIR spectra of: (a) BSA solution shows peaks of Amide I and II; (b) CoCrMo milled and centrifuged nanoparticles in BSA solution. (c) CoCrMo milled and centrifuged nanoparticles in BSA solution after the use of a 100 kDa MWCO ultrafilter (d) after the use 30 kDa MWCO ultrafilter. .... - 130 -
- Figure 5.19 - TEM analysis of synthetically produced CoCrMo nanoparticles on carbon support film; (A) a group of particles surrounded by a thick amorphous layer; (B) and (C) TEM/EDX of a representative particle, showing a composition consisting of cobalt and chromium with the presence of nitrogen and oxygen, note the deficiency in molybdenum signal (Mo K $\alpha$  is at 17.4 keV).- 132 -
- Figure 5.20 - TEM of reference materials (Co<sub>3</sub>O<sub>4</sub>, Cr<sub>2</sub>O<sub>3</sub> and MoO<sub>2</sub>) as received, which shows particles of less than 200 nm size diameter. .... - 133 -
- Figure 5.21 - TEM/EDX of Co<sub>3</sub>O<sub>4</sub> (JCPDS 42-1467), Cr<sub>2</sub>O<sub>3</sub> (JCPDS 38-1479) and MoO<sub>2</sub> (JCPDS 32-0671) reference materials incubated for 24h in BSA showing an amorphous biolayer containing nitrogen surrounding the particles. .... - 133 -
- Figure 5.22 - ICP-MS of the soluble elements of Co<sub>3</sub>O<sub>4</sub>, Cr<sub>2</sub>O<sub>3</sub> and MoO<sub>2</sub> reference materials incubated for a month in BSA containing stock. .... - 134 -
- Figure 5.23 - Zeta Potential titration of CoCrMo and reference materials in MilliQ water to establish the isoelectric point of the materials. The solution pH was titrated using HNO<sub>3</sub>. .... - 135 -
- Figure 5.24 - Zeta potential titration of reference materials incubated for 24h in BSA and CoCrMo milled in BSA at the same concentration. The solution pH was titrated using HNO<sub>3</sub>. .... - 136 -
- Figure 6.1 - Pourbaix diagram for cobalt in H<sub>2</sub>O, 37°C, molality 0.7 mol/ kg H<sub>2</sub>O, pressure 1 bar, simulated on HSC Chemistry 5.0 software. Lines (a) and (b) designate the limits of thermodynamic stability of water for the given conditions. Below line (a) water is unstable and must decompose to H<sub>2</sub> and above it is stable and any H<sub>2</sub> present is oxidised to H<sup>+</sup> or H<sub>2</sub>O. Above line (b) water is unstable and must oxidize to give O<sub>2</sub> and below it is stable and any dissolved O<sub>2</sub> is reduced to H<sub>2</sub>O. .... - 145 -
- Figure 6.2 - Pourbaix diagram for chromium in H<sub>2</sub>O, 37°C, molality 0.8 mol/ kg H<sub>2</sub>O, pressure 1 bar, simulated on HSC Chemistry 5.0 software. Lines (a) and (b) designate the limits of thermodynamic stability of water for the given conditions. Below line (a) water is unstable and must decompose to H<sub>2</sub> and above it is stable and any H<sub>2</sub> present is oxidised to H<sup>+</sup> or H<sub>2</sub>O. Above line (b) water is unstable and must oxidize to give O<sub>2</sub> and below it is stable and any dissolved O<sub>2</sub> is reduced to H<sub>2</sub>O. .... - 146 -
- Figure 6.3 - Pourbaix diagram using standard hydrogen electrode (SHE) for Cr in solutions containing chloride [212]. .... - 146 -

|   |       |
|---|-------|
| Figure 6.4 - Pourbaix diagram for molybdenum in H <sub>2</sub> O, 37°C, molality 0.4 mol/ kg H <sub>2</sub> O, pressure 1 bar, simulated on HSC Chemistry 5.0 software. Lines (a) and (b) designate the limits of thermodynamic stability of water for the given conditions. Below line (a) water is unstable and must decompose to H <sub>2</sub> and above it is stable and any H <sub>2</sub> present is oxidised to H <sup>+</sup> or H <sub>2</sub> O. Above line (b) water is unstable and must oxidize to give O <sub>2</sub> and below it is stable and any dissolved O <sub>2</sub> is reduced to H <sub>2</sub> O. .... | 147 - |
| Figure 6.5 - Anodic and cathodic polarization in BSA, PBS and BSA+PBS of: (a) Cobalt, (b) Chromium, (c) Molybdenum and (d) CoCrMo.....  | 148 - |
| Figure 6.6 - Secondary electron image of the surface of Co sample after anodic polarization in BSA including EDX analysis of the full area. Image with a scale bar of 10 μm. ....   | 151 - |
| Figure 6.7 - Secondary electron image of the surface of Co sample after anodic polarization in PBS. Image with a scale bar of 100 μm.....   | 152 - |
| Figure 6.8 - EDX mapping of the Co sample after anodic polarization in PBS. Image with a scale bar of 100 μm. ....  | 152 - |
| Figure 6.9 - Secondary electron images of the surface of Co sample after anodic polarization in BSA+PBS and also corresponding EDX mapping. Image with a scale bar of 100 μm. ....  | 153 - |
| Figure 6.10 - Secondary electron images and EDX of Cr samples after anodic polarization in : (a) BSA, (b) PBS and (c) BSA+PBS. Image with scale bar of 2 and 10 μm, respectively. ....  | 154 - |
| Figure 6.11 - SEM electron imaging and EDX mapping of the surface of Mo samples in BSA after anodic polarization. Image with a scale bar of 20 μm. ....   | 154 - |
| Figure 6.12 - SEM backscattered (a) and secondary (b) electron imaging of the surface of Mo sample in PBS after anodic polarization (a). EDX mapping corresponding to the image (a) included. Arrows indicate intergranular corrosion. Image with a scale bar of (a) 100 and (b) 2 μm.....  | 155 - |
| Figure 6.13 - SEM backscattered electron imaging and EDX mapping of the surface of Mo sample in BSA+PBS after anodic polarization. Image with a scale bar of 50 μm. ....  | 156 - |
| Figure 6.14 - SEM secondary electron imaging and EDX mapping of CoCrMo samples after anodic polarization in : (a) BSA, (b) PBS and (c) BSA+PBS. Salt particles are evident in (b) and (c). Images with a scale bar of 10 μm. ....   | 156 - |
| Figure 6.15 - XPS N1s scanning on (a) Co, (b) Cr, (c) Mo and (d) CoCrMo alloy, after anodic polarization in BSA.....  | 158 - |
| Figure 6.16 - XPS N1s spectra for: (a) Co, (b) Cr, (c) Mo and (d) CoCrMo alloy, after anodic polarization in BSA+PBS. ....  | 159 - |

|  |       |
|--|-------|
| Figure 6.17 - XPS C 1s spectra for: (a) Co, (b) Cr, (c) Mo and (d) CoCrMo alloy, after anodic polarization in BSA.....                 | 160 - |
| Figure 6.18 - XPS C 1s spectra for: (a) Co, (b) Cr, (c) Mo and (d) CoCrMo alloy, after anodic polarization in BSA+PBS. ....            | 161 - |
| Figure 6.19 - XPS P 2p spectra for: on (a) Co, (b) Cr, (c) Mo and (d) CoCrMo alloy, after anodic polarization in PBS.....              | 162 - |
| Figure 6.20 - XPS P 2p spectra for: (a) Co, (b) Cr, (c) Mo and (d) CoCrMo alloy, after anodic polarization in BSA+PBS. ....            | 162 - |
| Figure 6.21 - XPS Co 2p spectra for Co in: (a) BSA, (b) PBS and (c) BSA+PBS after anodic polarization.....                             | 164 - |
| Figure 6.22 - XPS Co 2p spectra for CoCrMo alloy in: (a) BSA, (b) PBS and (c) BSA+PBS after anodic polarization.....                   | 165 - |
| Figure 6.23 - XPS Cr 2p spectra for elemental Cr in: (a) BSA, (b) PBS and (c) BSA+PBS after anodic polarization.....                   | 166 - |
| Figure 6.24 - XPS Cr 2p spectra for CoCrMo alloy in: (a) BSA, (b) PBS and (c) BSA+PBS after anodic polarization.....                   | 167 - |
| Figure 6.25 - XPS Mo 3d spectra for elemental Mo in: (a) BSA, (b) PBS and (c) BSA+PBS after anodic polarization.....                   | 168 - |
| Figure 6.26 - XPS Mo 3d spectra for CoCrMo alloy in: (a) BSA, (b) PBS and (c) BSA+PBS after anodic polarization.....                   | 169 - |
| Figure 6.27 - ICP-MS on (a) Co, (b) Cr and (c) Mo after anodic polarization of elemental reference materials.....                      | 171 - |
| Figure 6.28 - ICP-MS in different biological solutions following anodic polarization of CoCrMo low carbon alloy.....                   | 171 - |
| Figure 6.29 - UV-VIS spectra of electrolyte following anodic polarization of CoCrMo and Cr samples in different biological media. .... | 173 - |

## List of Abbreviations

| <b>Acronym</b> | <b>Definition</b>                                      |
|----------------|--|
| AA             | Atomic Absorption                                      |
| ACS-I          | Iron-Supplemented Alpha-Calf Serum                     |
| ANOVA          | Analysis Of Variance                                   |
| ATR            | Attenuated Total Reflection                            |
| BCC            | Body-Centered Cubic                                    |
| BSA            | Bovine Serum Albumin                                   |
| BSE            | Backscattered Electrons                                |
| CoC            | Ceramic on Ceramic                                     |
| CPS            | Centrifugal Particle Sizing                            |
| DLS            | Dynamic Light Scattering                               |
| DMEM           | Dulbecco's Modified Eagle's Medium                     |
| EDX            | Energy Dispersive X-Ray                                |
| EFTEM          | Energy-Filtered Transmission Electron Microscopy       |
| FBS            | Fetal Bovine Serum                                     |
| FCC            | Face-Centered Cubic                                    |
| FEG            | Field Emission Electron Guns                           |
| FTIR           | Fourier Transform Infrared Spectroscopy                |
| HA             | Hyaluronic Acid  |
| HC             | High Carbon  |
| HCP            | Hexagonal Close-Packed                                 |
| HRTEM          | High-Resolution Transmission Electron Microscopy       |
| HSA            | Human Serum Albumin                                    |
| ICDD           | International Centre For Diffraction Data              |
| ICP            | Inductively Coupled Plasma                             |
| IEP            | Isoelectric Point                                      |
| IL-6           | Interleukin-6  |
| JCPDS          | Joint Committee On Powder Diffraction Standards        |
| LC             | Low Carbon   |
| Mc             | Millions Cycles  |
| MHRA           | Medicines And Healthcare Products Regulatory Authority |
| MoM            | Metal on Metal   |
| MS             | Mass Spectrometry                                      |
| MWCO           | Molecular Weight Cut-Off                               |
| NHS            | National Health Service                                |
| NJR            | National Joint Registry                                |
| OES            | Optical Emission Spectrometer                          |
| PBS            | Phosphate Buffered Saline Solution                     |
| SE             | Secondary Electrons                                    |
| SEM            | Scanning Electron Microscopy                           |
| SHE            | Standard Hydrogen Electrode                            |

|               |   |
|---------------|---|
| SSF           | Simulated Synovial Fluid                  |
| STEM          | Scanning Transmission Electron Microscopy |
| TEM           | Transmission Electron Microscopy          |
| TGA           | Thermogravimetric Analysis                |
| THR           | Total Hip Replacement                     |
| TNF- $\alpha$ | Tumor Necrosis Factor-Alpha               |
| UV-VIS        | Ultraviolet-Visible Spectroscopy          |
| XANES         | X-Ray Absorption Near Edge Structure      |
| XPS           | X-Ray Photoelectron Spectroscopy          |
| XRD           | X-Ray Diffraction                         |
| ZP            | Zeta Potential                            |

## **Chapter 1 - Introduction**

A prosthesis is a device implanted in the body to replace an absent organ or to restore a compromised function. These can be external, as in the case of prosthetic legs or arms, or internal, such as artificial teeth, knees or hips. Internal prosthesis are by far more complex, they do not depend only on mechanical properties but also on the surgeon's skills and biocompatibility of the material used.

### **1.1 Hip Replacement: A short overview**

The hip is one of the body's largest joints. This articulation is a ball-and-socket joint, where the ball is the femoral head, which is connected to the cup-shaped cavity of the acetabulum, in the pelvis. The bone surfaces of the ball and socket are covered with a cartilage, a smooth tissue that cushions the ends of the bones and enables them to move easily. A synovial membrane surrounds the hip joint, and in a healthy hip, provides a small amount of fluid that lubricates the cartilage and eliminates most of the friction during hip movement [1].

Some of the main functions of the hip are to support the body weight and balance the body in static and dynamic postures. Problems related to wear or loss of function often appear as a consequence of the high loads involved in hip movement. Arthritis has been the most common cause of hip pain and disability [2]. Although it can develop at any age, it frequently starts between the ages of 40 and 60. This disease can appear in the form of osteoarthritis, rheumatoid arthritis, traumatic arthritis, avascular necrosis and childhood hip disease [3].

Thomas Gluck was accredited with the first hip arthroplasty in 1890, however early reports about total hip replacement (THR) are dated 1950 and 1951 by Sven Kiaer and McKee-Farrar, respectively [4,5]. THR surgery is one of the most successful operations in all of medicine and has been a good alternative for arthritis treatment in terms of chronic pain. This procedure consists of a complete removal and replacement of a diseased ball and socket

of the hip joint with artificial materials. A metal ball with a stem (prosthesis) is inserted into the femur (thigh bone) and an artificial plastic or metal cup socket is placed in the acetabulum (see Figure 1.1).

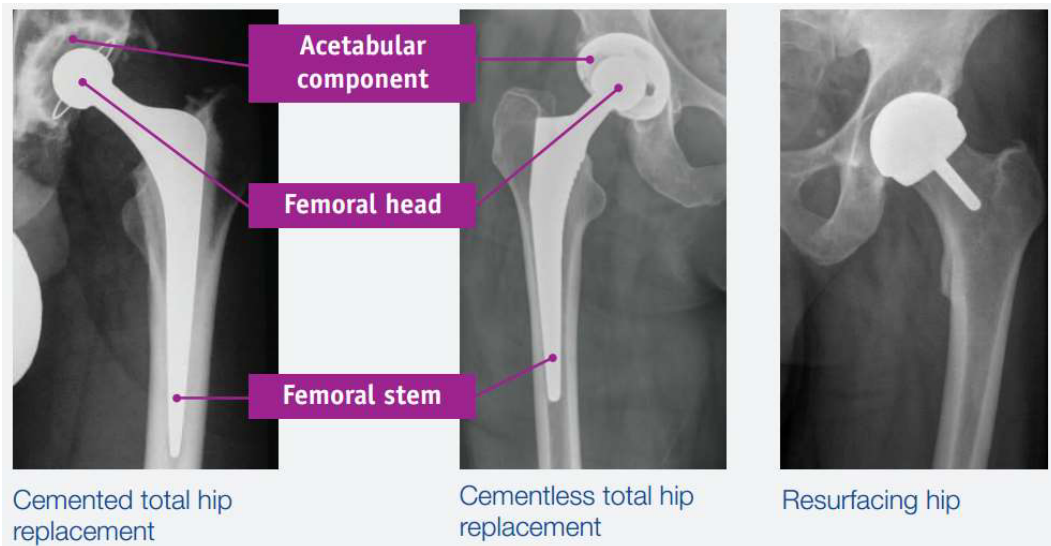


**Figure 1.1** - X-ray of an artificial total hip replacement [6].

The surgery provides significant pain reduction to patients with destructive joint disorders, as well as an improvement of articular function and a better quality of life. The clinical success achieved is based on revision rates and mortality, in which only 1.1% of primary hip replacements have been revised one year after primary surgery rising to 2.3% by year three, 3.5% by year five, and 4.7% by year seven. The risk of death in the first 30 days (0.3%) and 90 days (0.6%) after surgery is found to be similar to the overall risk of revision in these periods [7].

With about 270,000 replacements done each year in the USA, THR became a surgery widely popular in the medical community. The surgery is projected to increase in the USA by 174% between 2005 and 2030 [8]. The situation in England and Wales is similar, the National Joint Registry (NJR) reported that in 2010 there were 76,759 hip replacement procedures recorded, representing a 6% increase compared with the same reporting period in 2009. The same report noted that the mean age of a patient undergoing this surgical procedure is 67 years, however, 12% of patients are younger than 55 years [7].

Although increasing numbers of patients are opting for hip replacements, long term use is still a challenge principally because of the generation of wear particulates. Debris particles are an inevitable consequence of the relative motion between two opposite surfaces in contact. By this means, the removal of material due to mechanical action can generate millions of particles for each movement's cycle, which can then migrate into the tissues surrounding the implants.

For many years, polyethylene wear has been one of the main leading causes of THR failure [9]. The implication of polyethylene wear particles as the dominant cause of osteolysis has renewed the interest in metal-on-metal (MoM) and ceramic-on-ceramic (CoC) implants for total hip arthroplasty, especially because of the potential to improve wear performance.

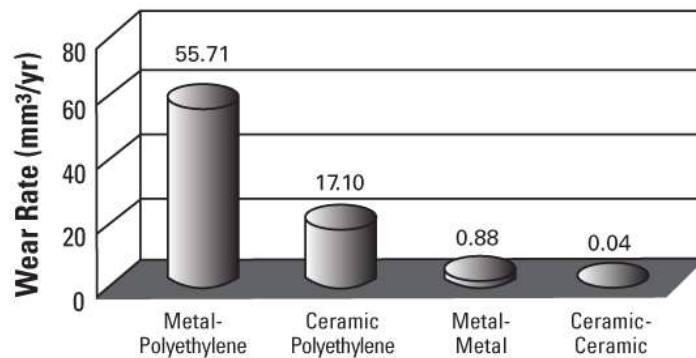


**Figure 1.2** - Wear rate comparison among different hip implants materials [10]

Ceramic-on-ceramic implants, such as Alumina and Zirconia, exhibit good wear performance. However, high product costs and the possibility of catastrophic fracture of the components due to the brittle nature of the material make this kind of joint an unattractive alternative [11].

Around the 1950s, orthopaedic devices started to use implants made entirely of metals, especially Ti alloys, stainless steels and Co alloys, however these were not approved for use in USA until 1999. Ti alloys erode easily under motion conditions, staining the tissues around the implant, and thus limiting the use in orthopaedic implants to pieces as stems [12]. Stainless steels can resist high loads, but are susceptible to crevice corrosion, and are linked to failures

associated with aseptic loosening [13]. Metal-on-metal (MoM) articulation is thus most commonly associated with a cobalt, chromium and molybdenum alloy.

MoM hip implants showed promisingly low wear rates since the first generation (1960), with some devices surviving *in-vivo* for long periods of time (approx. 20 years) [14]. The second generation of MoM (1988) modified the geometry of these implants by improving sphericity and diametral clearance, as well as surface finish, however surprisingly the wear rate and long term use did not show any superior behaviour. The results were attributed to the small head size produced, which increased the frequency of dislocations. The solution was to fabricate a couple with bigger heads, that should decrease the dislocation problem and give lower wear by favouring lubrication of the joint [8,15]. Whereas hip resurfacing has shown promising results with large femoral heads in men but not in women [16], MoM THR failed at high rates in both. The link between the head size of the implant and the MoM failure rate in THR was established by Smith et al (2012), with larger heads failing more quickly, equivalent to a 2% increase in the risk of failure for each 1 mm increase in head size [8]. Langton *et al.* (2012) showed that the failure of larger heads in THR were associated with the taper junction [17].

The apparent low wear rate of MoM hip implants has been recently related to the fact that most debris particles are found to be in the nanometric scale [18,19]. However, due to the small metal particle size, it is estimated that the number of metal particles can be up to 100 times greater than the number of polyethylene particles. Furthermore, the small size of the metal particles vastly increases the total surface area of the metal exposed to the aggressively corrosive environment of the body, increasing the propensity to release metal ions.

Concern about this kind of implant has grown exponentially since the first reports of unexplained failure of MoM implants [20]. Consequently, the nature of the wear debris and the ion release generated by these implants has become of great interest in biomaterials research [21,22].

The term wear implies some mechanical action on the wearing surface whereas corrosion involves the gradual degradation of some material by

chemical reaction with their environment [23]. Corrosion includes two simultaneous reactions: oxidation (dissolution) and reduction. The metal dissolution, when atoms move out of the solid, and leave electrons in it, is possible only if, simultaneously, these electrons are neutralized by the reduction reaction.

Biotribocorrosion of these implants, which are typically fabricated from CoCrMo alloys, involves both corrosion of the implant surface itself, which is stimulated by the wear process removing the passivating protective film, and mechanical wear of the surface to produce wear debris particles [24]. Such nanoparticles can be spread by lymphatic circulation and subsequently corrode. Both processes can therefore give rise to the release of metallic ions. Metal ions may have an inflammatory or toxic effect on cells and tissues, notably because certain metallic ions can complex with proteins and disable the primary function [25,26]. Current studies on CoCrMo alloy implants have indicated that levels of cobalt and chromium ions in the blood and urine rise after replacement surgery and could persist throughout an implant's life [27–29]. As a result there is an ongoing debate concerning the nature and level of the wear debris particles and metal ions released, the transport mechanisms of both the ions and the particles, and any link with inflammation [30].

Whilst the ion release mechanism from the bulk alloy is the focus of many studies, it is not unreasonable to expect further corrosion of particles once detached from the surface of the implant [31–33]. The mechanisms of ion release at this scale are still unclear along with the subsequent interaction between released metal-ions and biological media.

One option is to study *in-vivo* wear debris particles extracted from patients [19] or use experimental models in animals [34]. However, another possibility is to produce wear debris synthetically. The production of nanoparticles by wear of metal-on-metal prostheses can be achieved by using hip simulators that accurately match the loading and motion cycles experienced *in-vivo* and produce results that reflect the clinical wear situation well [21,35,36]. Nevertheless, these types of machine are complex and expensive to produce. Another technique used to generate synthetic wear debris is pin-on-plate, that unlike hip simulators, does not attempt to recreate the *in-vivo* conditions [37,38]. However again this takes a long time to produce a very

small amount of debris nanoparticles. Ball milling powders of the bulk CoCrMo alloy may be a very cost-effective way of producing large volumes of synthetic wear debris.

## 1.2 The Aims

The overall aim of this research project is to establish a new synthetic technique that allows the bulk production of significant amounts of representative CoCrMo alloy wear debris. This will allow the comprehensive testing of the corrosion and toxicity behaviour of such particles.

## 1.3 Objectives

The specific objectives are:

- The bulk production of CoCrMo wear debris with a good approximation to the size, shape and chemical composition of real wear debris found in patients;
- A comparison of the synthesis technique with common techniques already employed to produce CoCrMo wear debris;
- To improve the separation of ions and nanoparticles in solution in order to be able to correctly measure ion release during the corrosion process;
- To test the corrosion behaviour of the nanoparticles during their production in different biological media (dynamic corrosion);
- To compare ion release in terms of incubation time (static corrosion), pH and in the presence of different biological media;
- To test the binding affinity of the particles and ions to proteins;
- To induce corrosion in the alloy and in pure elemental standards by using cyclic polarization in relevant biological media to compare with the behaviour of synthetic wear debris;
- To produce enough particles to perform preliminary toxicological studies.

## 1.4 Chapter overview

This work presents a total of seven Chapters. Chapter 1 provides a short introduction to the work with general information about the hip implant surgery, different biomaterials used in hip implants and the concerns related to them. This is followed by an outline of the project aims and objectives.

Chapter 2 presents a detailed review of previous work on CoCrMo alloys and their properties, their failure, the characterization of wear debris derived from CoCrMo hip implants, the biological response to the degradation products (particles/ions), as well as a review of common methods to simulate wear debris in body simulation fluids.

Chapter 3 discusses all the different methods used to generate wear debris and study the corrosion of bulk and powder CoCrMo alloys. The characterization techniques employed are explained, followed by the sample preparation and the materials used. Analysis of the starting materials are presented at the end of this Chapter and are referenced in later Chapters.

In Chapter 4 an alternative mechanical milling method to generate synthetic wear debris is presented, together with a method for optimization of the process and followed by a validation of the products based on in-vivo characterization studies found in the literature and a comparison with a consolidated method.

Chapter 5 presents the static and dynamic corrosion behaviour of these synthetic particles in relevant media, using a new method to accurately measure the ionic release during biotribocorrosion. The chapter concludes with metal binding studies to proteins, which is essential to explain selective dissolution.

Chapter 6 presents the electrochemical corrosion of CoCrMo alloys and reference materials in biological media with a view to further explain the particle dissolution studies presented in previous chapters.

Final conclusions including the limitations of this study and the potential for future research work in this area are presented in Chapter 7.

## 1.5 Publications

### Papers:

1. **T. A. Simoes**, A.P. Brown, S. J. Milne and R. M. D. Brydson ( 2014). *CoCrMo nanoparticles produced by mechanochemical milling: a route to simulate wear debris from hip implants*, proceedings of XIII Brazilian Materials Research Society.
2. **TA Simoes**, AE Goode, AE Porter, MP Ryan, SJ Milne, AP Brown, RMD Brydson (2014). *Microstructural characterization of low and high carbon CoCrMo alloy nanoparticles produced by mechanical milling*, Journal of Physics: Conference Series, 522, 012059. Doi 10.1088/1742-6596/522/1/012059
3. **TA Simoes**, AP Brown, SJ Milne and RMD Brydson (2015). *Bovine Serum Albumin binding to CoCrMo nanoparticles and the influence on dissolution*, Journal of Physics: Conference Series. [in press]
4. **Simoes T**, Bryant M, Brown A, Milne S J, Ryan M, Neville A and Brydson R (2015). *Quantitative assessment of metal dissolution from CoCrMo alloys during Tribocorrosion*. [Manuscript submitted for publication]
5. Andrea L. Armstead, **Thiago A. Simoes**, Xianfeng Wang, Rik Brydson, Bing-Hua Jiang, Yon Rojanasakul, and Bingyun Li (2015). *Toxicity and oxidative stress response induced by nano- and micro-CoCrMo particles in human cells are cell specific*. [In Preparation]

### Conference Presentations:

1. Synthesis and characterization of Cobalt Chromium nanoparticles by mechanochemical milling route. European Microscopy Congress- EMC 2012, Manchester-UK. Poster Presentation.
2. Microstructural characterization of low and high carbon CoCrMo alloy nanoparticles produced by mechanical milling. Electron Microscopy and Analysis Group Conference-EMAG 2013, York-UK. Poster Presentation.

3. CoCrMo nanoparticles produced by mechanochemical milling: a route to simulate wear debris from hip implants. Brazilian Materials Research Society - BMRS 2014, Joao Pessoa-Brazil. Oral Presentation.
4. Bovine Serum Albumin binding CoCrMo nanoparticles: Study on dissolution effect over the elements on alloy. Microscience Microscopy Congress – MMC 2014, Manchester-UK. Poster Presentation.
5. Electrochemical corrosion of CoCrMo alloy and Co, Cr and Mo pure elements in biological media, Faraday Discussion, Royal Society of Chemistry RSC 2015, London-UK. Poster Presentation.
6. Corrosion of CoCrMo nanoparticles in the presence of biological media. Electron Microscopy and Analysis Group Conference - EMAG 2015, Manchester-UK. Poster Presentation.

## Chapter 2 - Literature Review

The following content presented in this chapter is a review of the literature related to the science of hip joint replacement, metallurgy, crystallography, degradation, wear simulation and interaction with human body, all related to CoCrMo alloys typically used for orthopaedic devices.

### 2.1 Metal-on-Metal hip replacements

Since the National Joint Registry (NJR) started to record data about of total hip replacements (THR) in 2003, up until 2011 Metal-on-Metal (MoM) devices have been implanted in over 31,171 (7.7%) patients in England and Wales of the total 402,051 primary hip replacements [4]. In the USA, statistics show that more than 30% of patients (about 500,000) have used metal-on-metal prostheses [33]. This market in the USA is currently dominated by two brands, Biomet and Depuy, which together hold more than 80% of the market share [34].

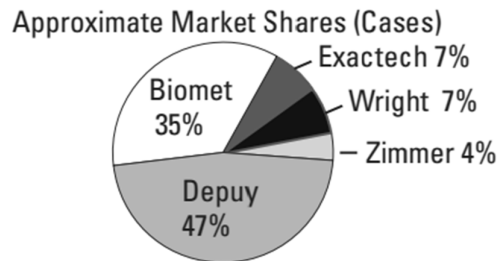


**Figure 2.1** - Market share in USA for MoM hip implants from [34]

Recently, the increasing number of failures of these implants has alerted the medical community to the risk of using MoM implants. The NJR report showed that, overall, 6.2% of MoM hips had failed within five years. At the same point, the failure rate for metal-on-plastic and ceramic-on-ceramic was only 1.7% and 2.3%, respectively [4].

Some studies have raised concerns about metal-on-metal implants in terms of higher revision rates and poorer patient outcomes (related to unexplained pain and function) compared with other bearing surfaces [5].

Following the implant degradation (corrosion/wear), there are concerns about the possibility of metal debris damage to soft tissue surrounding the joint (metallosis) and the uncertain effects of any release of metal ions and particles into the patient's bloodstream [36,37].

### 2.1.1 - Cellular reaction to the implant

Adequate bone healing, after implantation of an orthopaedic prosthesis, depends on a series of successive steps in which numerous cell types such as osteoblasts, osteoclasts and macrophages can play an important role in implant failure [28]. Bone mass is maintained by a balance between the activity of osteoblast cells, that form bone, and other cells called osteoclasts, that break it down. Macrophages, cells derived from monocytes<sup>1</sup>, have the function to phagocytose foreign elements in the body and /or secrete cytokines involved in inflammation activation [38], e.g. IL-6 (Interleukin-6) and TNF- $\alpha$  (Tumor necrosis factor-alpha). Because of this, macrophage cells are the "first line of defence" of an organism, as a result they are also responsible for implant biocompatibility.

Early macrophage interactions with the surface of a prosthesis occur moments after its implant, when surrounding tissues form a 10-100 nm thick biolayer on its surface [39]. The contact with macrophages is mediated by the activation of the complement system<sup>2</sup>, through the adsorption of proteins [40] such as fibronectin and vitronectin that adsorb on the surface of the implant, acting as binder for macrophages. These interactions are the first between the implant surface and macrophages and result in the release of pro-inflammatory cytokines, regardless of the success of the phagocytosis process [41–43]. Rajamaki *et al.* (2013) reported that due to chronic inflammation a local acidification (pH 6.0) could be developed [49].

---

<sup>1</sup> **Monocytes:** a group of cells which has the function of defending the organism from foreign bodies. They are called macrophages when they leave the bloodstream to penetrate a tissue, in order to defend the body against any attacker.

<sup>2</sup> **Complement system:** is a mechanism of the immune system responsible for mediating the inflammatory process with the antibodies. It consists of about 30 soluble and membrane proteins able to disrupt membranes of foreign cells, activate inflammation, enhancing phagocytosis and immune clearance.

Release of metallic ions may occur by both mechanical wear between the bearing surfaces and/or wear debris, as well as through a corrosion process mediated by macrophage contact. In this latter process, called dissolucytosis, macrophages dissolve metal from surfaces too large to be phagocytosed. These macrophages form a membrane of dissolution that is chemically controlled by lysosomes, which have an acid environment (pH about 4.5) potentially capable of dissolving material from implant surfaces [45].

## **2.2 CoCrMo alloy**

Cobalt-based alloys have been used in demanding applications. The characteristics of high-temperature performance (due to low thermal conductivity) and magnetic properties (similar to those of iron), fatigue resistance, corrosion resistance and biocompatibility have been widely explored by industry in several applications that include gas turbines (vanes and static components), orthopaedic implants and dental implants [46,47].

Cobalt-chromium alloys are one of the most common biomaterials used in orthopaedic implants today. The addition of chromium (between 19-30%wt) to cobalt alloys gives a better corrosion resistance due to the spontaneous formation of a passivating layer mainly formed by chromium oxide ( $\text{Cr}_2\text{O}_3$ ), and in minor amounts by Co- and Mo-oxides [48,49]. This protective layer is thought to be 1-4 nm thick [50], acting as a barrier against corrosive body fluids. If there is no metal oxide film formed, the metal surface could easily undergo pitting corrosion. Molybdenum is added to produce finer grains which results in higher strengths after casting or forging with good localized corrosion resistance that makes the surface oxide layer tougher, so chlorides and other pitting agents are less likely to break it down [46,51].

CoCrMo alloys have a high elastic modulus (210–330 GPa) similar to that of stainless steel (approx. 200 GPa) which is much higher than that of cortical bone (20–30 GPa) [46]. They are primarily used where high stiffness or a highly polished and extremely wear-resistant material is required. To achieve mechanical properties and biocompatibility required for CoCrMo alloy for surgical implants, the standard ASTM F75 alloy offers minimal and maximum

chemical specifications for cast alloys (Table 2.1) while ASTM F1537 provides specifications for wrought alloys.

**Table 2.1** - ASTM F75 specifications for chemical composition of cast CoCrMo for surgical implants [57]

| Element     | Composition, %<br>(Mass/Mass) |         |
|-------------|-------------------------------|---------|
|             | min                           | max     |
| Chromium    | 27                            | 30      |
| Molybdenum  | 5                             | 7       |
| Nickel      | ...                           | 0.5     |
| Iron        | ...                           | 0.75    |
| Carbon      | ...                           | 0.35    |
| Silicon     | ...                           | 1       |
| Manganese   | ...                           | 1       |
| Tungsten    | ...                           | 0.2     |
| Phosphorous | ...                           | 0.02    |
| Sulfur      | ...                           | 0.01    |
| Nitrogen    | ...                           | 0.25    |
| Aluminum    | ...                           | 0.1     |
| Titanium    | ...                           | 0.1     |
| Boron       | ...                           | 0.01    |
| Cobalt      | balance                       | balance |

### 2.2.1 - Production of CoCrMo Alloys

The alloy can be essentially categorized as either a Co-Cr-Mo alloy (which is usually used as a cast product) and a Co-Ni-Cr-Mo alloy, (which is usually wrought by hot forging). The castable Co-Cr-Mo alloy has been used in dentistry for a long time and most recently to make artificial joints. The wrought Co-Ni-Cr-Mo alloy is used to make the stems prostheses of heavily loaded joints such as the knee and hip [52]. CoCrMo alloy can form in two crystallographic phases; hexagonal close-packed (HCP) and face-centered cubic (FCC) (see section 2.2.3).

The main difference between wrought and cast alloys is that wrought alloys are ductile enough so as to be hot or cold worked during fabrication, whereas cast alloys are brittle to the degree that shaping by deformation is not possible and they must be fabricated by casting alone [53]. Casting is a fabrication process in which a totally molten metal is poured into a mould cavity

having the desired shape. After the solidification, the metal assumes the shape of the mould with some shrinkage [53]. Biomedical devices produced by casting could contain up to 0.35 wt% carbon to improve castability by lowering the melting temperature to ~1350 °C compared with the normal range of 1450 - 1500 °C. This elemental addition results also in a fine grain size<sup>3</sup> and allows for a decrease in the mould temperature. A wrought alloy is one that is worked by being forged or hammered at temperature and to stabilize the FCC phase which is more ductile than HCP due to an increased number of slip planes, a certain content of Ni, Fe or Mn is also necessary. After hot working, the typical CoCrMo microstructure contains a FCC matrix with fine HCP platelets [46].

These two process used in manufacturing of the alloy produce similar chemical compositions, however, there is a structural difference. The grain size of the wrought alloy is typically less than 10 µm, whereas the grain size for the cast material ranges from 30 to 1000 µm [54]. In addition, Jakobsen *et al.* (2007) showed that toxicological tests suggest as-cast CoCrMo alloy is more inert than wrought CoCrMo, generating less inflammation which might result in less osteolysis [45].

### **2.2.2 - The effect of carbon in CoCrMo alloys**

The ASTM F1537 standard divides wrought CoCr alloys for surgical implants into two categories: high carbon (HC), where the C content is between 0.15 -0.35 wt%; and low carbon (LC), where the C content is less than 0.15 wt%. These implants present differences in surface, structure, roughness, grain size and carbide formation (see in Figure 2.2).

---

<sup>3</sup> A grain is an individual crystal in a polycrystalline metal or ceramic. Grain size is normally quantified by a numbering system (fine or coarse). There are three methods of grain size evaluation, all described and standardized in the ASTM E112 and in related standards. Grain boundaries serve as barriers to dislocation motion; thus refining the grain size of a polycrystalline material renders it harder and stronger [59].

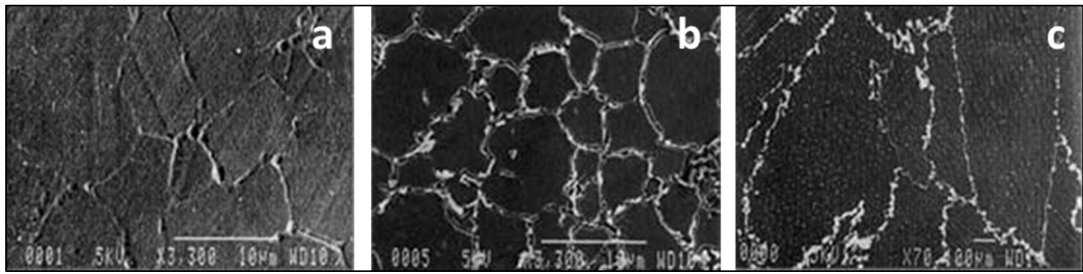


**Figure 2.2** - Scanning electron micrograph of (a) low carbon (3300x), forged alloy showing small grains ( $< 10 \mu\text{m}$ ), (b) high carbon (3300x), forged alloy showing small grain sizes ( $< 10 \mu\text{m}$ ) and small carbides at the grain boundaries and (c) high carbon, cast alloy showing larger grain sizes (30-100  $\mu\text{m}$ ) and larger carbides at the grain boundaries [55]

CoCrMo high carbon alloys show an increase in the formation of carbides, which coexist in large clusters of 30–40  $\mu\text{m}$  size range [49]. The thermal treatment undergone by the alloy defines the size and distribution of the carbides, which could present morphologies as blocky, particulate agglomerated or lamella eutectoid carbides [56]. Bettini *et al.* (2011) showed that Co, Cr and Mo are present in the carbides under different compositions and crystallography, as  $(\text{Cr}_{0.76}\text{Co}_{0.15}\text{Mo}_{0.09})_{23}\text{C}_6$  and  $(\text{Co}_{0.33}\text{Cr}_{0.30}\text{Mo}_{0.29}\text{Si}_{0.08})_6\text{C}$ . The regions containing carbides are harder than the surrounding CoCrMo areas, increasing the strength of the alloy in general, however, carbides could become initial sites for localized corrosion, due to localised depletion of chromium around the carbide during the formation of the particles [49].

Yan *et al.* (2006) studied the tribocorrosion behaviour of high and low carbon alloys tested in biological fluid (50% serum and DMEM), which showed that high carbon alloys had the best performance in terms of friction and low amount of material lost through wear [27].

### 2.2.3 - Crystallography

Two allotropic forms of Cobalt exist: a hexagonal close-packed (HCP) structure, stable up to 417 °C, and face-centered cubic (FCC) structure, stable at higher temperatures. This allotropic metal undergoes a martensitic transformation from  $\gamma$  (FCC) structure to an  $\epsilon$  (HCP) structure when cooled below 450°C. Chromium has a body-centered cubic (BCC) crystal structure.

The binary cobalt-chromium phase diagram (see Figure 2.3) shows the phases present below 2100 °C. The  $\gamma$  phase (FCC) that solidifies directly from

liquid is stable down to about 950 °C, and then the martensitic-like transformation to  $\epsilon$  phase (HCP) can occur. The transformation temperature is raised with an increase in Cr content because the  $\gamma$  phase is stabilized by the addition of Chromium [57].

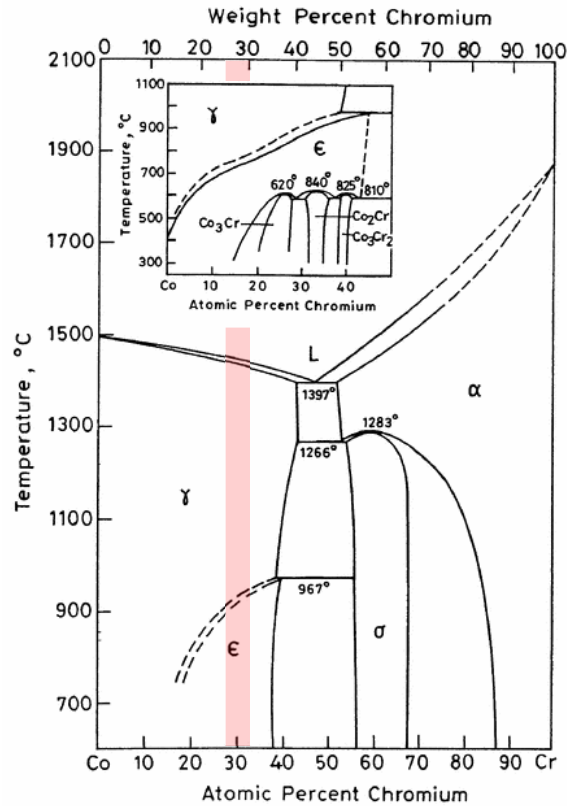


**Figure 2.3** - The binary Co-Cr phase diagram system [58], with the 27-30% Cr phase field highlighted in red.

CoCrMo alloys (containing 27-30 wt% Cr) for hip joints applications exhibit a metastable  $\gamma$  FCC phase for both cast or wrought products. This is due to a sluggish phase transformation, where the  $\gamma$  phase remains metastable instead of initiating the transition to the  $\epsilon$  phase. The sluggishness of the martensitic transformation in cobalt can be explained by the very low free energy difference ( $\Delta G$ ) between  $\epsilon$  and  $\gamma$  [59,60]. The alloy is however susceptible to shear slip and twinning-induced transformation from the FCC to HCP packing structure due to the relatively low stacking fault energy of the alloy [59]. Several studies have demonstrated the role shear plays in the re-

orientation of the CoCrMo alloy, hypothesising improved tribological properties [61,62].

Although the  $\epsilon$  phase increases the strength of the material, the implant can become brittle. Thus, it is essential to suppress the formation of the  $\epsilon$  phase in the as-cast CoCrMo alloys to improve the ductility. The  $\gamma$  phase satisfies the von Mises yield criterion<sup>4</sup>, which is required for good ductility [63]. The control of carbon content is one method for increasing forgeability and ductility of wrought CoCrMo alloys; Carbon additions to the CoCrMo alloys stabilize the  $\gamma$  phase and form inter- and intra- granular carbides.

### 2.3 Hip implant degradation and failure

It was originally expected that CoCrMo hip implants would last longer than conventional MoM implants, and be primarily used by young and highly active people [70]. However, in 2010 the NJR data identified higher than expected revision rates for the MoM implants with 13,61% against to 3.31% to 4.94% from non-MoM. Attention has focused on whether the problems could be associated with the use of larger femoral head sizes and particular designs. Mechanical failure in the form of disruption, decoupling and detachment of bone/implants are well known by the orthopaedists, and are easily detected by a wide variety of tests [71]. However, there are a range of pathologies that need to be further elucidated, in particular “unexplained pain” felt by a significant number of patients that is often related to high levels of metal ions detected in the blood, urine or serum [72–74]. This chronic pain can lead to a changes in the synovial fluid or even of the hip implant, in which the full economic cost of a hip revision is estimated at about £30,000 by the NHS [75,76].

Hip implant degradation is a complex subject, it can be triggered by a combination of physical, chemical and electrochemical reactions, which are known as Tribocorrosion [27]. The degradation caused by mechanical attrition

---

<sup>4</sup> **Von Mises yield criterion** - hypothesis defining the limit of elasticity in a material and the onset of plastic deformation under any possible combination of stresses. If von-Mises stress is greater than the material's yield stress, the material will fail.

between joint counter parts depends on loading and lubrication conditions. Furthermore, these effects can be combined with a corrosion process, in which metal dissolution occurs in the presence of body fluids [69]. According to Yan *et al.* (2006), the tribocorrosion system can be estimated in terms of total material loss (T) by the following equation:

$$T = W + C + S$$

**Equation 1 - Total materials loss in tribocorrosion**

Where  $W$  is the wear in the absence of corrosion,  $C$  represents the corrosion in the absence of wear, and  $S$  is the interaction between this two components.  $W$  can be determined by measuring the materials under cathodic protection, in order to protect the material from corrosion.  $C$  is usually determined by measuring the corrosion rate for a static system by using mass spectrometry to measure dissolution into the surrounding media. Examples of each quantification can be seen in the follow publications: [33,78,79].

Physical activities result in higher loads on the hip joint, increasing the propensity for the implant to fail; Friction, impact and compression are the physical reactions most relevant [70]. Damm *et al.* studied six patients (5 male, 1 female, mean age  $58 \pm 7$  years, body mass  $86 \pm 6$  kg, height  $174 \pm 5$  cm) during walking simulation and observed a median peak in resultant load of 266% of the body weight [71].

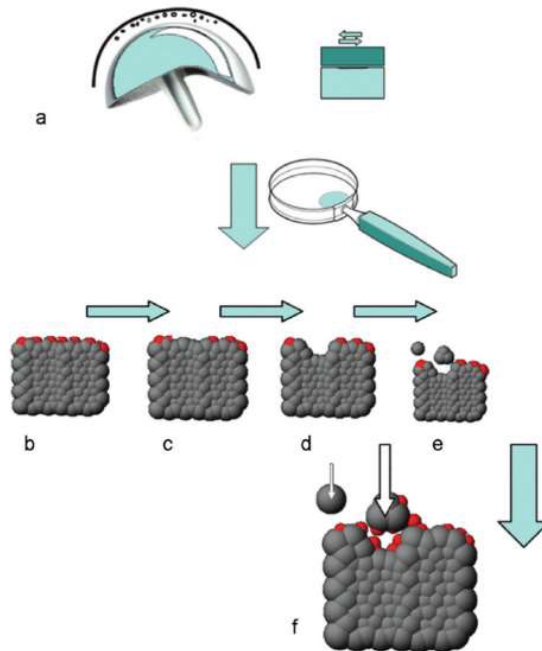


**Figure 2.4** - Schematic wear process: (a) generation of wear particles; (b) a metal alloy (gray scaffold) with an oxidized surface film on the upper surface (molecules marked in red); (c) damage to the passive surface film (e.g. by scratching or pounding); (d) occurrence of corrosion due to the lack of a protective layer; (e) liberation of soluble compounds and wear particles; and (f) repassivation of the surfaces including wear particles (arrows) [70].

Friction effects in combination with shear stresses could heat the contact surface during high loading, long lasting activities [72]. The peak temperature in implants with polyethylene cups can rise up to 43.1 °C after an hour of walking, but this can vary considerably depending on each individual [73]. Wimmer *et al* (2001) stated that the temperature at joint surfaces could possibly reach ~70 °C at a hard carbon-carbide contact [74]. This increase in temperature could start and/ or accelerate the corrosion process by basically increasing the conductivity of electrolytes, so increasing the electrochemical reactions that could take place [75].

Hip replacement wear debris in the human body can be generated by the articulating surfaces, but also from fretting wear of screws and the head against the stem [86,87]. Basically, this damage occurs at the asperities of contact surfaces between the bone and the stem/ screws, and is induced by vibrations of small amplitude. Silva *et al*. (2002) studied the average walking

activity of patients with well-functioning total hip replacements which was found to be close to 2 million cycles per year [78]. It is estimated that the processes can generate about  $64 \times 10^6$  nano- and micro- sized particles per cycle [88,89], that are released into the surrounding tissues, and could eventually migrate through the bloodstream to various part of the body such as the kidney and liver. The wear particles that remain between the joint counter parts can also contribute to degradation. These entrapped particles can act as an abrasive by scratching the bearing surface [80]. This process not only damages the joint surface, but also helps to decrease the size of the debris by grinding the particles.

The damage does not occur only where the joints are in contact, but anywhere where there is a tribological influence in combination with a corrosive fluid [69]. It is well known that proteins, presumably from synovial fluid, form an organic layer surrounding the implant, which changes the uppermost 50 to 200 nm of the surface [72]. The real contribution of these proteins to corrosion and/or wear is still a matter of controversy in the scientific community. Some studies [81,82] have found that proteins can enhance the corrosion of some metal alloys, whilst others researchers [83,84] have shown corrosion reduction. Yan *et al.* (2006) reported that although proteins can act as a lubricant and reduce friction, they can enhance material degradation due to an effect on corrosion and tribocorrosion processes [18]. The same group quantified the different tribological contributions in CoCrMo high and low carbon alloys in different environments, where corrosion accounts for between 22-47% of the total volume loss in 4 h, the remainder being attributed to mechanical wear (Figure 2.5).

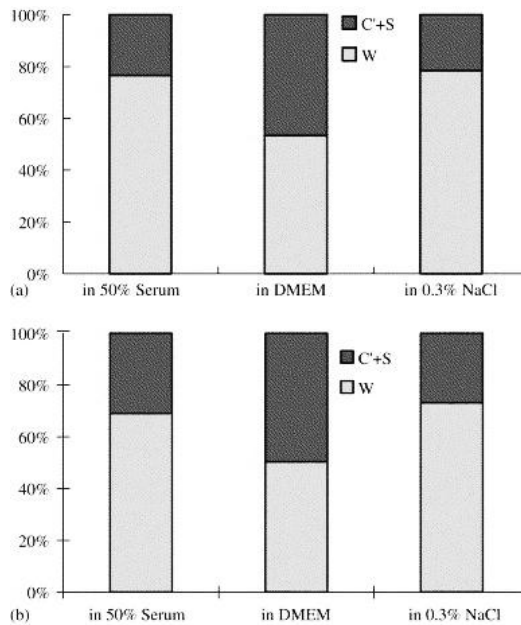


**Figure 2.5** - Components of volume loss for CoCrMo high (a) and low (b) carbon in 50% serum, DMEM (Dulbecco's Modified Eagle's Medium, a common cell culture media) and 0.3% NaCl [27]. W is the wear in the absence of corrosion, C represents the corrosion in the absence of wear, and S is the interaction between these two components.

## 2.4 Specification of wear debris and metal ions collected from patients with MoM hip implants

Despite the low wear rate from MoM hip implants (see Figure 1.2), the wear debris generated from these systems tend to be much smaller than in other systems, in the nanometre size range. It is estimated that these implants could annually produce between  $6.7 \times 10^{12}$  to  $2.5 \times 10^{14}$  wear particles [89], thus even a small volume of implant wear can produce a large number of nanoparticles.

The release of metal ions can vary in composition and amount, depending on the type of implant and time implanted. The ionic radius of the species released from CoCrMo can vary from a few picometers according to the ionic charge and spin: Co 67-88.5 pm, Cr 58-94 pm and Mo 73-83 pm [95]. The oxidation state of the material and the oxidising species generated can provide valuable clues to any inflammatory response. Metal ion release occurs when the stable oxide layer is mechanically or chemically disrupted, producing a flow of metal ions. Metal oxide particles are produced, and metal ions are dissolved

from the base of the alloy while the oxide film is restored [85]. Even metal implants unaffected by dynamic or static loads will still release metal ions when exposed to liquids [86,87].

Another potential source of metal ion release is the nanometre-size of the wear debris. According to the Ostwald-Freundlich relation, particle solubility is inversely proportional to particle size. The small size of metal particles vastly increases the total surface area of the metal exposed to the aggressively corrosive environment of the body, however only a few researchers have explored this corrosion contribution [32,88]. In addition, the changes in pH level in different cellular regions and in different regions of the human body could accelerate ionic release.

#### **2.4.1 - CoCrMo alloy wear debris**

Particle characterization is based on identifying size, morphology and chemical composition and a wide range of different sized wear debris particles from hip implants have been identified. Goode *et al.* (2012) noted that particle size and principally composition strongly depends on the time between particle generation and tissue collection for analysis, as well as how the tissue/particle structure is preserved during analysis [13].

Most publications isolate wear particles from serum, using protocols involving a series of washes with enzymatic solutions, centrifugation to concentrate the particles and sonication to re-suspend them, avoiding chemical degradation by the use of digestion reagents [17,89]. It is potentially possible however that during sample preparation, a fraction of the very small wear debris particles are lost when removing the supernatant (see Section 5 5.1.2).

Hart *et al.* (2010) analysed tissue from 6 MoM patients with unexplained failure of implants from four manufacturers. they used TEM/EDX (Figure 2.6) and also Microfocus X-ray spectroscopy using a synchrotron beam to assess the composition of wear particles in tissue; there being a relatively low particle concentration [90]. This study revealed Cr (III) phosphate in all four implant types analysed. Cobalt (Co) and molybdenum (Mo) were occasionally present in areas of high Cr. Co was normally found in a metallic state in the tissue, while Mo was found in an oxidized state.

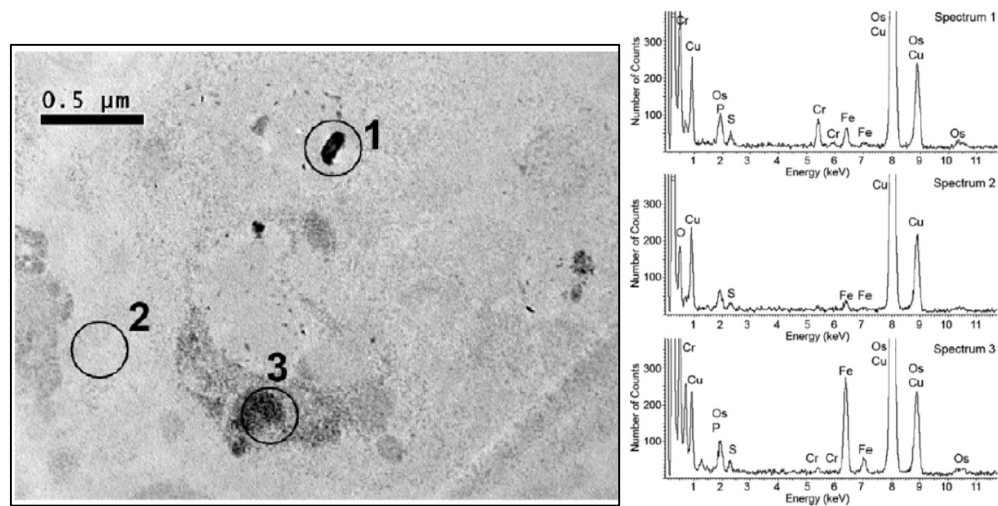


**Figure 2.6** - TEM image of a capsular tissue section fixed with osmic acid. The area imaged is the dense macrophage zone, just below the surface of the joint lining. The EDX analysis from region 1 shows an abundance of Cr in comparison with the background spectrum from region 2. There is a suspicion that the iron peaks, in region 3, are due to ferritin. No Co was detected [90].

Ward *et al.* (2010) analysed by TEM/EDX particles from the synovial fluid of failed CoCrMo hip implants (Figure 2.7), identifying metal wear debris ranging from 5 to 50 nm and agglomerations where particles were clustered inside the fluid. Particles were identified in three main compositions: close to that of the CoCrMo raw material; particles richer in Cr and Mo; and particles mainly composed of Cr and O [14].

Goode *et al.* (2012) examined nanoparticles from the tissue surrounding failed MoM hip implants using TEM/EDX (Figure 2.8), finding a large size distribution that varied from a few micrometres down to a few nanometres. Wear debris was commonly found clustered in areas of 1 μm. Most of the particles were spherical with a mean size of 30 nm and composed primarily of Cr. Chemical speciation was made using Scanning Transmission X-ray Microscopy and X-ray Absorption Spectroscopy, here two types of wear debris could be identified: a diffuse phase containing mainly Cr<sup>3+</sup> with trace amounts of oxidised Co; dense core-shell particles containing metallic Co, Cr and Mo in the core which was surrounded by Cr<sup>3+</sup>. Mo was only detected in a few particles, co-localised with metallic Co and was absent from the oxidised debris [13].

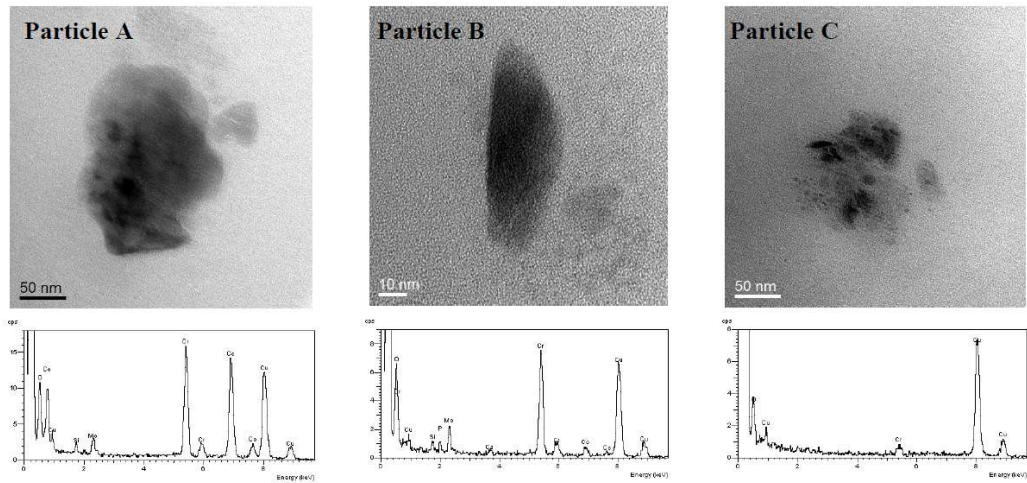


**Figure 2.7** - Examples of particles found within CoCrMo hip joint synovial fluid. Particle A (crystalline) is composed of the raw material, particle B (amorphous) is richer in Cr and Mo and particles C (amorphous) appear to be composed mainly of Cr and O [14].

Despite the most recent publications indicating Chromium oxides and phosphates as the main metallic wear debris found in implant surrounding tissue, this chemical specification could be a result of the decomposition of CoCrMo particles or from the raw implant surface due to corrosion, wear or a combination of both. The surface of the implant is known to be composed of a variety of chemical forms such as oxides ( $\text{Cr}_2\text{O}_3$ ,  $\text{CoO}$ ,  $\text{Co}_3\text{O}_4$ ,  $\text{MoO}_2$  and  $\text{MoO}_3$ ) [50,91], hydroxides ( $\text{Cr}(\text{OH})_3$ ,  $\text{Co}(\text{OH})_2$ ) [50,92], metal phosphates ( $\text{CrPO}_4$ ,  $\text{Co}_3(\text{PO}_4)_2$ ) [90], and pure metal (CoCrMo) [19]. Consequently, it could be possible that wear debris is formed from different microstructural regions, associated with the implant surfaces.

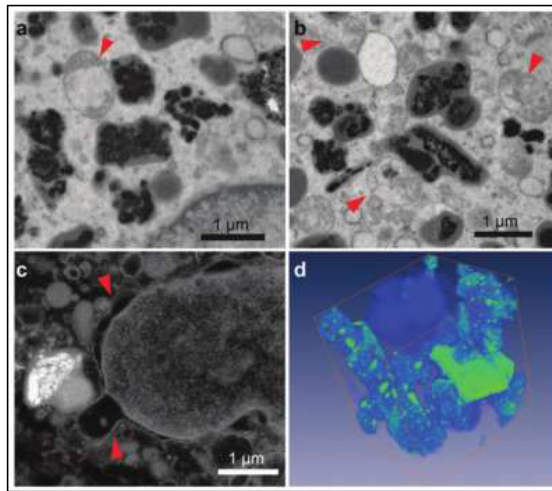


**Figure 2.8** - Transmission electron micrographs of macrophages containing wear debris (a-b) Bright field TEM images show electron dense debris (dark particles) and damaged mitochondria (arrows), (c) HAADF-STEM imaging reveals abnormal nuclear membrane structure (arrows) (d) 3D reconstruction of a volume within a cell, where wear debris appears green [13].

#### 2.4.2 - Metal ions

Several studies have shown an increase in metal ion levels after receiving MoM orthopaedic implants [93–95], however, there is no agreed threshold for the levels of Co, Cr and Mo that could indicate the failure of the joint. Sidaginamale *et al.* (2013) studied metal blood/serum levels in 3042 patients. These showed background concentrations of 1.5 µg/l for Cr and 0.5 µg/l for Co and only 3.22% and 0.033% patients presented concentrations > 2 µg/l for Cr and Co [107]. Hart *et al.* (2009) proposed acceptable upper limits of 2.56 µg/L for Cr and 2.02 µg/L (ppb) for Co in the whole blood [96]. Also, the Medicines and Healthcare Products Regulatory Authority (MHRA) suggests that if either cobalt or chromium ion levels are elevated above 7 µg/l a second test should be performed in order to identify patients who require closer surveillance and if the results persist, could indicate potential for soft tissue reaction.

It is also important to take into account the valence state of these metal ions, in light of the fact that species such as hexavalent chromium, have been associated with cytotoxic and genotoxic effects [97]. Metal ions complexed with proteins could also play an important role in terms of impact on the immune system [98].

Metal ion levels have been recorded in patients by the use of atomic absorption (AA) or inductively coupled plasma (ICP) mass spectrometry. In UK, most of the ICP-MS samples from hip patients are analysed at the Trace Elements External Quality Assessment Scheme (TEQAS). TEQAS can cover specimens that have been prepared using serum, whole blood, urine or dialysis fluids and drinking water as the base material, spiked with various concentrations of trace elements covering clinically relevant ranges. The source of the samples varies however these are mainly blood, urine or serum, meaning that results are not directly comparable. Smolders *et al.* (2011) proposed a formula to convert serum ion levels to blood levels, with prediction error below  $\pm 1.0 \mu\text{g/L}$  [99]:

$$\begin{aligned} \text{Cobalt in blood} &= 0.34 + [0.88 * \text{Co in serum}] \\ \text{Chromium in blood} &= 0.14 + [0.58 * \text{Cr in serum}] \end{aligned} \quad \begin{array}{l} \text{Equation 2 – Conversion of ions} \\ \text{levels from blood to} \\ \text{serum} \end{array}$$

Jantzen *et al.* (2013) did a careful review of 43 studies of Co and Cr ion concentrations analysed in blood and serum from different types of MoM hip implants [100]. The average Cr concentration ranged between 0.5 and 2.5  $\mu\text{g/L}$  in blood and between 0.8 and 5.1  $\mu\text{g/L}$  in serum. For Co, the range was 0.7–3.4  $\mu\text{g/L}$  in blood and 0.3–7.5  $\mu\text{g/L}$  in serum. An estimate of the average Co/Cr ratio for blood was calculated to be  $1.4 \frac{\text{max } 6.8}{\text{min } 0.3}$ , while for serum this was  $1.3 \frac{\text{max } 9.4}{\text{min } 0.1}$ .

The Ultima TPS modular MoM hip (DePuy, Leeds, UK) has a very poor clinical result [35], however it showed relatively low Co and Cr ion release according to the results of Clarke *et al.* (2003) [95] (shown in Figure 2.9). Although, serum Cr and Co levels have been shown to be a reliable indicator of anomalous wear and the risk of implant failure, they are not good predictors of immune system reaction.

Only a few researchers have included molybdenum for *in-vivo* ICP-MS quantification of dissolution from MoM hip implants. Savarino *et al.* (2002, 2006) did not find any significant change in Mo ion levels from serum samples relative to control samples [94, 101]. Masse *et al.* (2003) analysed samples from

blood and urine, and found that Co and Cr levels increased in both compared to pre-operative values, however Mo levels increased in urine only [21].

Figure 2.9 shows the average (mean<sup>5</sup>) of Cr and Co serum or blood ion concentrations calculated for the different implants, and used to compare with the upper acceptable limit proposed for Cr and Co in blood.

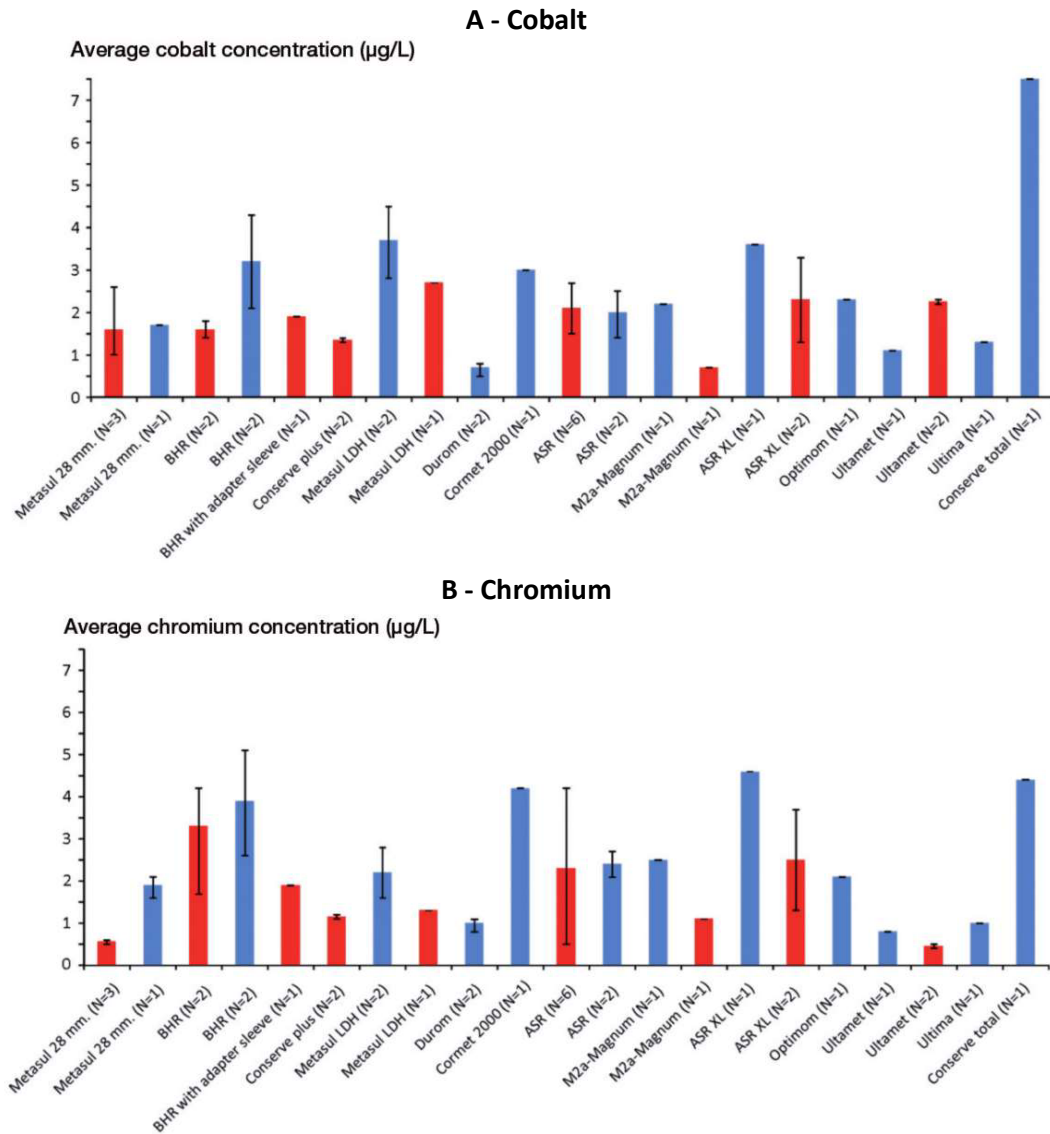


**Figure 2.9** - Average concentration and range, calculated from medians, in blood (red) and serum (blue) following various types of MoM hip arthroplasty for (A) Cobalt and (B) Chromium [112]

<sup>5</sup> **Mean** - refer to one measure of the central tendency either of a probability distribution or of the random variable characterized by that distribution.

## 2.5 Biological responses to CoCrMo wear debris and ions

Owing to the small size and large number concentration, nanoscale wear debris and also metal ions released by MoM implants could travel from the surrounding tissue to other parts of the body through the lymphatic system. Urban *et al.* (2000) showed that even micro-sized wear particles from metal on polyethylene (MoP) hip implants were found in lymph nodes, bone marrow and liver [102].

The biological response to metal nanoparticles and ions is complex, and involves a series of factors including protein adsorption and cellular migration [45]. Some reports have shown that monocytes/macrophages secrete cytokines (e.g., IL-6 and TNF $\alpha$ ) in response to metal ions and particles (Kaufman *et al.*, 2008). The particular binding of metallic ions and proteins may change their toxicity depending on partitioning between the free and bound forms.

Local tissue responses linked to MoM hip joints have been associated with wear rate, dose, patient susceptibility and immune reactions, but there are still controversial reports about the real contribution of wear debris to hypersensitivity reactions. Doorn *et al.* (1998) showed that pseudotumors could be initiated by CoCrMo wear debris [89] and Pandit *et al.* (2008) associated pseudotumours with metal-on-metal hip resurfacings. However, Matthies *et al.* (2012) concluded that pseudotumors are present in MoM patients but are unrelated to the wear rate, suggesting that this effect is instead related to patient pre-disposition [103].

Recently, some studies showed that Co could be the most relevant chemical species for triggering tissue reactions. Hart *et al.* (2012) conducted *in-vivo* investigations using Synchrotron radiation (4  $\mu$ m probe) of tissue sections extracted from regions adjacent to Ultima MoM implants as well as from non-Ultima MoM implants; both implants being constructed from both high (cup liner and stem) and low carbon (head) CoCrMo ASTM F75 alloys. The Co/Cr ratio found in periprosthetic tissue from Ultima was 1:1, while non Ultima was 1:10. Chromium phosphate was shown to be the predominant species in tissue surrounding the non-Ultima implants, however analysis of tissue surrounding the Ultima MoM implants revealed a mixture of metallic Co with a significant

amount of Co (II) as the main species together with some Cr phosphate [104]. In another paper from the same authors [90], they attempted to identify the chemical form of the metallic debris in tissues surrounding MoM hips following unexplained failure, XANES spectra of Mo identified octahedrally coordinated Mo, which was bound by oxygen and carbon. This was likely to be organic carbonyl ligands binding to Mo, although the data do not cover a sufficient energy range to be definitive about the speciation. It is known however that most metal carbonyls can produce a toxic effect [105,106].

An increase in the bioavailability of wear debris and ions after contact with serum and other body fluids could represent a significant danger for MoM patients. Rizzetti *et al.* (2009) reported a case of high metal concentrations even after the removal of the implant and an ion chelating treatment [23]. This report attributed loss of sight and sound to the implant fail. The patient partially recovered vision only after 8 months of chelating treatment to decrease metal ions levels.

### 2.5.1 - Toxicity of particles

For toxicological studies, often a large amount of particles is required to measure dose response effects. Particle size and shape may affect the cellular uptake; nanosized particles are taken up in most all types by pinocytosis<sup>6</sup> and endocytosis<sup>7</sup>, whereas larger particles are internalised by macrophages only [107].

Caicedo *et al.* (2009) showed that cobalt alloy particles 1-10  $\mu\text{m}$  in size with the composition of the ASTM F75 standard, induced activation of the inflammasome in human macrophages [108]. Papageorgiou *et al.* (2007) tested CoCr alloy particles, ranging from nano (30 nm) to micro size (2.9  $\mu\text{m}$ ), in human fibroblasts. Nano-sized particles were seen to dissolve faster and in the first 3 days caused more DNA damage and cell death [109]. Kwon *et al.* (2009)

---

<sup>6</sup> **Pinocytosis** - ingestion of liquid into a cell by the budding of small vesicles from the cell membrane.

<sup>7</sup> **Endocytosis** - process whereby cells absorb solid material outside their cell membranes and can be triggered by protein receptors in the cell membrane.

studied the dose-dependent cytotoxicity of cobalt and chromium nanoparticles (30-35 nm in size); cytotoxicity was observed only for cobalt nanoparticles at a concentration of  $10^{12}$  particles/mL [110].

### 2.5.2 - Toxicity of ions

Particular attention has been paid to Cr ion release from CoCrMo implants because of the potential hazard of the chromium VI valence state [111], which is known to be carcinogenic, cytotoxic and genotoxic to human lung cells [97]. However, the formation of this species in the human body is unlikely as the Pourbaix diagram for Cr in water at 25 °C suggests toxic chromium VI is released only at  $\text{pH} > 7$  and at high electrode potentials. The species generated under acidic conditions is  $\text{Cr}^{3+}$ , which has a much lower correlation with toxicological issues [112–114].

Catelas *et al.* (2003) tested both  $\text{Co}^{2+}$  and  $\text{Cr}^{3+}$  in macrophage cells, demonstrating a dose- and time-dependent response. Maximum cell death with  $\text{Co}^{2+}$  occurs at lower concentration than for  $\text{Cr}^{3+}$  [25]. Caicedo 2009 showed that all metal ions tested ( $\text{Co}^{+2}$ ,  $\text{Cr}^{+3}$  and  $\text{Mo}^{+5}$ ) produced from soluble  $\text{CoCl}_2$ ,  $\text{CrCl}_3$  and  $\text{MoCl}_5$  salts that can induce human macrophage pro-inflammatory responses through inflammasome multiprotein complexes in a concentration-dependent manner [108]. Akbar *et al.* (2011) studied the effects of  $\text{Co}^{2+}$  and  $\text{Cr}^{6+}$  exposed to human lymphocytes and the cells were found to be more sensitive to  $\text{Co}^{2+}$ . Using higher doses, cell proliferation and cytokine release decreased and apoptosis<sup>8</sup> increased [115].

## 2.6 Synthetic approaches to generating wear debris and metal ions

Due to the increasing medical concern with metal nanoparticles/ ions released by MoM hip implants and the implications of this not yet being very

---

<sup>8</sup> **Apoptosis** - the death of cells that occurs as a normal and controlled part of an organism's growth or development.

well understood, several studies have been conducted for the elucidation of the problem. Some of these studies have used analysis of nanoparticles arising from revisions of hip implants [18,19]. During this procedure, the synovial fluid or surrounding tissue is removed from patients and isolation of the particles by chemical treatment is used for a subsequent microstructural characterization. Studies beyond simple characterization cannot be done, as a result of the low amount of debris and the difficulties in properly isolating the particles without their alteration or damage.

Hip simulators are realistic models, which are heavily utilised and are able to realise a complete study of wear utilizing desired loading cycles and different surface charges to represent normal walking or high impact activities [30]. Joint simulators have become accepted tools to evaluate new prosthetic systems. Most recently the use of simulators has been redirected to produce and analyse MoM wear particles [17]. The process gives a good approximation of the particles produced *in-vivo* but they may still differ in size and composition. In addition, simulators are complex machines with a high cost to build and maintain.

Another technique used to generate wear debris and evaluate wear is the pin-on-plate method. This is a simple technique that, unlike hip simulator machines, does not attempt to recreate the *in-vivo* conditions, however it can simulate sliding speeds and contact stresses between two surfaces incubated in relevant biological media.

The aim of this thesis is to explore methods for obtaining nanoparticles that match with the nanoparticles released by MoM hip implants. A simple and effective method of powder preparation is mechanical attrition and dispersion by means of ball mills, which have found considerably application in the last 20 years [116]. The similarity of the mechanical process of friction/fracture during grinding compared to the generation of wear debris from implants makes milling a good route to synthetically produce these nanoparticles. Furthermore, high energy milling is capable of producing nanoparticles in bulk quantities. The presence of a surfactant increases the dispersion of the powder and changes the particle shape [117]. Despite the advantages, the process has been underexplored in this type of application, and in this sense, there are a scant number of publications in this field.

### 2.6.1 - Body fluid simulation

Body fluids have been proved to contribute to the degradation of biomaterials [81,118]. The fluid produced at the membrane in the joint, so-called synovial fluid, has been largely simulated by researchers, using a variety of combinations based on serum proteins. The most abundant protein in the human body is serum albumin, but specifically synovial fluid composition is more than 60% human serum albumin that is combined with  $\alpha$ -1-globulin,  $\alpha$ -2-globulin,  $\beta$ -globulin and  $\gamma$ -globulin [132].

The ISO standards (14243-1 and 14243-3) for knee simulation tests recommend the use of calf serum diluted with deionized water to a total protein concentration as low as 17 g/L. Nevertheless there are no recommendations for specific biochemical characteristics such as protein constituent fractions [119]. The fluid simulation composition from ISO is based on healthy joints, which contains 15-25 g/L of protein concentration. However, it is known that joints with diseases have much higher protein concentrations (in the range 36–54 g/L) [120].

Several researchers studied the ideal lubricant to simulate synovial fluids based on healthy joints [134–137]. However, Brandt *et al.* (2010) analysed different synovial fluid simulations comparing them with the composition of joints that suffered from osteoarthritis [119]. The results indicated that a combination of iron-supplemented alpha-calf serum (ACS-I) diluted in phosphate buffered saline solution (PBS) and adding Hyaluronic acid (HA) at a concentration of 1.5 g/L produced a more clinically relevant lubricant for simulation studies.

**Table 2.2** - Characteristics of Calf Sera from HyClone used for synovial fluid simulation [119]

| ACS-I                    |          |
|--------------------------|----------|
| Lot #                    | AQE23894 |
| Albumin (%)              | 66.3     |
| $\alpha$ -1-globulin (%) | 4.5      |
| $\alpha$ -2-globulin (%) | 8.2      |
| $\beta$ -globulin (%)    | 19.2     |

|                             |        |
|-----------------------------|--------|
| <b>γ-globulin (%)</b>       | 1.1    |
| <b>Total protein (g/L)</b>  | 41     |
| <b>Fe (mmol/L)</b>          | 0.0877 |
| <b>Ca (mmol/L)</b>          | <0.5   |
| <b>Inorganic P (mmol/L)</b> | <0.2   |
| <b>Mg (mmol/L)</b>          | 0.08   |
| <b>pH</b>                   | 7.71   |
| <b>Osmolality (mmol/kg)</b> | 283    |

### 2.6.1.1 - Serum Albumin

Serum albumin is a well-established protein for simulating body fluids. Human Serum Albumin (HSA) is a single-chain protein with a molecular weight of 66.5 kDa, containing 609 amino acids organized to form a heart-shaped protein [138]. The amino and carboxyl terminal sequences are present in man, cow and several other species. HSA has functions as a major antioxidant and transport protein. The morphology is a repeating series of helical subdomains that form a triangular shape with sides of ~8 nm and depth of ~3 nm. It is present as roughly 67% alpha-helical form with the remainder in turns and extended polypeptide form [122]. However, when the alpha-helix structure is decreased, the beta-sheet structure is increased. The current theory on knee simulations suggests that frictional processes contribute significantly to this conformational change, with a combination of shear stresses and a rise in local contact temperatures causing protein degradation. Polypeptides may degrade and become sheared into low-molecular-weight polypeptides that remain in the lubricant solution [123].

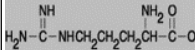
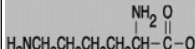
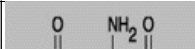
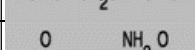
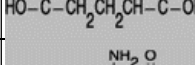
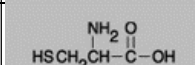
The isoelectric point (IEP) of HSA is about pH 5. There are pH-dependent conformational changes named neutral to basic transitions. The neutral and basic forms of HSA can bind ligands with different binding affinities. In phosphate buffer at about pH 6, HSA is in the neutral conformation and at pH 9 the base form is predominant [124]. HSA can serve as an almost universal transport and depot protein in the circulation since it can bind reversibly a large number of compounds. There are two major binding regions named site I and II in HSA which are related to binding aromatics and heterocyclic compounds [125].

The source of HSA is very limited and expensive, as it has to be donated from human plasma. Also, it carries the risk of transmission of pathogenic

viruses. Bovine albumin serum (BSA) has a similar structure to HSA, and is a more viable way to do relevant simulation studies.

BSA is a protein that is negatively charged at pH > 5 and exhibits an IEP between 4.7 and 4.9 pH [126]. In order to find out which amino acids govern BSA adsorption at which pH, Rezwan *et al.* (2005) calculated a protein-specific amino acid charge distribution at pH 7 [127]. Only Arginine and Lysine are positively charged and Aspartic acid and Glutamic acid negatively charged, while Histidine, Cysteine and Tyrosine do not carry any charge.

**Table 2.3** - Properties of the main amino acids present in BSA. Values collected from [127–129].  $pK_a$  is the negative logarithm of the dissociation constant for the  $-COOH$  group, and  $pK_b$  for the  $-NH_3^+$  group.

| Amino Acid    | IEP [pH] | % in 100g | Molecular Weight [Da] | Polarity               | $pK_a$ | $pK_b$ | Structure   |
|---------------|----------|-----------|-----------------------|------------------------|--------|--------|---|
| Arginine      | 10.76    | 5%        | 174.20                | Polar (Hydrophilic)    | 2.17   | 9.04   |    |
| Lysine        | 9.74     | 12%       | 146.19                | Polar (Hydrophilic)    | 2.18   | 8.95   |   |
| Aspartic acid | 2.77     | 9%        | 133.11                | Polar (Hydrophilic)    | 1.88   | 9.60   |  |
| Glutamic Acid | 3.22     | 15%       | 147.13                | Polar (Hydrophilic)    | 2.19   | 9.67   |  |
| Histidine     | 7.59     | 3%        | 155.16                | Polar (Hydrophilic)    | 1.82   | 9.17   |  |
| Cysteine      | 5.07     | 6%        | 121.16                | Nonpolar (Hydrophobic) | 1.96   | 10.28  |  |
| Tyrosine      | 5.66     | 5%        | 181.19                | Nonpolar (Hydrophobic) | 2.20   | 9.11   |  |

BSA particularly has been shown to play a diverse role in interacting with biomaterials at predetermined conditions. Vidal *et al.* (2010) studied the thermodynamics of the adsorption process of BSA onto CoCrMo, showing that the molecules have a strong affinity for the CoCrMo surface, with the gain in entropy representing the driving force for the adsorption process [130]. Also, the adsorption was suggested to be an endothermic process and the molecule

suffers structural changes when adsorbing onto the metallic surface. Karimi *et al.* (2011) showed that BSA enhances the alloy passive film stability at concentrations greater than 0.4 mg/ml [131]. Duong *et al.* (2012) showed that friction of the CoCrMo femoral head is dependent on the concentration of BSA, but there is a limit to the concentration (30 mg/ml) which can act as an effective boundary lubricant [132]. Immersion time was studied by Vidal and Munoz (2008), who showed time modifies the interface behaviour of the CoCrMo by decreasing the resistance of the passive film in the albumin solution (0.5 mg/ml mix with 0.14M NaCl) and increasing the resistance in Phosphate Buffered Solution (PBS) [48]. Espallargas *et al.* (2014), undertook CoCrMo alloy electro corrosion tests in albumin, and observed an increase in Mo concentration released into electrolyte when a potential was applied below the transpassive region, corresponding to ~53-62% of the total ions released from the alloy [133].

#### **2.6.1.2 - CoCrMo corrosion under incubation in Simulation Body Fluid**

Karimi *et al.* (2012) studied long term corrosion of CoCrMo pellets (to represent implants) in PBS solution with various concentrations of BSA (0, 0.2, 0.4, 2.0, 4.0 g/L) [118]. The results showed that all the samples lost weight up to 14 weeks and then started to gain weight. Inductively coupled plasma-optical emission spectrometer (ICP-OES) results, after an incubation period, showed that mainly Co and Mo were released from the alloy, and this started to decrease after 14 weeks (Figure 2.10). The decrease in dissolution and the increase in weight after 14 weeks was attributed to the precipitation of dissolved ions on the surface of the pellets.

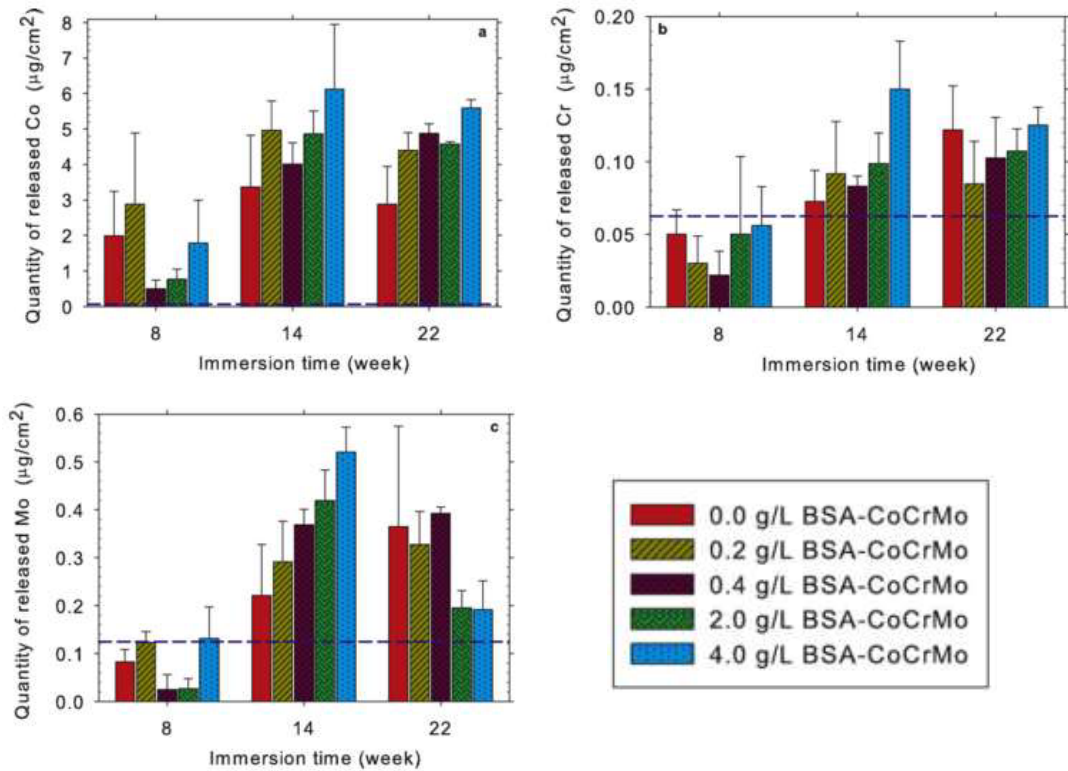


**Figure 2.10** - Amount of (a) Co, (b) Cr, and (c) Mo released from a Co–28Cr–6Mo alloy into PBS solutions containing various BSA concentrations (0–4 g/L) at 37°C following incubation for 8, 14 and 22 weeks in the media. The dashed line shows the analytical detection limit [118].

Metikoš-Huković *et al.*, (2006) carried out incubation studies using Co, Cr, Mo and CoCrMo alloy pellets immersed in Hank's solution<sup>9</sup> at pH 6.8. The results showed that Co and Mo pure metals released significantly more ions than the alloy (about x1000), while Cr dissolution from the alloy was slightly higher than that from pure Cr. By decreasing the pH to 2.0, the quantities of all metal ions released from the alloy increased. The same trend was observed for pure metals, except Mo, whose stability increased when the pH of the solution was decreased [134].

---

<sup>9</sup> **Hank's solution** - composed of a group of salts rich in bicarbonate ions, that are used as a buffer system in cell culture media and aid in maintaining an adequate physiological pH (roughly 7.0-7.4) for cellular growth.

### 2.6.2 - Hip Simulators

Hip joint simulators are a complex three-dimensional articulation that targets faithful reproduction of the physiological conditions of time/ loads at bearing surfaces. They provide control of variables such as speed, sliding distance and direction of movement; frequency, direction and magnitude of loading; as well as the chemical composition of the fluid and the temperature in the contact zone.

Firkins *et al.* (2001) investigated the size of wear debris from MoM low and high carbon hip implants generated by simulators and found a similar wear debris size of 25-36 nm [29]. Catelas *et al.* (2003) analysed wear particles from MoM hip simulator testing of high and low carbon wrought CoCrMo alloys and cast CoCrMo alloy tested in BSA (Figure 2.11). After 0.25 million cycles (Mc), similar particle sizes and shapes were found for all CoCrMo alloys tested. Particle length averaged about 52 +/- 4 nm, there was up to 21% needle-shaped particles composed mainly of CoCrMo, but the majority of particles remained round to oval in shape, composed mainly of chromium oxides [135].

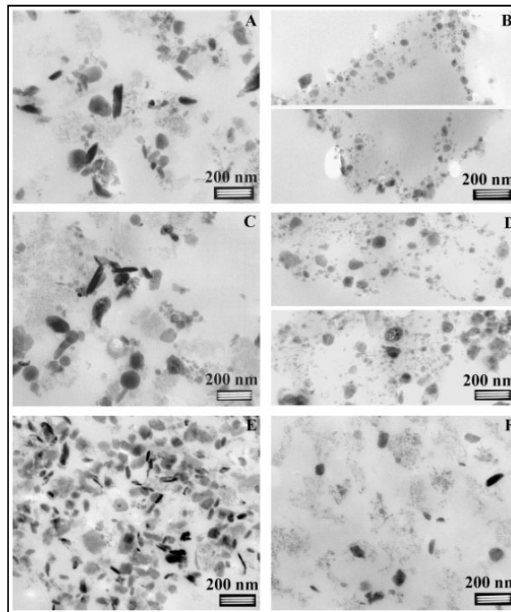


**Figure 2.11** - TEM bright field image of particles generated by a hip simulator testing of the MoM implant pair in 95% bovine serum for different test periods. (A,B\*) cast alloy after the 0.25 Mc and 1.75–2 Mc test periods, respectively; (C,D\*) micrographs obtained with the high carbon wrought alloy after the 0.25 Mc and 1.75–2 Mc, respectively; and (E,F) low carbon wrought alloy after the 0.25 Mc and 1.75–2 Mc test periods, respectively. \*Due to the smaller number of particles, (B) and (D) show the two areas of a representative micrograph that contained the most particles [135].

The wear debris particle composition determined by Catelas *et al.* (2003) (Figure 2.12) indicated that particles from the 1.75–2 Mc test period (steady-state wear) showed proportionally more chromium oxide particles and fewer needle-shaped particles (mainly CoCrMo) compared with those from the 0.25 Mc test period (run-in wear) [135].

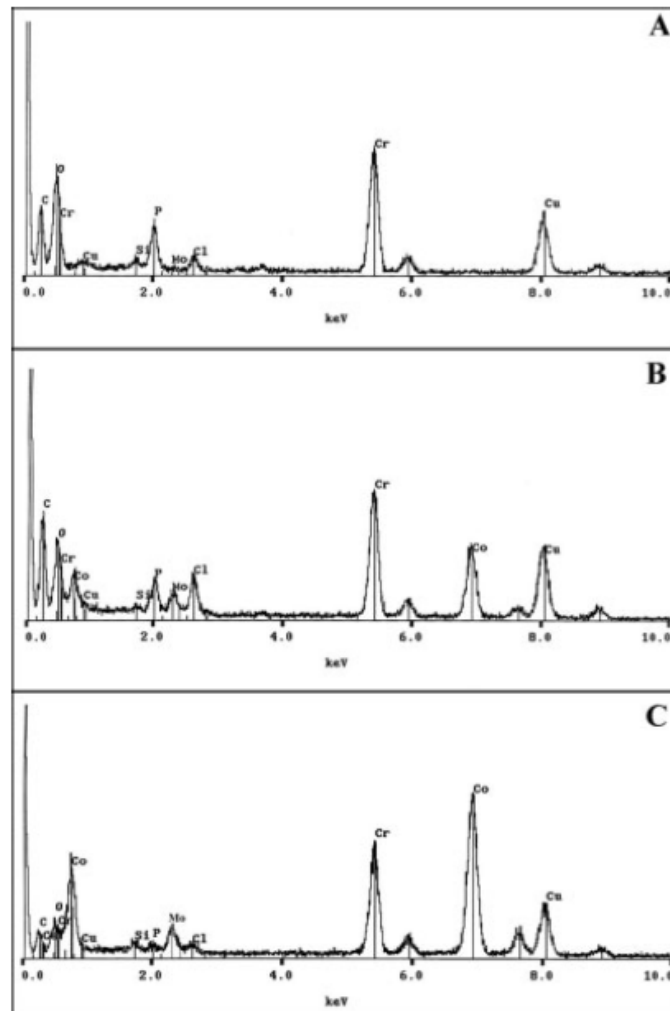


**Figure 2.12** - EDX of particles obtained from hip simulator testing of the metal-on-metal implants immersed in 95% serum after the 0.25 Mc test period. (A) representative spectrum with Cr, O, and P (chromium oxide particles most likely from the passivation layer); (B) spectrum with Co, Cr, Mo, and P, C with a higher Cr intensity peak than Co (CoCrMo particles most likely from the carbides); and (C) spectrum with Co, Cr, and Mo, with a higher Co intensity peak than Cr (CoCrMo particles most likely from the matrix material - below the passivation layer and away from the carbides) [135]. C and Cu background noise from the carbon TEM grid.

Leslie *et al.* (2008) tested MoM bearing sizes of 55 mm and 39 mm in a hip simulator for 15 Mc in a Newborn serum, analysing wear debris and ions released [136]. The wear debris isolated was oval in morphology in the size range 9–108 nm (mean size of 28 nm). Prior to ICP-MS, nitric acid microwave digestion was employed to dissolve wear particles. The Co levels measured at 0.13 Mc were significantly greater than at 3.6 Mc for both bearing sizes. After

0.5 Mc, the Co levels from the 39 mm bearings were significantly higher than for the 55 mm.

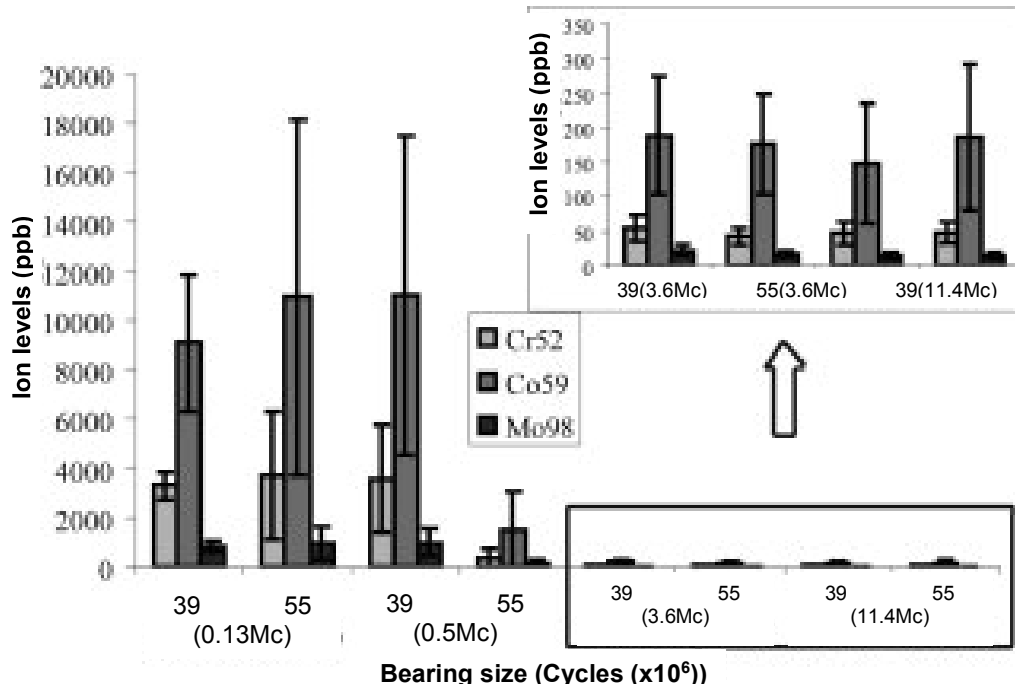


**Figure 2.13** - Levels of Co, Cr, and Mo in lubricant from 0.13, 0.5, 3.6, and 11.4 Mc (bottom), levels of Co, Cr, and Mo from 3.6 and 11.4 Mc only (top right) for 39 and 55 mm head size bearing [136]

Hesketh *et al.* (2013) studied metal ion formation during 1 Mc hip simulator tests in Foetal bovine serum diluted in PBS (18 g/L). The cumulative ionic release was determined by ICP-MS at 1/3, 2/3 and 1 Mc. ICP-MS samples were mixed with an equal volume of 5% nitric acid, centrifuged at 14,000 rpm for 10 min and then the supernatant was collected and filtered through a 0.4  $\mu$ m filter. At 1/3 and 2/3 Mc, the ratio of Cr, Co and Mo ions was fairly constant throughout the test: 29%, 59–60%, and 11–12%, respectively. At 1 Mc, there was more variation, Cr, Co and Mo abundance varied between 16–26%, 60–72% and 11–14%, respectively [25]. These values are close to the relative amounts of Cr, Co and Mo in the base alloy.

### 2.6.3 - Pin-on-plate

A pin-on-plate or pin-on-disc tribometer is an instrument that is used to investigate friction and wear properties of solid materials, both with and without a lubricant. Frictional behaviour is measured in terms of the coefficient of friction of sliding contact between a pin and a disc, whereas wear coefficients can be calculated by measuring the volume of material lost during the test. The wear factor can be calculated according to the equation [137]:

$$W_s = M_{loss} / w \times s \times \rho$$

**Equation 3 - Wear factor**

where  $M_{loss}$  is mass loss,  $w$  is the normal load,  $s$  is the sliding distance, and  $\rho$  is the density of the specimen.

Chen *et al.* (2014) studied wear using low and high carbon CoCrMo alloys in pin-on-disc tests under Hank's solution. The pin was mounted with a 9.8 N load and tested against a disc rotating at 20 mm/s (24 rpm). The temperature was set to 37°C in an argon atmosphere, and the rotation radius was 8 mm. The test was performed over a continuous period of 16.8 h, resulting in a total volume loss of ~0.32 mm<sup>3</sup> (2.61mg) and ~0.38 mm<sup>3</sup> (3.1 mg) for low and high carbon alloys, respectively [138].

Papageorgiou *et al.* (2007) produced CoCrMo nanoparticles (29.5 ± 6.3 nm in size) with a pin-on-plate MoM bi-directional motion machine set to a speed of 56 mm/s and a contact stress of 11 MPa over a 24 h period in water. The nanoparticles were found to be uniformly round to oval. The authors did not indicate the composition after the experiment, as well as the exact amount of wear debris produced, but they did mention that there was not enough nanoparticles for all toxicological studies [109].

Hank's solution and water used in the experiments cited before are not a good model to represent the synovial fluid and could generate different wear debris particles in terms of morphology and composition. However, the use of distilled water would facilitate the separation and sterilization of these for toxicological studies.

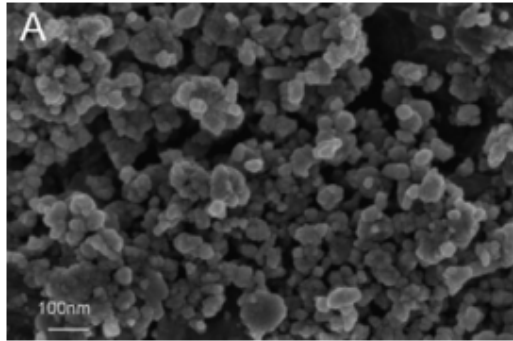


**Figure 2.14** - CoCrMo nanoparticles produced by pin-on-plate test after filtration of immersion fluid onto a 100 nm pore sized membrane filter in a sonic bath for 1 h [109].

### 2.6.4 - Mechanochemical Milling

Milling is a solid-state powder processing technique involving repeated welding, fracturing, and re-welding of powder particles in a high-energy ball mill [116]. The repetition of this phenomenon favours solid-state reactions leading to the formation of thin lamellar structures [139].

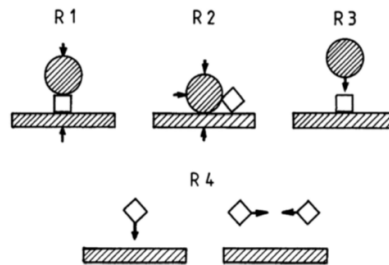


**Figure 2.15** - Main stress types in mills, R1 – compression, R2 – shear (attrition), R3 – impact (stroke), R4 – impact (collision), circle – mass of milling media, square – mass of material charge, rectangle – mass of mill wall [140]

What distinguishes milling from other grinding processes is that fracture and welding of the particles both occur. The fracture of the particles creates atomically clean surfaces that provide sites for chemical reactions. Therefore, the process requires an inert atmosphere for sample preparation prior to grinding if additional chemical charge to be avoided. The welding of particles may occur when these surfaces are forced together during subsequent collisions. Then, reactions may occur along this new inner surface [116].

The minimum energy required in a collision is the energy capable of providing enough power to enable fracture and welding occur. Any additional energy will simply accelerate the process, which occurs as a consequence of the increased plastic deformation and heating of the particle.

Particle size reduction is effected over time in the high-energy ball mill, as is a reduction in crystallite size, both of which reach minimum values at extended milling times [141]; this also depends on ductility of material being milled, as well as the vial/ balls employed.

The milling atmosphere plays an important role in the size reduction. Raghu *et al.* (2001) concluded that milling in air is appropriate to the welding process because particle size initially decreases and then increases, whereas fracture is dominant in milling under argon [142].

Most recently, milling has been used to form nanoparticles in new materials such as polymers [143] and metals [144], and improvements in the milling process that optimize the formation of nanoparticles continue to be made.

Most techniques to obtain nanoparticles from milling operate in a liquid media [117,144,145] to avoid the agglomeration formed after the welding process. Such a process is known as a mechanochemical route, where a chemical reaction is produced at the same time as mechanical deformation. This synthesis provides some advantages such as the control of particle morphology and size distribution.

A constant concern related to the milling process is contamination. These impurities arising from the milling media may be associated with the time of milling, the intensity of milling, the atmosphere in which the powder is milled, and the differences in the strength/hardness of the powder and the milling medium [116]. Fritsch has summarized the properties of materials used for milling media (Table 2.4).

**Table 2.4** - Main vials and balls materials used in high-energy milling [163]

| Material         | Main composition               | Density (g cm <sup>-3</sup> ) | Abrasion resistance |
|------------------|--------------------------------|-------------------------------|---------------------|
| Agate            | SiO <sub>2</sub>               | 2.65                          | Good                |
| Corundum         | Al <sub>2</sub> O <sub>3</sub> | > 3.8                         | Fairly good         |
| Zirconium oxide  | ZrO <sub>2</sub>               | 5.7                           | Very good           |
| Stainless steel  | Fe, Cr, Ni                     | 7.8                           | Fairly good         |
| Tempered steel   | Fe, Cr                         | 7.9                           | Good                |
| Tungsten carbide | WC, Co                         | 14.7–14.9                     | Very good           |

Despite the wide number of contamination issues, this problem can be minimised with good control of the experimental parameters, leading to low levels of contamination (less than 1 at%) [129].

### *Mixer Mill*

A wide diversity of mills are currently available. They differ in their capacity, efficiency of milling and additional arrangements for cooling, heating, etc. Shaker mills such as SPEX, mill about 10–20 g of powder at a time and are most commonly used for laboratory investigations and for alloy screening purposes. Most of the mills have one vial containing the sample and milling balls, secured in the clamp and swung energetically back and forth several thousand times a minute. The back- and- fourth shaking motion is combined with lateral movements of the end of the vial, so that the vial appears to be describing a figure eight or infinity sign as it moves [140].

Because of the amplitude (about 5 cm) and speed (about 1200 rpm) of the clamp motion, the ball velocities are high (of the order of 5 m/s), and consequently the force of the ball's impact is usually high [141,147].

### *Surfactants*

The term surfactant (surface-active-agent) designates a substance which exhibits some interfacial activity [148]. Surfactants may act as detergents, wetting agents, emulsifiers, foaming agents and dispersants.

Surfactants have been used with the milling technique to prevent aggregation and stabilize separated nanoparticles and may also be used to minimize contamination. This effect is achieved because the surfactant creates

a layer surrounding the particles, providing a barrier that prevents close contact of the fine particles. The coil dimensions (mileage) of surfactants are usually larger than the range over which the attraction forces between nanoparticles are active [149].

About 1–5 wt.% of the total powder charge in the mill is typically the percentage of surfactants that are used in mechanochemical milling [116]. Parameters such as composition and quantity of surfactants used and the type of powder milled determine the final size, shape, and purity of the powder particles. Use of a larger quantity of surfactants normally reduces the particle size by 2–3 orders by magnitude [149]. Lomayeva *et al.* (1999) showed that the presence of a surfactant enhances the dispersion in the resulting powders, and changes the particle shape [117].

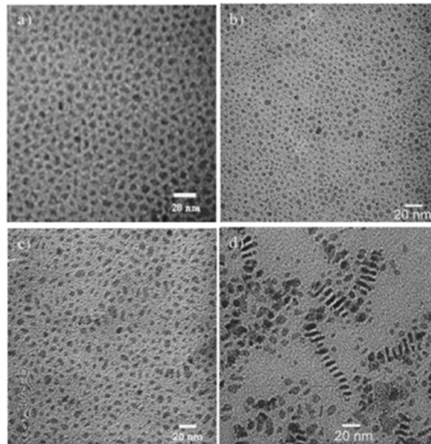
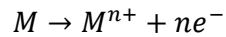


**Figure 2.16** - TEM images of nanoparticles produced by Milling Fe powders for: (a) 1 hr and (b) 5 hrs, and by milling SmCo5-based powders for (c) 5 hrs and (d) 25 hrs [144]

Chakka *et al.* (2006) showed a successful production of nanosize Fe particles using a mixture of heptane (99.8% purity) plus oleic acid (90% purity) or oleylamine (98% purity) as a solvent. During the experiment there was no significant change in morphology of the nanoparticles with milling times of up to 50 h [144].

## 2.7 - Electrochemical corrosion of hip implant alloys

Many corrosion phenomena can be explained in terms of electrochemical reactions. Biomaterials are susceptible to aqueous corrosion, which arises when a chemical or electrochemical reaction occurs on a metallic surface immersed in an aqueous electrolyte [48]. During this reaction, oxidation or removal of electrons from metal atoms and the reduction of oxidising agents or consumption of electrons by an oxidizing agent can both occur. Equation 4 represents the generalised equation for the anodic reaction where M represents a Metal:



**Equation 4 - Anodic reaction**

In order for corrosion to occur, electrons need to be consumed by cathodic reactions with the production of hydrogen, oxygen and water. At thermodynamic equilibrium, the rate of metal oxidation is balanced by the cathodic reactions. As a result, metal cations are released into solution, while the electrons are left inside the metal, forming an electric double layer with a potential difference across the metal surface. The metals with more negative potentials are more reactive to corrosion. From the Table 2.5, the potentials of Co, Cr and Mo are all negative, indicating that they are all reactive in aqueous solutions even in the absence of an applied potential [150].

**Table 2.5 - Co, Cr and Mo aqueous reaction**

| Reaction   | Potential [V] |
|--|---------------|
| $Cr^{2+} + 2e^{-} \leftrightarrow Cr$            | -0.91         |
| $Cr^{3+} + 3e^{-} \leftrightarrow Cr$            | -0.74         |
| $Cr(OH)_3 + 3e^{-} \leftrightarrow Cr + 3OH^{-}$ | -1.48         |
| $Co^{2+} + 2e^{-} \leftrightarrow Co$            | -0.28         |
| $Co(OH)_2 + 2e^{-} \leftrightarrow Co + 2OH^{-}$ | -0.73         |

|  |       |
|--|-------|
| $Mo^{3+} + 3e^{-} \leftrightarrow Mo$                | -0.20 |
| $MoO_2 + 4H^{+} + 4e^{-} \leftrightarrow Mo + 4H_2O$ | -0.15 |
| $MoO_3 + 6H^{+} + 6e^{-} \leftrightarrow Mo + 3H_2O$ | -0.07 |

Biomaterials are known to exhibit active-passive behaviour. The passivation behaviour and effects of inhibitors or oxidizers on specimens can be assessed by potentiodynamic polarization, where the samples are scanned in both the anodic and cathodic directions, indicating localised and general corrosion behaviour. Figure 2.17 represents a cyclic polarization curve of a passive material<sup>10</sup>. The metal is cathodic at potentials below the corrosion potential ( $E_{corr}$ ). As the potential is increased, passing the corrosion potential ( $E_{corr}$ ), the metal becomes anodic and remains active in the potential region just above the corrosion potential ( $E_{corr}$ ) until the passivation potential ( $E_{pp}$ ). However, when the maximum point of anodic dissolution is met ( $i_{cc}$ ) the current density drops to a very low value, called the passive current density ( $i_p$ ). This current drop is characterised by the formation of a protective oxide layer. During passivation, the metal could also corrode but at a significantly lower rate. When the material is in the transpassive region, there is a disruption of the passive layer, and the material starts to quickly corrode. How much the material will corrode, depends on the electrolyte [151].

---

<sup>10</sup> Note: here the independent variable (potential) is often plotted as the ordinate for historical reasons.

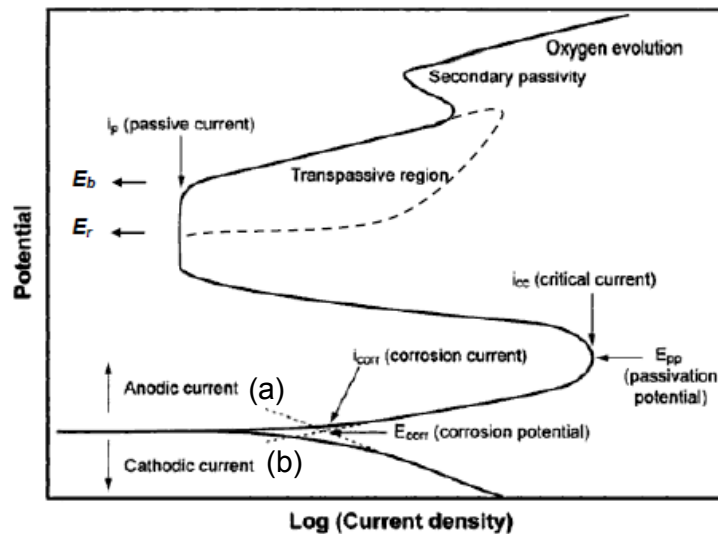


**Figure 2.17** - Cyclic polarization in a typically Evans Diagram for a passive material.

Tafel extrapolation is a technique that uses data obtained from cathodic and anodic polarization measurements. In Figure 2.17, the total anodic and cathodic polarization curves corresponding to hydrogen evolution and metal dissolution are superimposed as dotted lines, (a) and (b), respectively. To determine the corrosion rate from such polarization measurements, the Tafel region is extrapolated to the corrosion potential, as shown in Figure 2.17 [169,170]. At the corrosion potential, the rate of hydrogen evolution is equal to the rate of metal dissolution, and this point corresponds to the corrosion rate of the system expressed in terms of current density.

Bettini *et al.* (2013) noted that during electrochemical corrosion of CoCrMo alloy immersed in PBS, the relative fraction of ions detected in the transpassive region was close to the raw material elemental percentages, rather than being dominated by chromium dissolution. A much higher Cr dissolution was expected, once the CoCrMo alloy surface was dominated by a Cr oxide layer, and the corrosion takes place at the entire exposed surface [154].

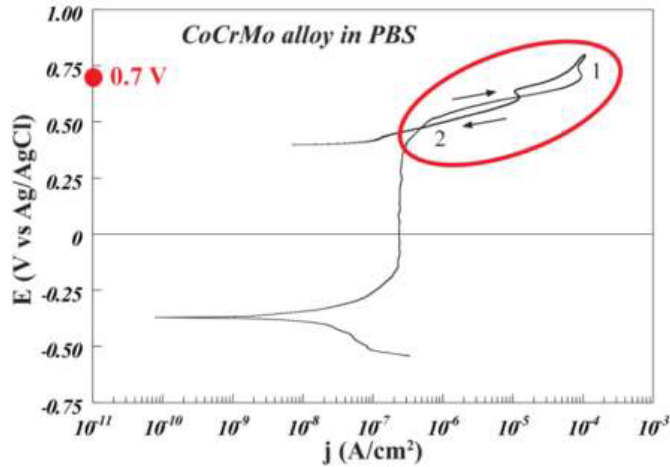


**Figure 2.18** - Cyclic polarization curve for the CoCrMo alloy in aerated PBS at room temperature (pH = 7.4), scan rate of 10 mV/min, with marked potential value applied to the sample during the potentiostatic polarization measurement followed by metal ion release analyses [154].

Milošev and Strehblow (2003) undertook electrochemical studies of CoCrMo alloy immersed in Hank's solution and found that a Cr<sub>2</sub>O<sub>3</sub> passive film was mainly formed at potentials below 0.24 V (relative to Ag/AgCl), after that the CoO fraction increased with the potential. In the region 0.40 to 0.56 V (Ag/AgCl), an equal composition of Co and Cr oxides were found, and after that cobalt decreased. Also, they noted that the content of Co was much lower in the surface oxide layer than in the bulk, although Cr and Mo in the oxide layer were higher than in the bulk [50].

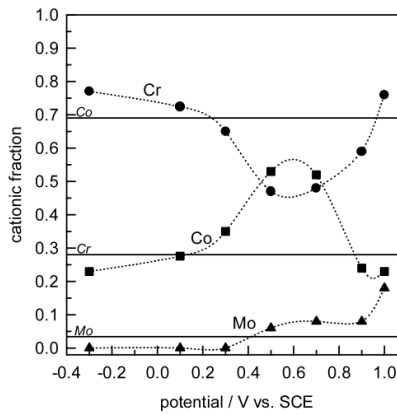


**Figure 2.19** - Composition of the passive layer after oxidation of CoCrMo alloy immersed in Hank's solution as a function of oxidation potential estimated by deconvolution of the peaks in X-ray photoelectron spectroscopy. Thin lines denote the atomic fractions for Co, Cr and Mo in the bulk alloy [50].

Karimi *et al.* (2011) studied the electrochemical corrosion of a CoCrMo alloy immersed in PBS containing different concentrations of BSA. They showed that the Open Circuit Potential (OCP) [-0.2 V(Ag/AgCl)] values changed to more cathodic potentials [about -0.4 V(Ag/AgCl)] when the BSA concentration increased. BSA enhanced the alloy passive film stability at higher concentrations, however, in the range of 0.2–2 g/L, BSA reduced the oxide layer stability [131]. Comparing the amount of proteins used in this experiment with the proposed by Brandt *et al* (2010), which contains much more proteins, it is expected a passivation layer much more stable to protect the alloy.

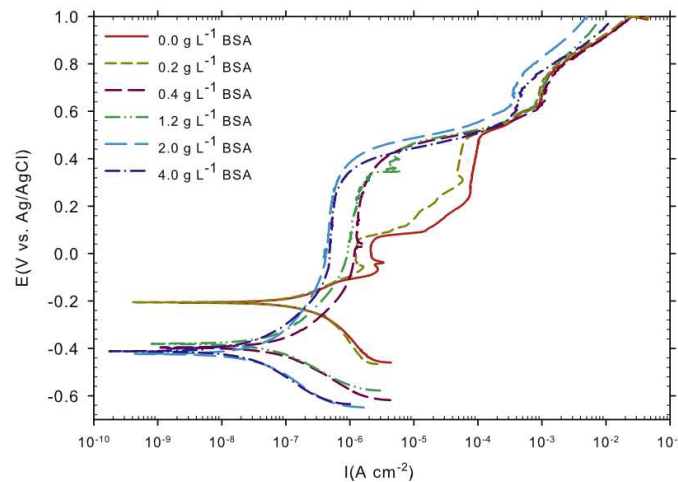


**Figure 2.20** - Potentiodynamic polarization curves of CoCrMo in PBS solutions at various BSA concentrations from 0.25 V (OCP) to 1 V (Ag/AgCl) with a scan rate of 0.167 mV/s in aerated conditions at 37°C and pH of 7.4 [131].

## 2.8 Summary

Much research effort has been undertaken to understand the high failure rate of MoM hip implants, especially in relation to the unexplained pain felt by patients after MoM hip surgery. Implant material loss can potentially initiate a cycle of inflammation and pain. What happens between the surgery and the first symptoms of implant failure remains unclear.

Wear debris have been found in-vivo over a wide particle size range, but several publications consistently note an average size of ~30 nm. Different compositions of wear debris particles have been found, including chromium-rich species as well as metallic Cobalt and oxidized Molybdenum (Mo) also

being regularly present. The latter suggest the result of a corrosive process suffered by the particles. Little is known about the real contribution of the wear debris in the release of ions.

It is known that proteins can play an important role in the degradation of both, the implant and wear debris particles, helping to prevent or accelerating metal dissolution. However, the mechanism and, especially, the preferential corrosion of the alloy need to be explained. Part of the understanding of preferential dissolution required could come from the contrasting dissolution results from in-vivo and hip simulators studies, which often report high levels of Co and Cr, versus immersion and electrochemical studies that reveal mainly Co and Mo species undergoing dissolution.

Cobalt species, instead of chromium, have been considered as the most relevant agent related to periprosthetic tissue reactions. No conclusive studies have been done in terms of Molybdenum species found in-vivo. Only a few in-vitro studies using CoCrMo nanoparticulate wear debris have been undertaken, most probably caused by the difficulties in generating large amounts of wear debris. This thesis has investigated the corrosion/dissolution of CoCrMo alloy nanoparticles produced in large amounts by mechanical milling in different relevant biological media.

## **Chapter 3 - Materials and Methods**

### **3.1 Wear debris simulation**

To produce synthetic wear debris metal particles, three techniques were used: hip simulators, pin-on-plate wear and mechanochemical milling. In the next few pages, the experiments will be described, as well as the apparatus and material used in each case.

#### **3.1.1 - Simulated Body Fluids**

Simulated body fluids are made with the intention to mimic the diversity of the body environment. All the wear debris syntheses have been performed in a wet environment, primarily with the purpose of simulating body fluids, especially, the synovial fluid. When samples (bulk material or particles) are immersed in liquid, the fluid composition could potentially enhance oxidation or corrosion processes that may occur.

In this study, several solutions were used both mixed and individually, in order to isolate their possible synergetic effects. The solutions studied were: Phosphate-buffered saline - PBS solution (10× concentrate from Sigma-Aldrich); Bovine Albumin Serum - BSA (purified by a heat shock process, pH 7.0 from Fisher Scientific); Fetal Bovine Serum - FBS (from Sigma-Aldrich); Iron-Supplemented Alpha-Calf Serum - ACS-I (heat inactivated from Fisher Scientific); Dulbecco's Modified Eagle's Medium -DMEM (from Sigma-Aldrich).

#### **3.1.2 - Hip Simulators**

Wear debris samples have been obtained by fatigue simulation of CoCrMo Hip Implants. The tests were performed in the Mechanical Engineering Department of the University of Leeds within the Institute of Functional Surfaces group.

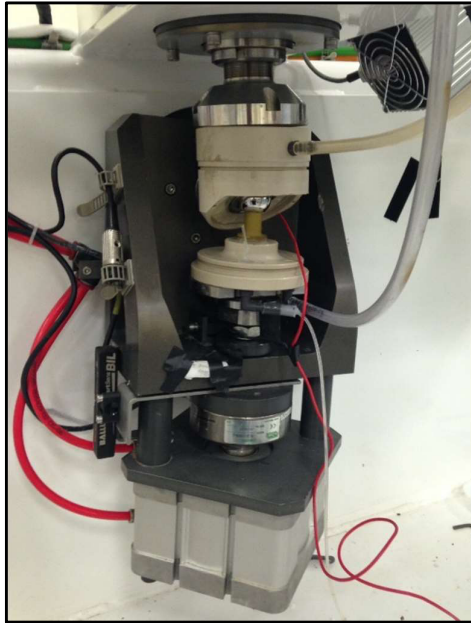


**Figure 3.1** - Prosim hip simulator

Particulate debris were generated from 28-36 mm diameter metal-on-metal hip bearing surface with a diametrical clearance of 85  $\mu\text{m}$ , tested in a Deep Flexion Prosim hip-simulator. The bearing material was wrought high-carbon CoCrMo (from Pinnacle, DePuy-UK) with a surface roughness ( $R_a$ ) of between 4-8 nm. Cups were mounted with an inclination angle of  $45^\circ$  to the horizontal. The lubricant used was distilled water with 25% foetal bovine serum supplemented with 0.03% sodium azide to retard bacterial growth.

The loading cycle employed was designed to simulate normal walking, in agreement with ISO 14242 standard load conditions. A typical twin peak loading cycle with a peak load of 3 kN and a swing phase of 150 N was run at a frequency of 1 Hz. Top axis rotation was between  $\pm 10^\circ$  whilst flexion and extension was between  $+35^\circ$  to  $-15^\circ$ . After 333,000 cycles the test was stopped and the lubricant was changed. At this point samples of the lubricant were taken for particle analysis.

### **3.1.3 - Pin-on-plate**

Wear debris was produced by pin-on-plate reciprocating tribometer (Biceri universal wear machine). The body and counter body material was a CoCrMo low carbon pellet (30 mm diameter) and a CoCrMo low carbon rod (10

mm diameter), from DePuy. The wear tests were carried out with a contact pressure of 5 and 20 MPa for a duration of 4 hours with a frequency of approximately 1 Hz. The tests were carried out in a wet condition with 20 mg/mL of BSA diluted in Milli-Q water and at room temperature. No centrifugal sedimentation was required as the majority of the particles were smaller than 300 nm.

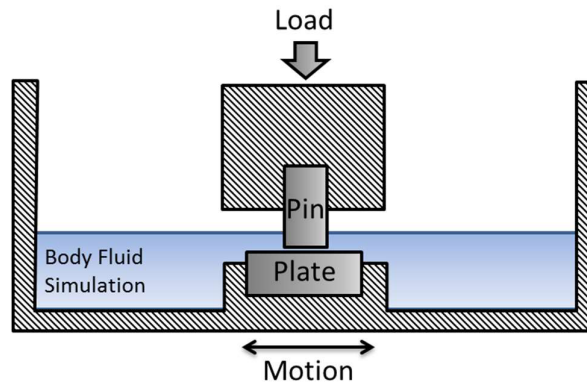


**Figure 3.2 - Pin-on-plate experimental scheme**

### **3.1.4 - Ball Milling**

CoCrMo starting powders used were bought from Sandvik Osprey Ltd and donated by Carpenter Powder Products, both are in accordance with ASTM F75 specifications (Table 3.1) and the alloys are used in the orthopaedic implant industry. The powders were obtained by a gas atomization process, which involves the use of high pressure fluid jets to break up a molten CoCrMo ASTM F75 stream into very fine droplets that cool down during their fall in the atomizing tower. The metal droplets solidify to spherically shaped particles in the micrometric scale, which have a high cleanliness level and the appropriate alloy composition [172,173].

**Table 3.1** - Elemental composition (wt%) of CoCrMo from powder suppliers

| Supplier  | Product                             | Co                   | Cr     | Mo    | C     | Others<br>Mn, Si, Fe, Ni |
|-----------|-------------------------------------|----------------------|--------|-------|-------|--------------------------|
| SANDVIK   | High Carbon<br>(Co212-C)            | Balance<br>(~63.39%) | 28.40% | 5.80% | 0.22% | 2.19%                    |
|           | Low Carbon<br>(Co212-H)             | Balance<br>(~63.24%) | 29.30% | 5.80% | 0.01% | 1.65%                    |
| CARPENTER | Low Carbon<br>(Micro-<br>Melt® CCM) | Balance<br>(~65.61%) | 27.15% | 5.47% | 0.05% | 1.73%                    |

Samples were prepared in a monovial SPEX mill 8000M (Figure 3.3), a compact laboratory mill capable of pulverizing samples in the 10 gram range. Basically, the vial was vibrated with amplitude of 50 mm and a frequency of 20 Hz for 15, 30, 60, 120 and 240 min. Zirconia vials and beads were used and vials were sealed before milling in an argon glove box in order to inhibit oxidation.



**Figure 3.3** - Spex milling machine used in the experiments

Milling was conducted in different fluids using 10 mL of: Milli-Q water with 20 and 40 mg/mL of BSA; pure DMEM; pure PBS; Simulated Synovial Fluid (SSF) - a mix of Calf Serum Iron-Supplemented diluted to a total protein content of 40 g/L with PBS; PBS with 40 mg/mL of BSA.

### **3.2 Reference materials for studies of corrosion during incubation and protein binding**

For corrosion investigation during incubation and also protein binding studies on reference elements, metal nanoparticles of less than 200 nm diameter were bought from Sigma-Aldrich: Cobalt(II,III) oxide ( $\text{Co}_3\text{O}_4$ ); Chromium(III) oxide ( $\text{Cr}_2\text{O}_3$ ); Molybdenum, which exhibits  $\text{MoO}_2$  at the surface. The particles were immersed for 24h, 48h and one month in Milli-Q water with 40 mg/mL of BSA.

### **3.3 Electrochemical corrosion**

In an attempt to understand the general corrosion behaviour of the ASTM F75 alloy and its major elements, a CoCrMo low carbon alloy and pure Co, Cr and Mo metal rods (10 mm diameter) were sourced from Pinnacle, DePuy-UK and Goodfellow-USA, respectively. The samples were evaluated by polarization curves (Figure 3.4), in the positive direction (anodic polarization) and negative direction (cathodic polarization). Three aerated and unstirred electrolytes solutions all at 37°C were used: Phosphate Buffered Saline (PBS); Milli-Q water with 40 mg/mL of BSA; PBS with 40 mg/mL BSA.

The specimens were cut into 6 mm pieces, bonded to Cu wires with conductive glue, and mounted in resin. The surfaces of the samples were ground with 600, 800, 1200, 2400 grit SiC paper, and then sequentially polished with 1  $\mu\text{m}$   $\text{Al}_2\text{O}_3$ , 0.3  $\mu\text{m}$   $\text{Al}_2\text{O}_3$ , and a colloidal  $\text{SiO}_2$  suspension to form mirror-like surfaces. Before the electrochemical tests, the samples were cleaned in distilled water, rinsed in ethanol and dried in hot air.

A Thermo-Scientific Sureflow Redox combination electrode, consisting of Ag/AgCl reference electrode and a Pt wire counter electrode was used. A working electrode of each sample was fixed at the bottom of the electrochemical cell, exposing an area of 0.78 cm<sup>2</sup> to the solutions. After the stabilization of the open circuit potential (OCP), the potential was stepped dynamically using an Autolab PGSTAT Potentiostat at a scan rate of 5 mV/min over a potential range from -0.5 to +1.5 V with respect to the OCP. Each measurement was carried out at least three times in order to check the repeatability of the experiments.

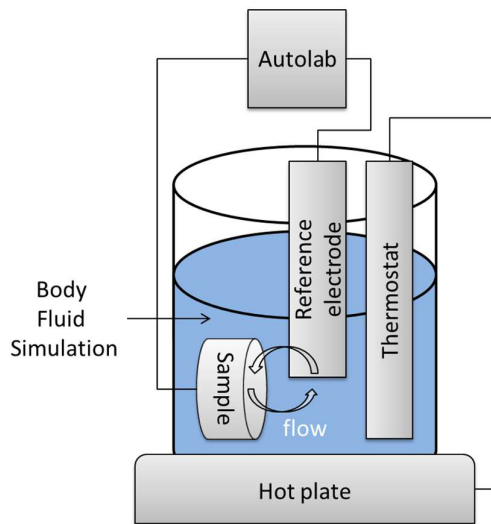


**Figure 3.4** - Experimental setup to induce electrochemical corrosion

### 3.4 Materials characterization techniques

Several characterization techniques were employed to analyse the nanoparticles and the liquid solutions in which the particles were produced. The sample surfaces and electrolyte following the electrochemical studies were also investigated. In this section, a brief introduction to each technique employed and how it can provide useful and relevant information will be provided.

Two techniques are highlighted in this study: Transmission Electron Microscopy (TEM) and Inductively Coupled Plasma-Mass Spectrometry (ICP-MS). TEM was the primary characterisation technique used, as it is particularly

suitable for studying nanoparticles, allowing the analysis of size, shape and composition of nanomaterials. ICP-MS allowed the investigation of the ionic products of the corrosion and tribochemical wear.

### 3.4.1 - X-ray diffraction

X-ray diffraction (XRD) is a bulk technique that was used to obtain crystallographic data from bulk and particulate samples. This technique is based on Bragg diffraction of X-rays and gives information on the phases, chemical composition, crystallite size and micro stress of samples.

When X-rays hit a material, they can be elastically scattered by the electrons of the atom. X-ray photons after scattering change trajectory, yet, keep the same phase and energy (Figure 3.5). If the atoms responsible for this scattering are organized systematically, as in a crystalline structure, diffraction will occur as represented by Bragg's Law (Equation 5) [59].

$$n\lambda = 2d \sin \theta$$

Equation 5 - Bragg's Law

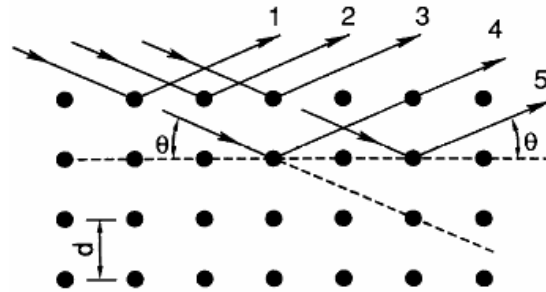


Figure 3.5 - X-ray diffraction and Bragg's law

Where  $n$  is the order of reflection,  $\lambda$  is the wavelength of the X-rays and  $d$  is the d-spacing of the diffracting planes. This equation can be used to calculate the d-spacings in the sample using the experimental  $2\theta$  values, thus giving structural information about any phases that are present in the sample [59].

In addition, X-ray diffraction can also give information about crystallite size and strain in polycrystalline samples, both important for understanding any decrease in particle size and stress caused by the mechanical wear process.

Characterisation by XRD was carried out using a Philips PANalytical X'Pert X-ray diffractometer with a monochromatized Cu  $K_{\alpha 1}$  X-ray source ( $\lambda = 1.545 \text{ \AA}$ ) scanning over a range of  $30\text{-}100^\circ 2\theta$ . Phase analysis was made by fitting the data with reference patterns from the International Centre for Diffraction Data (ICDD), formerly the Joint Committee for Powder Diffraction Standards (JCPDS). Examples are provided in Figure 3.12.

#### *General Sample Preparation*

Powders were mounted in a plastic sample holder (cylindrical form 25x1 mm) and the excess removed from the top with a glass slide. Particles in suspension were prepared by dropping the solution on a zero background plate, used as a sample holder, made of single crystal Silicon.

#### **3.4.1 - Scanning electron microscopy**

Scanning Electron Microscopy (SEM) is a technique used to show the surface and sub-surface structure of samples. The scanning process in a typical SEM (thermionic emission gun) occurs when electrons are emitted from a tungsten or lanthanum hexaboride ( $\text{LaB}_6$ ) filament and accelerated by an anode. The filament is often heated to high temperatures in the presence of an electric field, causing emission of electrons. The electrons are accelerated to the anode, a positive potential with respect to the filament in the range of 1 to 30 kV. During the passage of the electron beam to the sample, there are several electromagnetic lenses whose function is to focus the beam and scan it towards the point of analysis [174]. Different signals can be emitted by the sample including secondary electrons (SE) and backscattered electrons (BSE).

In a Field Emission Electron Guns (FEG), the field emission cathode is usually a wire of single-crystal tungsten fashioned into a sharp point and spot welded to a tungsten hairpin. The significance of the small tip radius, about 100 nm or less, is that an electric field can be concentrated. If the tip is held at negative 3-5 kV relative to the anode, the applied electric field at the tip is so strong that the potential barrier for electrons becomes narrow in width. This narrow barrier allows electrons to "tunnel" directly through the barrier and leave

the cathode without necessarily requiring any thermal energy to lift them over the work function barrier.

#### **3.4.1.1 - Secondary electrons**

Secondary electrons are low energy electrons arising from ionization of electrons in the specimen. Due to their low energy, these electrons originate from within a few nanometers of the sample surface. They are attracted into a detector due to a positive voltage (200 V) of the grid located in front of the detector. Inside the detector, electrons are accelerated up to 10 kV. This acceleration results in the emission of photons that are guided to a photomultiplier that produces a current. The amplified signal output of the photomultiplier is displayed as a two-dimensional intensity distribution that can be viewed and recorded on a video display [174]. The images produced characterize the surface topography of the specimen. Examples are provided in Figure 3.13.

#### **3.4.1.2 - Backscattered electrons**

The backscattered electron (BSE) signal consists of high-energy incident electrons of the electron beam, that are reflected or back-scattered out of the specimen interaction volume by elastic scattering interactions with the nuclei of atoms within. These electrons are detected using a large area solid state silicon detector [174]. The images produced are characterized by grey levels relating to the composition of the sample surface.

#### **3.4.1.3 - Energy dispersive X-ray spectroscopy**

Energy dispersive X-ray (EDX) spectroscopy is a technique which is based on analysing the X-rays emitted by the specimen in response to excitation by the incident electrons [175]. This technique is used to gain data on the elemental composition of samples.

EDX relies on the principle that each element has a unique atomic structure, so that X-rays emitted following ionization of secondary electron are

characteristic of this structure, which therefore identifies the element (see Figure 3.6) [175]

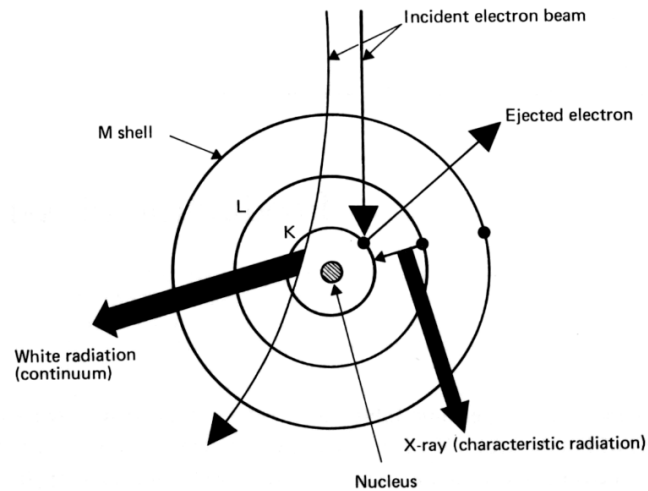


**Figure 3.6** - Electron movement after the incidence of an electron beam

SEM was performed using a LEO 1530 Gemini FEG-SEM operated at 3 keV, 3.0 mm working distance and employing an in-lens electron detector and an Oxford Instruments 80 mm<sup>2</sup> Silicon Drift EDX detector. Energy-dispersive X-ray (EDX) spectroscopy element mapping was used to identify sample composition in specific regions. The analysis and image acquisition was performed using Oxford Instrument's AZtec software. Examples are provided in Figure 4.7.

#### *General Sample Preparation*

Powder samples were fixed on a standard aluminium stub, and covered with a thin carbon layer. Loose particles were removed with the help of an air blower. Rod samples were fixed on the stub with carbon adhesive, and the sides were painted with conductive silver paint.

### **3.4.2 - Transmission electron microscopy**

Transmission Electron Microscopy (TEM) generates images from the interaction between electrons transmitted through a thin specimen. It can

provide information about particle size, size distribution and morphology of the particles as well as crystallography and internal structure. TEM can also produce a very small electron beam, typically  $<5$  nm and at best  $< 0.1$  nm in diameter, which allows analysis of individual nanoparticles.

The technique uses an electron beam produced by a tungsten filament that is accelerated through 200 kV and focused using a series of electromagnetic lenses (condenser lenses). After the electrons reach the sample, they can be reflected, absorbed, deflected elastically or inelastically or can be transmitted through the sample without deviation. The objective lens can form either an image or a diffraction pattern of the sample which is magnified, and then finally shown on a fluorescent viewing screen or digital camera (see Figure 3.7) [175].

Electron diffraction was used to gain data about crystal structure of the samples. In diffraction mode, the intermediate lenses are focused on the back focal plane, allowing diffraction patterns from the samples to be formed.

In order to form an image on TEM, contrast plays an important role. Contrast is basically the difference in intensity between two adjacent areas. In TEM, amplitude contrast and phase contrast contribute to an image formation, although one will tend to dominate according to the conditions selected [175].

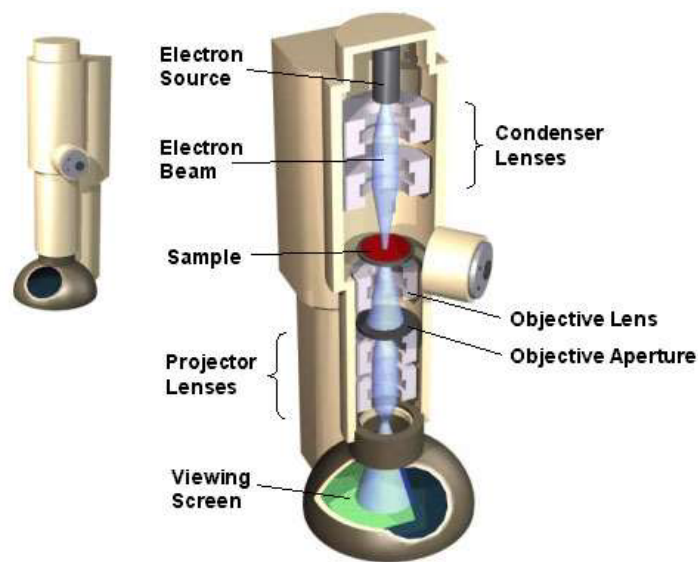


**Figure 3.7** - Schematic of a TEM

Usually, in order to get contrast in an image, an objective aperture is placed in the beam path at the back focal plane of the objective lens. Any electrons which are scattered by interaction with the sample are prevented from recombining to form the image by the aperture. Any regions where electrons are scattered will appear dark in the image. Because of this, the smaller the aperture used the greater the contrast, but at the expense of overall brightness [175].

Amplitude contrast results from variations in mass (Z number) or thickness or a combination of the two. Thicker (or higher Z) areas of the sample scatter more electrons than thinner (lower Z areas) and so appear darker in a Bright Field image [175].

Diffraction contrast is a special form of amplitude contrast where the scattering occurs at special (Bragg) angles. Whereby the electron beam undergoes Bragg scattering, which in the case of a crystalline sample, disperses electrons into discrete locations in the back focal plane. By the placement of apertures in the back focal plane, the Bragg reflections can be selected, thus only parts of the sample that are causing the electrons to scatter to the selected reflections will end up projected onto the imaging apparatus [175]. Examples are provided in Figure 3.17.

Phase contrast will occur whenever we have more than one beam contributing to the image interfere with each other. Phase-contrast images are widely used in three forms: Moire-fringes, Fresnel-contrast and images which relate directly to the structural periodicity of the crystalline specimen [175].

TEM imaging provides information on the morphology of the sample and allows monitoring of any size reduction of the particles produced by the experiments. Bright field (BF) images were used to capture images that were subsequently used for sizing the particles, as they were clearly discernible from the background support film (an ultrathin holey amorphous carbon film).

EDX detectors can also be attached to TEM to give compositional information at the sub-particle scale.

### 3.4.2.1 - Scanning transmission electron microscope

Scanning transmission electron microscopy (STEM-HAADF) images where the contrast is directly related to the atomic number (Z-contrast image). This technique is distinguished from conventional TEM by focusing the electron beam into a narrow spot which is scanned over the sample in a raster, a rectangular pattern of parallel scanning lines [175]. Examples are provided in Figure 5.10.

### 3.4.2.2 - Energy-filtered transmission electron microscopy

Energy-filtered transmission electron microscopy (EFTEM) is an analytical technique that makes use of the characteristic energy loss of electrons through a thin specimen. Its main advantage comes from the two-dimensional chemical information or "elemental maps" at nanometer resolution that can be extracted quickly from large sample areas.

The TEM image recorded on CCD camera is formed by electrons which have been dispersed in energy loss determined by a magnetic prism spectrometer after the sample and the projector lenses. Only electrons with a limited amount of energy loss by the slit position and the thickness of the sample form the image that contains information about the elements of the sample. Examples are provided in Figure 4.3.

TEM was performed on a FEI Tecnai F20 field emission gun TEM operated at 200 kV and fitted with an Oxford Instruments ultrathin window ISIS energy dispersive X-ray (EDX) system.

#### *General Sample Preparation*

Glass vials containing the samples were placed in an ultrasonic bath for 15 min to re-disperse the particles and then were dropped on a 400 mesh Cu grid with a holey carbon amorphous film (Agar Scientific Lfd). The grid was dried for 15 min before insertion into the TEM vacuum.

Particles were classified according to the values of the ratio ( $r$ ) of length to width giving information on particle shape: round if  $1 \leq r < 1.2$ , faceted if  $1.2 \leq r < 2.5$ , elongated if  $r \geq 2.5$ . These values were based on the shape characterization of Catelas *et al.* (2003) [152], however in their study spherical

particles were considered in a ratio  $1 \leq r < 1.5$ , whereas in this study a more conservative value was used.

### **3.4.3 - Inductively coupled plasma mass spectrometry**

Inductively Coupled Plasma-Mass Spectrometry (ICP-MS) is a technique used for the elemental characterisation of a liquid sample via ionization of the sample with an inductively coupled plasma followed by separation and identification of those ions using a mass spectrometer. The technique allows simultaneous quantification of most of the elements in the periodic table, at concentrations as low as parts per trillion (ppt).

The sample is provided in solution form, which is pumped to a nebulizer and converted into a fine aerosol. A high-voltage spark creates a source of electrons that form a plasma discharge (~10,000 K). The argon plasma generates temperatures of about 8000°C, resulting in atomization and subsequent ionization of the analyte elements, which are then introduced to the mass analyser. The ions are separated according to their mass-to-charge ratio by a quadrupole magnet. An ion detector identifies the element by mass-to-charge ratio and converts the ions into an electrical signal, which is then processed and converted into a concentration in ppb [176].

The technique is highly sensitive to a wide range of elements; therefore, matrix elements, formed during mass spectrometry, are complex and susceptible to element interferences. Matrix effects arise from the bulk composition of the sample, including water, organic compounds, acids and salts. Doubly charged or molecular ionic species can create difficulties in quantification. The matrix effect can be divided into two interferences categories: matrix induced spectral overlap problems and matrix induced signal intensity changes [177]. Another source of error could be from the sample preparation, in which the sample to be analyzed must be fully digested prior to analysis in order to dissolve the element(s) of interest [176,178].

Quantification of all elements was obtained from samples in order to determine any ion release during corrosion and tribocorrosion experiments, as well as identify impurities added during the process. Calibrations were performed using Co in 2-5% HNO<sub>3</sub>, Cr in 2-5% HCl and Mo in 2% NH<sub>4</sub>OH

standards from Reagecon, diluted in 10, 100 and 1000 ppb of MilliQ water. Investigations were carried out using a PerkinElmer SCIEX ELAN DRC-e ICP-MS with a PerkinElmer S10 Autosampler. The levels of isotopes Co 59, Cr 52 and Mo 96 were measured as well as they full chemical quantification. Examples are provided in Figure 5.7.

### *General Sample Preparation*

A Perkin Elmer, Elan DRcE, ICP-MS was used to quantify the release of metal ions. For ICP-MS sample preparation, in addition to centrifugation, a Vivacon® ultrafiltration spin column equipped with a Hydrosart cellulose membrane of 2 kDa molecular weight cut-off (MWCO), corresponding approximately to a pore size of 1.5 nm, was used (Figure 3.8).

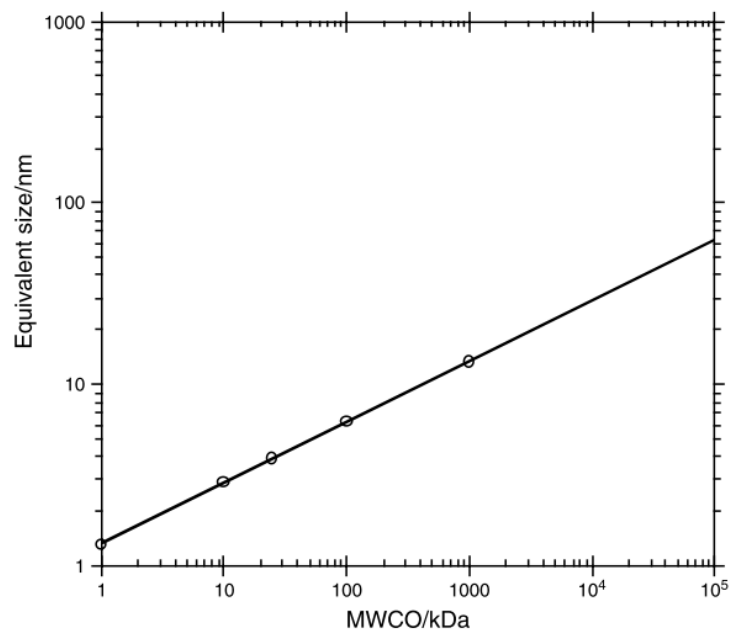


**Figure 3.8** - Relation between MWCO of filters/ ultrafilters and equivalent pore size [179]

Three different methods were employed to separate particles and ions in the hip simulator lubricant: firstly, centrifugation at 14000 rpm for 5-30 min; secondly ultracentrifugation using ~40000-60000 rpm (65000-150000 xg) for 30-60 min; and finally, centrifugation at 14000 rpm for 10 min, extraction of the

supernatant and then further centrifugation at 14500 rpm (14000 xg) for 30 min using ultrafilters of 2 kDa MWCO. For milling experiments, only centrifugation followed by ultrafiltration was undertaken. The supernatants of the ultracentrifuged samples were analysed by TEM/ EDX before acid digestion, as well as the supernatant following centrifugation and ultrafiltration.

Following each separation process, 1 mL of each sample was digested in 1 mL of 5% nitric acid for 30 min in an ultrasonic bath (65°C). The samples were then centrifuged again at 14000 rpm for 10 min and 0.5 mL of the supernatant was collected and diluted in 8 mL of MilliQ water.

#### **3.4.4 - X-ray photoelectron spectroscopy**

X-ray Photoelectron Spectroscopy (XPS) is a widely used technique to identify elements present on the surface of a sample (typically 3-5 nm in depth), as well as provide information regarding the chemical state of the elements detected and the stoichiometry of the elements.

During XPS analysis, the specimen is irradiated with X-ray photons of energy,  $h\nu$ , which are absorbed by atoms in the material leading to photoemission of electrons - the ejection of photoelectrons from the inner orbitals of atoms. The process of photoemission is shown schematically in Figure 3.9, where an electron from the K shell is ejected from the atom (1s photoelectron). The binding energy of the photoelectron can be calculated from the kinetic energy of the ejected electron which is measured by the instrument. The binding energy identifies specifically the element and atomic energy level from which the electron has been ejected [180]. The XPS spectrum produced, displays the binding energy (eV) on the x-axis versus the intensity of photoelectrons detected.

The specific chemical environment of an element can be determined by measuring the deviation of a peak binding energy position relative to the known elemental energy. The area under each peak is proportional to the amount of each element present in the analysed volume of the sample surface [180].

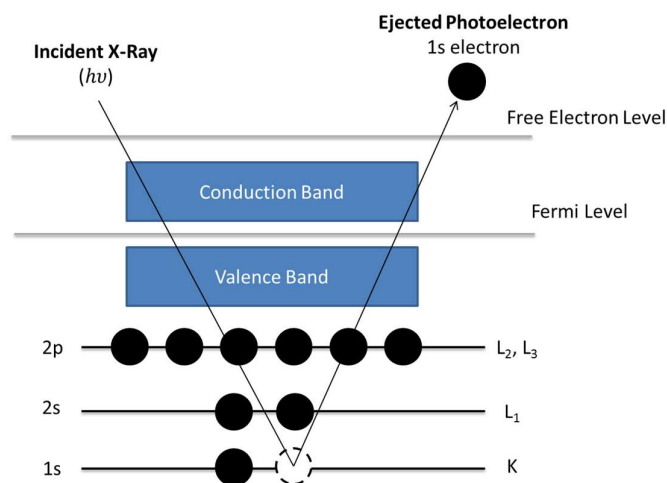


**Figure 3.9** - Schematic diagram of the XPS process

XPS measurements were performed using an AXIS Nova (Kratos Analytical) spectrometer with monochromated aluminium K- $\alpha$  X-ray source (Spot size diameter = 500  $\mu\text{m}$ ; Power = 150 W) at the NEXUS facility in Newcastle (<http://www.ncl.ac.uk/nexus>). The flood gun was turned on for all samples and elements in order to counteract sample charging. The binding energy scale was calibrated by setting the carbon 1s peak to 285 eV, and in particular cases by setting the O 1s peak to 530.45 eV. The operating mode of the instrument was the same for all the samples and the spectra were normalized prior to the analysis. Spectra were analysed using mixed Gaussian-Lorentzian peak fitting within the processing software CasaXPS [180–185]. Examples are provided in Figure 6.22.

### 3.4.5 - Dynamic light scattering

Dynamic light scattering (DLS), is one of the most popular light scattering techniques because it allows the measurement of the hydrodynamic size of particles over a wide range. The technique measures the light scattered from a laser that passes through a colloidal solution and, by analysing the modulation of the scattered light intensity as a function of time, the hydrodynamic size of the particles and agglomerates can be determined [186].

The speed at which particles diffuse due to Brownian motion is defined by a property known as the translational diffusion coefficient,  $D$ . This can be

used to calculate the hydrodynamic diameter (based on a sphere) by the Stokes-Einstein equation:

$$d(H) = \frac{kT}{3\pi\eta D}$$

**Equation 6** - Hydrodynamic diameter

Where  $d(H)$  is the hydrodynamic diameter,  $D$  is the translational diffusion coefficient,  $k$  is Boltzmann's constant,  $T$  is the absolute temperature and  $\eta$  is the viscosity of the suspending fluid [186].

The hydrodynamic diameter can be affected by surface structure of particles, the ionic strength of the medium and the presence of non-spherical particles. When DLS sizing data is compared with Transmission Electron Microscopy images of the primary particle size, the agglomeration or aggregation state of the particles can be determined. In an unagglomerated suspension, the measured DLS diameter will be similar or any slightly larger than the TEM size. If the particles are agglomerated, the DLS measurement is often much larger than the TEM primary particle size and can have a high polydispersity index (a large variability in the particle size).

Dynamic light scattering measurements were carried out using a Malvern Zetasizer Nano ZS instrument. The DTS Nano software was used to determine the particle size distribution. Examples are provided in Figure 4.1.

#### *General Sample Preparation*

Glass vials containing the samples suspended in water based solutions were placed in an ultrasonic bath for 20 min immediately before analysis. The value of CoCrMo refractive index used was 2.064 which was calculated by Raghunathan, V. K. *et al* [187] using the proportions of metals in the alloy (wt% Co: 64.3%, Cr: 28.0% and Mo: 6.0%) and their refractive indices (at  $\lambda = 488\text{nm}$ ) derived from tables [188]. The light absorption coefficient of the particles was calculated in a similar manner and is 3.595. For DLS, the concentration was changed to 0.1% w/v to optimize the attenuator which varies the intensity of the laser and hence varies the intensity of the scattering.

### 3.4.6 - Zeta Potential

The zeta potential (ZP) is a function of the surface charge which develops when any material is placed in a liquid. The ZP indicates the degree of electrostatic repulsion between adjacent, similarly charged particles in dispersion and gives a good indication of the suspension stability.

Particles when placed in a solution are surrounded by a stationary layer, formed of an opposite charge to the particle, and a diffusion layer, which is electrically neutral (see Figure 3.10). During ZP measurement, a voltage is applied to the solution; particles are attracted to the electrode of the opposite polarity.

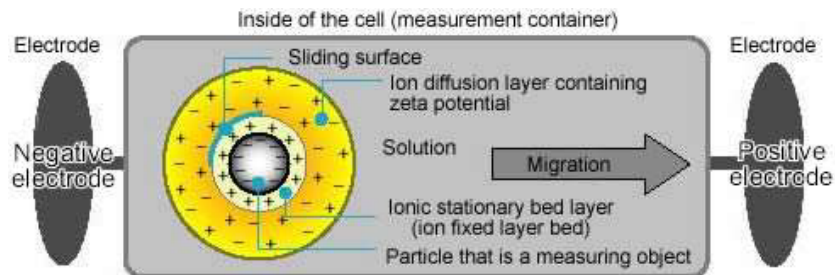


**Figure 3.10** - Particle migration in Zeta Potential

(from [http://nition.com/en/products/zeecom\\_s.htm](http://nition.com/en/products/zeecom_s.htm))

The potential at the boundary shear plane between the particle with its ion atmosphere and the surrounding medium, is known as the Zeta Potential. The ZP is a function of the surface charge of a particle, any adsorbed layer at the interface with the media/ solution and the nature and composition of the surrounding medium in which the particle is suspended [189]. Zeta potential can be calculated with Smoluchowski's formula:

$$\zeta = \frac{\pi\eta}{\varepsilon} \cdot U \cdot 36 \cdot 10^6$$

**Equation 7** – Zeta Potential

$$U = \frac{v}{V/L}$$

**Equation 8** - Electrophoretic mobility

Where  $\zeta$  is the zeta potential (mV),  $\eta$  is the viscosity of solution,  $\epsilon$  is dielectric constant,  $U$  is the electrophoretic mobility in which  $v$  is the speed of particles (cm/s),  $V$  is the voltage (V) and  $L$  is the distance of electrode.

Zeta Potential measurements were carried out using a Malvern Zetasizer Nano ZS instrument. In this study, the change of zeta potential as a function of the amount of protein adsorbed on the surface of colloidal nanoparticles in solutions was investigated. Examples are provided in Figure 5.23.

#### *General Sample Preparation*

Glass vials containing the samples were diluted in different concentrations (0.05, 0.01, 0.5 and 1 %w/v) and placed in an ultrasonic bath for 20 min immediately before analysis.

### **3.4.7 - Fourier transform infrared spectroscopy**

Fourier Transform Infrared Spectroscopy (FTIR) uses a beam containing many frequencies of infra-red light, and measures the absorption of the different frequencies by a sample, allowing the identification of chemical groups and compounds. For a given sample, specific chemical bonds are absorbed at characteristic frequencies related to the vibrational energy of the chemical bond, and the remaining infrared signal is transmitted through the sample [190].

FTIR characterization was carried out using a Thermo Scientific Nicolet iS10 FTIR spectrometer running OMNIC processing software, fitted with an attenuated total reflection (ATR) accessory. The ATR contains a diamond crystal that internally reflects the IR beam allowing for improved transmission into the sample (0.5-5  $\mu\text{m}$ ). This technique was employed to follow protein conformational changes during milling. Examples are provided in Figure 5.18.

#### *General Sample Preparation*

Bulk samples were placed straight in contact with the diamond crystal. A weight is placed over the sample, applying a pressure that encourages maximum contact with the crystal surface. Liquid samples were dropped onto the crystal and pressed with a concave tip.

### **3.4.8 - Ultraviolet-visible spectroscopy**

Ultraviolet-visible spectroscopy (UV-VIS) is based on the absorption of light over the wavelength range from ultraviolet up to the start of the infrared. In this region molecules undergo electronic transitions during absorption or reflectance of incident light and this affects the perceived colour of the chemicals involved.

In this study, a Perkin Elmer Lambda XL spectrophotometer was used to scan the complete UV-VIS spectrum. It was used to analyse the presence of metal ions in solution as a result of the wear simulations and electrochemical corrosion. Examples are provided in Figure 6.29.

#### *General Sample Preparation*

Glass vials containing the samples were placed in an ultrasonic bath for 20 min immediately before analysis. The solutions were dropped into the sample holder.

### **3.4.9 - Thermogravimetric analysis**

Thermogravimetric analysis (TGA) was performed in order to evaluate the concentration of the nanoparticles produced in a liquid. This technique consists in monitoring the change in mass of a sample as a function of temperature or time in a temperature controlled environment and atmosphere.

TGA was conducted using a TGH 1000 (Stanton Redcroft) under an argon atmosphere, to avoid oxidation, fitted with a digital precision balance of 0.1 mg sensitivity. The sample was heated from 100 °C to 900 °C, at a rate of 10 °C/min. Examples are provided in Figure 4.24.

#### *General Sample Preparation*

A precision pipette was used to drop 0.1mL of the sample solution onto the sample holder.

### 3.4.10 - Centrifugal Particle Sizing (CPS)

CPS uses differential centrifugal sedimentation to measure particle size distributions. Particles settle in a fluid under a gravitational field according to Stokes Law [191,192]. Sedimentation velocity increases as the square of the particle diameter, so particles that differ in size by only a few percent settle at significantly different rates. Large particles sediment faster than small particles. The disadvantage of sedimentation is that small particles with low density might take a long time to sediment.

During CPS, particles sediment inside an optically clear rotating disc (see Figure 3.11). When these particles approach the outside edge of the rotating disc, they scatter a portion of a light beam that passes through the disc. The change in light intensity is continuously recorded, and converted by the operating software into a particle size distribution.

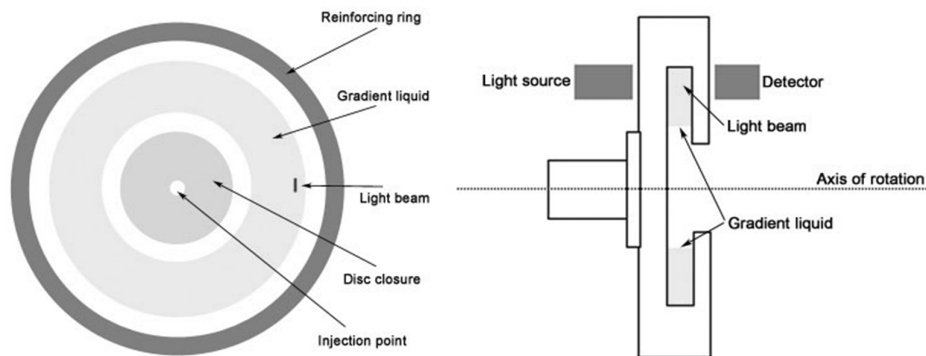


**Figure 3.11** - CPS disk centrifuge scheme.

Analysis time will depend of the range of sizes that is being analysed and the density of the particles measured. The majority of applications use times in the range of 3 to 15 minutes for each sample. The results are highly reproducible with a typical 95% confidence range for reported peak sizes in replicate analyses being  $\pm 1\%$ .

CPS was conducted using a CPS DC24000 UHR (CPS Instruments), where the disc was loaded with a sucrose solution, which creates a density gradient as the disc spins. Under these conditions, particles were injected into

the centre of the spinning disc, which separates them according to differences in their size and density.

### 3.5 Characterization of as-Received Materials

#### 3.5.1 - CoCrMo powder alloy

Figure 3.12 shows indexed XRD patterns of the CoCrMo high and low powder. The presence of two crystallographic phases was found: a dominant face-centered cubic (FCC) and hexagonal close-packed (HCP). These peaks were indexed according to the patterns with reference code of 00-015-0806 (Cubic Cobalt) and 00-001-1278 (Hexagonal Cobalt) from International Centre for Diffraction Data (ICDD) base.

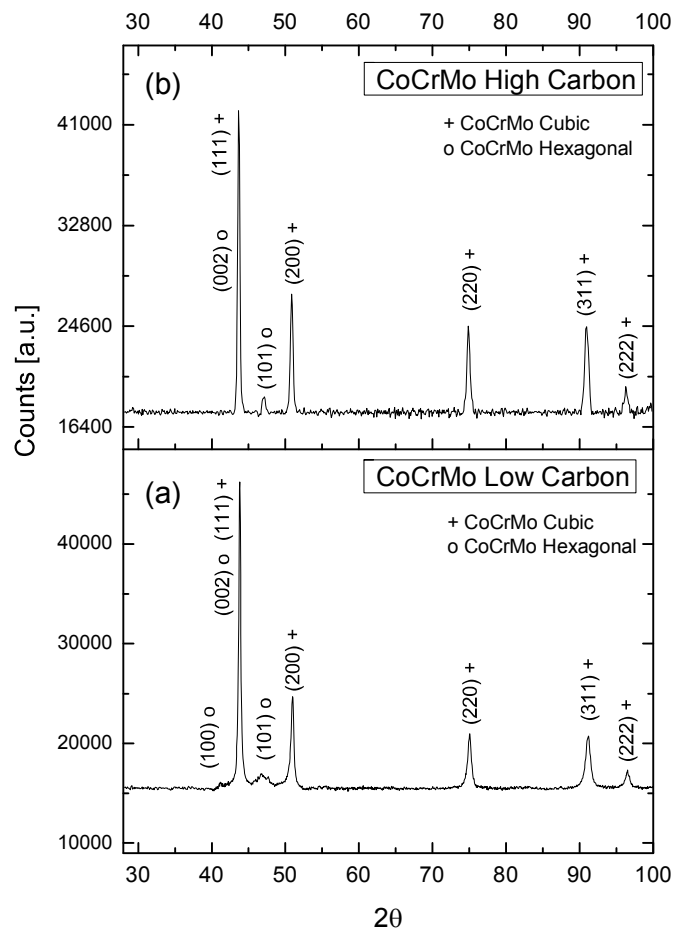


**Figure 3.12** - XRD of starting CoCrMo ASTM75 powder: (a) low carbon and (b) high carbon.

Five peaks are well defined in this diffraction pattern, most from Cobalt FCC, taking in account the high percentage of this component in the alloy. Moreover, the occurrence of very small additional peaks may signify the presence of the HCP phase. Salinas and Rodriguez (1996) [112] showed that the presence of HCP phase is most visible in fine-grained material (7  $\mu\text{m}$ ) rather than in coarse grain (70  $\mu\text{m}$ ). Zeng et al. (2012) [113] also have reported a predominant HCP structure in particles of 5 nm range, however HREM also indicated the possibility of FCC phase.

The industrial process to obtain this powder raw material uses gas atomization, with means that the alloy suffers fast cooling. Using the CoCr phase diagram Figure 2.3, after heating the CoCr (Cr 27 wt%) alloy up to 1000  $^{\circ}\text{C}$ , the alloy present a FCC phase. With fast cooling, the alloy tends to retain the same phase. A similar process occurs with the CoCr hip implants that pass through a heat treatment of water quenching, but in this case, just the surface of the implants should present a FCC phase, whereas inside the implant could present also the HCP phase.

Figure 3.13 displays SEM images of the CoCrMo alloy powder (both high and low carbon) from Sandvik Osprey. The images show particles of CoCrMo with a dense distribution and a spherical morphology. The particles were measured using ImageJ image analysis software and showed an average particle size of  $4.8 \mu\text{m} \pm 3$  and  $9.1 \mu\text{m} \pm 6$ , respectively. Figure 3.14 shows EDX of random particles showing that there was little variation in composition.

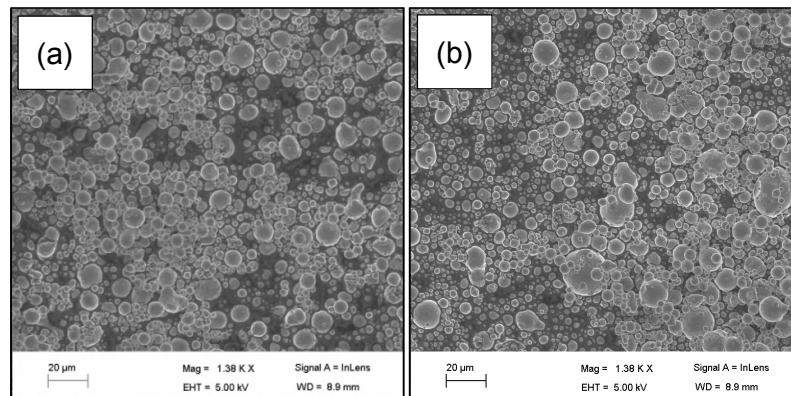


**Figure 3.13** - SEM of the CoCrMo ASTM75 gas atomized raw material: (a) low carbon and (b) high carbon powder.

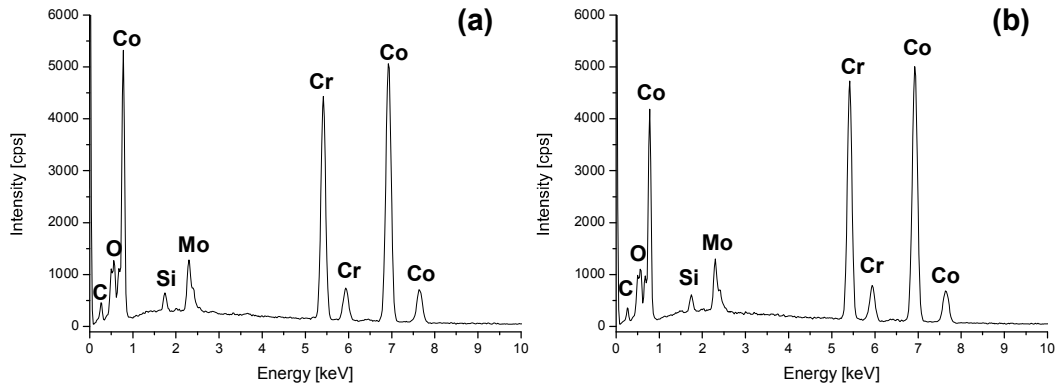


**Figure 3.14** - SEM/EDX of the CoCrMo ASTM75 gas atomized raw material:  
(a) low carbon and (b) high carbon powder.

In summary, the raw material presented a homogenous composition and a wide size distribution. Particles were found to be spherical and XRD pointed to the dominance of the FCC phase.

### 3.5.2 - CoCrMo bulk alloy

Figure 3.15 shows the XRD patterns obtained from the Co, Cr and Mo reference materials as well as the CoCrMo alloy commercial rods, with the phases indicated above each peak. The peaks are consistent with ICDD database listed in the Table 3.2. A cubic phase is present in all samples in the form of body-centered cubic (bcc) for Co and CoCrMo and a face centered cubic (fcc) phase for Cr and Mo, whereas some presence of a hexagonal (hcp) phase was found in the Co and CoCrMo samples. The CoCrMo alloy exhibits a similar diffractogram to the CoCrMo gas atomised powder studied in the previously, where it was demonstrated that there was evidence of a FCC(metastable)→HCP phase transformation.

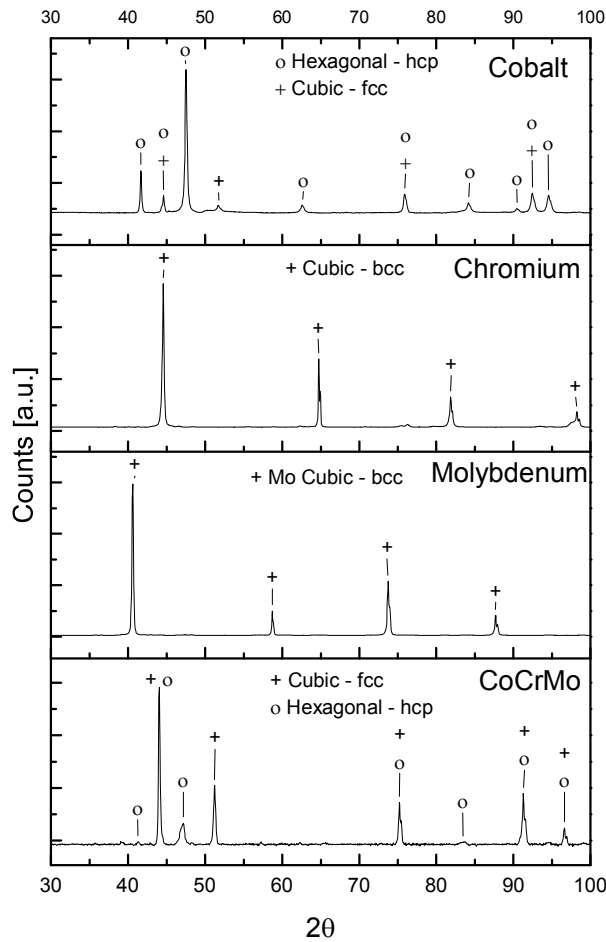


**Figure 3.15** - XRD of the polished surfaces of Co, Cr, Mo and CoCrMo rods.

**Table 3.2** - Reference XRD pattern from ICDD corresponding to the sample peaks

| <i>Reference Pattern</i> | <i>Name</i> | <i>Crystal System</i> | <i>Formula</i>   | <i>Lattice Parameter</i> |
|--------------------------|-------------|-----------------------|--|--------------------------|
| 04-006-8067              | Cobalt      | Cubic (fcc)           | Co   | a = 3.53 Å               |
| 04-003-3863              | Cobalt      | Hexagonal (hcp)       | Co   | a = 2.50 Å<br>c = 4.06 Å |
| 04-004-9049              | Chromium    | Cubic (bcc)           | Cr   | a = 2.88 Å               |
| 04-001-1814              | Molybdenum  | Cubic (bcc)           | Mo   | a = 3.14 Å               |
| 04-016-6869              | CoCrMo      | Cubic (fcc)           | Co <sub>0.64</sub> Cr <sub>0.32</sub> Mo <sub>0.04</sub> | a = 3.59 Å               |
| 04-016-6870              | CoCrMo      | Hexagonal (hcp)       | Co <sub>0.64</sub> Cr <sub>0.32</sub> Mo <sub>0.04</sub> | a = 2.56 Å<br>c = 4.12 Å |

Figure 3.16 shows backscattered electron imaging of the CoCrMo raw material used in the corrosion experiment. The relative large percentage of carbon is due the presence of carbides with particle diameters less than 2 μm. EDX analysis of the selected area in red shows the presence carbides rich in

Cr and Mo. Bettini et al (2011) observed the presence of carbides in the same composition and some clusters with ca. 20  $\mu\text{m}$  size suggested different carbides coexisting [54].

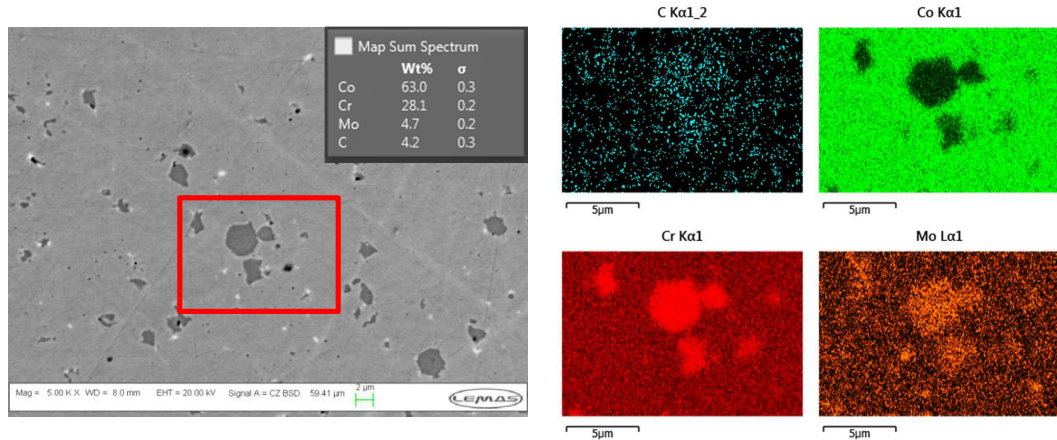


**Figure 3.16-** SEM backscattered electron imaging and EDX mapping of a selected area of the surface of CoCrMo ASTM75 raw material. Image with a scale bar of 2  $\mu\text{m}$ .

Figure 3.17 shows a TEM bright field image of a thin section of the CoCrMo low carbon alloy used during the experiments. Electron diffraction analysis shows the presence of a mixed phase comprising CoCrMo fcc (strongly diffracting) and for  $\text{Cr}_2\text{O}_3$  orthorhombic (weakly diffracting), which also showed lattice fringes.

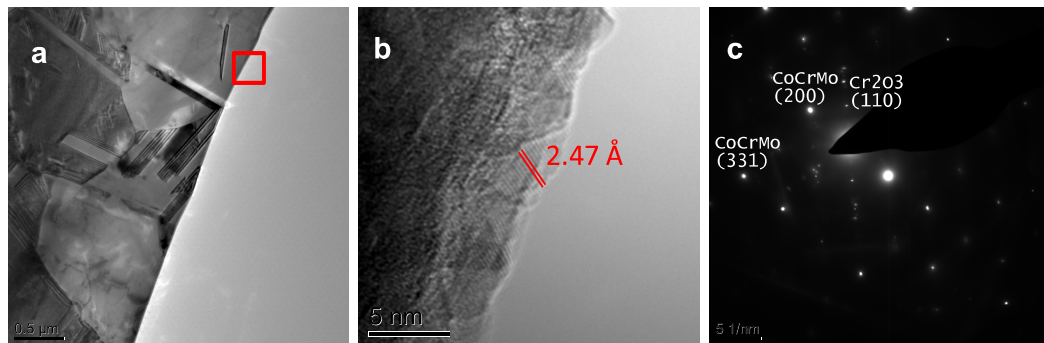


**Figure 3.17** – (a) TEM bright field of a thin section of CoCrMo low carbon standard showing the presence of a mixed phase of CoCrMo (fcc) and  $\text{Cr}_2\text{O}_3$  (orthorhombic) (b) on the surface identified by electron diffraction (c) according to ICDD 04-016-6869 and 04-002-5942, respectively.

TEM/EDX of the CoCrMo low carbon alloy standard (Table 3.3) shows Co and Cr within the ASTM standard limit whereas Mo was found slightly above the limit recommended. The use of a standard k factor for EDX quantification and the small region covered by the beam during TEM/EDX could be the reason for the deviation of the results, compared with bulk analysis.

**Table 3.3** - TEM/EDX on CoCrMo low carbon standard showing the average weight composition in 30 different areas of the sample.

| Wt%            | Co    | Cr    | Mo   |
|----------------|-------|-------|------|
| Mean           | 65.0% | 27.3% | 7.2% |
| Std. deviation | 0.7%  | 0.5%  | 0.5% |
| Max.           | 66.2% | 28.3% | 9.4% |
| Min.           | 63.6% | 26.3% | 6.8% |

### 3.6 Materials Sample Preparation

Sample preparation for materials used in the different studies are described and linked here with the respective sections.

#### 3.6.1 - Mechanochemical milling using 440C Hardened Steel vial/beads (Section 4.2.1)

Particles were produced by mechanochemical milling for 240 min using a SPEX mill with a vial and a bead (12.7 mm) made of 440C hardened steel (from SPEX SamplePrep) and CoCrMo ASTM F75 gas atomized low carbon alloy powder (from Sandvik Osprey) immersed in heptane with 10% oleylamine with 5:1 ball-to-powder weight ratio. Particles were analysed using the general powder sample preparation described for TEM and DLS.

### 3.6.2 - Mechanochemical milling using Zirconium Oxide Vial/Beads (Section 4.2.2)

Particles were produced by mechanochemical milling for 15, 30, 60 and 120 min using a SPEX mill with a vial and two beads (12.7 mm) made of zirconium oxide (from SPEX SamplePrep) and CoCrMo ASTM F75 gas atomized low carbon alloy powder (from Sandvik Osprey) immersed in heptane with 10% oleylamine with 10:1 ball-to-powder weight ratio. Particles were analysed using the general powder sample preparation described for TEM, DLS and SEM for powder.

### 3.6.3 - Mechanochemical milling Optimization (Section 4.3.1)

Particles were produced by mechanochemical milling according to the parameters described in Table 3.4 using CoCrMo ASTM F75 gas atomized low carbon alloy powder (from Sandvik Osprey). Particles were analysed using the general sample preparation described for DLS, CPS, XRD (for particles in suspension) and SEM (for powder).

**Table 3.4** - Description of the milling parameters in the factorial design experiment.

| Samples |            |                      |   |       |
|---------|------------|----------------------|---|-------|
| #       | Time [hrs] | Ball-to-Powder [g/g] | Surfactant [% of oleylamine to heptane] | Balls |
| 1       | 2          | 10:1                 | 10                                      | 3     |
| 2       | 10         | 10:1                 | 10                                      | 3     |
| 3       | 2          | 5:1                  | 10                                      | 3     |
| 4       | 10         | 5:1                  | 10                                      | 3     |
| 5       | 2          | 10:1                 | 20                                      | 3     |
| 6       | 10         | 10:1                 | 20                                      | 3     |
| 7       | 2          | 5:1                  | 20                                      | 3     |
| 8       | 10         | 5:1                  | 20                                      | 3     |
| 9       | 2          | 10:1                 | 10                                      | 2     |
| 10      | 10         | 10:1                 | 10                                      | 2     |
| 11      | 2          | 5:1                  | 10                                      | 2     |
| 12      | 10         | 5:1                  | 10                                      | 2     |
| 13      | 2          | 10:1                 | 20                                      | 2     |
| 14      | 10         | 10:1                 | 20                                      | 2     |
| 15      | 2          | 5:1                  | 20                                      | 2     |
| 16      | 10         | 5:1                  | 20                                      | 2     |

### **3.6.4 - Simulating wear debris from hip implants (Section 4.3.4)**

Following optimization of the milling procedure, particles were produced by mechanochemical milling for 150 min using a SPEX mill with a vial and three beads (12.7 mm) made of zirconium oxide (from SPEX SamplePrep) and CoCrMo ASTM F75 gas atomized low carbon alloy powder (from Sandvik Osprey) immersed in 0.2 g of BSA diluted in 10 mL of deionized water with 3:2 ball-to-powder weight ratio. Particles were centrifuged for 10 min at 14 000rpm and analysed using the general sample preparation described for TEM, DLS, TGA and SEM.

### **3.6.5 - Accurate ICP-MS measurement (Section 5.1)**

Particulate debris were generated from a 28 mm diameter metal-on-metal hip bearing surface in a Deep Flexion Prosim hip-simulator for 30,000 cycles under ISO load conditions. The bearing material was wrought CoCrMo High Carbon alloy (DePuy). The lubricant used was 12 g/L Foetal Bovine Serum (FBS) plus Phosphate Buffered Saline solution (PBS) supplemented with 0.03% sodium azide to retard bacterial growth (Sigma-Aldrich).

A Perkin Elmer, Elan DRCe, ICP-MS was used to quantify the release of metal ions. For ICP-MS sample preparation, in addition to centrifugation, a Vivacon® ultrafiltration spin column equipped with a Hydrosart cellulose membrane of 2 kDa molecular weight cut-off (MWCO), corresponding approximately to a pore size of 1.5 nm, was used. Three different methods were employed to separate particles and ions in the hip simulator lubricant: firstly, centrifugation at 14000 rpm for 5-30 min; secondly ultracentrifugation using ~40000-60000 rpm (65000-150000 xg) for 30-60 min; and finally, centrifugation at 14000 rpm for 10 min, extraction of the supernatant and then further centrifugation at 14500 rpm (14000 xg) for 30 min using ultrafilters of 2 kDa MWCO. The supernatants of the ultracentrifuged samples were analysed by TEM/ EDX before acid digestion, as well as the supernatant following centrifugation and ultrafiltration. To prepare TEM samples, the grids were simply immersed for 24h in the corresponding liquid, collected and then dried.

Following each separation process of the hip simulator lubricant, 1 mL of each sample was digested in 1 mL of 5% nitric acid for 30 min in an ultrasonic

bath (65°C). The samples were then centrifuged again at 14000 rpm for 10 min and then 0.5 mL of the supernatant was collected and diluted in 8 mL of MilliQ water. Finally, the levels of isotopes Co 59, Cr 52 and Mo 96 were measured by ICP-MS. Particulate dispersions at the various stages of sample preparation for ICP-MS were analysed by Transmission Electron Microscopy (TEM).

### **3.6.6 - Microstructural characterization of low and high carbon CoCrMo alloy nanoparticles produced by mechanical milling (Section 5.2)**

CoCrMo gas atomized powders (ASTM75), both high and low carbon, were purchased from Sandvik Osprey. Bovine Serum Albumin (BSA), heat shock, pH 7.0 was acquired from Fisher Scientific, and used in solution during milling as a process control agent. The solution was composed of 0.4g of BSA diluted in 10 mL of deionized water. The powders were ball milled for 150 min in a high energy Spex 8000M mill using zirconia ceramic vial and balls. Before milling, the vial was fully filled with an inert gas (Argon) to avoid atmospheric contamination. A ball-to-powder weight ratio of 3:2 was used. After collection, samples were centrifuged in a Heraeus Megafuge for 10 min, at 25°C and a centrifugal force of 8000G. This procedure removes part of the BSA and coarse particles, maintaining most of the fine particles in dispersion.

### **3.6.7 - Corrosion of CoCrMo alloy in relevant media (Section 5.3)**

Synthetic wear debris were obtained by mechanochemical milling of a CoCrMo High Carbon powder (Sandvik Osprey – Co212-c) in a SPEX 8000M mill for 150 min, using a ball-to-powder ratio of 3:2, and 40 g/L of Bovine Serum Albumin (BSA) purified by a heat shock process, pH 7.0 (Fisher Scientific), diluted in MilliQ Water. Milling was also performed in pure PBS solution and Simulated Synovial Fluid (SSF) - a mix of Iron-Supplemented Calf Serum diluted to a total protein content of 40 g/L with PBS (Sigma-Aldrich).

The mechanochemically milled samples were diluted 20x and only the centrifugation plus ultrafiltration (2 kDa ultrafilter) protocol was used prior to ICP-MS analysis.

### **3.6.8 - Bovine Serum Albumin binding to CoCrMo nanoparticles and the influence on dissolution (Section 5.4)**

CoCrMo high carbon gas atomized powders (ASTM75, ~ 60% Co, 27% Cr, 6% Mo) was purchased from Sandvik Osprey. Bovine Serum Albumin (BSA), heat shock, pH 7.0 was acquired from Fisher Scientific, and used during milling as a process control agent. The solution used was composed of 0.4 g of BSA diluted in 10 mL of deionized water. The powder was ball milled for 150 min in a high energy Spex 8000M mill using zirconia ceramic vials and balls. Before milling, the vial was filled with an inert gas (Argon) to avoid atmospheric contamination. A ball-to-powder weight ratio of 3:2 was used. After collection, samples were centrifuged in a Heraeus Megafuge for 10 min, at 25 °C and a centrifugal force of 8000 G. This procedure removes the excess BSA and coarse particles (>200nm), maintaining most of the fine particles in dispersion (20 mg/mL).  $\text{Co}_3\text{O}_4$ ,  $\text{Cr}_2\text{O}_3$ , Mo nanoparticles (which exhibit  $\text{MoO}_2$  on the surface) were purchased from Sigma Aldrich and suspended in BSA (20 mg/mL) for 24h, washed in distilled water and finally re-suspended in ethanol. The washing procedure removed excess BSA due to its high affinity with ethanol.

In order to demonstrate the effect of milling fluid on the size and stability of CoCrMo nanoparticles when in the presence of serum proteins, the samples were analysed by Transmission Electron Microscopy (TEM), Energy-Dispersive X-ray spectroscopy (EDX), Inductively Coupled Plasma Mass Spectrometry (ICP-MS) and Zeta Potential (ZP) measurements.

## Chapter 4 - Production of synthetic CoCrMo wear debris

### 4.1 Introduction

Metal-on-Metal hip implants were intended to offer improved durability, releasing a lower volume of wear debris than traditional implant designs. Some studies have highlighted that these wear debris particles are numerous at the nanometre scale [21]. Since then, wear debris from CoCrMo metal on metal implants has been linked to an inflammatory response in vivo. The toxicology of CoCrMo nanoparticle wear debris remains unclear as little is known about the transport and distribution of particles/ ions in the body [20].

Statistically significant toxicological studies require relatively large amounts of wear debris because most of the studies are based on dose-response of triplicate assays, which could require more than hundred milligrams of nanoparticles [121,193]. However, producing large volumes of wear debris particles which match the composition size and morphology of those generated in actual hip replacements is extremely difficult. Laboratory hip simulators and pin-on-plate methods produce particles with a good approximation to the real wear debris observed in-vivo but this can take a long time to produce a small volume of material. Some studies have shown successfully large scale nanoparticle production using mechanochemical milling [130,158,162]. This technique allows the production of nanoparticulates using micro-sized starting powder alloys that degrade by the action of a combination of high energy impact/ friction and corrosion in the milling environment (liquid or gas).

In this chapter, CoCrMo nanoparticles were produced by a mechanochemical milling procedure, which was optimized and results compared with debris observed in the literature and that found using the pin-on-plate method, a consolidated technique to generate synthetic wear debris. These tests mainly assessed the particle size, shape and composition taking into account the amount of wear debris and the production time.

In all simulation methods, the raw materials are under tribocorrosion conditions, in which the degradation mode includes wear, mostly by friction, and corrosion related to the chemical and electrochemical interactions between

the metal and the aqueous environment. The techniques are all different tribosystems which are related to the sample geometry and the directions involved in the friction (unidirectional sliding or reciprocating motion). Hip simulators are submitted to multidirectional sliding and pin-on-plate technique is in a reciprocating mode. In mechanochemical milling, the friction plays a minor role compared to impact in the overall degradation process.

Dynamic Light Scattering (DLS) and X-ray diffraction (XRD) analysis allowed bulk identification of the particle and crystallite size range and phase identification of the crystalline material, respectively. Transmission Electron Microscopy (TEM) and Energy-dispersive X-ray spectroscopy (EDX) provided an accurate analysis in terms of size, morphology and composition of the CoCrMo nanoparticles procedure. Thermogravimetric analysis (TGA) of a suspension allowed determination of the particle concentration generated by the different techniques. The full description of methods and materials used in this section can be found in Section 3.6.

## **4.2 Mechanochemical Milling**

### **4.2.1 - 440C Hardened Steel Vial/beads**

Figure 4.1 shows a DLS histogram of preliminary milling studies using a SPEX mill with a vial and beads made of 440C hardened steel (from SPEX SamplePrep) and CoCrMo low carbon alloy powder immersed in heptane with 10% oleylamine used as a process control agent. The volume distribution [Figure 4.1 (c)] showed two distinct peaks which were well defined, whereas the distribution by number of particles [Figure 4.1 (a)] showed a wide main peak at  $53.2 \text{ nm} \pm 10.7 \text{ nm}$ , in contrast with the intensity distribution [Figure 4.1 (b)] which is dominated by the scattering of large particles at  $243.8 \text{ nm} \pm 119.0 \text{ nm}$ , as expected. The results indicated a significant size decrease following milling from the initial size of  $4.8 \text{ }\mu\text{m} \pm 3.0$  of the gas atomized powder particles shown in Section 3.5.1.

DLS measurements can be affected by scattering from the larger particles that swamps the signal from the smaller ones (the scattered intensity varies as the sixth power of the particle diameter). This means that it is difficult

with DLS to measure a wide range of particle sizes as produced by milling, where particles can vary between 10 nm and 1,000 nm.

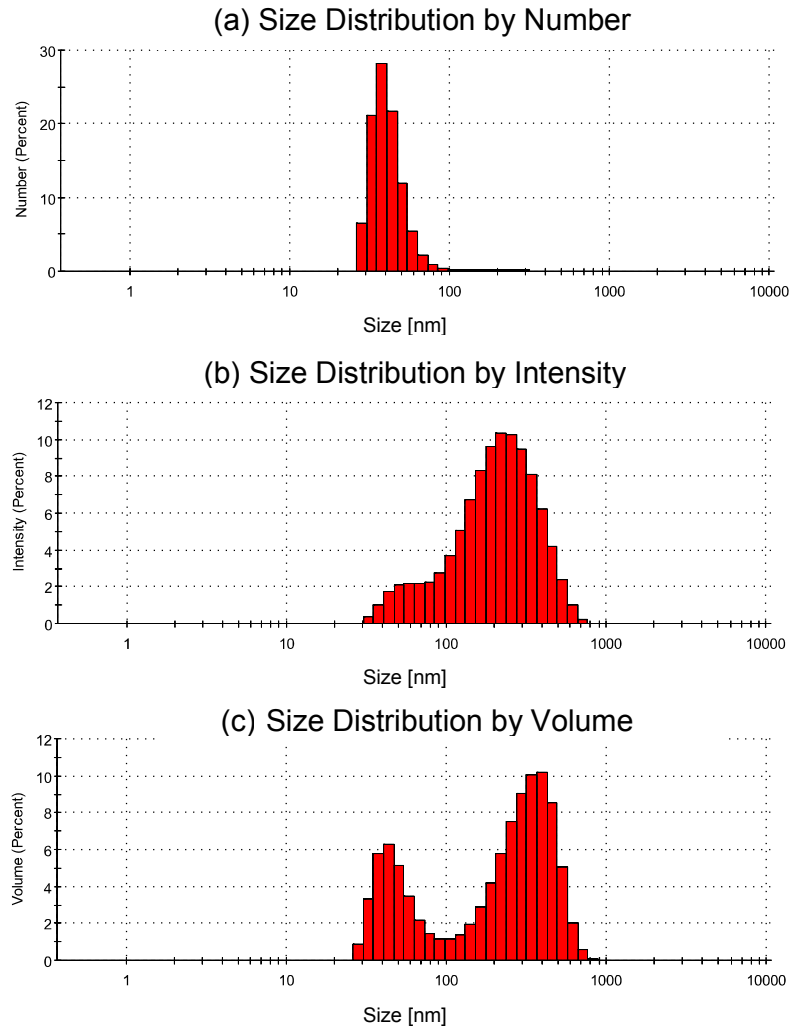


**Figure 4.1** - DLS of ASTM75 CoCrMo low carbon milled for 4h in heptane with 10% oleylamine showing size distribution by: (a) number, (b) intensity and (c) volume.

Figure 4.2 shows a TEM micrograph from a typical large milled particle with a size ca. 92 nm surrounded by a dense concentration of small particles ca. 6 nm [labelled (b) and (c)] probably arising as a result of the dispersant action during milling. EDX of the particles showed particle (a) was mainly composed of cobalt and sulphur, with a relative wt% elemental ratio for Co, Cr and Mo of 82%, 18% and 0%, respectively. Particles (b) and (c) showed major peaks of sulphur, with relative elemental ratios (in wt%) of Co-51% Cr-49% Mo-

0% and Co-54% Cr-46% Mo-0%, respectively. High amounts of oxygen were found for all the particles, indicating oxidation, whereas no molybdenum (Mo  $K_{\alpha}$  at 17.44 keV) was detected, possibly as a result of corrosion or the detection limit of the technique. EDX highlighted the large presence of contamination as S, Na, Mg and K that may come from the jar and beads previously used with other materials. The presence of iron in 40% of the particles analysed indicated a contribution of the steel vial and ball in contamination of the sample, presumably due to the hardness of the CoCrMo alloy compared to the 440C hardened steel.

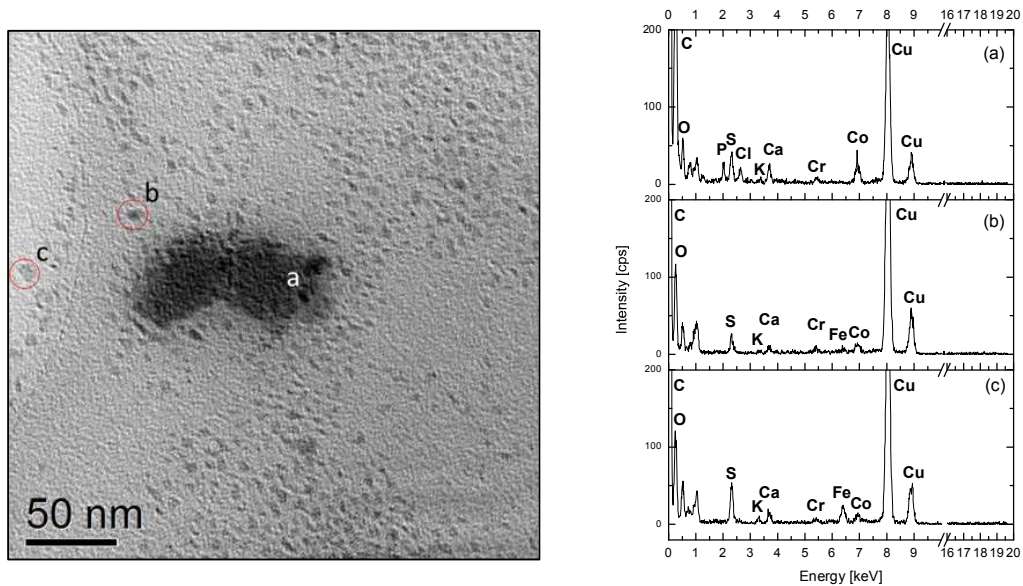


**Figure 4.2** - Bright field image and EDX of ASTM75 CoCrMo low carbon alloy powder milled for 4h using heptane with 10% oleylamine in steel vial/beads.

Energy-Filtered Transmission Electron Microscopy (EFTEM) in Figure 4.3 (b) showed the presence of chromium in the large particle, and in some, but not all of the small particles.

Particles found here showed a wide variety of sizes and a high level of contamination from the beads and the vial. Even with the good particle size reduction, the steel vial/beads demonstrated a high level of contamination, mainly of iron, which was present in the majority of the particles analysed. The

high levels of iron contamination may potentially interfere in toxicological studies.

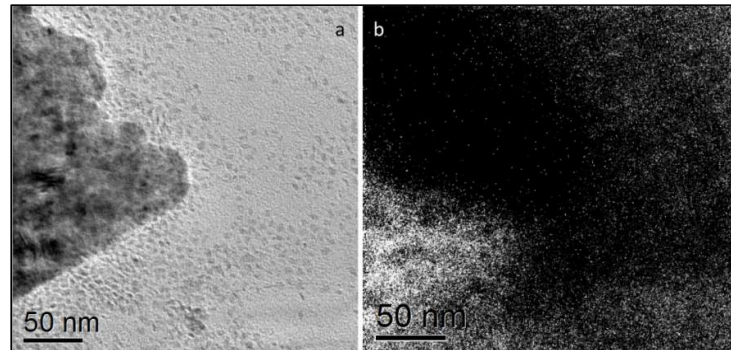
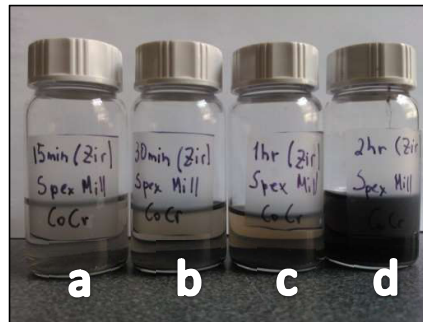


**Figure 4.3** - EFTEM of ASTM75 CoCrMo low carbon alloy powder milled for 4h in heptane with 10% oleylamine in steel vials/ beads: (a) Zero loss filtered image; (b) Cr L<sub>2,3</sub> – edge elemental map.

#### 4.2.2 - Zirconium Oxide Vial/Beads

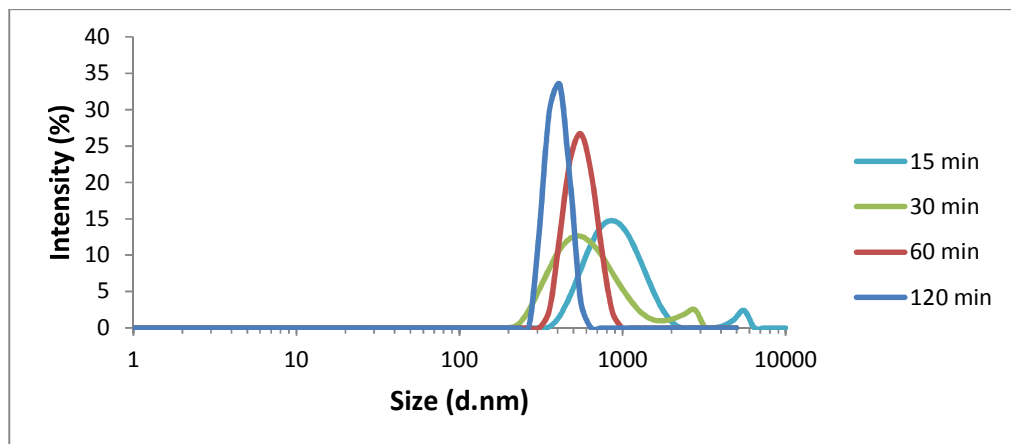
According to Table 2.4, a good material for the vial/beads is zirconium oxide (also known as zirconia), which has an extremely high resistance to abrasion, wears very slowly, and results in little contamination, according to SPEX SamplePrep [163]. In addition, due to their poor solubility, zirconium compounds have low systemic toxicity [194], being a good alternative milling media for CoCrMo corrosion and toxicological studies.

CoCrMo ASTM F75 low carbon alloy powder was milled for 15, 30, 60 and 120 min in heptane with 10% oleylamine using zirconium oxide vial/beads. The coloured liquids shown in Figure 4.4 contained a dispersion of nanoparticles after wet milling with heptane and oleylamine. Very fine particles remained suspended in the liquid while coarse particles were sedimented at the bottom of the glass jar. The influence of the surfactant on the liquid was noted in the colouration, for low milling times the liquid was clear with the liquid darkening as the milling time increased indicating improved particle dispersion in the liquid.



**Figure 4.4** - Liquid dispersion of CoCrMo particles following wet milling in heptane with 10% oleylamine for (a) 15 min, (b) 30 min, (c) 60 min and (d) 120 min.

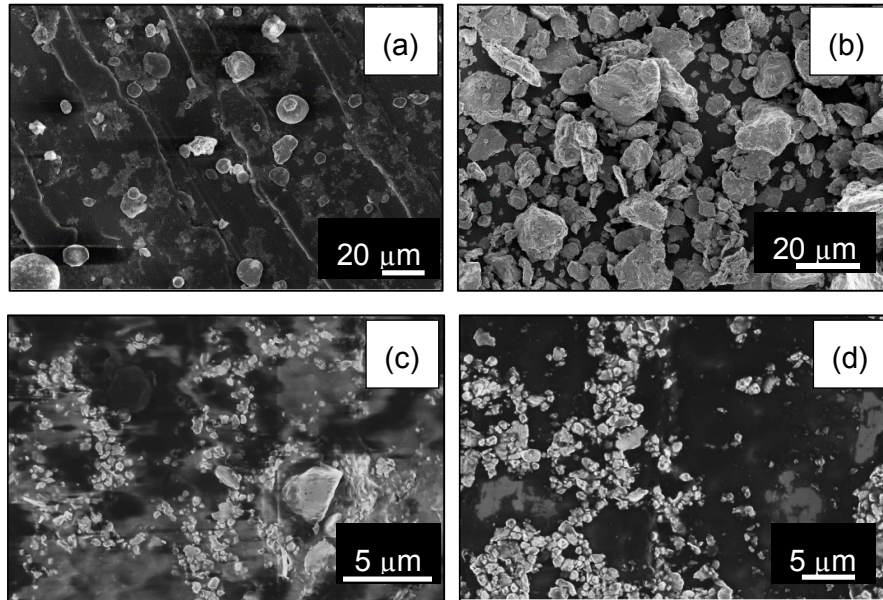
Figure 4.5 shows the DLS intensity plots of the CoCrMo milled particles for 15, 30, 60 and 120 min. The results show the relation between milling time and the size of the particles. For particles milled for 15 and 30 min, the DLS results showed a bimodal size distribution, characteristic of polydispersed particles, whereas for longer times (60 and 120 min) the particles were found to be in a more narrow size range.



**Figure 4.5** - DLS intensity plot of the milled CoCrMo particles at different times.

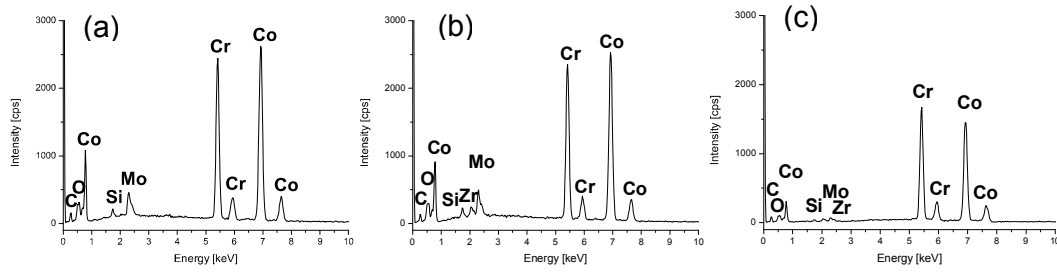
Figure 4.6 shows SEM micrographs of CoCrMo particles milled for 15, 30, 60 and 120 min. For 15 and 30 min, only a few particles remained dispersed in the liquid, so more drops of the solution were required during SEM sample preparation. For 15 min, several particles were unaffected by milling, showing the same round shape and size as the raw material. For 30 min, SEM

images showed some large particles with a lamellar structure, typical of the early stages of milling. In this stage, the particles tend to increase from their initial size and then start to decrease in size. After 60 min, particles showed a visible size reduction, with only a few large particles present. Finally after 120 min, the particles exhibited a homogeneous size distribution, similar to that observed by DLS.



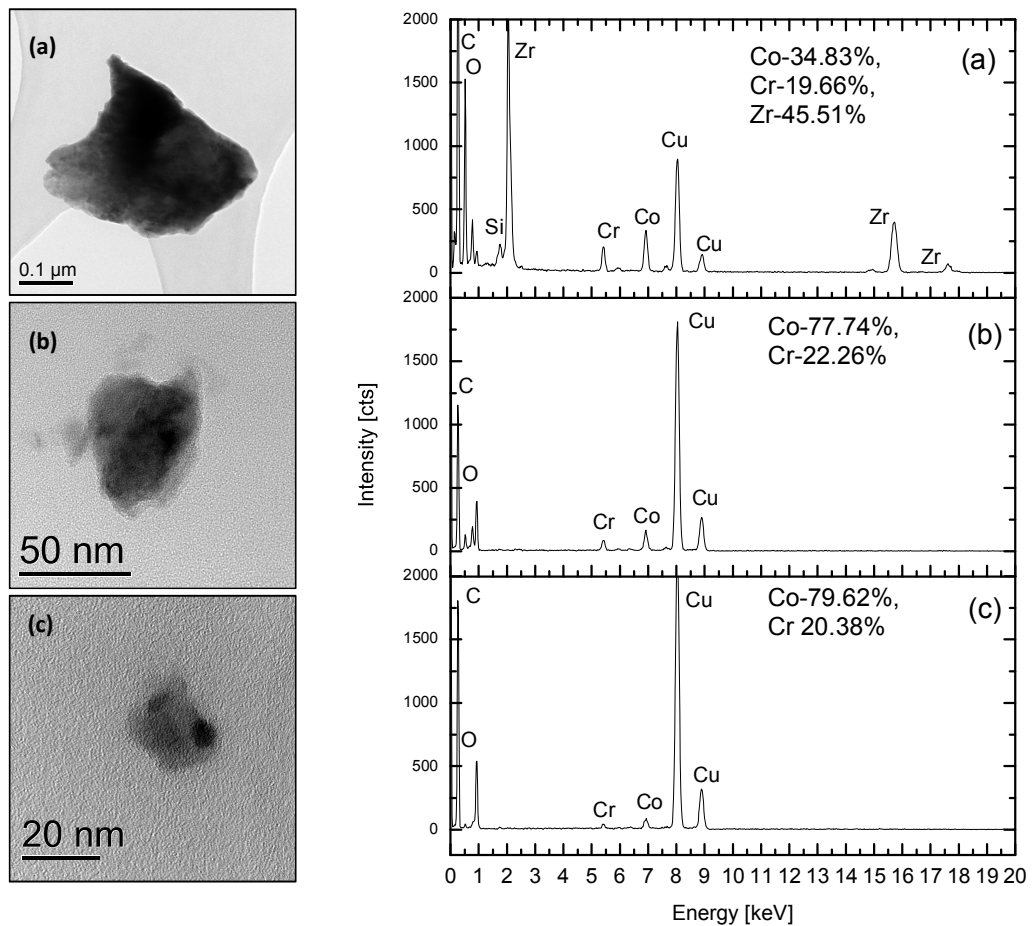
**Figure 4.6** - SEM secondary electron image of CoCrMo milled for: (a) 15 min, (b) 30 min, (c) 60 min and (d) 120 min.

SEM-EDX of the micron-sized particles milled for 120 min suggested a similar composition (in wt%) to the raw material, Co-65% Cr-28% Mo-7%, with Zr contamination from vial/beads at about 10% relative to other metallic debris (Figure 4.7). Few Cr-rich particles were found as shown in Figure 4.7 (c). Zr contamination appeared more often in large particles. As the size of the particles decreased, the EDX peaks of Zr were not detected.



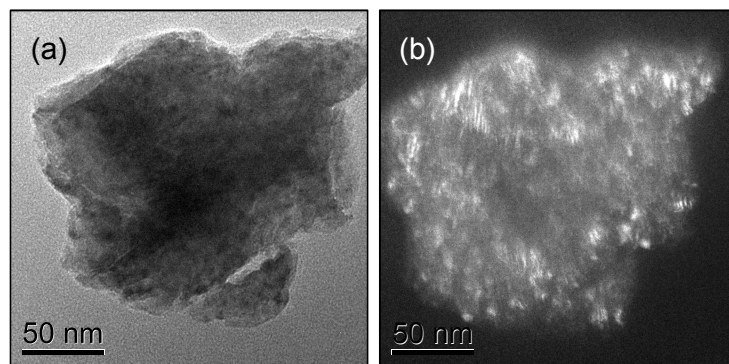
**Figure 4.7** - SEM-EDX of the micron-sized milled particles: (a) typical CoCrMo with ASTM75 composition, (b) CoCrMo with traces of Zr and (c) Cr-rich particles with traces of Zr.

Figure 4.8 displays TEM bright field images and EDX spectra of particles milled for 120 min that showed: (a) faceted particles with a major composition of zirconium oxide; (b) and (c) alloy particles with a faceted and spherical shape and respective size of 60 nm and 20 nm.



**Figure 4.8** – TEM bright field images and EDX analysis (wt%) of CoCrMo powder milled for 120 min.

The CoCrMo particles are polycrystalline (grain size ca. 10 nm) as shown by TEM dark field in Figure 4.9. The electron diffraction pattern presented in Figure 4.10 suggested the major presence of the FCC (+) phase of CoCrMo (ref. code 04-016-6869) and also some of the HCP (o) phase (ref. code 04-016-6870). Plastic deformation during milling can induce the dynamic phase transformation from FCC to HCP with a decrease in particle and crystallite size.



**Figure 4.9** – TEM bright field (a) and dark field (b) images of a CoCrMo particle milled for 60 min.

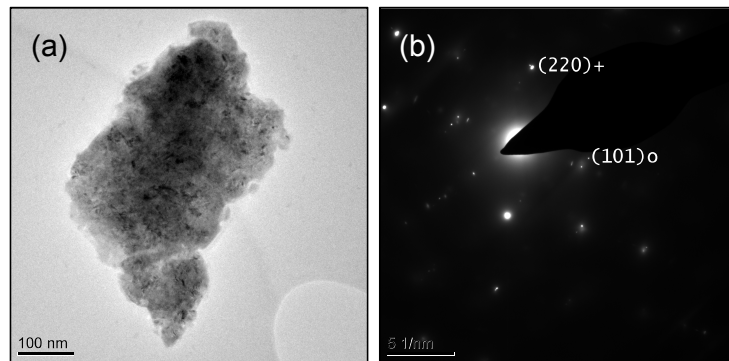


**Figure 4.10** - TEM bright field image (a) and selected area electron diffraction pattern (b) of CoCrMo particle milled for 60 min.

Particles milled with zirconium oxide vial/beads exhibited good control of contamination, considering that most of the contamination was found in large particles. Some adjustment in the weight ratio of ball-to-powder could help to

decrease this contamination even further. Moreover, after milling, the beads surfaces and the vial walls were completely covered by a CoCrMo solid layer. It is expected that after several milling runs, this layer will increase in depth and decrease the contamination arising as a result of the erosion of the zirconium oxide walls.

In conclusion, zirconium oxide vial/beads showed a superior performance than 440C hardened steel milling media. Nanoparticles were obtained in large amounts using both materials, however, zirconium oxide took less time to produce a narrow size distribution of particles with less contamination than the steel material. Because the Zr contamination was found mostly in the large particles, there is also a possibility to decrease the contamination level even further by separating the large particles from the smaller milled powder material.

### **4.3 Optimization of the Milling Process**

Mechanical milling using a high energy SPEX mill has been employed to produce large amounts of wear debris. Basically, milling is a process of grinding which could be applied for several purposes such as: particle size reduction, amorphization, change of particle shape, solid state blending and change of materials properties. There are three stages of milling: the first stage is the initial compaction, rearrangement and restacking of particles followed by the particles sliding past each other producing a fine and irregular shape. Stage two is the compaction involving elastic and plastic deformation and this may cause cold welding for a metallic substance. The third stage of compaction involves particle fracture which results in further deformation or fragmentation of particles into the micro- or nanometre size range [164]. When particle fragments decrease in size, the tendency to aggregate increases and the fracture resistance will also increase, so the size reduction will reach a limit and if the milling process continues energy will be wasted without any further size reduction [164].

The process is affected by many variables such as: the type of mill; milling container; milling speed; milling time; type, size, and size distribution of

the grinding medium; ball-to-powder weight ratio; extent of filling of the vial; milling atmosphere; process control agent and temperature of milling. All these process variables are not completely independent. For example, the optimum milling time depends on the type of mill, size of the grinding medium, temperature of milling, ball-to-powder ratio, etc.

In the process of milling the CoCrMo nanoparticles, some of the variables are fixed by the purpose of the milling or by the laboratory resources. The other variables can be accordingly manipulated so as to optimize the process. A factorial experiment is a simple statistical method that compares the maximum and minimum levels of a variable in the experiment and the combining effect of all variables to analyse the influence in the desirable outcome [195]. Useful exploratory analysis tools for factorial experiments include main effects plots, interaction plots, and a normal probability plot of the estimated effects. In this study a factorial design experiment was used to investigate the effect of milling variables on both size reduction and contamination, obtaining an optimum condition through the use of optimized parameters.

Samples from the experiment were characterized by using Scanning Electron Microscopy (SEM) for particle morphology and particle size, Energy Dispersive X-Ray Spectroscopy (EDX) for the sample composition and contamination level and Dynamic Light Scattering (DLS) to obtain the average size of the particle in each sample. Factorial design has been carried out to obtain the effect of the variables and the optimum conditions to obtain the maximum size decrease with the minimum level of contamination.

#### **4.3.1 - Characterization of the milled particles from factorial design**

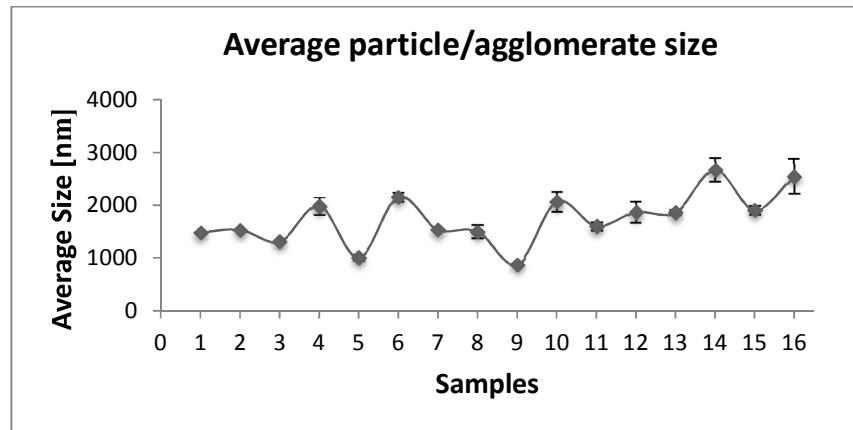
At the end of 16 experiments with the 4 parameters listed in Table 4.1 [the milling time, the ball-to-powder weight ratio, the level of surfactant (oleylamine in heptane) and the number of balls], the average particle size was measured by DLS. All the experiments showed a doublet peak in DLS intensity plots, representing both large and small particles. By DLS number, the small particles are the majority in the samples, however for statistical purposes the

use of the average particle size gives a good estimation of the overall size reduction during milling. Zr contamination during the experiments was measured using SEM/EDX of different large areas in each sample.

**Table 4.1** - Description of the milling parameters in the factorial design experiment plus the size reduction and contamination level in wt% relative to Co, Cr and Mo.

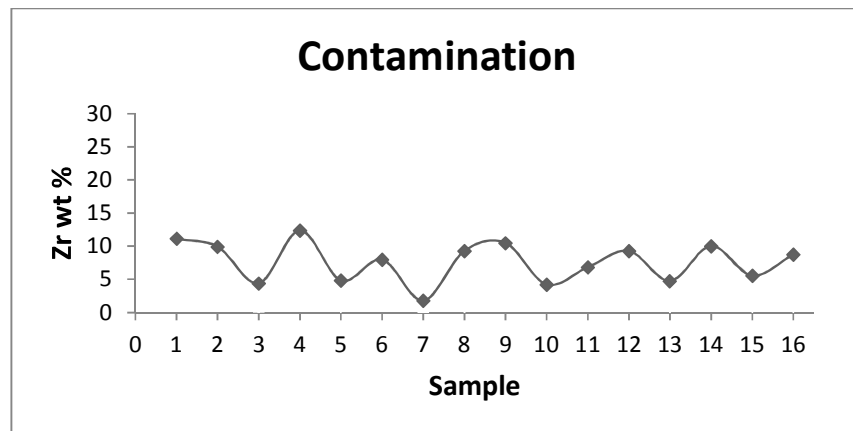
| Samples |            |                      |   |       | DLS        |       | SEM/EDX |      |
|---------|------------|----------------------|---|-------|------------|-------|---------|------|
| #       | Time [hrs] | Ball-to-Powder [g/g] | Surfactant [% of oleylamine to heptane] | Balls | Z-Ave [nm] | Std   | Zr [%]  | Std  |
| 1       | 2          | 10:1                 | 10                                      | 3     | 1482.7     | 5.5   | 11.1    | 7.6  |
| 2       | 10         | 10:1                 | 10                                      | 3     | 1533.3     | 16.0  | 9.9     | 6.1  |
| 3       | 2          | 5:1                  | 10                                      | 3     | 1312.5     | 21.5  | 4.4     | 4.5  |
| 4       | 10         | 5:1                  | 10                                      | 3     | 1984.0     | 156.5 | 12.4    | 11.7 |
| 5       | 2          | 10:1                 | 20                                      | 3     | 1005.9     | 55.1  | 4.8     | 6.4  |
| 6       | 10         | 10:1                 | 20                                      | 3     | 2157.5     | 82.5  | 8.0     | 7.1  |
| 7       | 2          | 5:1                  | 20                                      | 3     | 1539.0     | 15.0  | 1.8     | 1.8  |
| 8       | 10         | 5:1                  | 20                                      | 3     | 1504.5     | 121.5 | 9.3     | 9.7  |
| 9       | 2          | 10:1                 | 10                                      | 2     | 874.6      | 26.2  | 10.5    | 9.2  |
| 10      | 10         | 10:1                 | 10                                      | 2     | 2065.0     | 180.0 | 4.2     | 2.6  |
| 11      | 2          | 5:1                  | 10                                      | 2     | 1603.5     | 72.5  | 6.8     | 8.2  |
| 12      | 10         | 5:1                  | 10                                      | 2     | 1867.0     | 192.0 | 9.3     | 8.6  |
| 13      | 2          | 10:1                 | 20                                      | 2     | 1863.3     | 47.5  | 4.8     | 8.9  |
| 14      | 10         | 10:1                 | 20                                      | 2     | 2670.0     | 211.5 | 10.0    | 8.5  |
| 15      | 2          | 5:1                  | 20                                      | 2     | 1905.5     | 80.5  | 5.5     | 8.4  |
| 16      | 10         | 5:1                  | 20                                      | 2     | 2547.7     | 327.5 | 8.8     | 9.5  |

Figure 4.11 shows the average particle size measured by DLS in a triplicate assay (i.e. three separate DLS measurements). Time was the most pronounced effect, where a 2h milling time (odd numbered samples) tended to influence more significantly the particle size reduction compared to 10h milling time (even numbered samples). This implies that after 10h of milling there was cold welding between the metal particles, and the surfactant was no longer able to prevent aggregation [129].



**Figure 4.11** - Average size of the particles produced during factorial design study as measured by DLS.

SEM/ EDX analysis on milled samples indicated Zr traces on CoCrMo particles with an average of  $7.6\% \pm 3$  (wt%). When performing high-energy milling to synthesize nanomaterials, contamination from the materials that the balls and vials are made of is virtually unavoidable.



**Figure 4.12** – Contamination for samples produced in factorial design study measured by SEM/EDX.

### 4.3.2 - Analysing the effects of variables and the interactions

To estimate the main effect for a factor (S), the average size measurements of all experimental runs for the variable at a high level ( $\bar{y}_{max}$ ) is subtracted with the corresponding average size measurement for runs with the same variable at a low level ( $\bar{y}_{min}$ ):

$$S = \bar{y}_{max} - \bar{y}_{min} \quad \text{Equation (4.1)}$$

The differences among effects and the interaction of variables were analysed using Analysis of Variance (ANOVA, with a 90% confidence levels) in the software Minitab 17. Figure 4.13 shows the ANOVA model for the factorial design experiment with size reduction as the response. The results indicated that at a significance level of 0.1, only milling time influences the size reduction, with most of the others variables including their interactions appearing as noise with a low variance in the normal plot [Figure 4.13 (a)]. The Pareto chart of effects shows the second most relevant variable was the number of balls inside the vials.

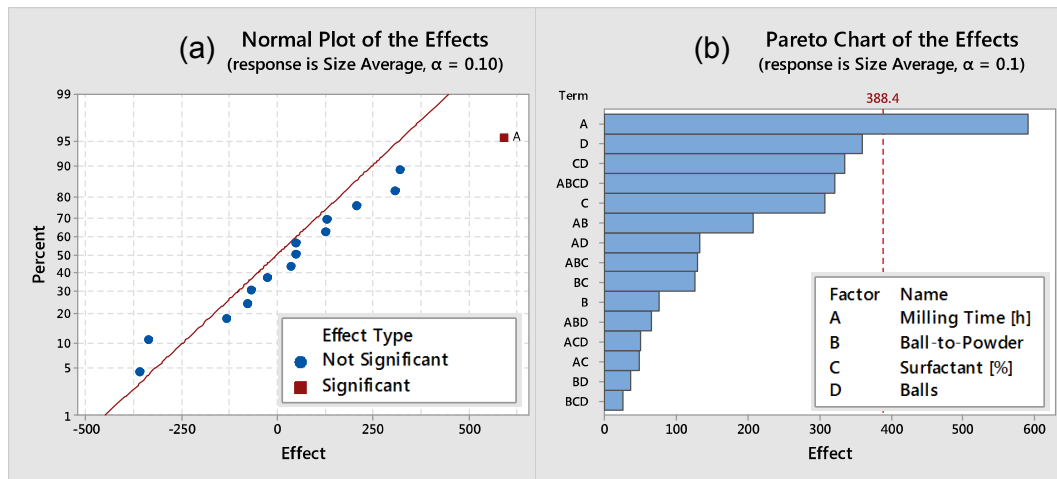


**Figure 4.13** - ANOVA of the effect of variables during milling using size reduction as the response: (a) Normal plot of the effects and (b) Pareto chart of the effects.

A contour plot indicates in which direction two variables can reach their target values (maximum size reduction or minimum contamination) using constant values for the other two parameters. Figure 4.14 shows the contour plot for two variables with the most significant effects: milling time and number of balls. The graph indicates that by decreasing the milling time and increasing the number of balls in the vial it is possible to achieve an average particle size of less than 1400 nm.

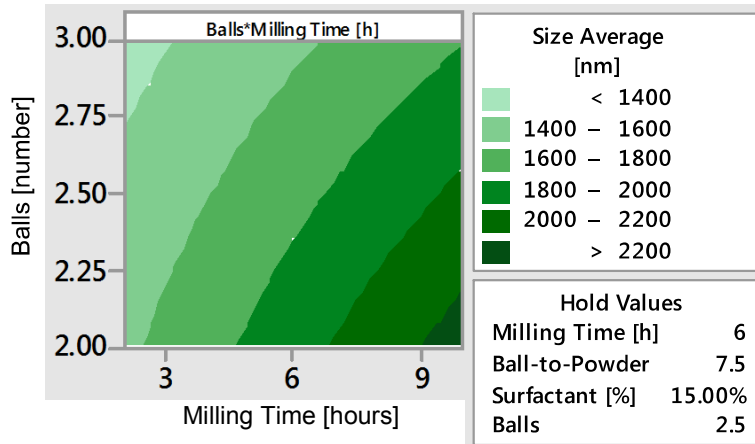


**Figure 4.14** - Contour plot of size average for number of balls versus milling time.

Figure 4.15 shows the ANOVA model for the factorial design experiment with contamination as response. The results indicate that milling time and the interaction of milling time and ball-to-powder ratio significantly affected the level of contamination during milling. It was expected that by increasing the milling time the contamination would increase. Also, decreasing the ball-to-powder ratio means an increase in the amount of starting powder inside the vial, which diminishes the contact between the Zirconium Oxide vial and beads because the powder occupies more space inside the vial during the attrition and sliding loads. This effect is more pronounced with an increase in milling time, which also increases the contact between the Zirconium oxide vial and beads because of the agglomeration of the particles. Both tendencies can be observed by the contour plot of contamination for milling time and ball-to-powder ratio (Figure 4.16), which estimates Zr contamination below 5% for milling times of about 2 hours and ball-to-powder ratio of about 5:1.

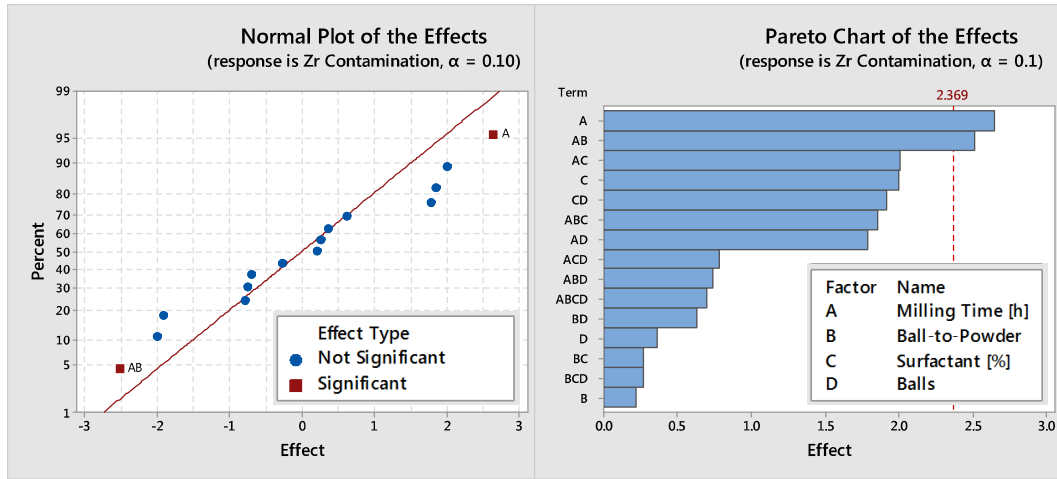


**Figure 4.15** - ANOVA of the variables effects of the factorial design  $2^4$  during milling using contamination as response: (a) Normal plot of the effects and (b) Pareto chart of the effects.

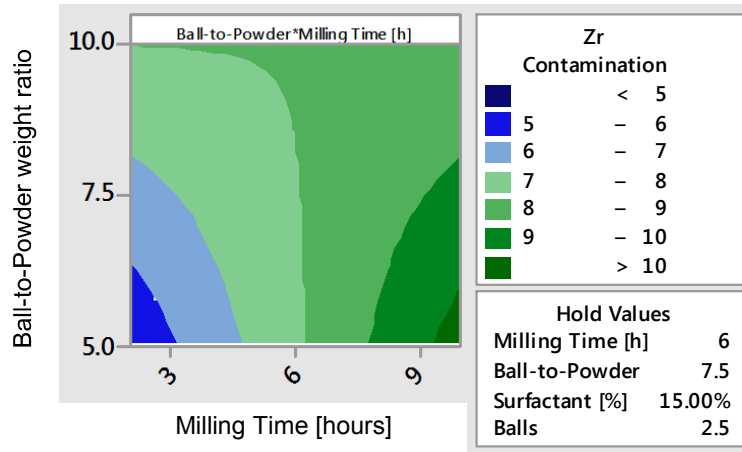


**Figure 4.16** - Contour plot of Zr contamination for Ball-to-Powder weight ratio versus Milling Time.

To achieve optimized conditions for both average particle size and contamination, Minitab 17 identified the combination of input variable settings that jointly optimize a single response or a set of responses. The optimal solution found for the input variable combinations were: 2 ½ hours milling time, 5:1 ball-to-powder weight ratio, 20% of surfactant (oleylamine in heptane) and 3 zirconium oxide balls, which gives a particle size average of about 1.5  $\mu\text{m}$  and less than 2.5 wt% of Zr contamination.

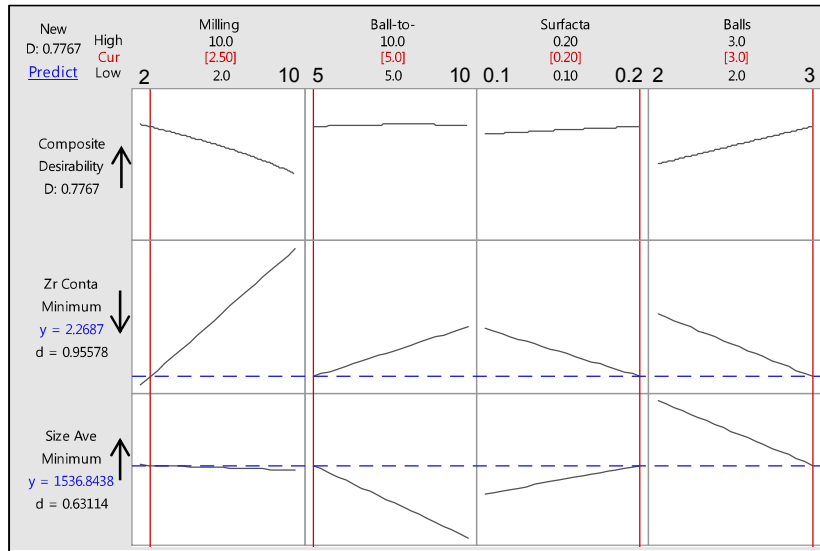


Figure 4.17 - Optimization plot for the factorial design.

### 4.3.3 - Isolating Nanoparticles

Centrifugal Particle Sizing (CPS) with high resolution was used to analyse the centrifugation time required to remove coarse particles, which are related to the unmilled and welded particles. This procedure also decreased the Zr contamination that was specifically related with the coarse particles.

CoCrMo milled particles with a density estimated at  $8.3 \text{ g/cm}^3$ , were centrifuged at 14000 rpm for 10 min. Figure 4.18 shows the CPS results, which demonstrate an effective sedimentation time of up to 7 minutes, removing particles above ca. 500 nm in diameter.

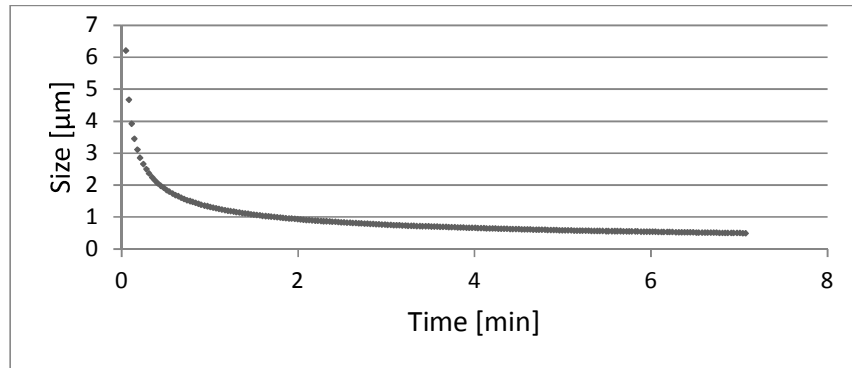
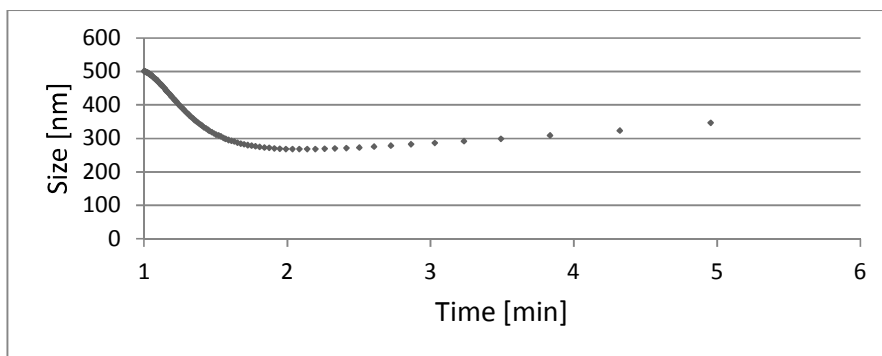


Figure 4.18 - CPS of milled CoCrMo particles centrifuged for 10 min at 14000 rpm.

In order to investigate the size fraction after longer centrifugation times, another run was carried out using the supernatant of samples after an initial centrifugation for 7 min. The results in Figure 4.19 showed that the limit for centrifugal sedimentation at the rotational speed of 14 000 rpm is ca. 10 min.



**Figure 4.19** - CPS of milled CoCrMo and centrifuged particles for 7 min.

XRD indicated the presence of  $ZrO_2$  amongst milled particles and gave a good indication of large amounts of contamination as compared to the small sample volumes probed by TEM-EDX. Figure 4.20 shows the presence of main peak (101) of tetragonal zirconia with (JCPDS 083-0113) after milling, however, after centrifugal sedimentation, the large zirconia particles are removed from the dispersion, and the corresponding  $ZrO_2$  XRD peak is absent.

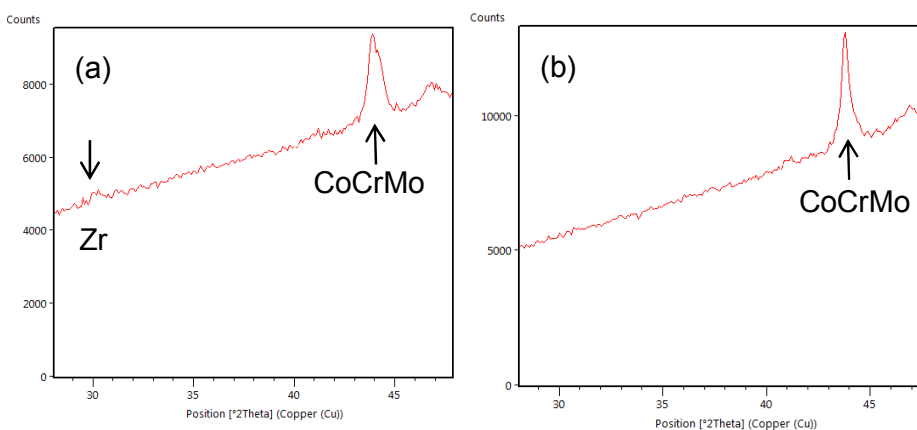


**Figure 4.20** - XRD of CoCrMo particles: (a) after milling and (b) after milling and centrifuged.

#### **4.3.4 - Simulating wear debris from hip implants**

The hip degradation process can be initiated by physical and/or chemical reactions. Impact, compression and friction are physical reactions more relevant to hip implants and milling can, in principle, reproduce these forces, however the process may use different loads and timescales. During milling, metal particles are continually submitted to a welding, fracture and re-welding process. Bovine serum albumin (BSA), often used as surrogate for proteins present in-vivo, will be shown for the first time that can also act as a surfactant, creating a protective biolayer on the surface of the CoCrMo particles that inhibits the welding process. As a result, milling in BSA is dominated by the fracture process, reducing significantly the size of the particles. The optimum conditions for both milling time (2 ½ hours) and ball number (3) found for milling in oleylamine /heptane were applied for the case of milling in 0.2 g of BSA diluted in 10 mL of deionized water (used as surfactant). The ball-to-powder weight ratio was extrapolated to 3:2, so as to reduce the contact between Zr balls and vial.

CoCrMo ASTM F75 gas atomized particles were characterized as received in Section 3.5.1, and were found to have an average size of  $4.8 \mu\text{m} \pm 3.0$  mainly with a spherical shape. EDX showed particles with a narrow composition (wt %) of Co  $63.3\% \pm 1.1$ , Cr  $30.2\% \pm 0.7$  and Mo  $6.5\% \pm 1.2$ . Figure 4.21 shows a TEM micrograph of the CoCrMo particles after milling, in which a wide range of particle sizes were found (ca. 8-2000 nm), hence a centrifugation for 10 min at 14 000rpm was used to obtain a narrower size distribution which was more representative of that observed in real wear debris [21]. This procedure also removed part of the BSA and most of the coarse particles (>200 nm), maintaining most of the fine particles in dispersion within the supernatant.

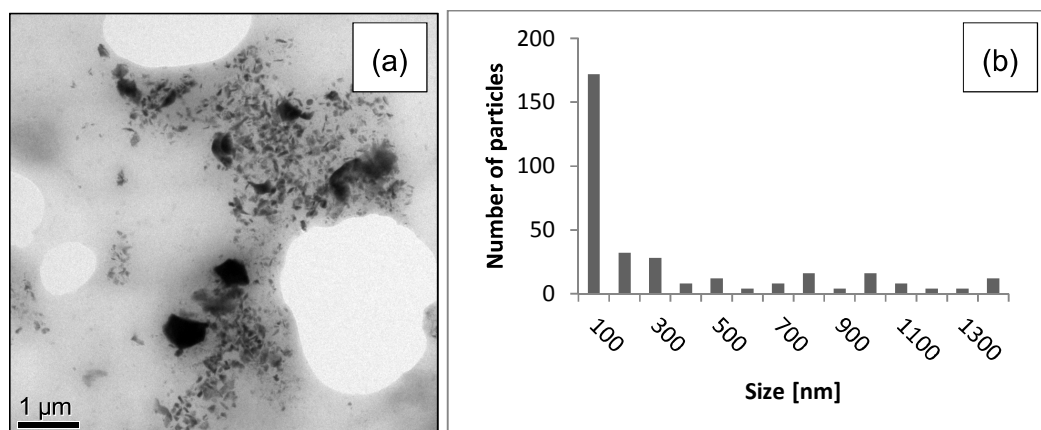


**Figure 4.21** - CoCrMo low carbon milled particles in BSA for 2h30, using 3:2 ball-to-powder weight ratio and 3 balls: (a) TEM bright field image; (b) size distribution by TEM image analysis.

Figure 4.22 shows a TEM micrograph of the CoCrMo nanoparticles after centrifugal sedimentation where the large particles were now absent. A particle size measurement from TEM images indicated an average size of  $22 \pm 30$  nm, whereas the particle shape was found to be approximately: 72% of particles were faceted, 3% elongated and 25% spherical.

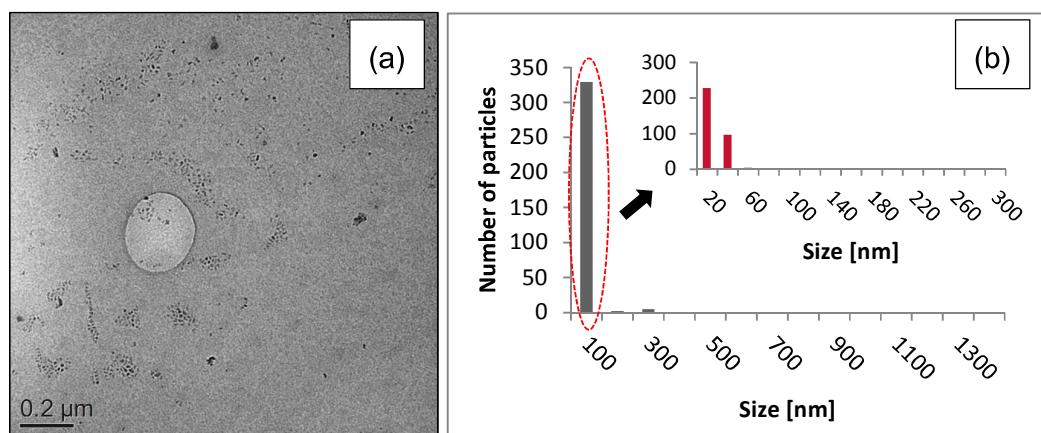


**Figure 4.22** - CoCrMo low carbon milled particles in BSA for 2h30, using 3:2 ball-to-powder weight ratio and 3 balls, following centrifugation for 10 min at 14 000 rpm: (a) TEM bright field image; (b) size distribution, by TEM image analysis with an expanded view of the small size region.

TEM-EDX results showed that particle size reduction was accompanied by changes in composition. After milling, a significant decrease of cobalt and molybdenum could be observed relative to the CoCrMo raw material. EDX

showed mainly two particle types: particles mainly composed of cobalt and chromium and molybdenum with a similar composition to the raw material [see Figure 4.23 (a)] and with all three shape forms, as well as faceted and spherical particles rich in cobalt and/or chromium with no molybdenum (Mo  $L_{\alpha}$  2.292 keV,  $K_{\alpha}$  17.44 keV) detected [Figure 4.23 (b)] (presumably as a result of the limit of detection of the technique and equipment or the effect of corrosion during milling). The average elemental composition (wt %) of nanoparticles measured indicated Co  $54\% \pm 16$ , Cr  $42\% \pm 16$  and Mo  $4\% \pm 8$ . Only 4% of the particles analysed showed a level of Cr higher than that of Co.

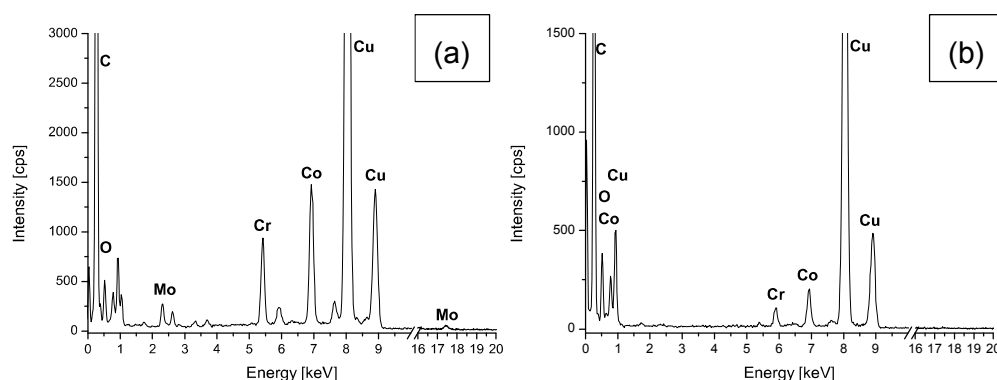


**Figure 4.23** - Energy Dispersive X-ray Spectroscopy (EDX) of two representative types of CoCrMo ASTM F75 low carbon alloy milled particles: (a) CoCrMo, similar to the raw material and (b) Co and Chromium rich.

TGA analysis on the supernatant of the milled and centrifuged CoCrMo sample was used to measure the concentration of particles in the solution. This is necessary since a large fraction of the powder and BSA was removed by centrifugation. Figure 4.24 shows 2 sample weight loss zones that can be attributed to the loss of water (3.64 mg) and bovine serum albumin (2.2 mg) thus giving an indication of the mass fraction of the 3 components: water (0.105 mL), BSA (1.44 mg) and CoCrMo (2.2 mg) particles. Knowing the total weight analysed (109.1 mg) allows us to estimate a concentration of ca. 20 mg/ mL and ca. 15 mg/ mL of CoCrMo nanoparticles and BSA, respectively.

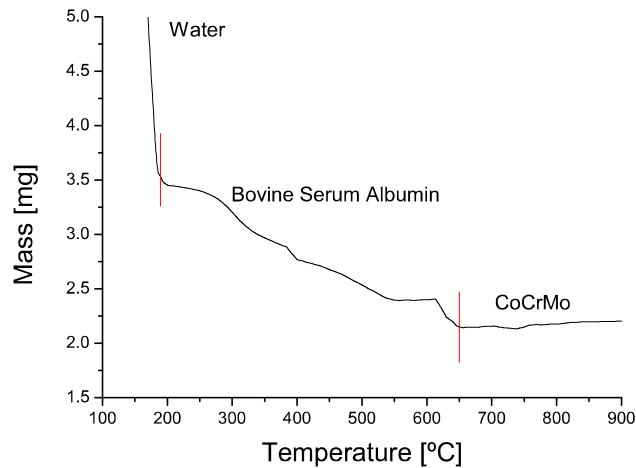


**Figure 4.24** - Thermogravimetric analysis of the centrifuged supernatant of CoCrMo milled in BSA for 2h30, using a 3:2 ball-to-powder weight ratio and 3 balls.

#### **4.4 Validation of CoCrMo milled particles with hip wear debris from literature**

Particle characterization is based on identifying size, morphology and chemical composition. In the literature a wide range of different sized wear debris particles can be produced in-vivo from MoM hip implants have been identified. Here a comparison between particles often found from hip implants that have been reported in the literature and particles obtained by the synthetic milling procedure in BSA for 2 ½ hours, using a 3:2 ball-to-powder weight ratio and 3 balls has been carried out.

##### **4.4.1.1 - Size**

Milled particles were found consistently in the size range of 5-40 nm (see Figure 4.22), which was more evident after centrifugal sedimentation removed larger particles. Ward *et al.* (2010) identified wear debris from synovial fluid of patients which was in the range of 5-50 nm [19]. Goode *et al.* (2012) found wear debris clustered over areas of 1 µm with a mean size of 30 nm in microtomed sections of surrounding tissue. Catelas *et al.* (2003) analysed particles after hip simulation for 0.25 million cycles, sizing the

particles mainly in the range 20-80 nm, with an average particle size of ca. 50 nm [152].

#### **4.4.1.2 - Morphology**

In this study, morphology characterization was carried out based on the procedure used by Catelas *et al.* (2003), which used ratios of the maximum dimension of each particle measured along orthogonal directions. After milling, particles were mainly found to be faceted (or oval), whereas for Catelas *et al.* (2003), particles were oval or needle shaped. Goode *et al.* (2012) reported the majority of the particles found were spherical, however the paper did not specify how the classification was carried out.

#### **4.4.1.3 - Chemical Composition**

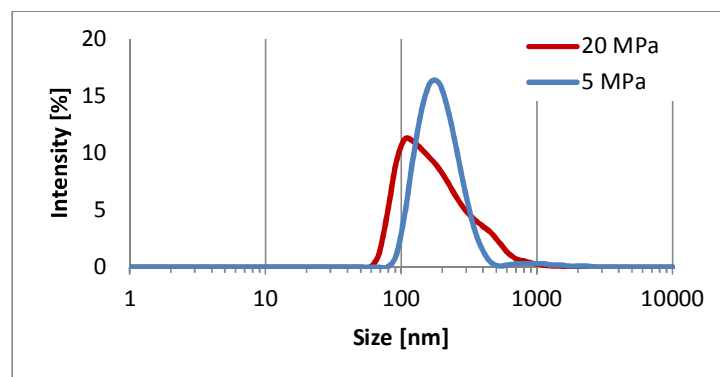
Mainly two different compositions were found following milling: cobalt and chromium-rich particles and particles with a similar composition to the raw material. Ward *et al.* (2010) identified wear debris in three main compositions: CoCrMo raw material; particles richer in Cr and Mo; and particles mainly composed of Cr and O. Goode *et al.* (2012) noted two types of wear debris particles: Cr<sup>+3</sup> containing particles with trace amounts of Co and dense core-shell particles containing metallic Co, Cr and Mo surrounded by Cr<sup>+3</sup> containing shell.

#### **4.4.1.4 - Brief Summary**

Both types of milled particles were comparable in terms of size, shape and composition to particles reported in the literature [19,21], however Cr-rich wear debris particles were only found on rare occasions following milling. In bulk hip implants, CoCrMo bulk materials form a protective oxide layer of Cr<sub>2</sub>O<sub>3</sub> that could be disrupted during wear. Another possible source of Cr rich particles could be the result of the long term corrosion of particles of the raw material that could suffer preferential dissolution of Co and Mo. In that sense, corrosion studies of milled particles could help to better understand the origin of the Cr-rich particles.

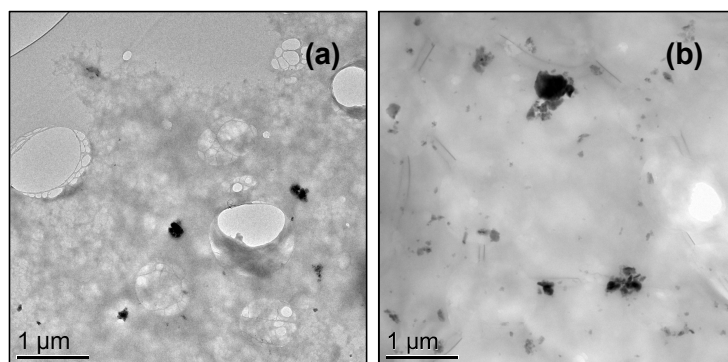
#### 4.5 Pin-on-plate Method for Production of Synthetic Wear Debris

DLS results shown in Figure 4.25 revealed that using contact pressure of 5 and 20 MPa produced relatively similar size particles; however a 20 MPa load exhibited an extended area in the DLS intensity plot similar to a doublet peak, indicating the presence of large particles in the dispersion. The particles were significantly bigger than those produced by milling followed by centrifugation, as well as those produced using a pin-on-plate method by Raghunathan et al. [187] for 24 h using 11 MPa load, which showed a particle size of  $29.5 \text{ nm} \pm 6.3$ .



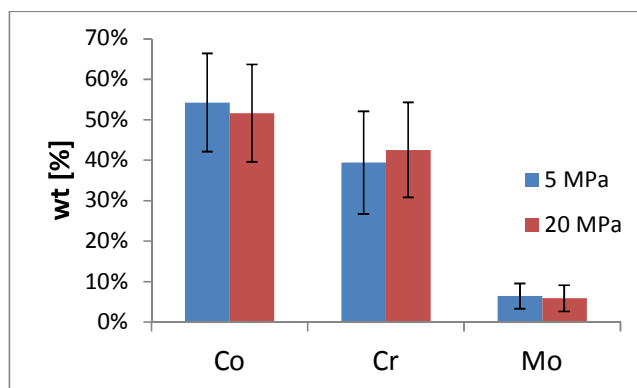
**Figure 4.25** - Size distribution of CoCrMo particles generated by Pin-on-Plate for 4 h immersed in BSA using contact pressure of: 5 and 20 MPa.

Figure 4.26 shows TEM bright field images of Pin-on-Plate produced particles. A size distribution for 300 particles showed an average size of  $86.3 \text{ nm} \pm 30$  for the experiment with a 5 MPa load, and  $112 \text{ nm} \pm 49$  for the 20 MPa load. The particle shape found for the 5 MPa load was: 67% of particles faceted, 19% elongated and 14% spherical. These were slightly different for the 20 MPa load which presented more elongated particles: 62% faceted particles, 32% elongated and 6% spherical. An increase in the applied load tends to increase the coefficient of friction proportionally [196], producing more elongated particles.



**Figure 4.26** - TEM bright field image of CoCrMo low carbon wear debris generated from pin-on-plate for 4 h at different contact pressure: (a) 5 and (b) 20 MPa.

Elemental composition of pin-on-plate particles produced using two loads was shown to be very similar, with most of the particles showing a Co deficiency relative to the composition of the bulk alloy. TEM-EDX of the pin-on-plate particles revealed an average composition (in wt%) of Co-54% ± 12, Cr-39% ± 13 and Mo-6% ± 3 and Co-52% ± 12, Cr-42% ± 12 and Mo-6% ± 3 for 5 and 20 MPa, respectively. Cr levels were higher than Co in 35% of the particles when using a 20 MPa load and in 29% when using a 5 MPa load.



**Figure 4.27** – Elemental composition measured by TEM/EDX of pin-on-plate CoCrMo wear debris particles using different loads.

Mainly two types of particles were found (see Figure 4.28): (a) particles similar to the raw material composition and (b and c) particles rich in chromium (and oxygen) with or without the presence of molybdenum.

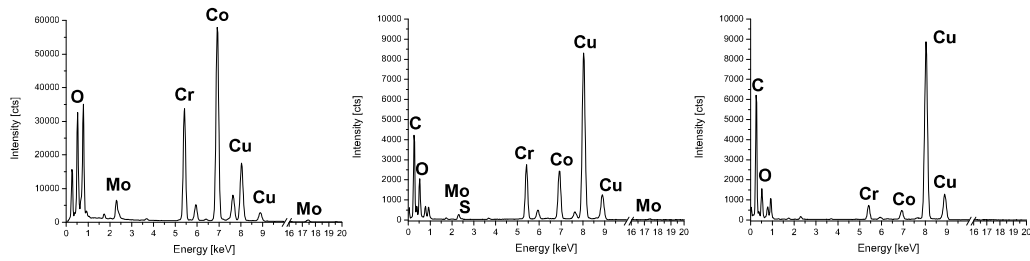


**Figure 4.28** - TEM-EDX of pin-on-plate particles: (a) particles exhibit composition similar to raw material, Cr-rich particles with (b) and without (c) the presence of Mo.

TGA was carried out on the pin-on-plate sample that used the 20 MPa load, which from TEM exhibited more particles than obtained at a load of 5 MPa. Figure 4.29 showed two major mass losses related to loss of water (3.50 mg) and BSA (0.36 mg). The total mass loss measured was 165.40 mg. CoCrMo particles were only a very small mass and were estimated by TGA to be ca. 0.36 mg which gives a concentration of 2.2 mg/mL of CoCrMo particles. The BSA concentration was 19.38 mg/mL, which was close to the BSA concentration at the start of milling. The particle size measured by TEM was at least 4x bigger than for CoCrMo milled particles. The contribution of large and hence heavier wear debris from pin-on-plate wear indicated the presence of fewer particles in the dispersion as compared to the milled particles.

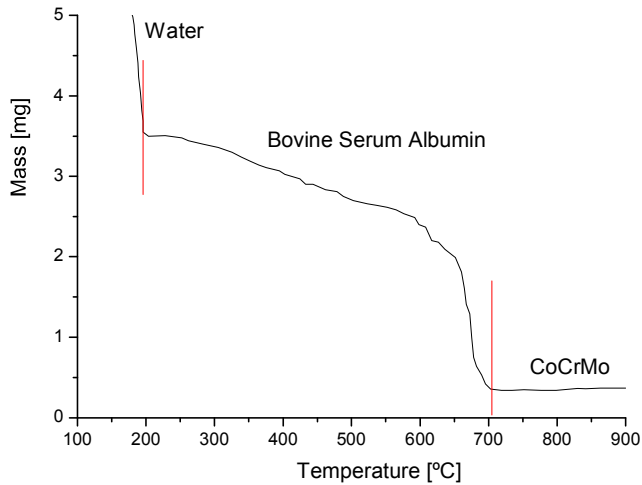


**Figure 4.29** - Thermogravimetric analysis of the solution of CoCrMo low carbon alloy immersed in 20 g/L of BSA diluted in MilliQ water for 4 h during pin-and-plate experiment using 20 MPa load.

## 4.6 Summary

Several studies have tried to determine the exact size, morphology and chemical composition of MoM wear particles generated in MoM hip prostheses [18–23]. There seems to be general agreement that CoCrMo wear debris particle size ranges between 30 to 70 nm. Some authors also reported larger particles linked to the occurrence of agglomeration [16, 17, 20]. The shape of wear particles appears to vary slightly from study to study, including round, oval and needle shaped particles. Regarding the chemical composition, most studies reported that particles were chromium-oxide or of CoCrMo alloy or alloy carbide origin [19, 20]. Since the alloy consists mostly of cobalt (~ 64 wt%), this could suggest that Co and Mo are being corroded and released into the solution, whereas mainly oxidized chromium would remain as particles. Another possibility may be that the chromium oxide particles originate from the passive oxide layer initially covering the implant surface.

However, before particles exit the tribological interface, they may be exposed to high mechanical load when trapped between surface asperities of the head and cup during contact. A protective film of proteins could be partly disrupted allowing oxidation or corrosion of the particles.

In this project a hitherto unexplored approach employing mechanochemical milling to produce a large amount of mimetic CoCrMo nanoparticle wear debris over short time scales has been used. Here, it was demonstrated to be a simple and efficient method to generate synthetic nanoparticles similar in size and shape to CoCrMo wear debris from hip implants. A wide range of particle sizes can be obtained and then separated by centrifugation. The particle composition was close to that of observed wear debris and similar to the raw material. However, only a few Cr rich particles were found, which could be related to the subsequent corrosion of CoCrMo particles.

The milling technique was also shown to produce more particles than pin-on-plate in less time. The amount of elongated particles produced through the pin-on-plate method was higher than milling, indicating probably that this

shape is related to the amount of frictional forces applied. During milling, there was a predominance of faceted and spherical particles. In terms of composition, Cr levels were higher than Co in about 30% of the particles pin-on-plate and only in 4% of milled particles, but in both the majority of the particles presented similar relative compositions to CoCrMo raw material.

The concentration obtained for a 10 mL milled sample is equivalent to ~20 years of debris generated from a real hip implant, based on the estimates of Yan *et al.* [38]. The large amount of nanoparticles produced in one run is suitable for a range of studies including: corrosion in relevant media, studies of protein binding and toxicity assays.

## **Chapter 5 - Tribocorrosion of Nanoparticulate and Wear Debris**

Metal-on-metal hip implant degradation leads to the release of metal ions and nanoparticles, which persist through the implant's life and could be a possible cause of health complications. The degradation of orthopaedic devices has been investigated via tribocorrosion for a number of interfaces [31–33,78,82,150], however degradation of the debris produced as a result of wear is not well understood [38,197].

In this chapter a modified ICP-MS sample preparation procedure has been used to measure the release of ions from CoCrMo alloys during wear simulation in different media. It is shown that the use of ultrafiltration following centrifugation, separates nanoparticulate wear debris from dissolved ions and provides an accurate estimate of metal ion release during tribochemical wear studies using hip simulators and also in milling experiments. Using this procedure, a study of the mechanochemical milling of CoCrMo nanopowder alloys (containing both high and low carbon) in relevant biological media has been undertaken. The chapter concludes with a study that correlates preferential binding between proteins and metal alloy nanoparticles to the alloy's corrosion behaviour and the release of metal ions.

### **5.1 Accurate ICP-MS measurement: the influence of sample preparation**

The established technique to analyse levels of metallic ions in simulation fluids is by inductively coupled plasma mass spectrometry (ICP-MS) conventionally following a sample preparation route involving centrifugation, extraction of the supernatant, acid digestion and prior to analysis. The centrifugation, digestion and dilution procedures are used to minimize clogging of the ICP-MS injector tube as well as minimize the influence of any matrix effects which may cause either (mass) spectral overlap problems or matrix-induced changes in the intensity of an analyte signal during analysis. In this study, the ionic release from CoCrMo high carbon (Co-60%, Cr-29%, Mo-7%) hip simulator debris generated over 30,000 cycles immersed in FBS mixed with

PBS was measured using three distinct methods of ICP sample preparation: centrifugation; ultracentrifugation; centrifugation and ultrafiltration. The full description of methods and materials used in this section can be found in Section 3.6.5.

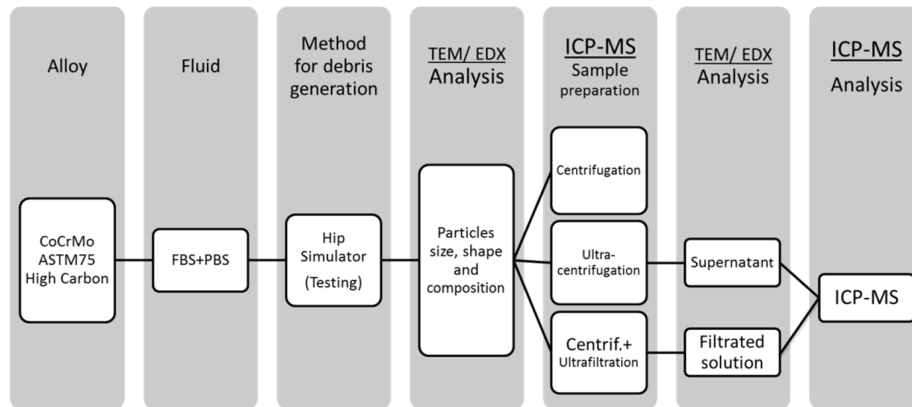


**Figure 5.1** - Flow chart with overall tests and analysis undertaken in this section.

### **5.1.1 - TEM/ EDX analysis of wear debris from hip simulator prior to ICP-MS measurements**

As an initial measure of the wear debris produced following wear testing in the hip simulator, approximately 100 wear debris particles suspended in the lubricant (without any centrifugation) were analysed by TEM, measuring particle size, shape and composition. Statistical significance of the results was calculated by ANOVA with a 95% of confidence level.

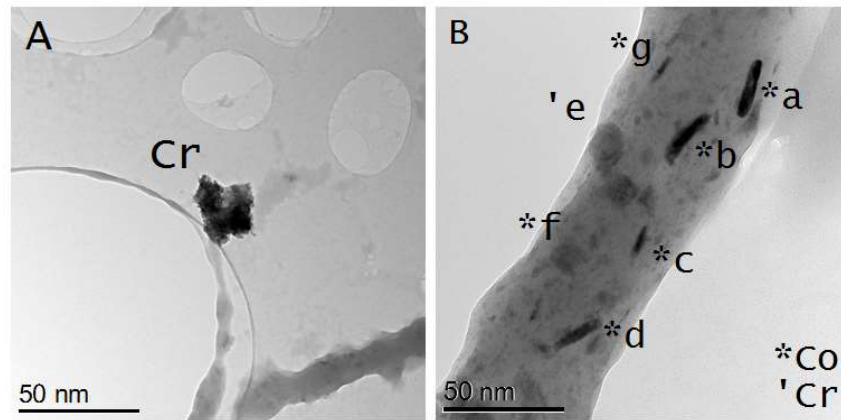


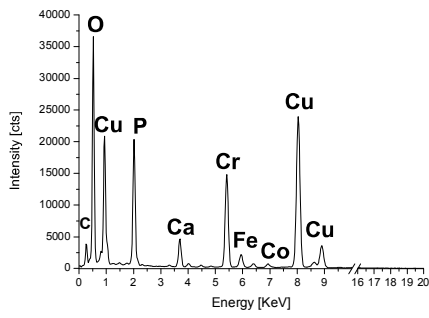
**Figure 5.2** - A and B, bright field TEM images of: different types of wear particles from the hip simulator test with Foetal Bovine Serum (FBS) in Phosphate-Buffered Saline solution (PBS) used as the lubricant.

Particles were found to be well dispersed and have an average size of  $25.3 \pm 20.7$  nm in the range of 4.6 – 183 nm, with 43% of particles faceted, 32% spherical and 25% elongated. The majority of the larger particles were found to be Cr-rich and to be associated with P and O (an example is shown in Figure 5.2 – A with EDX spectra shown in Figure 5.3). The smaller particles, often more acicular, were generally enriched in Co and Mo and associated with the presence of O and S (see Figure 5.2 – B with associated EDX spectra shown in Figure 5.3).

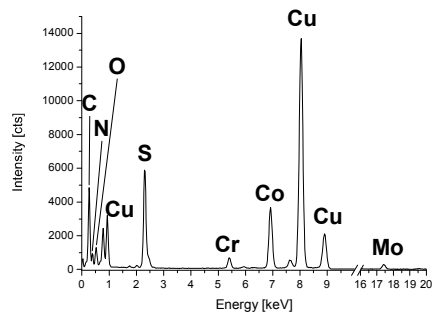
**Table 5.1** - Classification of CoCrMo high carbon wear particle's shape and length generated by hip simulator over 30,000 cycles.

|                  | n   | %    | Size average<br>[nm] | StD | max | min |
|------------------|-----|------|----------------------|-----|-----|-----|
| <b>Spherical</b> | 35  | 32%  | 22                   | 11  | 48  | 4.8 |
| <b>Faceted</b>   | 46  | 43%  | 27                   | 29  | 183 | 4.6 |
| <b>Elongated</b> | 27  | 25%  | 27                   | 10  | 50  | 8.2 |
| <b>TOTAL</b>     | 108 | 100% | 25                   | 21  | 183 | 4.6 |

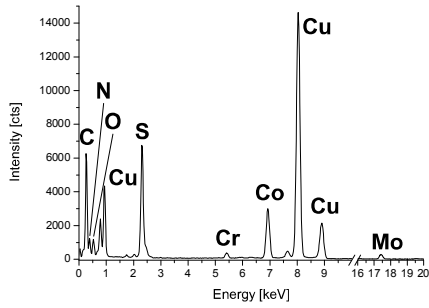
Particle A – Co 6%, Cr 94%, Mo 0%



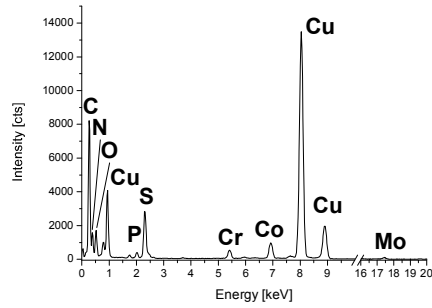
Particle B.a - Co 79%, Cr 15%, Mo 6%



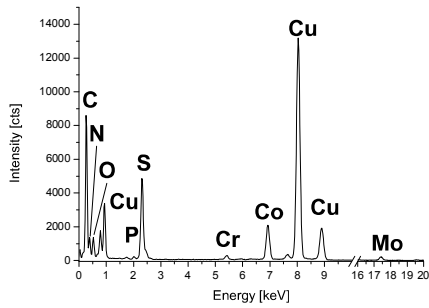
Particle B.b - Co 82%, Cr 11%, Mo 7%



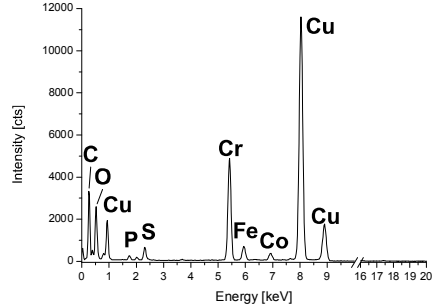
Particle B.c - Co 61%, Cr 37%, Mo 3%



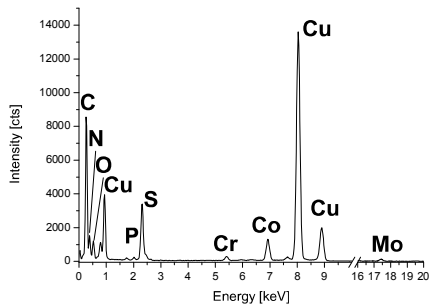
Particle B.d - Co 80%, Cr 11%, Mo 8%



Particle B.e - Co 7%, Cr 93%, Mo 0%



Particle B.f - Co 75%, Cr 17%, Mo 8%



Particle B.g - Co 66%, Cr 30%, Mo 4%

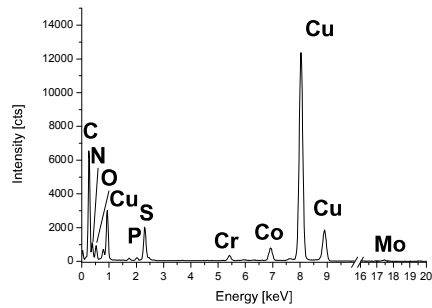


**Figure 5.3** - EDX of the particles generated by hip simulator shown and labelled in Figure 5.2.

### 5.1.2 - TEM/ EDX analysis of supernatant from hip simulator samples after ultracentrifugation

After analyses of the severest conditions used for centrifugal sedimentation of the hip simulator lubricant, i.e. after ultracentrifugation at 60,000 rpm for 60 min, TEM/EDX revealed that the supernatant still contained particles. For this case 75 particles in the supernatant were analysed and a preponderance (~55%) of salt particles was found. Less than 5% of the particles were found to be relatively large and rich in Cr, O and P together with evidence of a thick amorphous coating (see Figure 5.4 - A), whereas roughly 40% of particles were observed to be very small Co particles, with only some traces of Cr and Mo and these were again observed to be suspended in an amorphous or gel like coating (see Figure 5.4 - B).

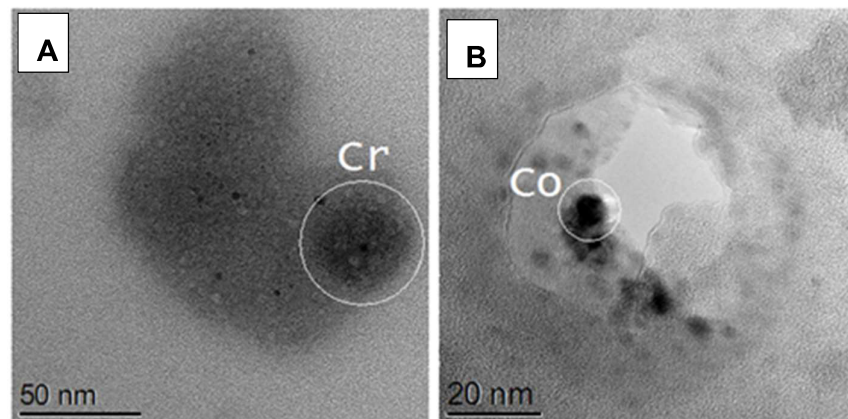


**Figure 5.4** - A and B, bright field TEM images of: different particles in the supernatant of the lubricant following ultracentrifugation at 60,000 rpm for 60 min.

This implies that even the most severe ultracentrifugation step is not fully sedimenting metallic particles in the wear debris. Importantly, samples which had undergone centrifugation followed by ultrafiltration showed an absence of any kind of particles on the TEM grid.

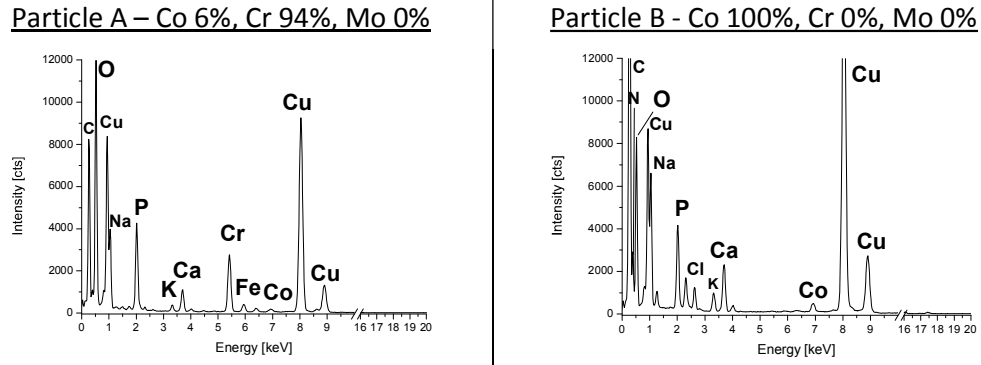


**Figure 5.5** - EDX of particles found on supernatant after ultracentrifugation (60,000 rpm for 60 min) shown are labelled in Figure 5.4: (A) Cr rich particles, (B) Co rich particle.

### 5.1.3 - Ionic release after hip simulator test in FBS+PBS with different ICP-MS sample preparation procedures

Following the different sample preparation procedures (centrifugation, ultracentrifugation and centrifugation plus ultracentrifugation), the released metal ions were measured by ICP-MS of the isotopes Co 59, Cr 52 and Mo 96 in a duplicate assay, and results are compared in Figure 5.6. The statistical significance of the methods used was calculated by ANOVA with a 95% confidence level.

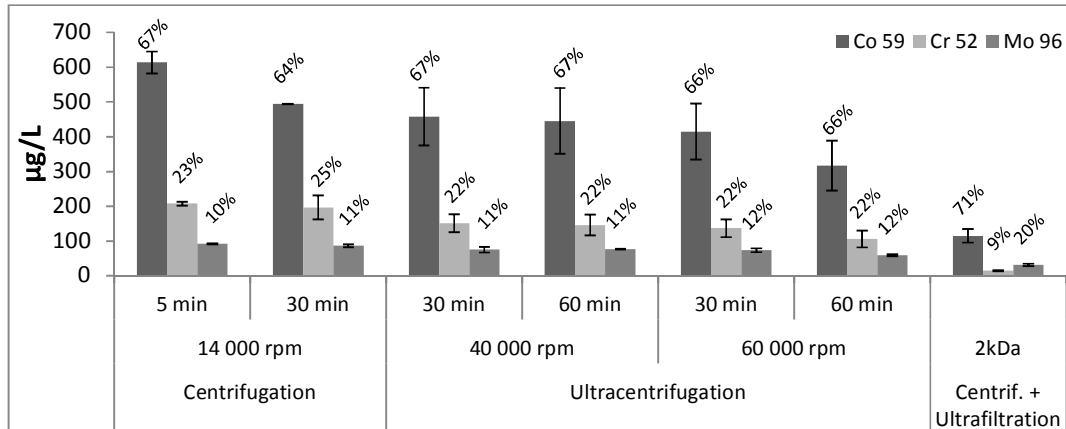


**Figure 5.6** - Metallic elemental levels in supernatants (8x diluted in MilliQ water) by ICP-MS after different sample preparation procedures, given as the average of duplicate assays, with the error bar indicating standard deviation. The percentage values refer to the relative elemental composition for comparison with the bulk alloy (Co-60%, Cr-29%, Mo-7%).

For the hip simulator lubricant samples submitted to just centrifugation or ultracentrifugation, the elemental ratios are broadly comparable to the bulk alloy composition (Co-60%, Cr-29%, Mo-7%) but with Mo and Co levels raised by a few percent and Cr levels lowered by similar percentage (Figure 5.6). With a 95% confidence level (student t-test assuming unequal variances) we can affirm that there is a statistically significant difference between ICP-MS results for all elements for centrifugation compared with centrifugation plus ultrafiltration ( $p = 0.03, 0.01, 0.01$  for Co, Cr and Mo respectively). The metallic particles already identified in the centrifuged only supernatants by TEM (Figure 5.4) could easily be dissolved by the digestion process, or measured directly during ICP-MS, hence causing the differences in the ICP-MS results.

Using ultracentrifugation, the overall levels of dissolved metal ions were reduced, especially at higher centrifuge speeds and longer times, however the elemental ratios remained identical within experimental variation. No statistical significance ( $p > 0.05$ ) in both methods centrifugation and ultracentrifugation was found by either increasing the time or speed.

The use of an ultrafiltration step decreases the overall level of metal ions by about 6 times compared to centrifugation alone and about 2 times when compared to ultracentrifugation alone. Importantly, there is a significant change in the relative elemental ratios (from the base alloy composition) following ultrafiltration, suggesting much higher levels of Mo (and to a lesser extent Co) dissolution together with a very low release of Cr during the walking cycle simulation.

#### **5.1.4 - Co, Cr and Mo ionic standards through ultrafilters**

The retaining properties of the ultrafilters were assessed using Co, Cr and Mo ionic standards mixed in MilliQ water at a concentration of about 100  $\mu\text{g/L}$  for each element. The essays were accomplished in triplicate under different conditions and are shown in Figure 5.7.

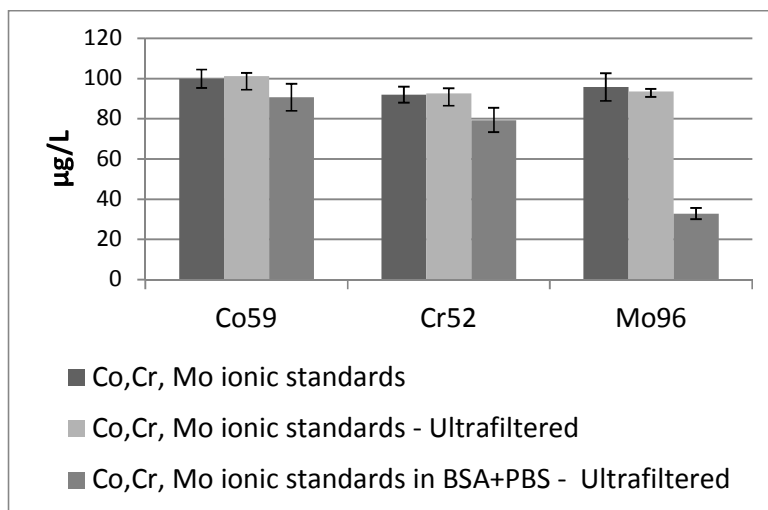


**Figure 5.7** - ICP-MS of Co, Cr and Mo ionic standards in three conditions: only mixed, mixed and passed through ultrafilter (2 kDa MWCO) and finally mixed with BSA+PBS and passed through ultrafilter (2 kDa MWCO).

The results show no significant difference in the Co, Cr and Mo ions measured in MilliQ water with or without the use of ultrafiltration. Even when Co and Cr ions were placed in BSA+PBS solution, the amounts found were inside the standard variation. However, Mo suffers a significant drop in ionic concentration after the exposure to BSA+PBS. This is probably due to Mo ions complexing with the proteins present in BSA [198]. The ultrafilter used can remove particles bigger than 1.5 nm (ultrafilter size pore) as well as proteins larger than 2 kDa.

### 5.1.5 - Brief Summary

In this section, it was demonstrated that centrifugal sedimentation alone is not sufficient to separate nanoparticulate wear debris suspended in simulation media from metal ions dissolved in the media. This implies that the established general method used to separate particles from ions before ICP-MS, are overestimating the true amount of ions in solution [37]. It was shown that centrifugation and ultrafiltration are required for representative ICP-MS analysis of the products of *in-vitro* biotribocorrosion.

## **5.2 Microstructural characterization of low and high carbon CoCrMo alloy nanoparticles produced by mechanical milling**

Both high (0.15 -0.35 wt%) and low carbon (< 0.15 wt%) CoCrMo alloys are utilised in MoM hip implants. The carbon plays an important role in the strength, ductility and wear resistance of the implants. Nevertheless, the carbon can induce the formation of carbides and these may become sites for localized corrosion (dissolution) [54]. As a consequence, ions and/or particles released in this process may interact with the surrounding tissue and lead to an inflammatory response.

This part of the study investigates ball milling in BSA of low and high carbon CoCrMo alloy gas atomized powders in order to help understand the effects of mechanical wear of the alloy during implant use. The characterization of the size, shape, composition and phase structure of these nanoparticles gives relevant information about the physicochemical behaviour in relevant biological media and any preferential dissolution of the elements. CoCrMo powders have been milled in bovine serum albumin (BSA) achieving a particle size reduction to the nanometre scale.

The samples were analyzed by Transmission Electron Microscopy (TEM) (in terms of size and shape), Energy-Dispersive X-ray spectroscopy (EDX) (composition) and High-Resolution Transmission Electron Microscopy (HRTEM) (phase identification). These results are compared to bulk techniques such as X-ray Diffraction (XRD), Dynamic Light Scattering (DLS) and Inductively Coupled Plasma Mass Spectrometry (ICP-MS), demonstrating the effect of milling fluid on the size and stability of CoCrMo nanoparticles when in the presence of serum proteins. The full description of methods and materials used in this section can be found on Section 3.6.6.

### **5.2.1 - Particle size and shape**

The nature of the milling process could be comparable to the way that real wear debris particles are mechanically generated. The process includes the interaction between two moving CoCrMo surfaces, creating damage on the

surface of the alloy. Shear bands are characteristic of this process and are often observed in particles – see Figure 5.8.

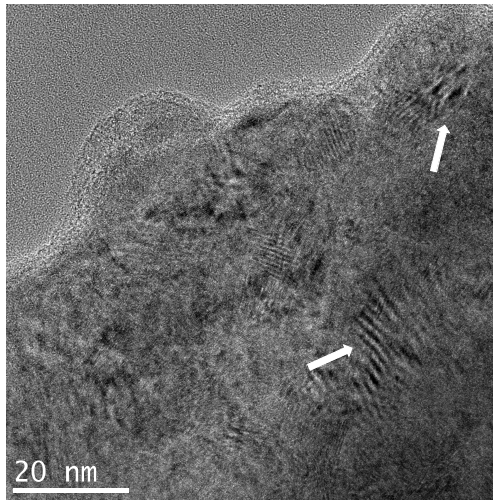


**Figure 5.8** - CoCrMo high carbon particles after ball milling for 150 min in BSA diluted in deionized water, presenting surface degradation (shear bands) as a consequence of mechanical interactions.

The raw CoCrMo atomized powder shows perfectly round particle morphologies. After milling, DLS analysis (Figure 5.9) showed a significant decrease in particle size to below 800 nm in either, high and low carbon. The high carbon alloy shows a primary peak between 10 – 200 nm, with a maximum percentage at 70 nm. The secondary peak at 400 nm is more widespread between 200 - 800 nm and has a much lower percentage content. The low carbon alloy shows a lower primary peak (between 10 - 50 nm) than high carbon, with a secondary peak between 100 - 500 nm. For both milled powders, the majority of the particles were found in the range 10 - 200 nm.

DLS results agree with TEM analysis of ~300 nanoparticles shown in Figure 5.10. By TEM, the low carbon alloy generated almost 50% more nanoparticles in the range of 10 - 200 nm than the high carbon alloy. The low carbon nanoparticles were found in large amounts below 60 nm, while the high carbon particles had a more even distribution below 80 nm.

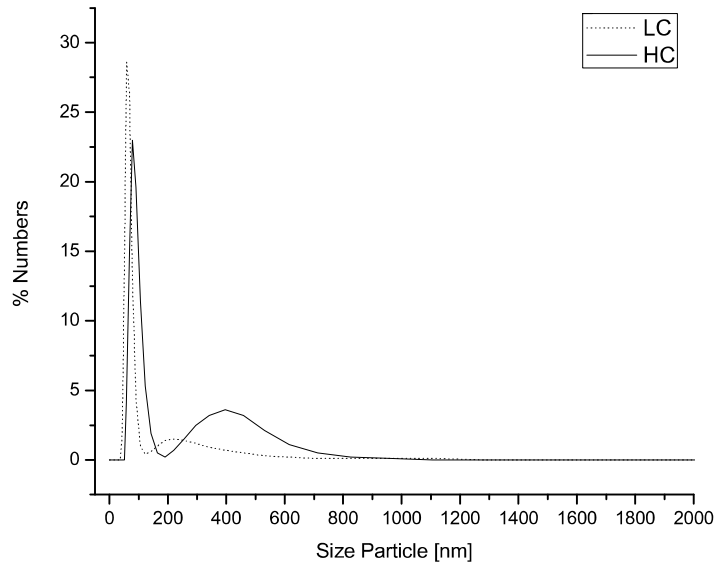


**Figure 5.9** - DLS particle size distributions by number for the high and low after ball milling for 150 min in BSA diluted in deionized water.

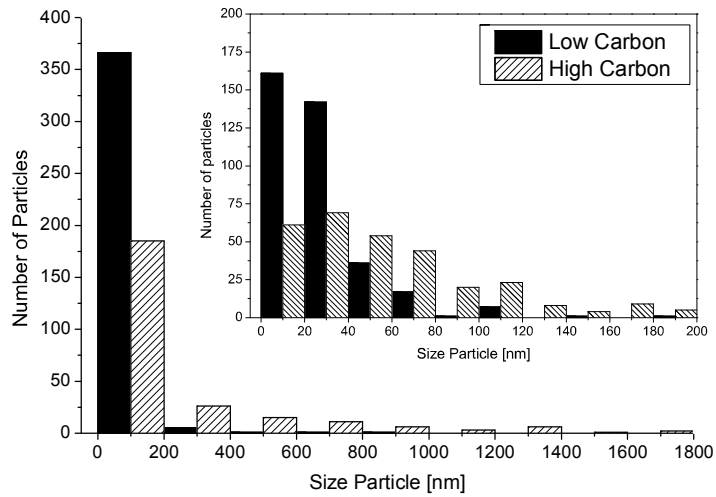


**Figure 5.10** - TEM particle size distributions for the high and low carbon alloys after ball milling for 150 min in BSA diluted in deionized water.

### 5.2.2 - Phase analysis

XRD of the raw material showed that both high [Figure 5.11 (a)] and low [Figure 5.11 (b)] carbon alloy powders, were dominated by the presence of the CoCrMo face-centred cubic phase (fcc, ICDD 04-16-6869). Traces of the CoCr hexagonal close-packed phase (hcp, ICDD 04-002-1030) were also evident.

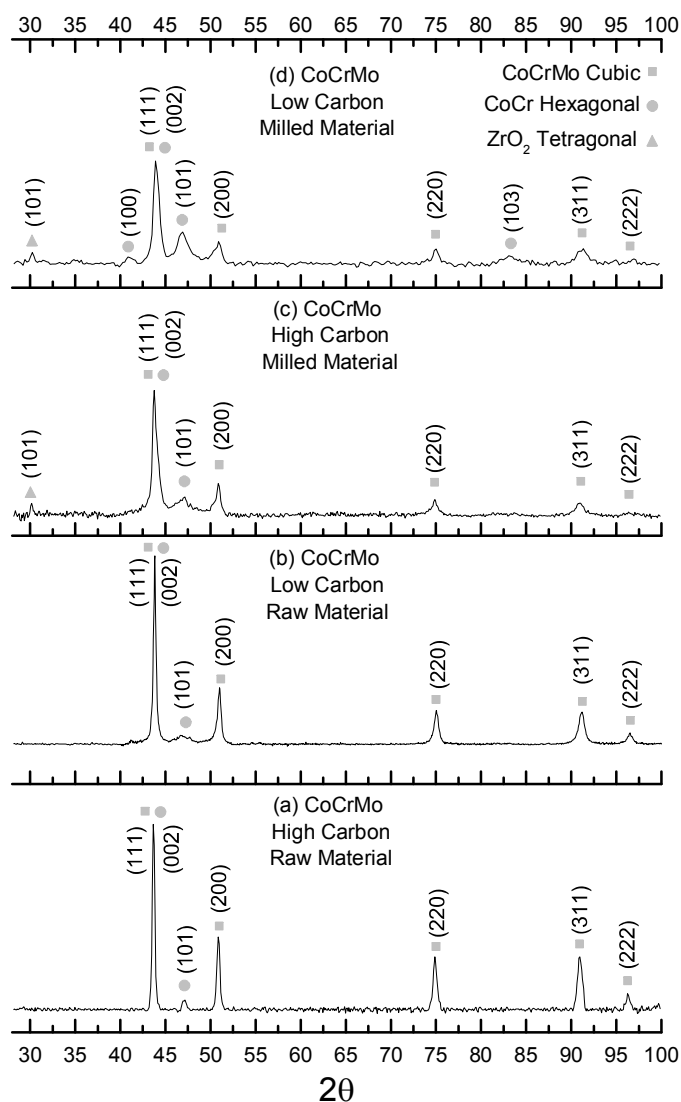


**Figure 5.11** – Phase identification by XRD: (a) high carbon raw material, (b) low carbon raw material, (c) high carbon milled material and (d) low carbon milled material, after ball milling for 150 min in BSA diluted in deionized water

With the mechanical action of milling, post-milled material showed a significant increase in peak broadening and a decrease in crystallite size induced by strain and an increase in the hexagonal phase, especially in the CoCrMo low carbon alloy. This phase transformation is a strain induced fcc-hcp transformation (SIT), where temperature usually plays an important role, however in this case, stress is the most important contribution [199]. The presence of carbon substantially altered the retention of the fcc phase after milling which is expected because carbon is known to stabilize this phase [69,200]. In addition, XRD showed the appearance of traces of zirconia

(tetragonal, ICDD 01-083-0113) as a result of contamination by erosion of the balls/vial of the mill, possibly by hydrothermal degradation [201].

S(TEM) analysis revealed coarse particles (> 200 nm size) were dominated by the fcc phase [Figure 5.12 (b)], whereas fine particles (less than 200 nm) were predominantly hcp [Figure 5.12 (a)]. This effect probably occurs due to the higher energy required to produce the fine particles.

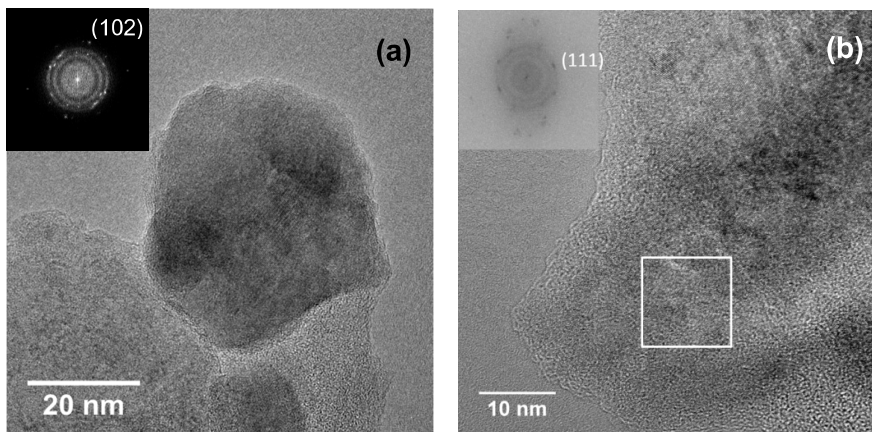


**Figure 5.12** - Phase identification in post milled CoCrMo particles by measuring distances between atomic planes in high resolution transmission electron microscopy: (a) hcp phase on high carbon (102),  $1.49 \text{ \AA} \pm 0.27 \text{ \AA}$ ; (b) fcc phase on low carbon (102),  $2.04 \text{ \AA} \pm 0.27 \text{ \AA}$ .

### 5.2.3 - Composition

The raw bulk materials were analysed in terms of composition by SEM Energy Dispersive X-ray Spectroscopy (EDX). TEM-EDX (Figure 5.13) of individual particles showed that the low carbon milled material contained 75% of the particles measured with a cobalt composition below that of the raw material, accompanied by a corresponding increase in chromium. Following milling, both low and high carbon alloys particles presented a wide distribution in composition. Some of the very small particles (about 10 nm) were composed of almost 100% cobalt. However, 50% of the high carbon alloys particles were found with a cobalt composition below that of the raw material. In both high and low carbon alloy powders, ca. 50% of the particles showed no presence of molybdenum (or a level below the detection limits of EDX), with the remaining 50% showing 10% to 20% Mo, above that found in the raw material.

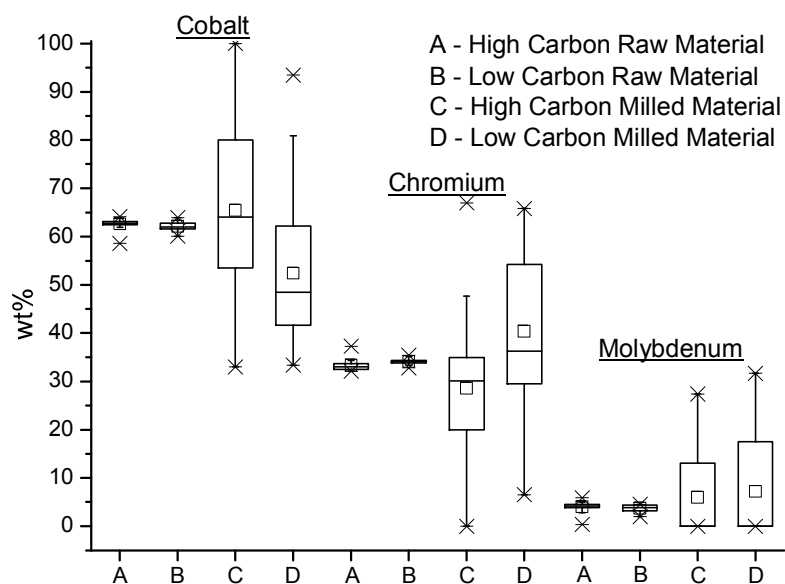


**Figure 5.13** - Boxplot<sup>11</sup> of TEM/SEM EDX of high and low carbon, raw and milled material.

ICP-MS results [Figure 5.13 (a)] strongly suggest that cobalt and molybdenum undergo dissolution during the milling process in the presence of serum protein in agreement with the TEM results. This behaviour is apparently independent of the amount of carbon in the alloy. The difference in the absolute degree of dissolution between the high and low carbon alloy powders shown in ICP is likely related to the Ostwald-Freundlich relation, where the particle solubility is inversely proportional to particle size. DLS and TEM having both revealed that the low carbon alloy produced more nanoparticles. Moreover, ICP indicates that chromium is most resistant to the corrosion process.

<sup>11</sup> The bottom of each box is the 25th percentile; top is the 75th percentile; line in the middle is the median value; square inside the boxes represents the average; "Whiskers" above and below each box represent 1.5 of the average values; crosses are the outliers.

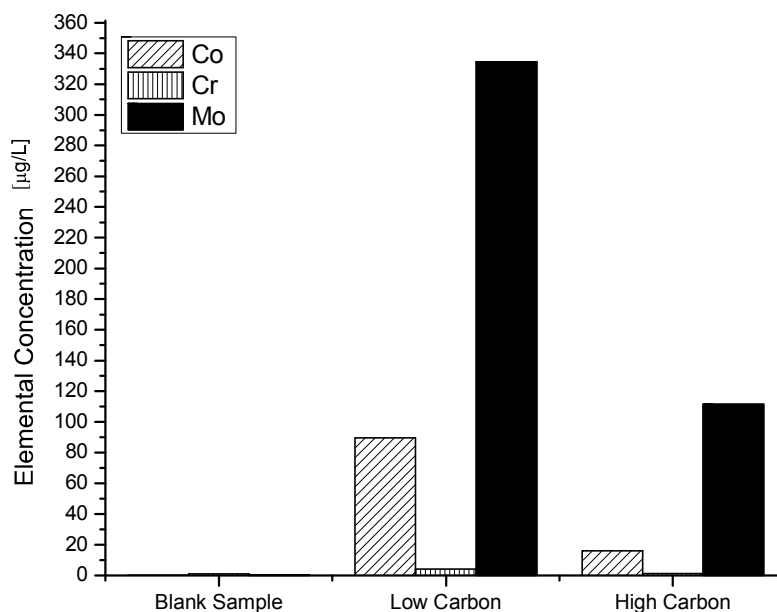


**Figure 5.14** - ICP-MS of low and high carbon post milled material

#### **5.2.4 - Brief Summary**

During milling, low carbon alloy powders generated more nanoparticles than the high carbon alloy, which is may be directly related to the mechanical properties of the alloy and the stabilization of the fcc phase by carbon [200]. ICP-MS together with SEM/TEM EDX gave an indication of cobalt and molybdenum dissolution in the presence of serum albumin proteins for both high and low carbon alloy milled powders. TEM shows good agreement with bulk techniques, and allows differentiation of dissolution results in terms of particle size.

### **5.3 Corrosion of the CoCrMo alloy in relevant media**

Mechanochemical milling was also employed to compare the release of ions in dynamic conditions from CoCrMo alloy powders in different media such as PBS, BSA and SSF. Milled particles were then incubated (in static conditions) and a sample of the solution was used to measure the ionic release by ICP-MS. The full description of methods and materials used in this section can be found on Section 3.6.7.

ICP-MS analysis showed that CoCrMo particles milled in PBS release Co and Mo ions in a ratio of about 5:1 (Table 5.2). The presence of serum proteins (SSF and in particular pure BSA) during milling drastically increased the proportion of dissolved Mo by up to 70% ( $p = 0.001$ ).

**Table 5.2** - Metallic elemental levels in supernatant samples following centrifugation plus ultrafiltration and ICP-MS of CoCrMo powders milled in different environments (diluted 20x). Results are given in both absolute terms ( $\mu\text{g/L}$ ) and also relative terms (%).

|  |              | Cobalt            |     |       | Chromium          |     |       | Molybdenum        |      |       |
|--|--------------|-------------------|-----|-------|-------------------|-----|-------|-------------------|------|-------|
|  |              | $[\mu\text{g/L}]$ | Sdt | [%]   | $[\mu\text{g/L}]$ | Sdt | [%]   | $[\mu\text{g/L}]$ | Sdt  | [%]   |
| <b>Dynamic Conditions (Milling)</b>      | PBS [pH 7.2] | 174.4             | 2.3 | 82.9% | 0.3               | 0.0 | 0.2%  | 35.6              | 3.9  | 16.9% |
|  | BSA [pH 7.2] | 33.1              | 5.5 | 30.0% | 0.6               | 0.0 | 0.5%  | 76.7              | 11.8 | 69.5% |
|  | SSF [pH 7.2] | 157.0             | 2.6 | 74.5% | 0.8               | 0.0 | 0.4%  | 52.9              | 4.6  | 25.1% |
| <b>Static Conditions (incubated 24h)</b> | BSA [pH 7.2] | 0.7               | 0.1 | 9.6%  | 0.2               | 0.1 | 2.7%  | 6.4               | 0.7  | 87.7% |
|  | BSA [pH 4.8] | 16.4              | 0.2 | 69.2% | 4.8               | 0.2 | 20.3% | 2.5               | 0.2  | 10.5% |

Following milling of the CoCrMo alloy powders in BSA at pH 7.2, static dissolution studies (incubation) shown at the bottom of Table 5.2, were then conducted over a period of 24 h under neutral and acid pH conditions, adjusted using HCl, all employing only the centrifugation plus ultrafiltration procedure prior to ICP-MS analysis. These results showed significant solubility of Mo at pH 7.2 and an increase in Co and Cr solubility at low pH.

The exposure of milled particles for longer times in BSA (Figure 5.15) shows Mo as a preferential corrosion product, while PBS (Figure 5.16) and SSF (Figure 5.17) preferentially corrode Co from the particles. In terms of total amount of ionic product released, the salt rich solution PBS and SSF release at least twice as many ions than BSA. Cr showed no significant corrosion in all three solutions tested. In addition it was possible to observe an increase in the overall levels of Mo ionic release with an increase of serum concentration in solution (BSA > SSF > PBS). However, serum appears to play an inverse role in cobalt dissolution. Extended exposure time greatly enhances the release of Mo in the presence of BSA, however BSA only slightly affects Co corrosion in all solutions tested.

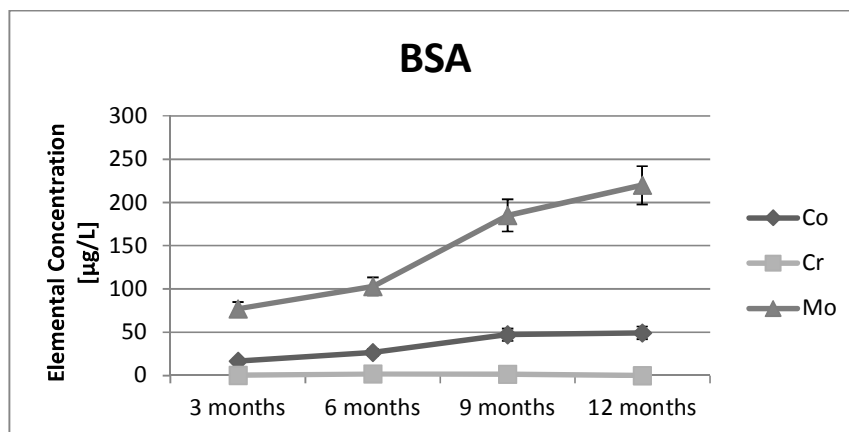


**Figure 5.15** - Ionic release of CoCrMo milled in BSA particles over time, as measured by ICP-MS with centrifugation plus ultrafiltration procedure.

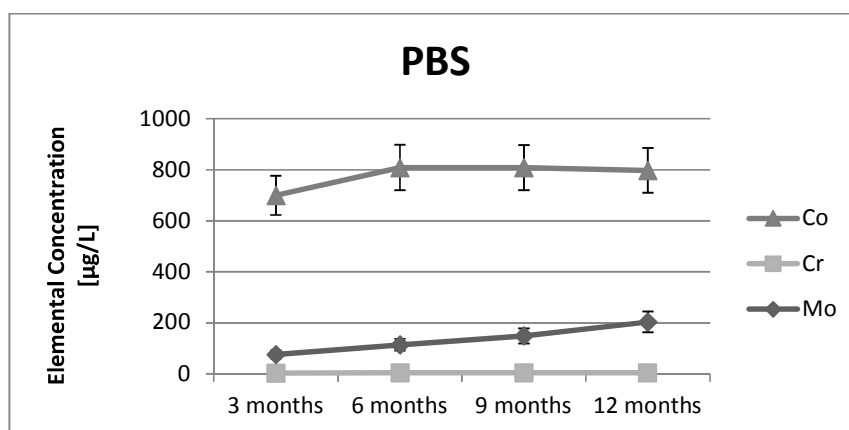


**Figure 5.16** - Ionic release of CoCrMo milled in PBS particles over time, as measured by ICP-MS with centrifugation plus ultrafiltration procedure.

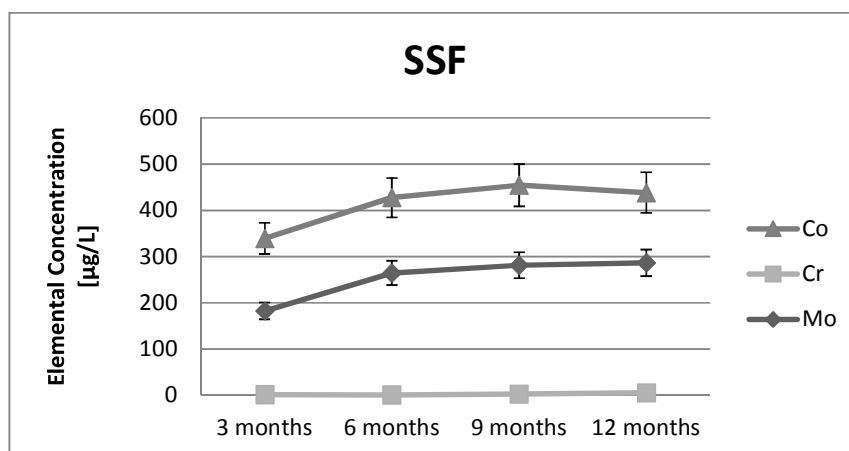


**Figure 5.17** - Ionic release of CoCrMo milled in SSF particles over time, as measured by ICP-MS with centrifugation plus ultrafiltration procedure.

### **5.3.1 - Fourier Transform Infrared Spectroscopy (FTIR)**

FTIR of pure BSA and CoCrMo milled in BSA followed by centrifugal sedimentation was carried out with and without ultrafilters. The particles in BSA analysed have size diameters less than 200 nm, as shown in section 4.3.4. Figure 5.18 (a) displays FTIR for BSA diluted in MilliQ water following centrifugation, which indicated the presence of primary and secondary amide [202]. The same absorbances are seen in Figure 5.18 (b) which shows FTIR of CoCrMo particles milled in BSA following centrifugation with an increase in absorption, possibly due to the protein coverage on the particle surface. Figure 5.18 (c) shows FTIR of the solution after CoCrMo milled particles in BSA had been centrifuged and ultrafiltered with a 100 kDa ultrafilter, which removes most of the nanoparticles present in solution. These nanoparticles interacted with the amide groups in the BSA and with the removal of these particles, the signal related to amide was absent. The solution that remains exhibited absorbances due to  $C \equiv O$  and  $C = O$ , as well as peaks assigned to metal carbonyl, which could form with the remaining ions in solution. However, this could also be due to the degradation of the proteins in BSA post-milling, which are formed from more than 500 amino acids, mainly by the ones cited in the Table 2.3 . Finally, Figure 5.18 (d) shows FTIR in the solution after CoCrMo milled particles in BSA been centrifuged and ultrafiltered with a 30 kDa ultrafilter, which removes up to 95% of the proteins in solution, where no significant signal was detected in the FTIR spectra.

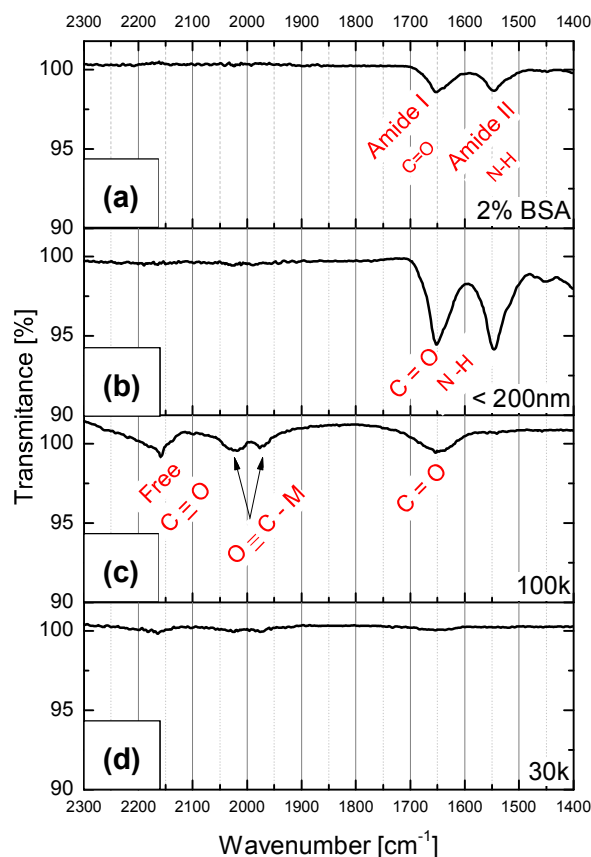


**Figure 5.18** - FTIR spectra of: (a) BSA solution shows peaks of Amide I and II; (b) CoCrMo milled and centrifuged nanoparticles in BSA solution. (c) CoCrMo milled and centrifuged nanoparticles in BSA solution after the use of a 100 kDa MWCO ultrafilter (d) after the use 30 kDa MWCO ultrafilter.

### 5.3.2 - Brief Summary

This revised ICP-MS preparation method has allowed the identification of the dissolution of specific metallic elements in different biological media and pH environments. This has revealed the preferential dissolution of Mo in the presence of serum proteins, and that, based on the pH dependence, it is likely that more significant Co and Cr solubility will only occur if debris particles are taken up by phagocytic cells and digested in lysosomes. Also, FTIR showed that part of the metal ions are possibly forming complexes as a result of the dissociation of the amino acids found on BSA by the energy input from the milling process.

#### **5.4 Bovine Serum Albumin binding to CoCrMo nanoparticles and the influence on dissolution**

Most research in the literature has concentrated on corrosion studies of bulk pieces of CoCrMo hip implants, exploring the influence of possible body environments, in either static or dynamic situations [38,68,203]. It is well known that in a biological environment, the surfaces of biomaterials are modified by adsorption of biomolecules such as proteins, which mediates the interaction between cells and foreign materials [204]. Metal nanoparticles could be fully coated with proteins, effectively becoming a complex biological unit that changes the way in which the body identifies the particles [205,206]. Depending on the nature of the material, proteins can either enhance or inhibit metal dissolution: a corrosion protection effect is related to protein adsorption on the surface of a material, acting as barrier against corrosive body fluids [207]; whereas complexation of a metal by the amino acids present in proteins could potentially increase corrosion in some materials. It is therefore interesting to investigate whether serum albumin, the most abundant protein found in the circulatory system, may bind to alloy wear debris particles and change the surface, bioavailability and chemical behaviour such as dissolution.

The purpose of this section is to investigate the interaction of CoCrMo nanoparticles with proteins, specifically isolating the effect of bovine serum albumin. To complement this study,  $\text{Co}_3\text{O}_4$ ,  $\text{Cr}_2\text{O}_3$  and Mo metal nanoparticles (which exhibits  $\text{MoO}_2$  all over the surface) were used as reference materials as they all may be associated with the surface of the CoCrMo hip implants.

In order to demonstrate the effect of milling fluid on the size and stability of CoCrMo nanoparticles when in the presence of serum proteins, samples were analyzed by Transmission Electron Microscopy (TEM), Energy-Dispersive X-ray spectroscopy (EDX), Inductively Coupled Plasma Mass Spectrometry (ICP-MS) and Zeta Potential (ZP) measurements. The whole description of methods and materials used in this section can be found on Section 3.6.8.

### 5.4.1 - TEM/EDX on milled particles and reference materials immersed in BSA

Wear debris from hip implants was synthetically produced by milling CoCrMo high carbon ASTM75 gas atomized powder in Bovine Albumin Serum (BSA). The reduction in particle size is mainly related to friction and impact during milling; however, the interaction with BSA could also play an important role in both the size reduction and the nanoparticle composition. The size fraction of 5 - 200 nm, commonly found in real wear debris in synovial fluid, was generated here by post-milled centrifugal sedimentation (10 min, 25 °C, centrifugal force of 8000 G) prior to testing and analysis.

Initial TEM examination (Figure 5.19) showed most of the CoCrMo milled particles were surrounded by a thick amorphous layer (note darker contrast than the support film surrounding the group of particles) that could potentially be a protein corona. BSA is formed by a large sequence of amino acids, composed of carboxylic and amine groups, thus the presence of BSA could be distinguished from the TEM carbon support film by the detection of nitrogen. EDX spectra show that particles were mainly composed of cobalt and chromium with a deficiency in molybdenum (relative to the alloy composition), but also reveal the presence of nitrogen and oxygen [Figure 5.19 (c)]. A comparison with the composition of the raw material before milling indicates a decrease in cobalt weight percentage in the milled material of only about 5%.

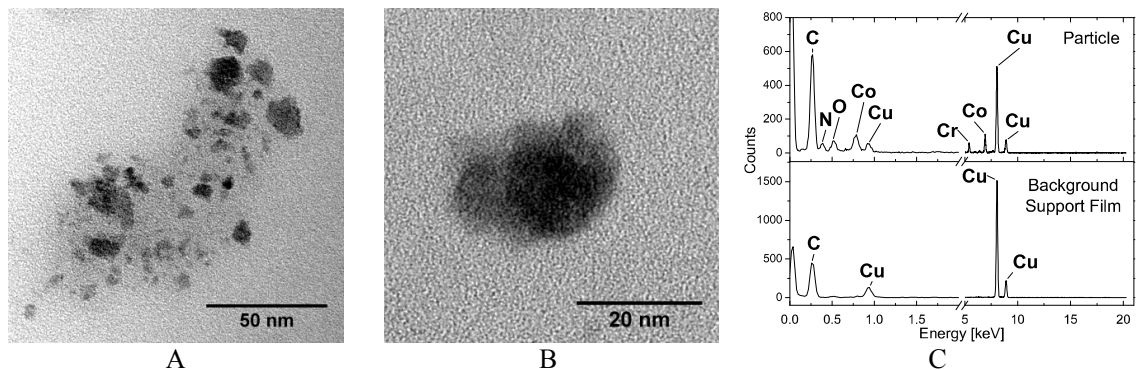


**Figure 5.19** - TEM analysis of synthetically produced CoCrMo nanoparticles on carbon support film; (A) a group of particles surrounded by a thick amorphous layer; (B) and (C) TEM/EDX of a representative particle, showing a composition consisting of cobalt and chromium with the presence of nitrogen and oxygen, note the deficiency in molybdenum signal (Mo K $\alpha$  is at 17.4 keV).

The reference materials (Figure 5.20) showed all particles to be less than 200 nm in diameter with an average size of 100 nm and standard deviation of 41 nm. The particles were incubated as received for 24 h in BSA, washed and then analyzed by TEM. The results show the clear formation of a protein biofilm (generally less than 5 nm in thickness) on the surface of all the particles (see Figure 5.21).

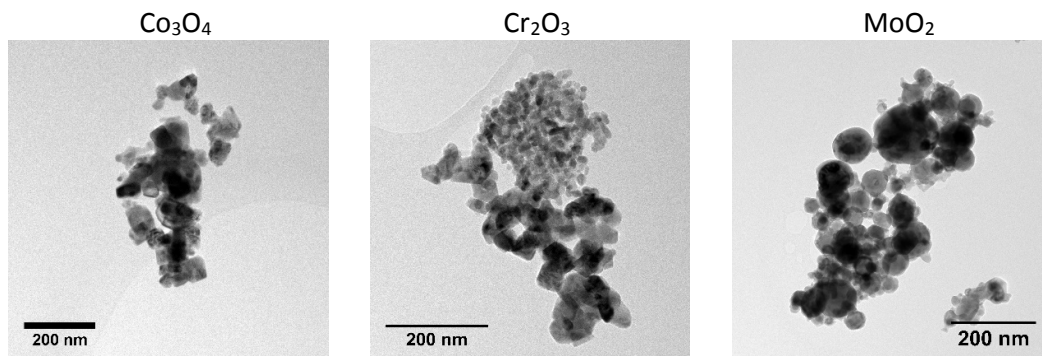


**Figure 5.20** - TEM of reference materials ( $\text{Co}_3\text{O}_4$ ,  $\text{Cr}_2\text{O}_3$  and  $\text{MoO}_2$ ) as received, which shows particles of less than 200 nm size diameter.

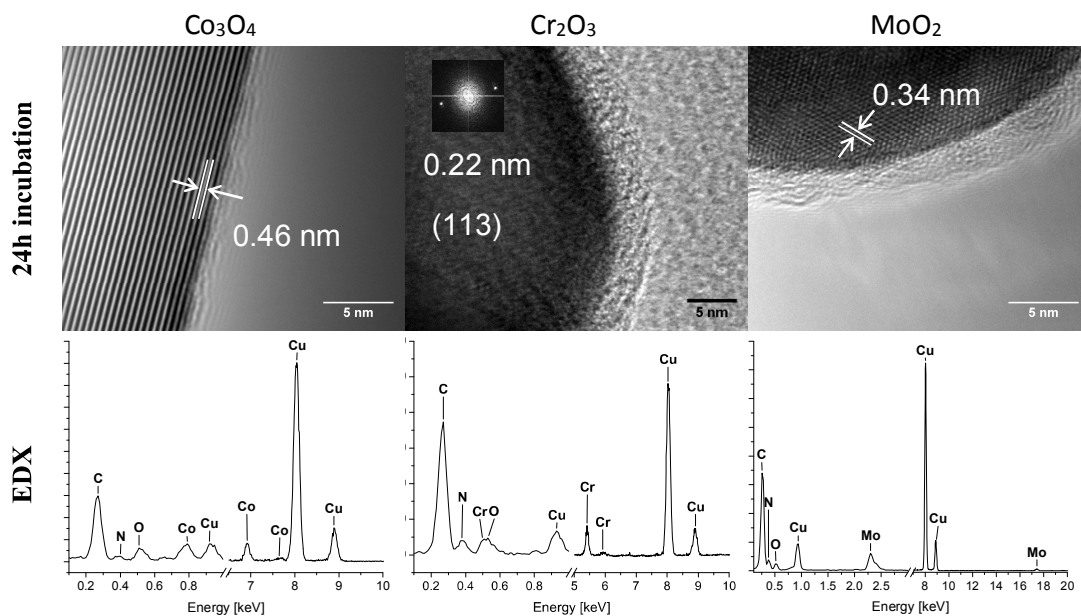


**Figure 5.21** - TEM/EDX of  $\text{Co}_3\text{O}_4$  (JCPDS 42-1467),  $\text{Cr}_2\text{O}_3$  (JCPDS 38-1479) and  $\text{MoO}_2$  (JCPDS 32-0671) reference materials incubated for 24h in BSA showing an amorphous biolayer containing nitrogen surrounding the particles.

### 5.4.2 - Static dissolution of the reference materials

Dissolution of the reference materials after one month immersion in a BSA containing solution was measured by ICP-MS (Figure 5.22) following centrifugation and ultrafiltration to remove any small nanoparticulates. The levels of Co and Cr ions were found to be low, possibly as a result of biolayer formation inhibiting contact with the solution. Molybdenum however, showed high levels of dissolution in the presence of albumin.

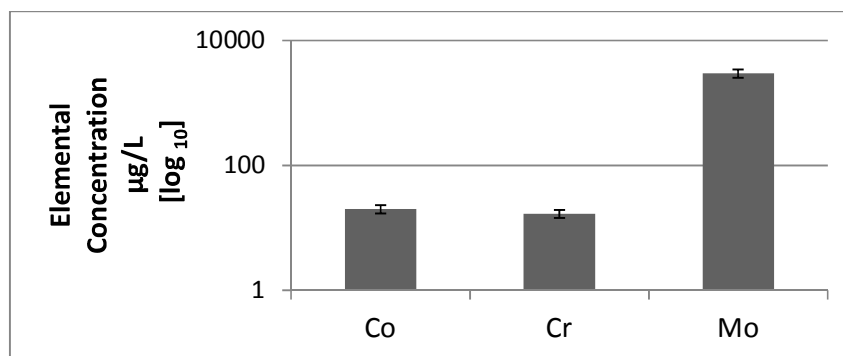


**Figure 5.22** - ICP-MS of the soluble elements of  $\text{Co}_3\text{O}_4$ ,  $\text{Cr}_2\text{O}_3$  and  $\text{MoO}_2$  reference materials incubated for a month in BSA containing stock.

### 5.4.3 - Zeta Potential to measure protein binding between metal particles and BSA

The zeta potential represents the surface charge in the presence of an aqueous solution when functional groups dissociate or ions adsorb onto surfaces from the solution. The IEP is the pH at which a species exhibits a net zeta potential (approximating to surface charge if specifically adsorbed ions are present) equal to zero. At the IEP of a protein, its structure is more hydrophobic, more compact and less stable due to the absence of inter-particle repulsive forces.

The isoelectric point of each sample was estimated by zeta potential titration of CoCrMo and standard materials in MilliQ water (Figure 5.23). The CoCrMo alloy exhibits an IEP (~ pH 6.6) very close to that of  $\text{Cr}_2\text{O}_3$  (~ pH 6.7), while the IEP of  $\text{MoO}_2$  is more acidic (~pH 2.6) and  $\text{Co}_3\text{O}_4$  IEP more basic (~pH 8.1).

### Zeta Potential Titration in MilliQ Water

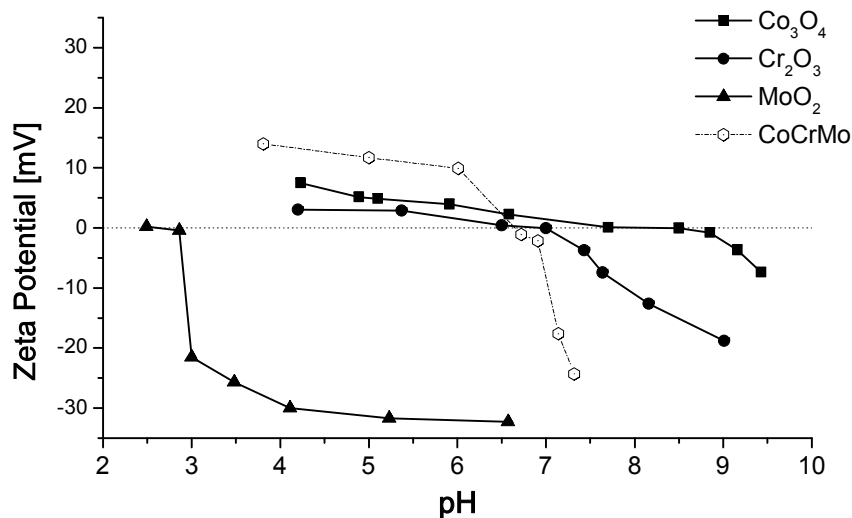


**Figure 5.23** - Zeta Potential titration of CoCrMo and reference materials in MilliQ water to establish the isoelectric point of the materials. The solution pH was titrated using HNO<sub>3</sub>.

Zeta potential titration results of the reference materials incubated in BSA showed that the standard IEP of the metal oxide reference materials in water all changed to become closer to that of BSA (pH 5) presumably due to the surface coverage by the protein (Figure 5.24). Molybdenum oxide showed the highest affinity for BSA, and cobalt the lowest. The CoCrMo alloy particles milled in BSA also showed a similar IEP to BSA. Electrostatic forces mediate the protein corona formation, molybdenum (oxide) particles are negatively charged at all pH values > 2.5, whereas surface charge of chromium and cobalt oxides is positive below pH ~7 (Figure 5.24).

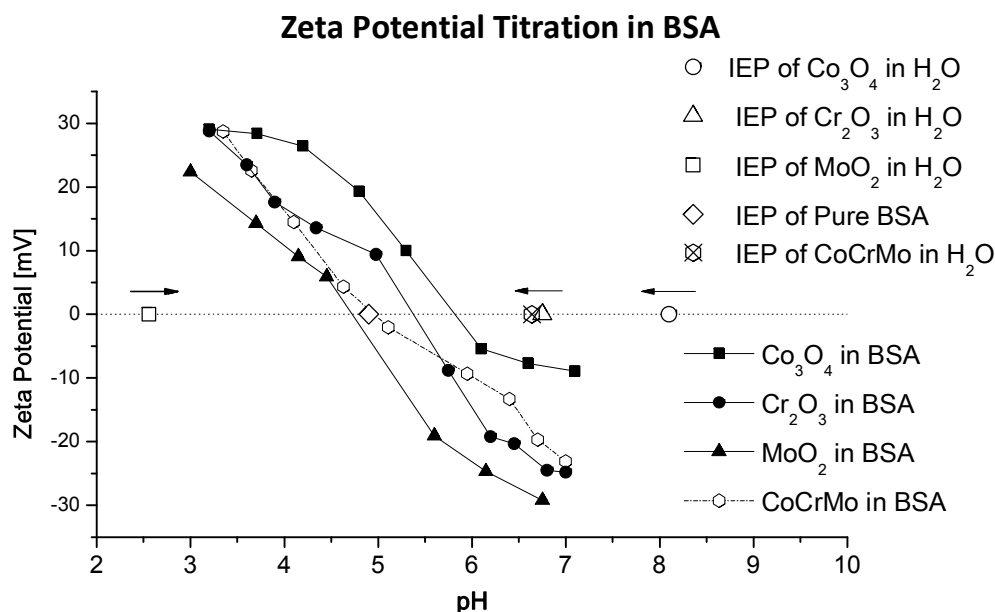


**Figure 5.24** - Zeta potential titration of reference materials incubated for 24h in BSA and CoCrMo milled in BSA at the same concentration. The solution pH was titrated using HNO<sub>3</sub>.

#### 5.4.1 - Brief Summary

TEM analysis suggests the formation of a protein corona on synthetic CoCrMo wear debris particles incubated with BSA and the particles were found to be deficient in Molybdenum by EDX (Figure 5.19). An interaction with proteins was also seen for elemental reference oxide materials where ICP-MS showed that the reference materials underwent dissolution of predominantly molybdenum ions under static incubation in the presence of BSA (Figure 5.22). Using the same amount of particles and protein concentration, molybdenum nanoparticles showed the highest affinity to BSA, demonstrating that in the presence of serum proteins, the effective surface charge is very close to the IEP of BSA (Figure 5.24). Taken together these results indicate the importance of binding between albumin proteins and molybdenum, which may directly influence the strong dissolution of this element when CoCrMo alloy nanoparticles are produced as hip-implant wear debris in the presence of serum albumin.

## 5.5 Discussion

Studies of total mass loss of hip implants due to wear and corrosion have used a general sample preparation route for ICP-MS analysis involving centrifugation and acid digestion to show that simulated wear debris has similar composition to the bulk alloy [136,193,194]. Yan et al. [31] attempted to separate wear debris particles and ions, produced by pin-on-plate testing in biological solutions by using centrifugation (10 min, 14,000 rpm) prior to ICP-MS. Their results suggest that metal ion contents under open circuit conditions are similar to the bulk alloy ratio composition.

The results presented in this chapter show that the corrosion product of CoCrMo ASTM75 are very different from the bulk alloy composition for all situations tested. A variation in the preferential ionic release was found to be strongly dependant on the environment in which the particles are immersed. The source of variation in the results found in the literature and those presented in this chapter are most likely related to the ICP-MS sample preparation procedure.

Two main types of particles were found following hip simulation: Cr rich particles with the presence of O and P and Co rich particles. Both were consistent in size, shape and composition to those found by Catelas *et al.* (2003) [152]. The particles rich in Cr and O found are presumably generated by disruption of the passivating chromium oxide layer on the alloy surface, possibly associated with phosphates from the lubricant. These hard oxide particles ( $\text{Cr}_2\text{O}_3$  hardness ~2898 Vickers [210]) entrapped in the joint (CoCrMo ASTM75 hardness ~400 Vickers [210]) can act as abrasives, increasing the hip implant surface degradation. The sliding action between the two counter-surfaces can give a round shape to the entrapped Cr rich particles. The environment rich in proteins could retard Cr autopassivation properties [211] exposing a Co-rich surface. This process could give rise to Co rich particles, which in Section 5.1.1 were often associated with acicular shape particles. Both types of particles were found in the supernatant after centrifugation and the particles show elements associated with salts. These had presumably precipitated from the PBS itself during drying (possibly NaCl, KCl,  $\text{Na}_2\text{HPO}_4$  or  $\text{KH}_2\text{PO}_4$ ). The metallic nanoparticles identified could be easily ionised by ICP-

MS. TEM revealed that the solution that was centrifuged and ultra-filtrated did not contain particles. The implication of these results is that, unless ultrafiltration is employed, ICP-MS will be analysing both the underlying ion levels in solution arising as a result of dissolution and the alloy wear debris nanoparticles themselves.

Dissolution results from the hip simulator using the centrifugation plus ultrafiltration protocol revealed a decrease in the overall level of metal ions by about 6 times compared to centrifugation and about 2 times when compared to ultracentrifugation. The elemental results showed important differences compared to the current literature: Cr shows very low release of ions and Mo levels are more close to those of Co. Despite elemental Mo being pretty much insoluble, the oxides formed on its surface – as the product of the passivation on hip implants ( $\text{MoO}_2$  and  $\text{MoO}_3$ ), when placed in alkaline solution, tend to release ions and form molybdates ( $\text{MoO}_4^{2-}$ ) [212]. In hip implants, these molybdates can help avoid pitting corrosion by covering the surface and acting as a barrier against electrochemical attack [56,213]. However, a different behaviour occurs with nanoparticles since the ionic complexes do not remain on the surface, but are released into solution as shown early in this chapter.

Mechanical milling of CoCrMo ASTM75 alloy gas atomized powders showed that low carbon alloys produce significantly more and smaller nanoparticles than high carbon alloys. Some publications shown that the wear performance of high carbon CoCrMo is superior to low carbon [33,214], especially under tribocorrosion conditions. During the milling process, strain induces an fcc to hcp CoCrMo phase transformation in both alloys, however this is more pronounced in CoCrMo low carbon alloy after milling. It is known that an increase in carbon substantially increases the retention of the fcc phase [200] and Lee *et al.* (2008) showed that hcp phase formed along the interdendritic region during the solidification gives rise to brittle fracture [69]. Therefore, the observation that CoCrMo low carbon alloy produces a large amount of nanoparticles that are relatively smaller than those from a high carbon alloy could be attributed to the low capacity to retain the metastable fcc phase in the low carbon alloy.

After milling CoCrMo low and high carbon alloys, evidence for cobalt and molybdenum dissolution in the presence of serum was confirmed by ICP-MS

and TEM EDX techniques. These findings are consistent with the data for the centrifuged plus ultrafiltered hip simulator samples shown in Figure 5.6 and are in agreement with the published electrochemical corrosion studies of Espallargas *et al.* [133], which indicated that BSA could increase Mo dissolution.

Previous studies measuring whole blood metal ions have reported varying levels with the majority converging to a Co/Cr ratio about 1 for the first 3-6 months [111,112,209]. After this initial period, Co ionic levels were superior to the Cr ions. Ilo *et al.* (2015) studies using THA and hip resurfacing showed that, in both, failed implants presented Co/Cr > 1 (mean 2.3:1) whereas healthy joint presented Co/Cr ratio about 1 [215]. In the failed THA group the median Cr level was 4.15 µg/l (32% > 7 µg/l) and median Co level was 7.25 µg/l (52% > 7 µg/l). In the failed THA group 60% of Co/Cr ratios were greater than a 1.5:1 ratio, compared to only 28% in the failed resurfacings group. Whilst variation in measured levels of metal ions between studies may be explained by different implant design. There is no obvious explanation for the variation in Co/Cr in studies which use a material with the same chemical composition. The passivated layer can be disrupted in the presence of wear and fretting. In this case, metal oxide particles can be subsequently corroded into human body releasing metal ions. These can reach different amounts compared to the CoCrMo element alloy, once that the oxide film is basically formed by Cr.

Overall, corrosion results in the relevant media show that Cr dissolution from CoCrMo alloys is minimal in biological media under neutral pH, but more pronounced at low pH, such as that which may be found in a lysosome, as discussed by Gill *et al.* [127]. A Pourbaix diagram for Cr in water at 25 °C suggests toxic chromium VI is released only at pH > 7 and high electrode potentials, and the species generated under acidic conditions is Cr<sup>3+</sup>, which has a much lower correlation with toxicological issues [112–114]. Co dissolution appears to be more significant, particularly in the presence of salt-rich solutions (e.g. PBS) and at low pH; here the dominant species should be Co<sup>2+</sup> as is discussed in recent MoM hip implant literature [117,125]. The hydrophobic components present in the serum may play an important role in the reduction of the contact between water and the metal particles, reducing further reaction with dissolved oxygen. However, significant dissolution of Mo was observed in

the presence of serum proteins and at neutral pH. It has been reported that molybdenum ions are essential to the formation of an organic film on the surface of hip implants, which can help avoid pitting corrosion and act as a barrier against electrochemical attack [51,198]. We have shown that the Mo is apparently more mobile in media containing serum proteins. This may be due to the ion ( $\text{Mo}^{2+}$  or  $\text{MoO}_4^{2-}$ ) complexing with the serum proteins present in the media [110,198], as result of secondary non-electrochemical reactions at the interface.

FTIR showed that after the removal of nanoparticles through the use of ultrafiltration, the peaks related to amides were removed from FTIR spectra indicating protein attachment to the CoCrMo nanoparticles. Another interesting result from FTIR was the appearance of different peaks after the removal of the nanoparticles from the solution. There was a change in signal intensity following ultrafiltration, so the peaks in the region of  $2200\text{-}1900\text{ cm}^{-1}$  could be present before filtration, but due to the strong signal from BSA, they were masked. These weak peaks can be related to BSA protein degradation [216] during milling. The amino acids present in BSA solution can provide multiple binding sites for metal free ions. These binding sites may include  $-\text{NH}$ ,  $-\text{SH}$ ,  $-\text{COOH}$ , and  $-\text{OH}$  groups, which could give rise to these peaks. The hypothesis of the formation of metal carbonyl species is thought unlikely because the synthesis process often includes reduction at high temperature and pressure [217]. However, Hart *et al.* (2010) detected molybdenum metal carbonyl in tissue from MoM hip patients using X-ray Absorption Near Edge Structure (XANES) [21]. This study indicated an octahedrally coordinated molybdenum species bound by oxygen and carbon in the second coordination sphere. In addition, Dolamic and Burgi (2011) have shown that the degradation of amino acids such as L-asparagine and L-glutamic acid, both present in BSA, can give rise to new complexes with metallic species [218]. The importance of identifying the possible existence of metal carbonyl as a result of wear from hip implants is related to the high toxicity of these species [219,220].

Finally this work correlates preferential binding between proteins and metal alloy nanoparticles to the alloy's corrosion behaviour and the release of metal ions. TEM images show the formation of a protein corona in all particles immersed in albumin containing solutions. Only molybdenum release was

significant in these tests, suggesting high dissolution of this element when CoCrMo alloy nanoparticles are produced as wear debris in the presence of serum albumin. The same trend was observed during extended exposure of molybdenum reference nanoparticles to albumin.

Using the same amount of particles and protein concentration, molybdenum nanoparticles showed the highest affinity to BSA, demonstrating that in the presence of serum proteins, the effective surface charge is very close to the IEP of BSA. Electrostatic forces are expected to play a significant role in protein binding. Albumin, when ionized in water at  $\text{pH} > 4.9$  (the isoelectric point - IEP), is a negatively charged protein that often shows affinity for hydrophobic surfaces, however it does exhibit a distinct positive patch on one of the triangular protein surfaces [205]. Mo showed an IEP of 2.6, being negative for values above the IEP, which can electrostatically bind the positive patch of BSA. According to Goyer and Clarkson (1996) proteins with specific metal binding properties play a special role in both the transport of metals from plasma to tissues and in the transport of metals across cell membranes and within the cell. Metals bound to albumin may be carried into cells by endocytotic mechanisms [219].

Taken together these results suggest the importance of binding between albumin proteins and molybdenum, which may directly influence the strong dissolution of this element when CoCrMo alloy nanoparticles are produced as hip-implant wear debris in the presence of serum albumin. Molybdenum is added to the alloy to impart corrosion resistance and its depletion in the presence of BSA, even at pH 7, could then leave the material open to greater corrosive attack.

## **5.6 Conclusion**

In this work it was highlighted that the commonly reported techniques of separating nanoscale wear debris from lubricant fluids using only centrifugation or ultracentrifugation are sub-optimal and lead to residual wear nanoparticles suspended in the analyte fluid. This can cause a large overestimation of the absolute and relative amounts of ionic dissolution that occurs during the

tribochemical wear of CoCrMo alloy samples. The use of a centrifugation plus ultrafiltration step during ICP-MS sample preparation can efficiently remove nanoparticulate wear debris that remain in the supernatant after centrifugal sedimentation. This, more accurate method of separating the wear particles from dissolved ions allows us to identify a significant ion release pathway through the body, hitherto unexplored.

Mechanical milling of CoCrMo alloys has been shown to decrease particle size to between 10-200 nm which is comparable with that seen in real wear debris released by hip implants. During milling, low carbon alloy powders generated more nanoparticles than the high carbon alloy, which is directly related to the alloys mechanical properties and the stabilization of the fcc phase by carbon. ICP-MS together with SEM/TEM EDX gave an indication of cobalt and molybdenum dissolution in the presence of serum for both high and low carbon alloy milled powders.

The corrosion studies in different media have revealed the preferential dissolution of Mo in the presence of serum proteins, and that, based on the pH dependence, it is likely that more significant Co and Cr solubility will only occur if particles are taken up by phagocytic cells and digested in lysosomes.

TEM analysis suggest the formation of a protein corona on synthetic CoCrMo wear debris particles incubated with BSA and the particles were found to be deficient in molybdenum by EDX. An interaction with proteins was also seen for elemental reference oxide materials where ICP-MS showed that the reference materials underwent dissolution of predominantly molybdenum ions under static incubation in the presence of BSA. During zeta potential titration, CoCrMo and Molybdenum nanoparticles showed the highest affinity to BSA.

Overall these results gives a good indication of the importance of binding between albumin proteins and molybdenum, which may directly influence the strong dissolution of this element when CoCrMo alloy nanoparticles are produced as hip-implant wear debris in the presence of serum albumin.

These findings are important as it highlights the interaction of Mo rich surfaces with amide groups in serum proteins plus identifies the formation of metal complexes both of which can modify biological molecules, altering their ability to function properly.

## Chapter 6 - Electrochemical Corrosion Studies of Bulk Materials Immersed in Biological Media

### 6.1 Introduction

So far in this study, the data presented have mainly focused on the corrosion and biotribocorrosion of CoCrMo particles and reference materials. In an attempt to understand the general corrosion behaviour of the ASTM75 alloy and its major elements, the CoCrMo alloy plus pure Co, Cr and Mo metal reference samples were each immersed in Bovine Serum Albumin (BSA), Phosphate Buffered Saline (PBS) solution and a mix of both at a temperature of 37°C, and were assessed through electrochemical measurement techniques (scheme shown in Figure 3.4) with a view to further investigate the particle dissolution studies presented in previous chapters.

The corrosion of metallic biomaterials in appropriate media is a complex phenomenon, however an electrochemical corrosion study of the alloy solubility and the separate alloying elements could give relevant data to understand any selective dissolution in biological media. Each alloying element in cobalt-based alloys plays an important role in the implant: Cr is mainly responsible for corrosion protection, as it forms a passive oxide barrier layer on the surface of the alloy, that is mainly composed of Cr<sub>2</sub>O<sub>3</sub> [50]; Mo is essential to the alloy as it provides maximum stability of the passive film and also acts to retard localized corrosion propagation in the case that the passive film is disrupted [204]. Some authors have suggested that the oxidation of Co and Cr occurs independently, in a process comparable to the oxidation of the pure metals [3], despite this, Zimmermann *et al.* (2010) have shown that there is a driving force for the development of the external oxide layer, which depends on the relative amount of Cr atoms at the surface layer [4]. Therefore, caution must be taken in interpretation of the alloy behaviour, which could differ from that of the pure metals due to the interactions and synergistic affects between the alloying elements.

Polarization tests can provide useful information regarding corrosion mechanisms, corrosion rate and the susceptibility of specific materials to corrode in specific environments. Here, the corrosion behaviour of the samples

was evaluated by cyclic polarization curves, in a positive direction (anodic) and a negative direction (cathodic) both related to OCP, in three different aerated and unstirred electrolytes. Each measurement was carried out at least three times in order to check the repeatability of the experiments.

Pourbaix diagrams of cobalt, chromium and molybdenum were simulated in water at 37°C, under atmospheric conditions by using HSC Chemistry software version 5.0 from Autotec [222]. These diagrams helped to predict the corrosion behaviour related to different pHs and potentials.

Complementary techniques such as Scanning Electron Microscopy/Energy Dispersive X-Ray Spectroscopy (SEM/EDX), X-ray photoelectron spectroscopy (XPS), Inductively Coupled Plasma Mass Spectrometry (ICP-MS) and Ultraviolet–visible Spectroscopy (Uv-ViS) were employed to analyse the surface of the samples and the electrolyte solutions, which allowed investigation of corrosion damage, the fundamental reaction kinetics and the preferential dissolution of certain elements. The full description of methods and materials used in this section can be found in Section 3.3.

## 6.2 Pourbaix diagram for Co, Cr and Mo

Standard Pourbaix diagrams in the literature are for elements relative to a standard hydrogen electrode (SHE) in water (H<sub>2</sub>O) at 25 °C. Pourbaix diagram simulations for the reference metals relative to Ag/AgCl electrode in water (H<sub>2</sub>O) at 37 °C are presented and these show the theoretical domains of corrosion, passivation and immunity for a given potential and pH, based on the Nernst equation for the possible reactions. Each diagram indicates the conditions of thermodynamic stability of the elements studied and those derivatives of it which can exist in the presence of water or aqueous solutions free from substances with which the elements can form soluble complexes or insoluble salts (non-complexing solutions).

According to the theoretical diagram (Figure 6.1), cobalt is highly susceptible to corrosion in water based solution at 37°C, releasing Co<sup>+2</sup> ions at pH < 8 and potentials above -0.75 V<sub>Ag/AgCl</sub>. The region of immunity, where the

metal is not attacked, could be achieved cathodically by lowering the electrode potential to a value below  $-0.75 V_{\text{Ag/AgCl}}$  in neutral solution.

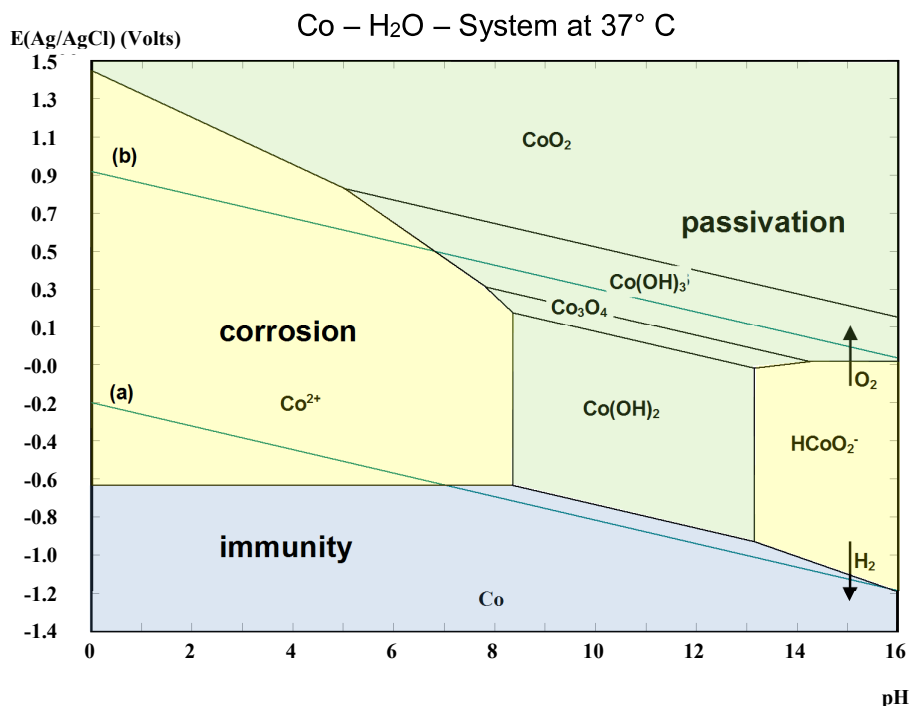


**Figure 6.1** - Pourbaix diagram for cobalt in H<sub>2</sub>O, 37°C, molality 0.7 mol/ kg H<sub>2</sub>O, pressure 1 bar, simulated on HSC Chemistry 5.0 software. Lines (a) and (b) designate the limits of thermodynamic stability of water for the given conditions. Below line (a) water is unstable and must decompose to H<sub>2</sub> and above it is stable and any H<sub>2</sub> present is oxidised to H<sup>+</sup> or H<sub>2</sub>O. Above line (b) water is unstable and must oxidize to give O<sub>2</sub> and below it is stable and any dissolved O<sub>2</sub> is reduced to H<sub>2</sub>O.

In Figure 6.2, Chromium in the presence of acidic solutions tends to decompose water with the evolution of hydrogen, dissolving as Cr<sup>2+</sup> and Cr<sup>3+</sup> ions. Under neutral and slightly alkaline solutions, Cr tends to become covered with chromic oxide or hydroxide, and in the presence of very alkaline non-oxidant solutions, it tends to dissolve as chromite ions. The active corrosion state is produced by contact with reducing solutions or species, HCl or H<sub>2</sub>SO<sub>4</sub>, depassivation or by cathodic polarization. Pourbaix (1964) showed that for solutions containing chlorides (Figure 6.3) Cr solubility increases, thus, the passivation region decreases drastically in contrast with the corrosion region [212].

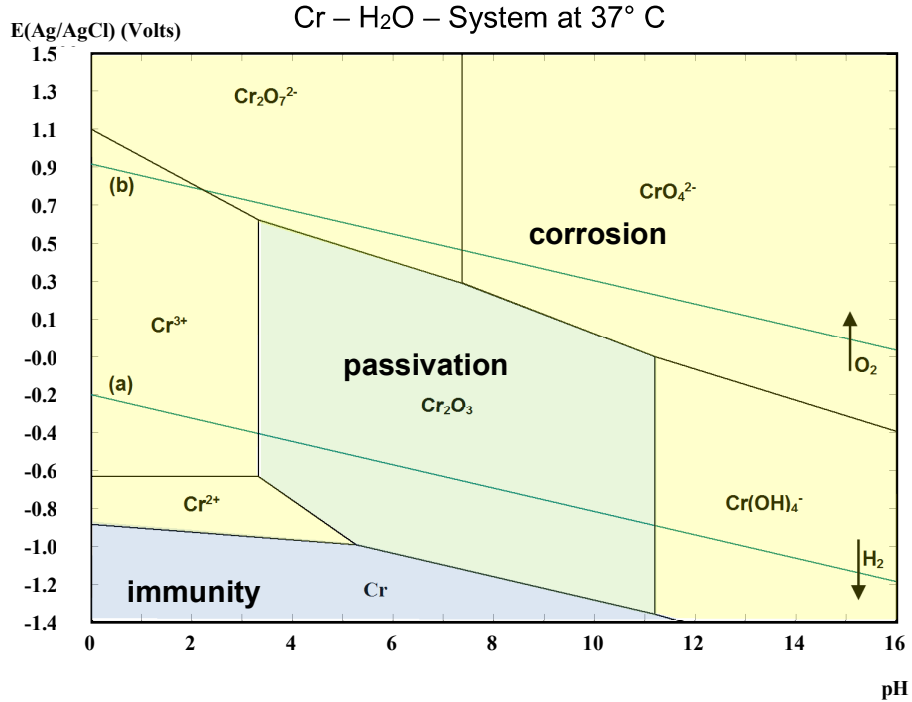


**Figure 6.2** - Pourbaix diagram for chromium in H<sub>2</sub>O, 37°C, molality 0.8 mol/ kg H<sub>2</sub>O, pressure 1 bar, simulated on HSC Chemistry 5.0 software. Lines (a) and (b) designate the limits of thermodynamic stability of water for the given conditions. Below line (a) water is unstable and must decompose to H<sub>2</sub> and above it is stable and any H<sub>2</sub> present is oxidised to H<sup>+</sup> or H<sub>2</sub>O. Above line (b) water is unstable and must oxidize to give O<sub>2</sub> and below it is stable and any dissolved O<sub>2</sub> is reduced to H<sub>2</sub>O.

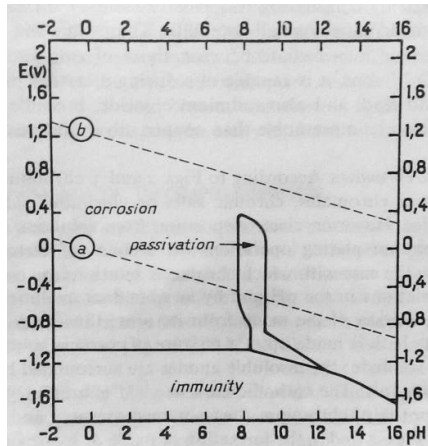


**Figure 6.3** - Pourbaix diagram using standard hydrogen electrode (SHE) for Cr in solutions containing chloride [212].

Molybdenum (Figure 6.4) in the presence of alkaline solutions has a small tendency to decompose water with the evolution of hydrogen, dissolving

in the hexavalent state as molybdate ions  $\text{MoO}_4^{2-}$ . For neutral or slightly acid solutions, Mo tends to form  $\text{MoO}_2$ . According to Pourbaix, when Mo metal is attacked by hydrochloric acid, it is probable that a film of insoluble chloride is formed which passivates the metal. When exposed to nitric acid, the metal is covered with a  $\text{MoO}_3$  oxide layer, which protects the metal against further attack.

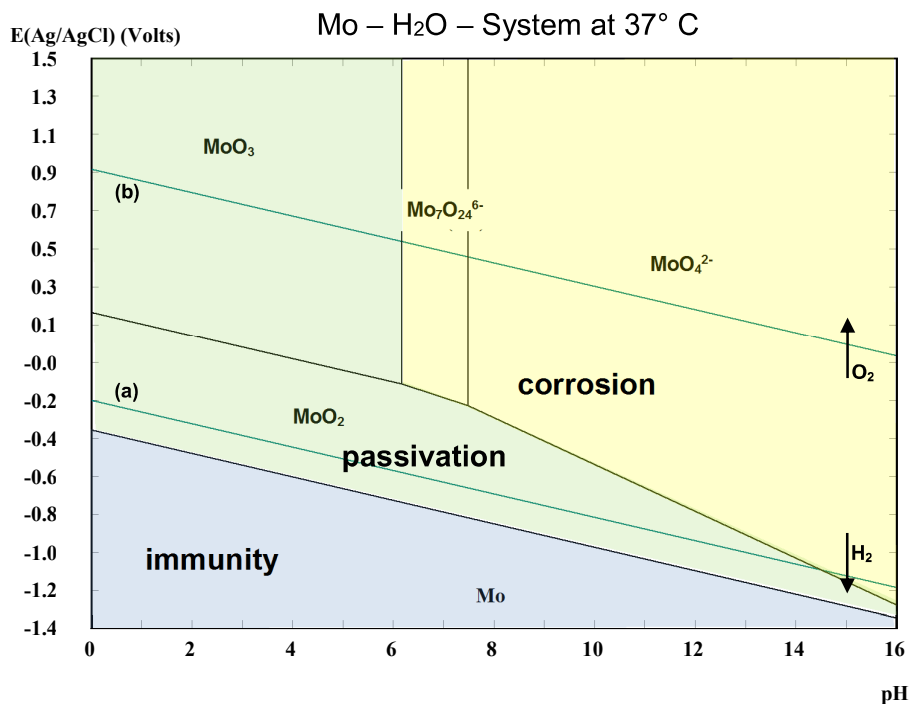


**Figure 6.4** - Pourbaix diagram for molybdenum in H<sub>2</sub>O, 37°C, molality 0.4 mol/kg H<sub>2</sub>O, pressure 1 bar, simulated on HSC Chemistry 5.0 software. Lines (a) and (b) designate the limits of thermodynamic stability of water for the given conditions. Below line (a) water is unstable and must decompose to H<sub>2</sub> and above it is stable and any H<sub>2</sub> present is oxidised to H<sup>+</sup> or H<sub>2</sub>O. Above line (b) water is unstable and must oxidize to give O<sub>2</sub> and below it is stable and any dissolved O<sub>2</sub> is reduced to H<sub>2</sub>O.

### 6.3 Polarization Curves

The polarization curves of Co, Cr, Mo and the CoCrMo alloy in different simulated body fluids (pure BSA, pure PBS and BSA plus PBS) are shown in Figure 6.5. For all solutions tested, the open circuit potential (OCP) achieved a stable value within less than 300 s. Table 6.1 shows data extracted from these measurements.

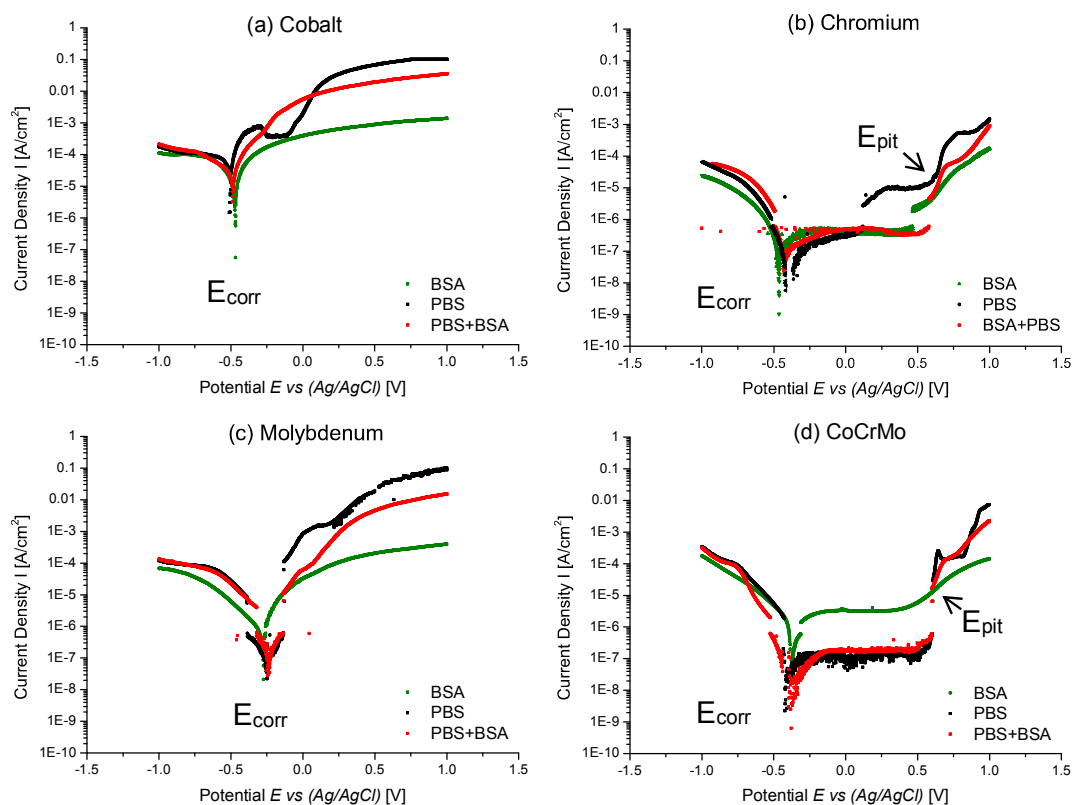


**Figure 6.5** - Anodic and cathodic polarization in BSA, PBS and BSA+PBS of: (a) Cobalt, (b) Chromium, (c) Molybdenum and (d) CoCrMo.

No significant variation in the corrosion potential ( $E_{\text{corr}}$ ) was observed for the elements in the three solutions tested. The cathodic potential domains for Co, Cr, Mo and CoCrMo are found below the  $E_{\text{corr}}$ , where the current density was determined by the reduction of water and dissolved oxygen. In all samples, BSA slightly decreased the current density for the cathodic domain, compared with PBS-containing solutions.

In all three solutions, polarized Co samples [Figure 6.5 (a)] showed an  $E_{\text{corr}}$ , in naturally aerated conditions, which was within the corrosion domain predicted by the Pourbaix simulation (Figure 6.1) and above the equilibrium line (a). Thus, the anodic dissolution  $Co \leftrightarrow Co^{2+} + 2e^-$  was thermodynamically spontaneous and there was no hydrogen reduction. Consequently, Co exhibited active dissolution leading to overall deterioration of the Co sample in these conditions. In the presence of BSA, Co showed more resistance to

increased current density than when in PBS, resulting in less overall corrosion at the end of the polarization sweep.

Mo polarized samples [Figure 6.5 (c)] also showed an apparent active dissolution in all three solutions. The  $E_{\text{corr}}$  values for all three solutions were found to lie inside the passivation region on the simulated Pourbaix diagram. However, during the increase in the potential, a breakdown of the  $\text{MoO}_2$  film will occur leading to accelerated dissolution. This may be due to the formation of porous and extremely permeable molybdenum oxides. In pure molybdenum, BSA appears to play a similar trend as in pure cobalt, by increasing the resistance compared to PBS. However, when the solution contains PBS, the graph showed a small region where the current density was constant, possibly an attempt at passivation, whereas BSA showed continuous active dissolution. Mo in BSA at a potential of 50 mV above  $E_{\text{corr}}$  also shows a higher current density than Mo in PBS (see Table 6.1).

A passive region is present in the Cr and CoCrMo alloy samples [Figure 6.5 (b) and (d), respectively], which can be seen in all three solutions, from  $E_{\text{corr}}$  to breakdown potential  $E_{\text{pit}}$  (see Table 6.1), with  $E_{\text{pit}}$  determined as the potential at which the current density reaches  $10 \mu\text{A}/\text{cm}^2$  [223,224]. CoCrMo in BSA at a potential of 50 mV and 100mV above  $E_{\text{corr}}$  exhibited a higher passive current ( $I_p$ ) compared to the others, which implies the dissolution of the passive film (see Table 6.1).

The chromium passivation domain (see Table 6.1) decreases when the electrolyte used is PBS. This result represents the possible disruption of the passive film within which pitting then occurs, however, the metal surface was quickly able to re-passivate the protective film, decelerating the metal dissolution process. This phenomenon suggests that in this condition, the passive films formed were less thick, making them unable to withstand an overvoltage. In BSA, the passivating current density slightly increases, and the pitting potential ( $E_{\text{pit}}$ ) shifts towards higher values. A lower  $E_{\text{pit}}$  value indicates increased chance of breakdown of the passive film and an early start to pitting and crevice corrosion.

Cr and CoCrMo in PBS-containing solutions both show a shoulder at about  $0.6 V_{\text{Ag}/\text{AgCl}}$ . This effect was also observed by Milosev *et al.* (2003) and

Vidal *et al.* (2008) in CoCrMo [53,55] and was attributed to the development of phosphate–chromium ion complexes that activate transpassive dissolution.

Muñoz and Mischler (2007) studied the corrosion behaviour of CoCrMo alloy in simulated body fluids containing BSA and PBS. They found that both play a significant role in the electrochemical properties of the metal, oxide and electrolyte interface and that the presence of albumin increases the passive current density while phosphate decreases it [225]. Identical behaviour was observed here for CoCrMo, however the same is not true for Cr.

**Table 6.1-** Corrosion data extracted from polarization curves.

| Sample | Solution | pH<br>before | $E_{corr}$<br>(V) | $E_{pit}$<br>(V) | Passivation<br>domain<br>$E_{pit} - E_{corr}$ (V) | $I$ (A/cm <sup>2</sup> )    | $I$ (A/cm <sup>2</sup> )     | Tafel<br>extrapolation |            |
|--------|----------|--------------|-------------------|------------------|---|-----------------------------|------------------------------|------------------------|------------|
|        |          |              |                   |                  |   | 50mV<br>above<br>$E_{corr}$ | 100mV<br>above<br>$E_{corr}$ | $E_{corr}$             | $I_{corr}$ |
| Co     | BSA      | 7.20         | -0.47             | -                | -   | 3.58E-05                    | 7.14E-05                     | -0.47                  | 7.69E-06   |
|        | PBS      | 7.40         | -0.52             | -                | -   | 1.27E-04                    | 3.76E-04                     | -0.51                  | 4.25E-05   |
|        | PBS+BSA  | 7.35         | -0.48             | -                | -   | 4.87E-05                    | 1.74E-04                     | -0.48                  | 1.58E-05   |
| Cr     | BSA      | 7.20         | -0.46             | 0.68             | -1.14   | 1.50E-07                    | 3.16E-07                     | -                      | -          |
|        | PBS      | 7.40         | -0.42             | 0.60             | -1.02   | 3.48E-08                    | 2.90E-08                     | -                      | -          |
|        | PBS+BSA  | 7.35         | -0.43             | 0.63             | -1.06   | 6.47E-07                    | 1.12E-06                     | -                      | -          |
| Mo     | BSA      | 7.20         | -0.27             | -                | -   | 7.30E-06                    | 1.11E-05                     | -0.29                  | 9.67E-07   |
|        | PBS      | 7.40         | -0.24             | -                | -   | 3.54E-07                    | 1.61E-04                     | -0.23                  | 5.34E-07   |
|        | PBS+BSA  | 7.35         | -0.24             | -                | -   | 5.23E-07                    | 1.74E-05                     | -0.24                  | 1.62E-07   |
| CoCrMo | BSA      | 7.20         | -0.38             | 0.60             | -0.98   | 1.55E-06                    | 2.29E-06                     | -                      | -          |
|        | PBS      | 7.40         | -0.42             | 0.60             | -1.02   | 3.18E-08                    | 1.23E-07                     | -                      | -          |
|        | PBS+BSA  | 7.35         | -0.38             | 0.60             | -0.98   | 2.08E-08                    | 5.56E-08                     | -                      | -          |

For the CoCrMo alloy, the passive domain showed a slight variation and the passivating layer was formed at a higher current density in a BSA environment. No significant changes occurred in  $E_{pit}$ , however in PBS, the sample exhibited multiple pitting potentials associated with the dissolution of different active phases before pitting corrosion of the matrix alloy.

Overall, the presence of BSA was shown to improve the resistance for Co and Mo, while for Cr similar behaviour was observed in PBS and

BSA+PBS. There is a suggestion that BSA is initially more aggressive to CoCrMo alloys at low potentials.

## 6.4 Surface analysis

### 6.4.1 - Scanning Electron Microscopy

In this section, the changes in the morphology of the surface of samples following anodic polarization are revealed using SEM, with an emphasis on the form of surface degradation and the presence of electrolyte components (C, O, N, Na, Cl, P, etc.) at the surface.

The surface of the cobalt sample immersed in BSA after anodic polarization, shown in Figure 6.6 at relatively high magnification, revealed minimal surface damage, mostly composed of a few scratches from the sample polishing. EDX analysis of the full area showed the presence of only carbon and oxygen.

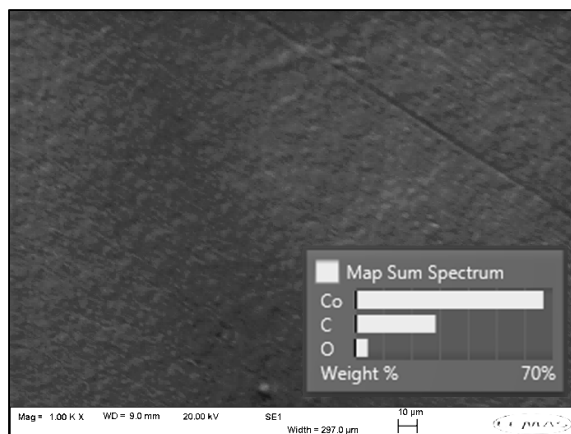


**Figure 6.6** - Secondary electron image of the surface of Co sample after anodic polarization in BSA including EDX analysis of the full area. Image with a scale bar of 10  $\mu\text{m}$ .

The surface of the cobalt sample immersed in PBS after anodic polarization, shown in Figure 6.7 at lower magnification, revealed severe corrosion damage all over the sample surface with only a few parts of the Co surface being preserved.

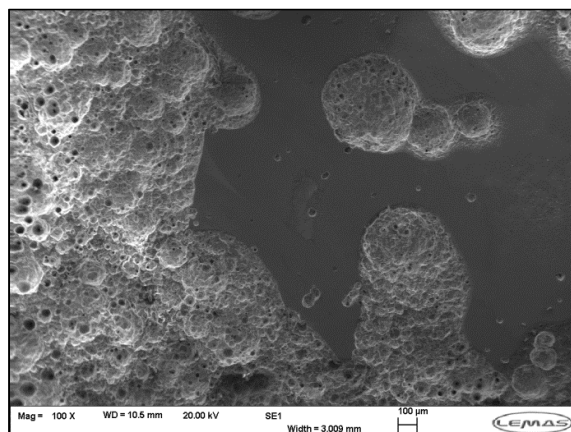


**Figure 6.7** - Secondary electron image of the surface of Co sample after anodic polarization in PBS. Image with a scale bar of 100  $\mu\text{m}$ .

EDX analysis on the surface of the Co in PBS sample in a smaller area (Figure 6.8) indicated that inside the pits there is a high concentration of salts such as NaCl. The solution and corrosion products in the bottom of the pit could change the pH in this region promoting growth of the pit.

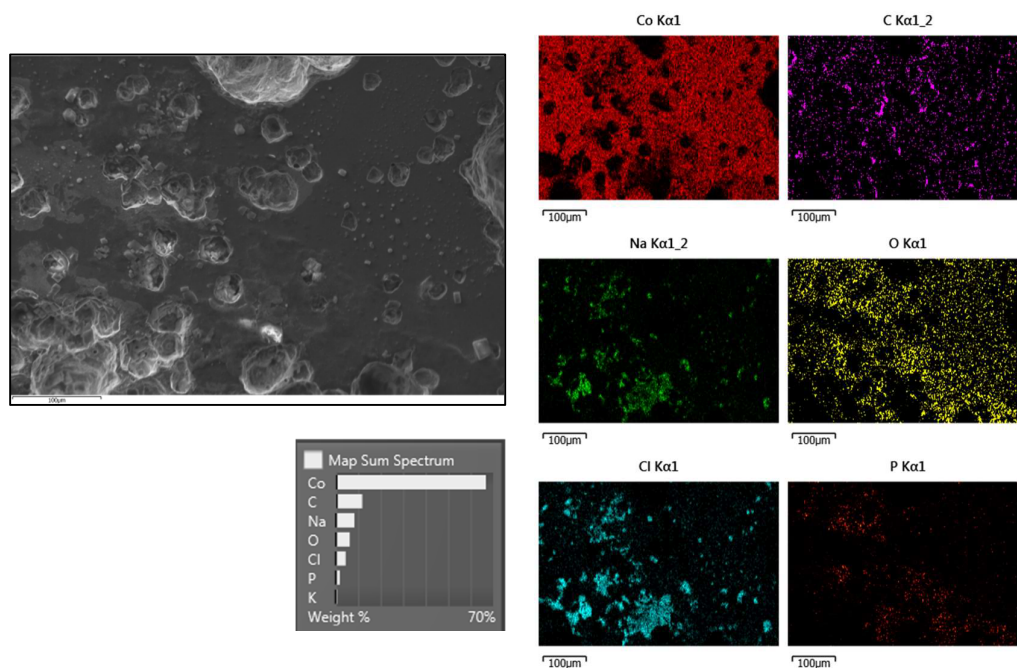


**Figure 6.8** - EDX mapping of the Co sample after anodic polarization in PBS. Image with a scale bar of 100  $\mu\text{m}$ .

The surface of the cobalt sample immersed in BSA plus PBS after anodic polarization (Figure 6.9) also showed severe corrosion that was spread

all over the surface of the sample. However the degradation appeared to be less than for the Co in PBS sample and pits were more uniformly sized with a diameter of ca. 20  $\mu\text{m}$ . EDX analysis of the surface of the Co in BSA plus PBS sample indicated that the surface was mostly covered by cobalt, oxygen and carbon, with minor amounts of Na, P and Cl which were found to be spread over the surface of the sample.

The  $I_{\text{corr}}$  value, obtained by Tafel extrapolation, was higher for the Co samples immersed in PBS than for the Co samples in pure BSA, therefore, the corrosion rate was lower for the BSA-coated sample. For this reason together with our SEM results, we can conclude that the BSA provides protection to Co samples from pitting and general corrosion.

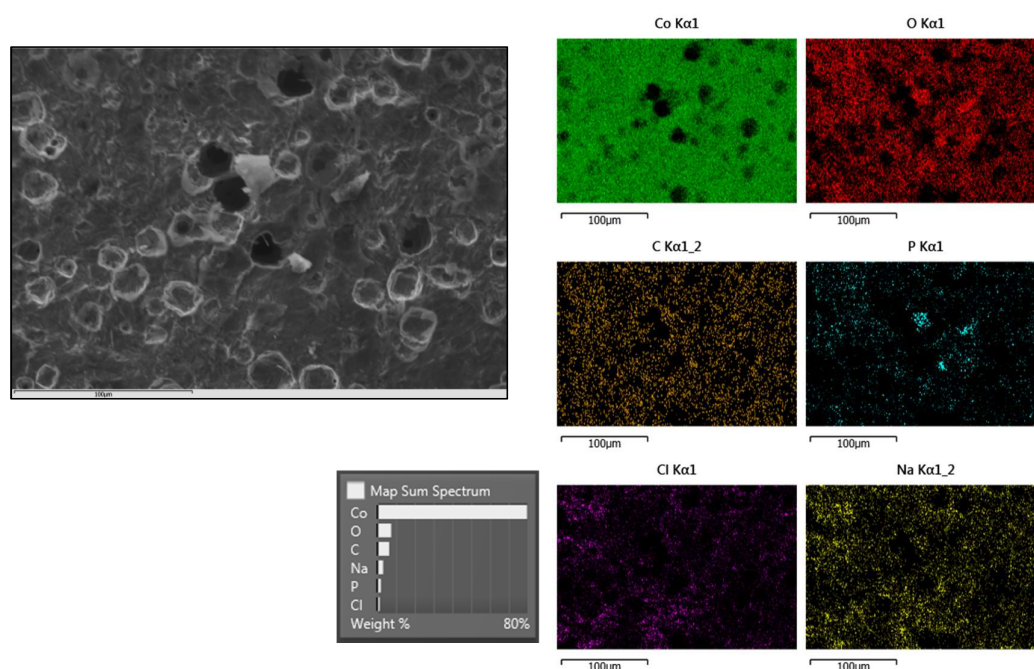


**Figure 6.9** - Secondary electron images of the surface of Co sample after anodic polarization in BSA+PBS and also corresponding EDX mapping. Image with a scale bar of 100  $\mu\text{m}$ .

Secondary electron images of Cr samples after polarization (Figure 6.10) showed barely visible degradation of the surface of PBS- and BSA+PBS-immersed samples, exhibiting nanometre-sized pits only (circled in red). Scratches from the sample polishing were difficult to remove due to the very hard nature of Cr oxides present on the surface. EDX analysis showed the surfaces of the samples were coated with the electrolyte elements used during polarization, which could be confirmed by EDX analysis from larger areas.

Arrows indicate the presence of precipitated salts in PBS and BSA+PBS samples, whereas carbon was found in significant amounts on the BSA sample surface.

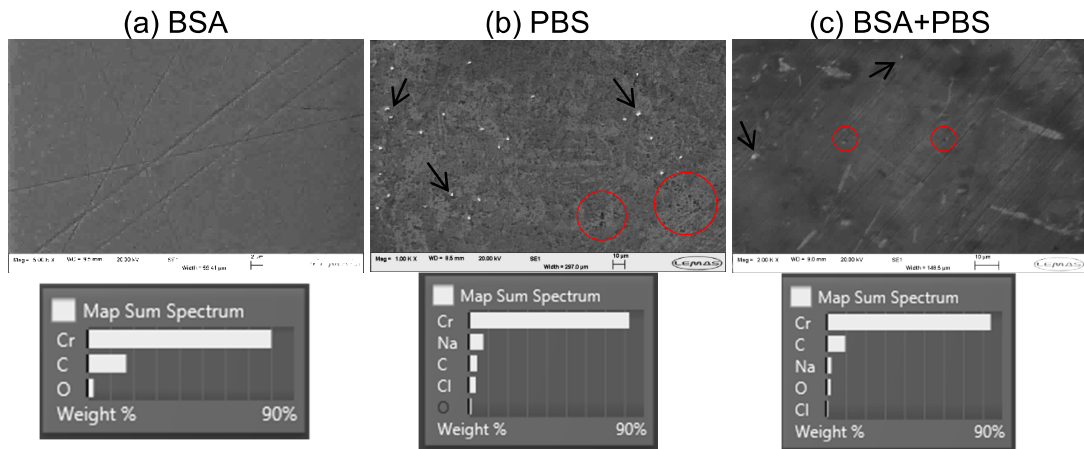


**Figure 6.10** - Secondary electron images and EDX of Cr samples after anodic polarization in : (a) BSA, (b) PBS and (c) BSA+PBS. Image with scale bar of 2 and 10 μm, respectively.

Secondary electron imaging of the Mo sample after immersion in BSA (Figure 6.11) revealed pits of small diameters ca. 2 μm with some as large as ca. 20 μm. From EDX, the surface of the sample was mainly covered with C at a level close to that of Mo, together with significant amounts of O and N.

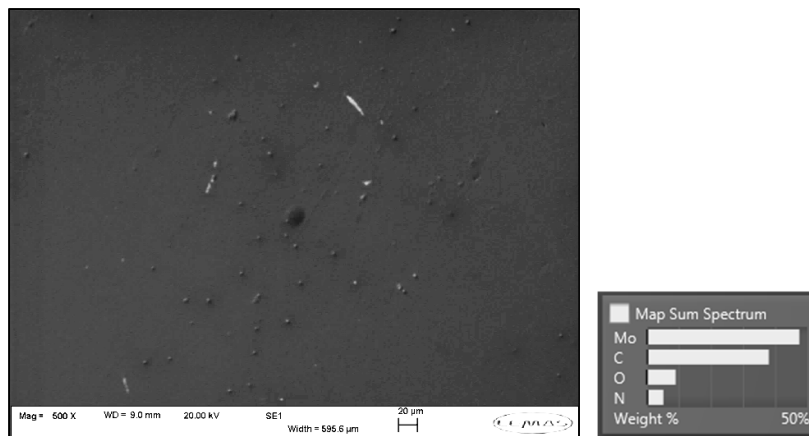


**Figure 6.11** - SEM electron imaging and EDX mapping of the surface of Mo samples in BSA after anodic polarization. Image with a scale bar of 20 μm.

Anodic polarization of Mo in PBS (Figure 6.12) showed pitting corrosion with pits (of ca. 2  $\mu\text{m}$  diameter) surrounded by cracks on the surface of the sample, as well as some evidence of intergranular corrosion (indicated by arrows). The appearance of microcracks could possibly be related to the formation of a brittle molybdenum oxide layer. EDX mapping showed the oxide to be evenly spread over the surface, whereas salt precipitation (Na and Cl) was evident in some areas.

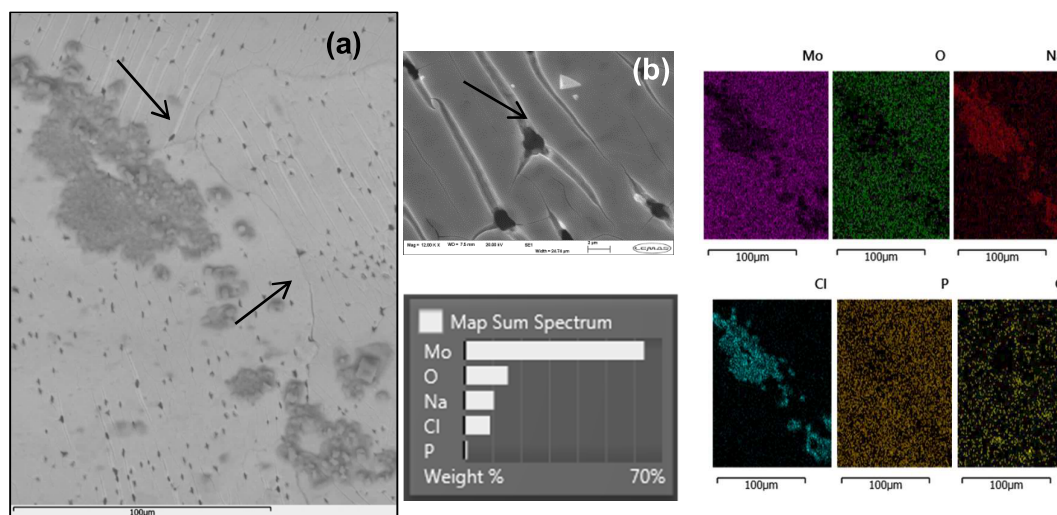


**Figure 6.12** - SEM backscattered (a) and secondary (b) electron imaging of the surface of Mo sample in PBS after anodic polarization (a). EDX mapping corresponding to the image (a) included. Arrows indicate intergranular corrosion. Image with a scale bar of (a) 100 and (b) 2  $\mu\text{m}$ .

Mo anodic polarization in BSA+PBS (Figure 6.13) showed multiple cracks on the surface of the sample, to a somewhat greater extent than for PBS, however no pitting could be found. EDX mapping showed a surface composition similar to the case of Mo in BSA, with a very carbon-rich surface.

SEM of the CoCrMo alloy immersed in BSA, PBS and BSA+PBS after anodic polarization only revealed pitting corrosion when immersed in PBS and showed pit diameters of ca. 2  $\mu\text{m}$  with salt precipitation observed as white contrast (Figure 6.14). In BSA and BSA plus PBS the corrosion damage was less evident showing nanometre-sized pits only. EDX showed no significant change in the relative ratio of the Co, Cr and Mo at the surface compared to the raw material (wt%: Co 66%, Cr 29%, Mo 5%).

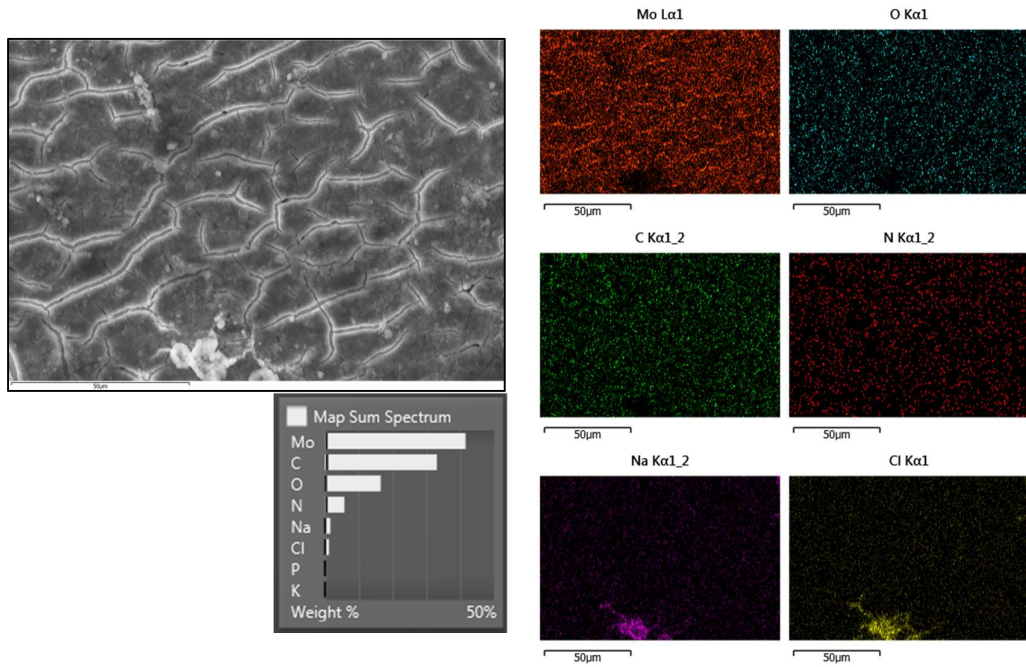


**Figure 6.13** - SEM backscattered electron imaging and EDX mapping of the surface of Mo sample in BSA+PBS after anodic polarization. Image with a scale bar of 50  $\mu\text{m}$ .

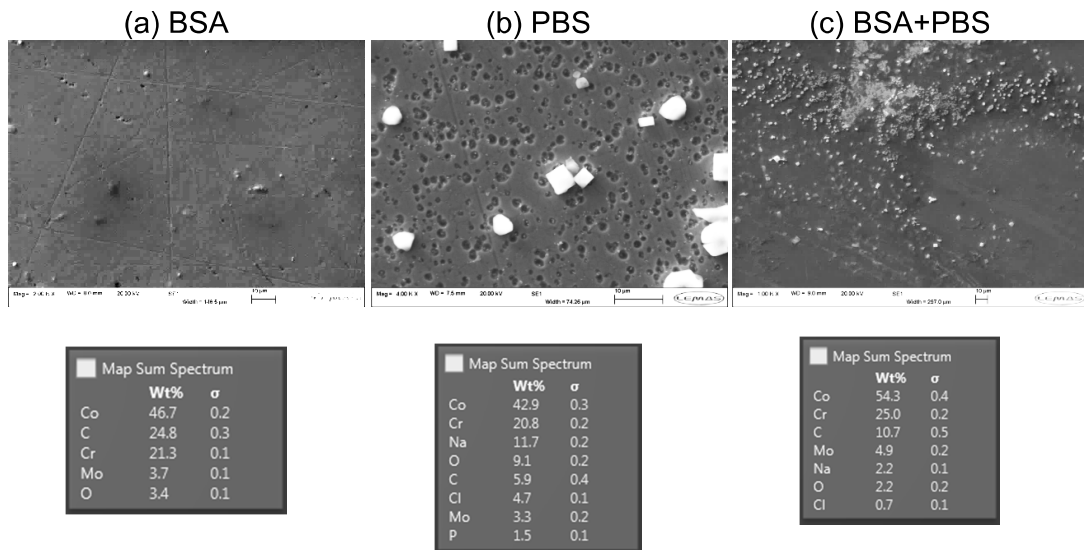


**Figure 6.14** - SEM secondary electron imaging and EDX mapping of CoCrMo samples after anodic polarization in : (a) BSA, (b) PBS and (c) BSA+PBS. Salt particles are evident in (b) and (c). Images with a scale bar of 10  $\mu\text{m}$ .

Alemon *et al.* (2014) detected a high density of pits on the surface of a CoCrMo low carbon alloy after anodic polarization in simulated body fluid with 4 g/L of BSA. The pits were comparable in size to those obtained in this study and the authors also highlighted the presence of saline elements of the

immersion fluids and corrosion products in the bottom of the pit [32]. Mathew *et al.* (2014) studied CoCrMo low carbon alloy polarization in simulated body fluid with a total protein composition of 30 g/L, and these samples also showed an abundance of pits [226].

Bettini *et al.* studied CoCrMo alloy potentiodynamic polarization between 0.5-0.7  $V_{Ag/AgCl}$  in PBS. They showed that the commonly observed high increase in current density at 0.5  $V_{Ag/AgCl}$  is followed by some metal dissolution, however no visible topography change was observed at 0.65  $V_{Ag/AgCl}$  [171].

In conclusion, SEM analysis has shown that the main mechanism of degradation related to anodic polarization is pitting corrosion. PBS vastly increased the incidence of pitting, where the presence of salts was seen inside the pits. If proteins were present in solution, the material was homogeneously deposited on the surface of the samples, this being slightly less evident for Co. BSA was shown to play an important protection role against corrosion for all elements tested presumably coating the surface of the samples (with a carbon-rich layer) and increasing the corrosion resistance.

#### **6.4.2 - X-ray Photoelectron Spectroscopy**

In order to further investigate the surface composition of the anodically polarized samples, XPS was performed. For the samples polarized in different media, this technique allows analysis of depths of up to 3-5 nm from the specimen surface and is mainly used to determine the chemical state of near-surface elements. High resolution spectra were acquired for the main bulk compositional elements and adsorbates: Co 2p, Cr 2p, Mo 3d, C 1s, N 1s, P 2p and O 1s. Peaks were fitted and deconvoluted using CasaXPS software. Any element species with total contribution below 3% found to be overlapped was treated as not detected.

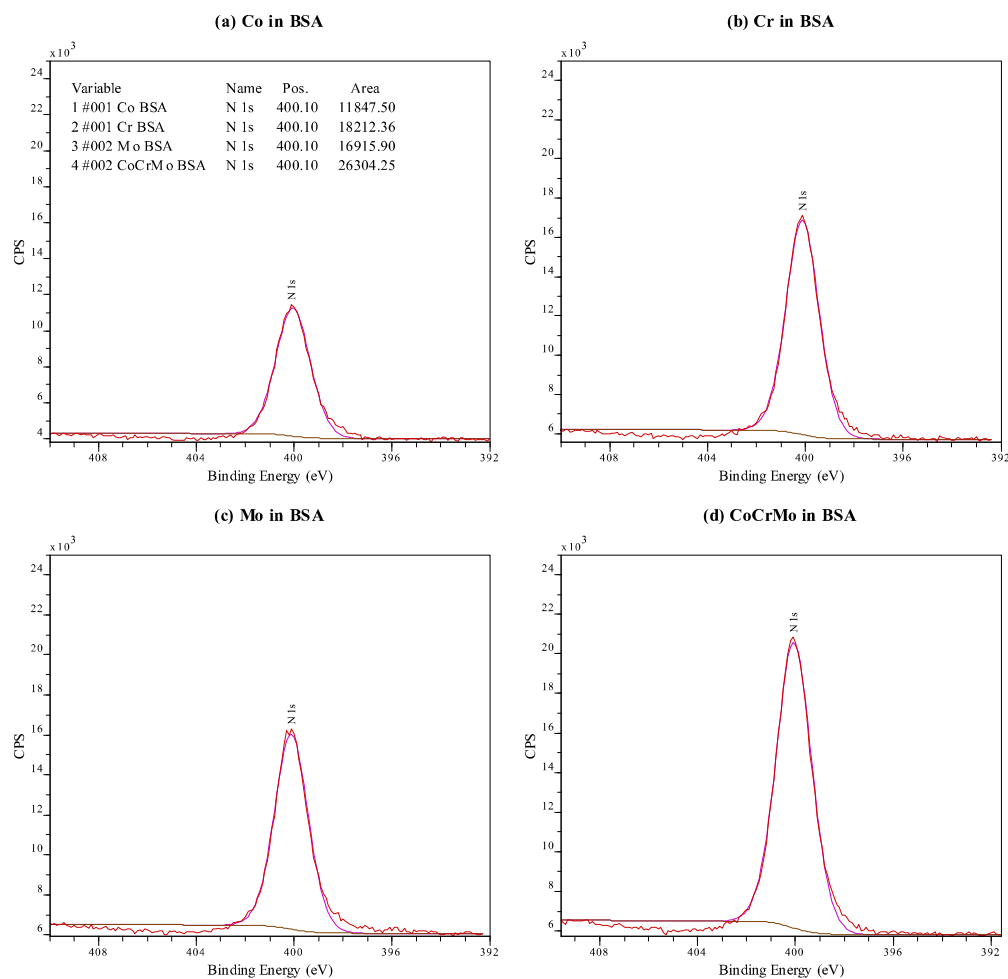
The N 1s and C 1s peaks, located at 400.1 eV and 284.5 eV respectively, are typically associated with protein adsorption [204,227]. The N 1s peak is more reliable than the C 1s peak to correlate with protein adsorption because it is less susceptible to contamination during the experiment. A clean metallic surface is very reactive and can adsorb water vapour and atmospheric contaminants. Carbon can often be present because of adsorbed hydrocarbons

and carbon oxides; oxygen is expected from instantaneous oxide formation, as well as adsorbed water vapour and carbon dioxide.

For ease of comparison, XPS results from different samples were initially grouped in the same X-ray photoelectron spectral regions: N 1s, C 1s and P 2p regions.

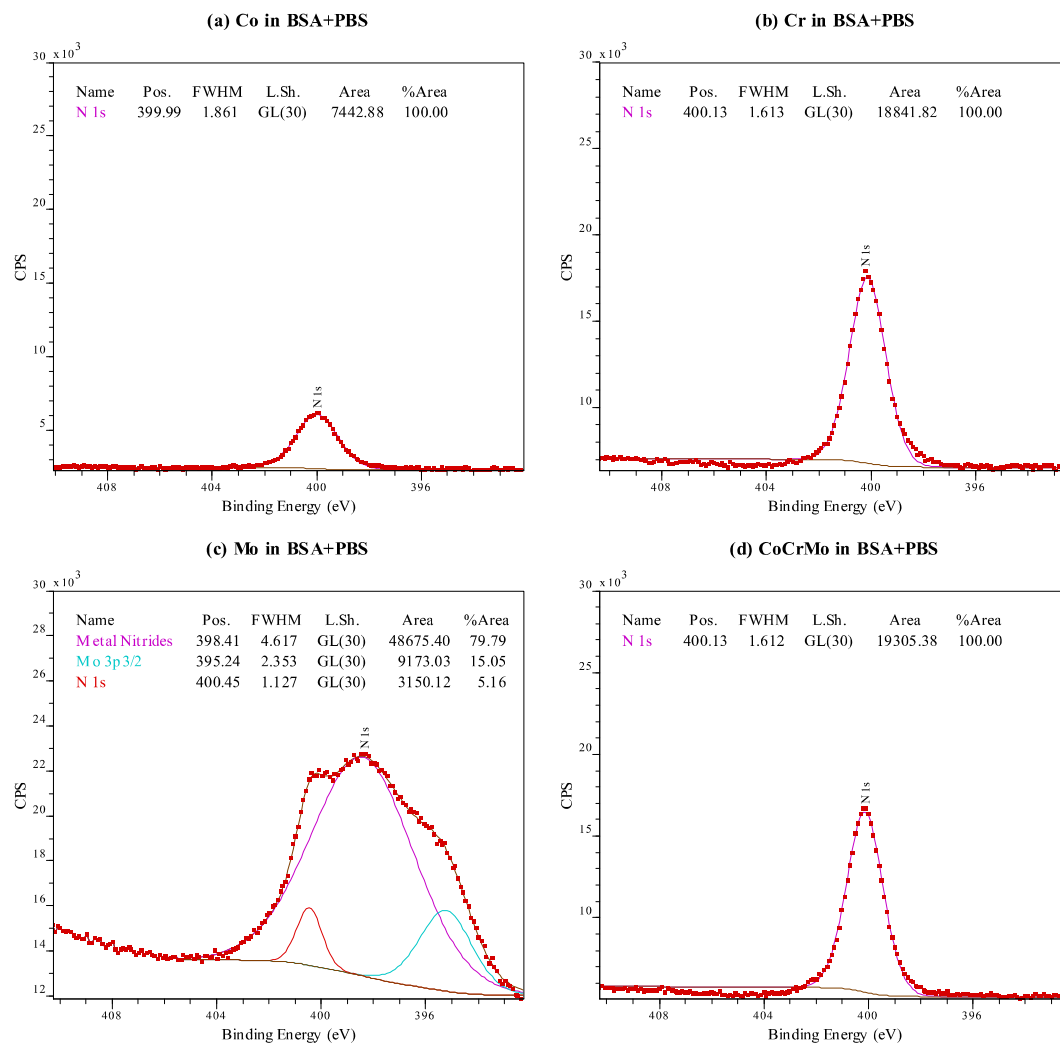
### 6.4.2.1 - Nitrogen (1s), Carbon (1s) and Phosphorous P (2p) Photoelectron Lines

Figure 6.15 shows a comparison of the analysis of the areas under the photoelectron N 1s peaks taken to indicate the adsorbed amounts of BSA. All samples studied presented some level of attachment to the BSA proteins, with the CoCrMo alloy showing the highest intensity, Mo and Cr with similar values, and Co with the lowest (see values for the area under the N 1s peak).



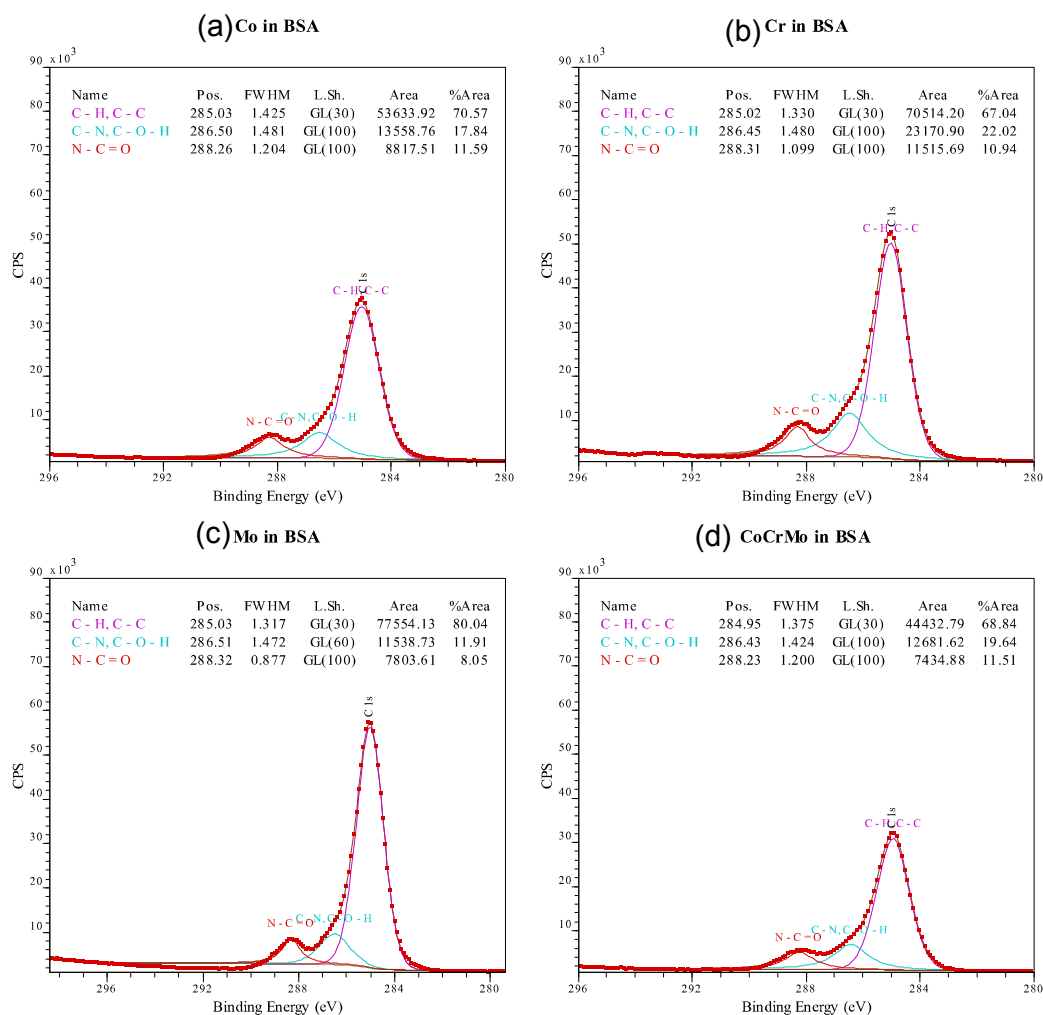
**Figure 6.15** - XPS N1s scanning on (a) Co, (b) Cr, (c) Mo and (d) CoCrMo alloy, after anodic polarization in BSA.

The anodically polarized samples in BSA plus PBS (Figure 6.16) showed a similar trend for Cr, whereas there was a decrease in N 1s intensity for Co and CoCrMo, possibly as a result of a synergy between the BSA and PBS components. Mo previously showed the presence of Metal-Nitrogen bonds, similar to those observed in metal nitrides [228], at the surface of the sample that were not found for the Mo anodically polarized sample in BSA [see Figure 6.15 (c)]. This is possibly due to the amount of BSA at the surface of the sample that forms a thick layer, and consequently XPS does not reach the depth where the metal-protein interactions are located. In BSA+PBS this layer is nominally thinner, making this interaction layer visible to XPS. The low N intensity for Co possibly indicates a poor adhesion of proteins to the metal surface due to competitive adsorption with phosphate ions.



**Figure 6.16** - XPS N1s spectra for: (a) Co, (b) Cr, (c) Mo and (d) CoCrMo alloy, after anodic polarization in BSA+PBS.

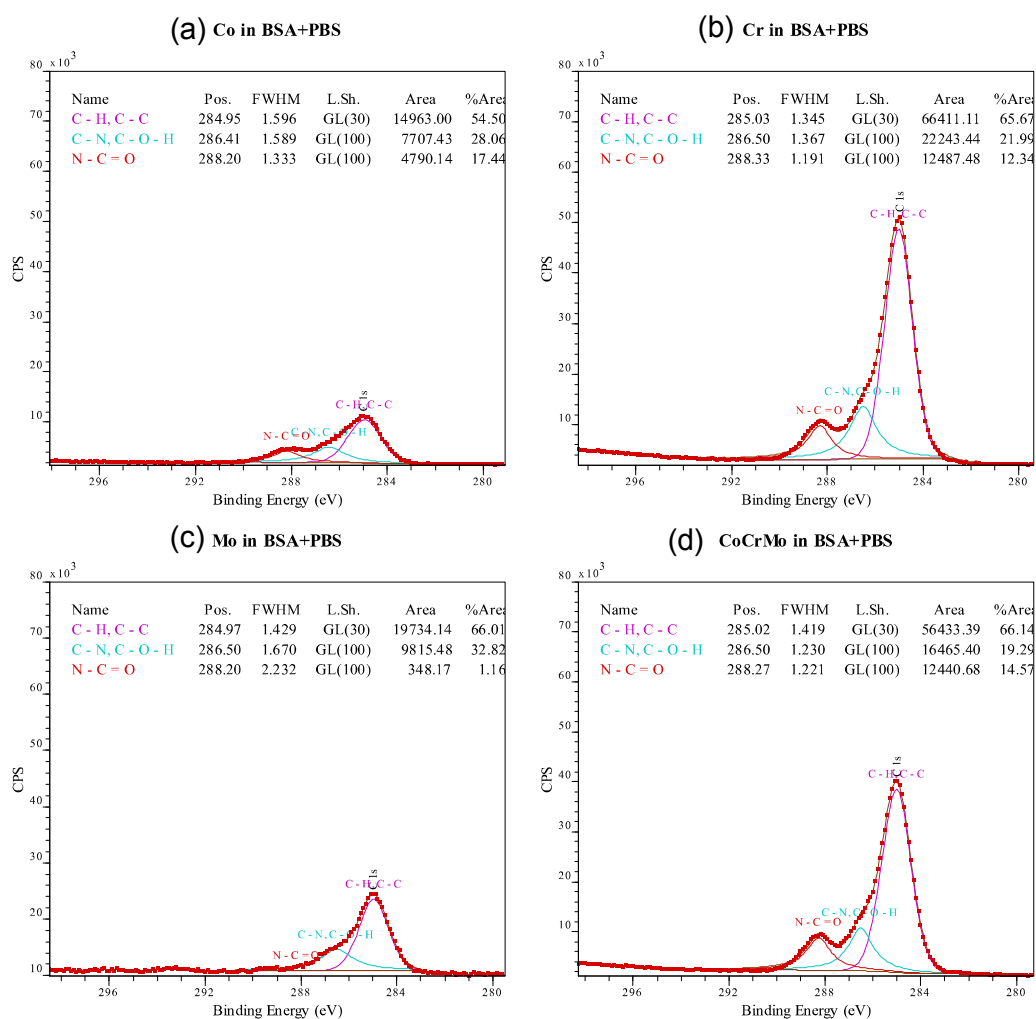
C 1s spectra (Figure 6.17) were fitted by three peaks with binding energies for hydrocarbon ( $285 \pm 0.1$  eV), carbon singly bonded to either O or N ( $286.5 \pm 0.2$  eV) and carboxyl and/or amide groups ( $288.1 \pm 0.2$  eV) [204,227]. The samples in BSA indicated a similar carbon chemical state at the surface of Co, Cr and CoCrMo, with a slight variation in composition: 285 eV peak (67-70%), 286.5 eV peak (17-22%) and 288.1 eV (10-11%). Mo in BSA presented the most significant variation compared to the other samples showing more hydrocarbon (80%) and less carboxyl and amide groups (8%) on the surface.



**Figure 6.17** - XPS C 1s spectra for: (a) Co, (b) Cr, (c) Mo and (d) CoCrMo alloy, after anodic polarization in BSA.

The C 1s peaks were also fitted to the samples anodically polarized in PBS+BSA (Figure 6.18), showing for Co and Mo an overall decrease in both the total area and in the hydrocarbon peak associated with an increase in the carbon single bond to oxygen. However Mo showed a significant decrease in

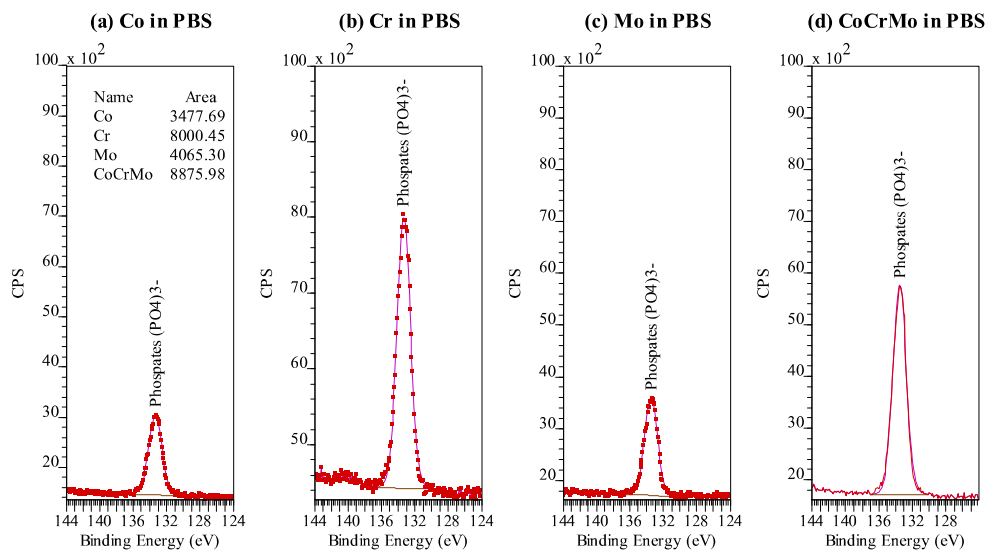
carboxyl and amide groups, whereas Co showed an increase. Cr and Mo maintained almost the same relative amount of species as observed in BSA. The significant decrease in 288 eV peak area (amide group) in Mo in BSA+PBS [Figure 6.18 (c)] compared to Mo in BSA [Figure 6.17 (c)] and an increase in peak 286.5 eV peak area (carbon single bond to N or O) may be related to the dissociation of amino acid groups on the surface of the protein and the rise of the metal-nitrogen bonds seen in Figure 6.16 (c) for Mo in BSA+PBS. The Mo surface and/or ions could electrostatically bind to the amide group NH<sub>2</sub>.



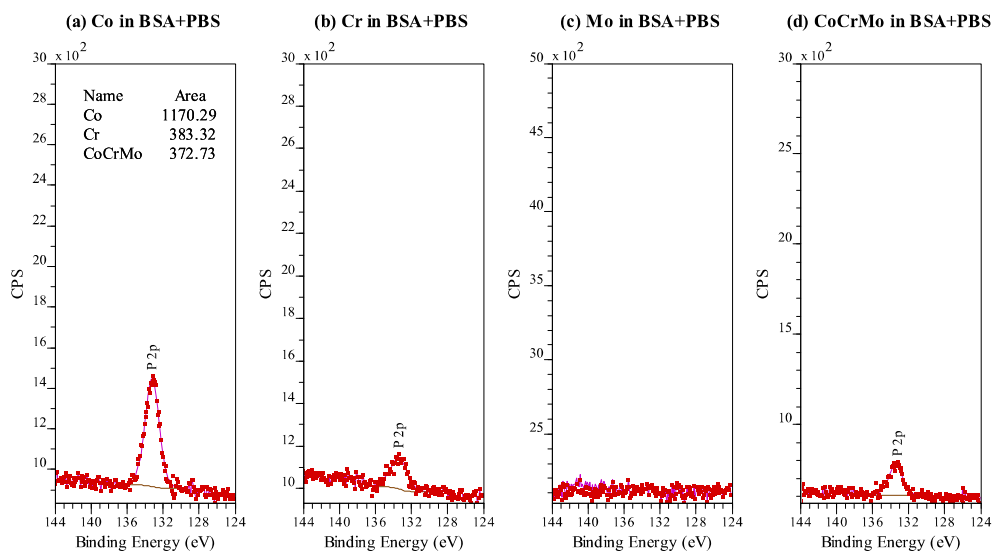
**Figure 6.18** - XPS C 1s spectra for: (a) Co, (b) Cr, (c) Mo and (d) CoCrMo alloy, after anodic polarization in BSA+PBS.

Figure 6.19 and Figure 6.20 show the P 2p spectra for the samples polarized in PBS and BSA+PBS, respectively. All show the presence of

phosphate  $\text{PO}_4^{3-}$  in PBS, the Cr and CoCrMo samples exhibited almost twice as much phosphate intensity than for the Co and Mo samples. In BSA+PBS there was no signal for the Mo sample which could imply that is predominantly covered with proteins on the surface, whereas Cr and CoCrMo showed a drastically reduced amount of phosphate at the surface of the samples relative to just PBS. The Co sample in BSA+PBS retained a large part of the phosphates, as compared with Co in PBS.



**Figure 6.19** - XPS P 2p spectra for: on (a) Co, (b) Cr, (c) Mo and (d) CoCrMo alloy, after anodic polarization in PBS.



**Figure 6.20** - XPS P 2p spectra for: (a) Co, (b) Cr, (c) Mo and (d) CoCrMo alloy, after anodic polarization in BSA+PBS.

#### 6.4.2.2 - Cobalt (2p), Chromium (2p) and Molybdenum (3d)

All the peaks in this section were fitted according to reference data in [180–185,229–231]. Figure 6.21 shows the XPS Co 2p spectra for the Co samples in all electrolytes tested. The fitting shows that the surface of these samples were covered with Co (+2) (see Table 6.2), mostly consisting of oxides with some traces of hydroxides in the case of BSA. Co samples in PBS and BSA+PBS showed a preponderance of Co (+2), principally as hydroxides. Also, metallic cobalt (778 eV peak) was only found (albeit in small amounts) when anodic polarization was carried out in pure PBS.

Table 6.3 shows the XPS Co 2p spectra for CoCrMo samples, which exhibited a very low signal when anodic polarization was conducted in BSA and BSA+PBS. This implies that the deposited layer is primarily organic. CoCrMo in PBS showed the presence of Co (+2), mainly comprising hydroxides.

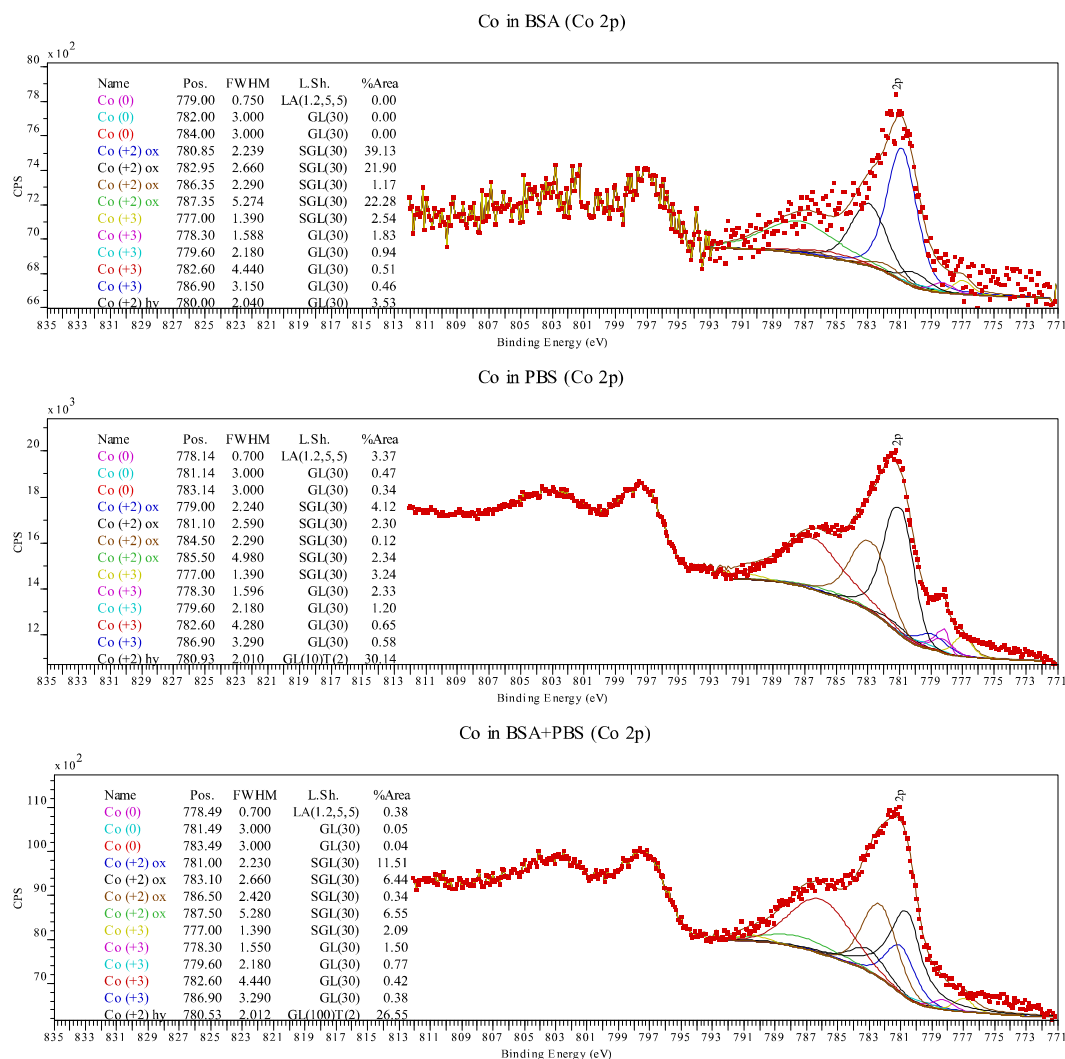
In the presence of BSA, the XPS Cr 2p spectra (Figure 6.23) showed a very low signal. In the presence of PBS and BSA+PBS, the Cr pure surface was covered by metallic Cr (0) probably existing as an underlayer below a Cr (+3) oxide/ hydroxide, which formed a passive layer of  $\text{Cr}_2\text{O}_3$  as predicted by Pourbaix diagrams (Figure 6.2).

Figure 6.24 shows the XPS Cr 2p spectra for the CoCrMo alloy, which exhibited a similar Cr oxidized surface independent of the electrolyte used. The passivating layer is principally a  $\text{Cr}^{3+}$  oxide/ hydroxide.

Mo 3d XPS spectra from anodically polarized elemental Mo surface (Figure 6.25) showed that in BSA and BSA+PBS the surface was mostly composed of Mo in the metallic form and Mo (+6), whereas in PBS it was mainly composed of Mo (+4). According to the simulated Pourbaix diagram (Figure 6.4) it can be assumed that a thin layer of  $\text{MoO}_2$  is always present at the surface of the Mo sample. At higher potentials, Mo (+4) further oxidizes to Mo (+6), and this reaction appears to be accelerated by the presence of BSA in the solution during anodic polarization.

Figure 6.26 shows the Mo 3d spectra from the CoCrMo anodically polarized samples, where BSA-containing solutions formed a layer that tends to avoid the oxidation of molybdenum metal in the alloy, probably by decreasing

contact with H<sub>2</sub>O. In pure PBS solution, the surface exhibited mainly molybdenum oxidation states +4, a minor amount of Mo (0) and no Mo (+6).



**Figure 6.21** - XPS Co 2p spectra for Co in: (a) BSA, (b) PBS and (c) BSA+PBS after anodic polarization.

**Table 6.2** - Co 2p XPS quantification for elemental Co sample after anodic polarization in BSA, PBS and BSA+PBS. Co (+2) included oxides and hydroxides.

| Solution | Co (0) | Co (+2) | Co (+3) |
|----------|--------|---------|---------|
| BSA      | 0%     | 94%     | 6%      |
| PBS      | 4%     | 88%     | 8%      |
| BSA+PBS  | 0%     | 95%     | 5%      |

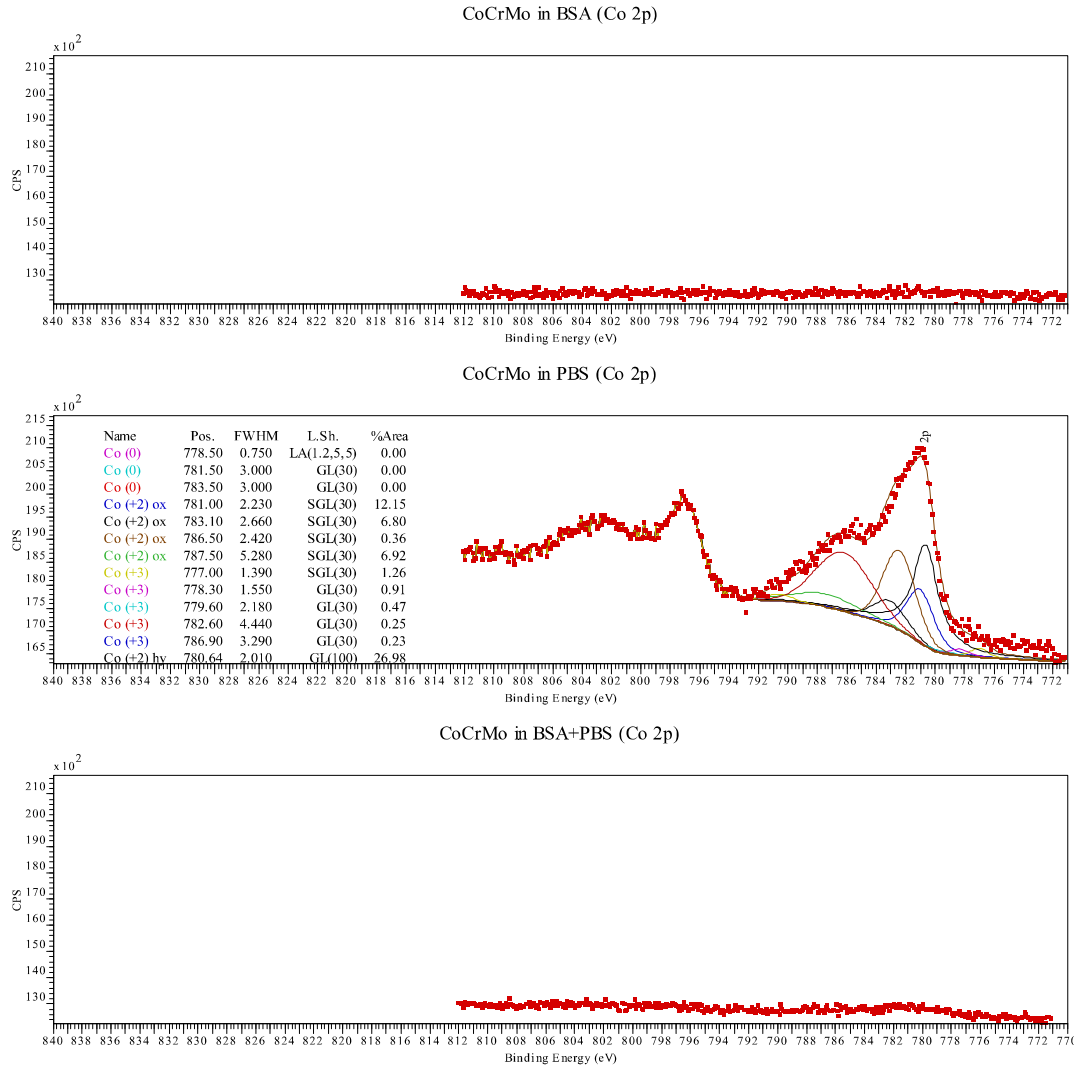


**Figure 6.22** - XPS Co 2p spectra for CoCrMo alloy in: (a) BSA, (b) PBS and (c) BSA+PBS after anodic polarization.

**Table 6.3** - Co 2p XPS quantification for CoCrMo alloy after anodic polarization in BSA, PBS and BSA+PBS.

| Solution | Co (0) | Co (+2) | Co (+3) |
|----------|--------|---------|---------|
| BSA      | 0%     | 0%      | 0%      |
| PBS      | 0%     | 97%     | 3%      |
| BSA+PBS  | 0%     | 0%      | 0%      |

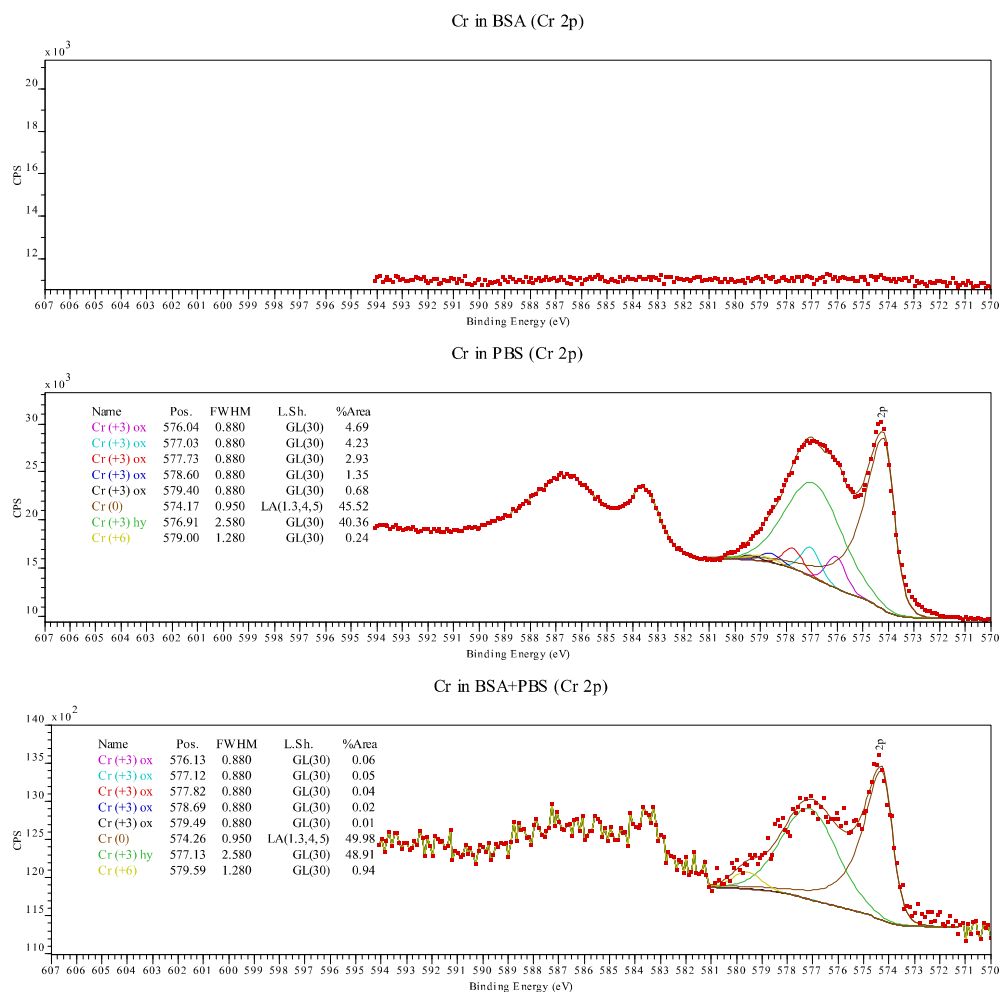


**Figure 6.23** - XPS Cr 2p spectra for elemental Cr in: (a) BSA, (b) PBS and (c) BSA+PBS after anodic polarization.

**Table 6.4** - Cr 2p XPS quantification for elemental Cr sample after anodic polarization in BSA, PBS and BSA+PBS.

| Solution | Cr (0) | Cr (+3) | Cr (+6) |
|----------|--------|---------|---------|
| BSA      | 0%     | 0%      | 0%      |
| PBS      | 46%    | 54%     | 0%      |
| BSA+PBS  | 50%    | 50%     | 0%      |

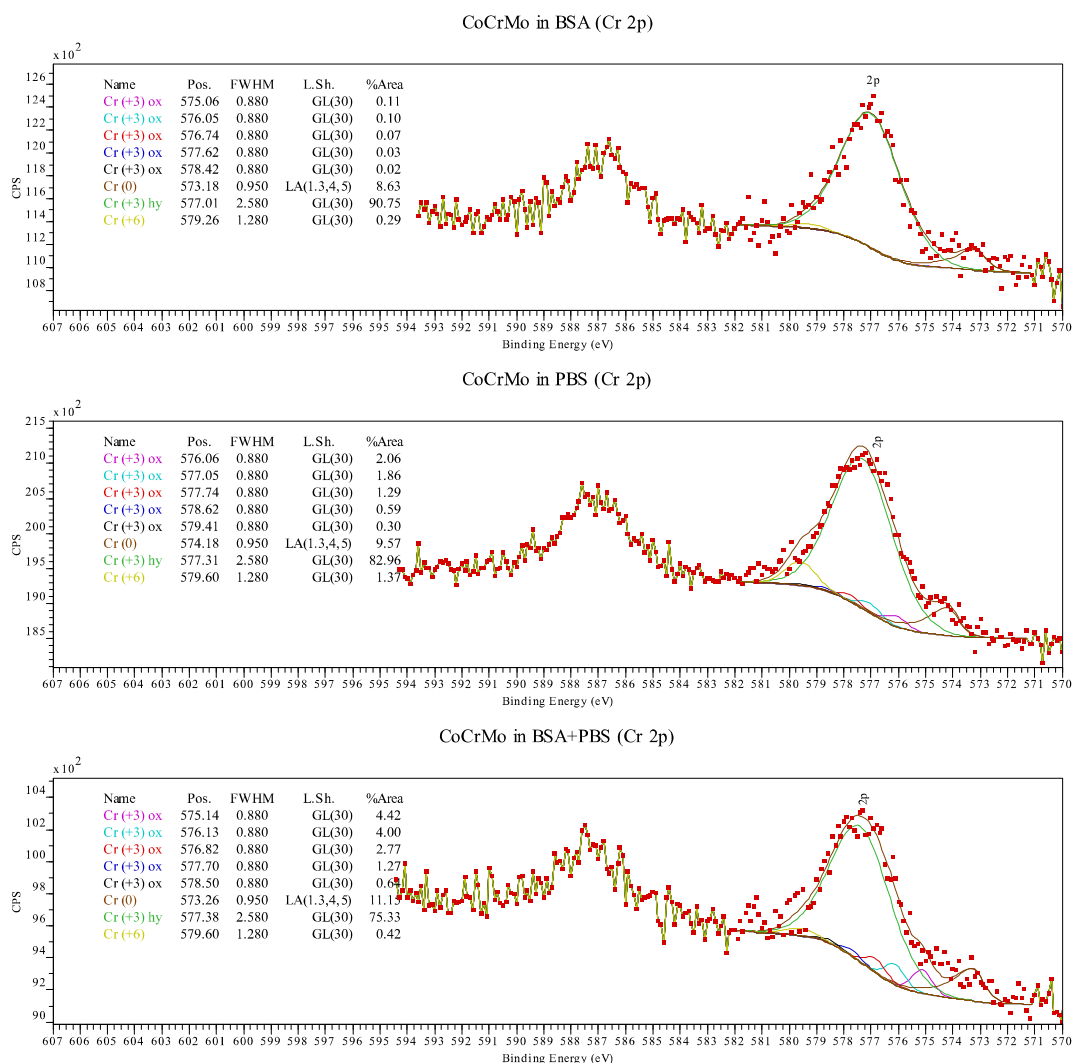


**Figure 6.24** - XPS Cr 2p spectra for CoCrMo alloy in: (a) BSA, (b) PBS and (c) BSA+PBS after anodic polarization.

**Table 6.5** - Cr 2p XPS quantification for CoCrMo alloy after anodic polarization in BSA, PBS and BSA+PBS.

| Solution | Cr (0) | Cr (+3) | Cr (+6) |
|----------|--------|---------|---------|
| BSA      | 9%     | 91%     | 0%      |
| PBS      | 10%    | 90%     | 0%      |
| BSA+PBS  | 11%    | 88%     | 0%      |

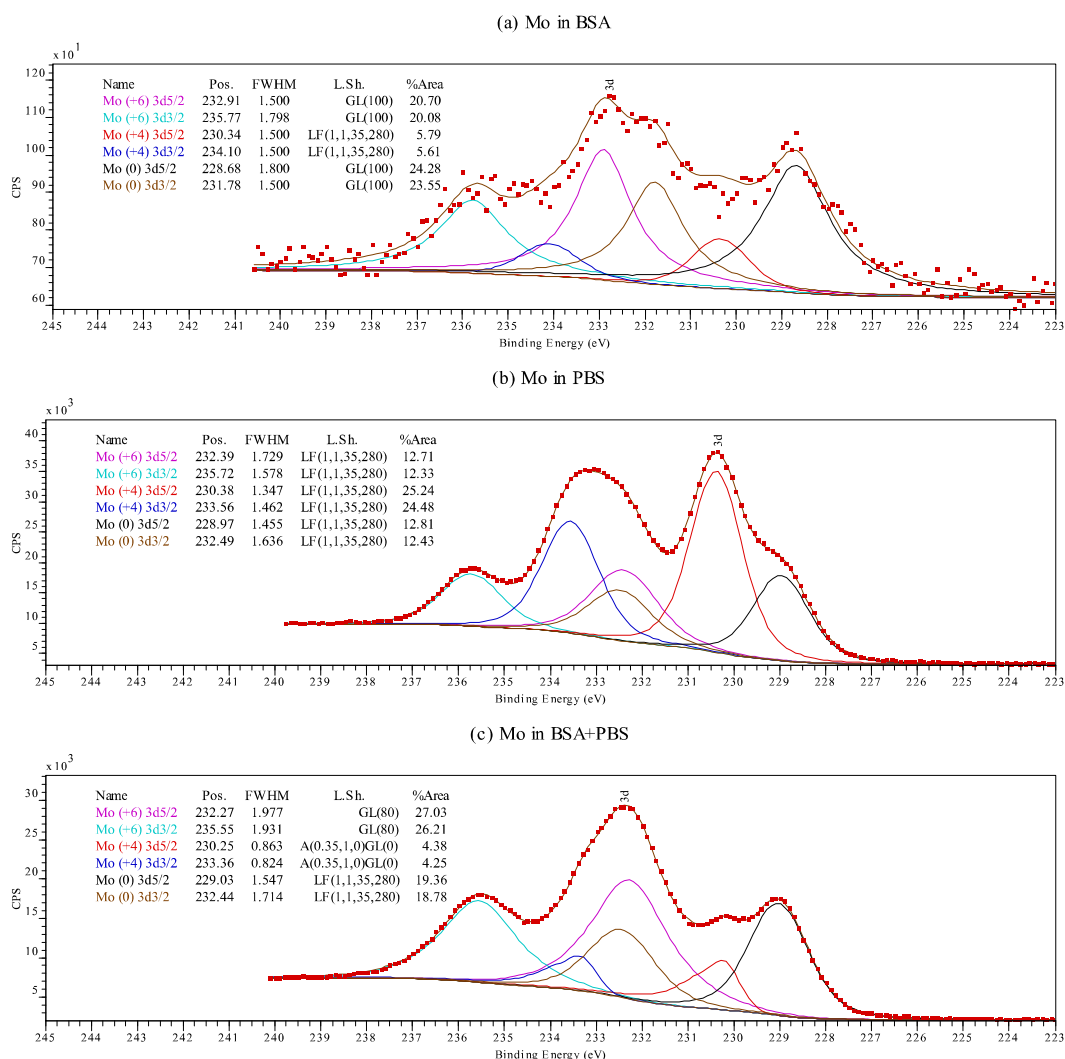


**Figure 6.25** - XPS Mo 3d spectra for elemental Mo in: (a) BSA, (b) PBS and (c) BSA+PBS after anodic polarization.

**Table 6.6** - Mo 3d XPS quantification for elemental Mo sample after anodic polarization in BSA, PBS and BSA+PBS.

| Solution | Mo (0) | Mo (+4) | Mo(+6) |
|----------|--------|---------|--------|
| BSA      | 48%    | 11%     | 41%    |
| PBS      | 25%    | 50%     | 25%    |
| BSA+PBS  | 38%    | 9%      | 53%    |

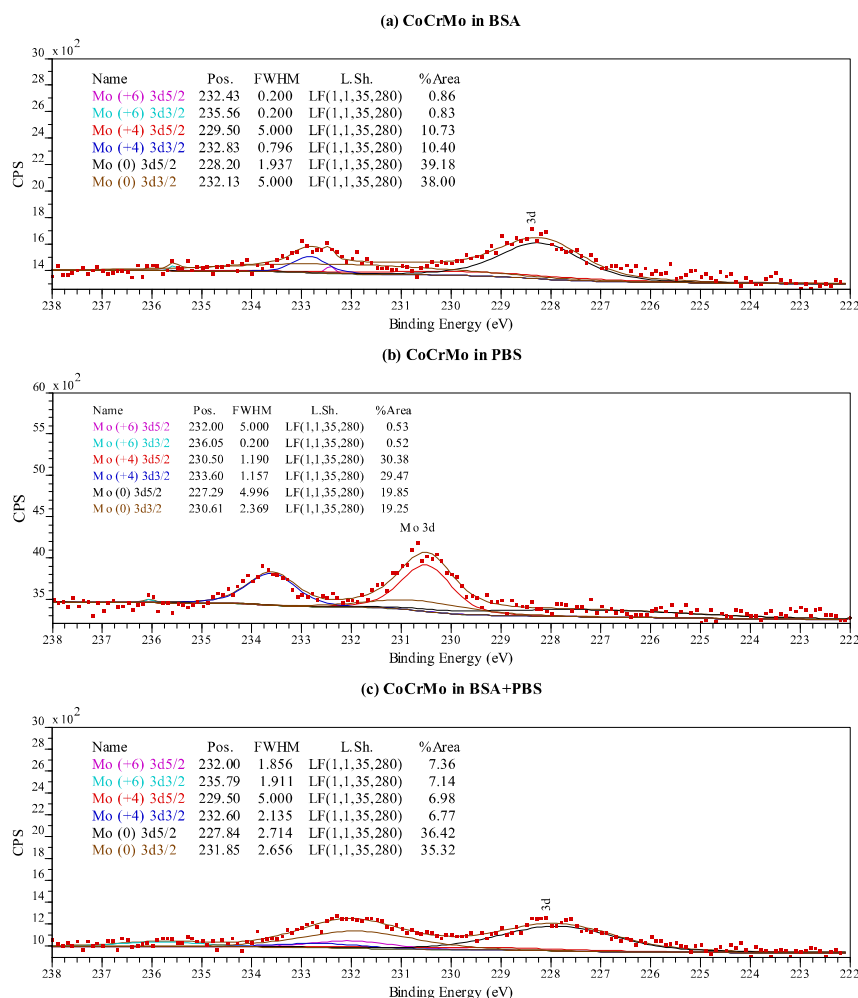


**Figure 6.26** - XPS Mo 3d spectra for CoCrMo alloy in: (a) BSA, (b) PBS and (c) BSA+PBS after anodic polarization.

**Table 6.7** - Mo 3d XPS quantification for CoCrMo alloy after anodic polarization in BSA, PBS and BSA+PBS.

| <i>Solution</i> | <i>Mo (0)</i> | <i>Mo (+4)</i> | <i>Mo(+6)</i> |
|-----------------|---------------|----------------|---------------|
| BSA             | 78%           | 22%            | 0%            |
| PBS             | 40%           | 60%            | 0%            |
| BSA+PBS         | 70%           | 14%            | 16%           |

In conclusion, XPS analysis indicates protein attachment to the metal surface to be less prominent in elemental Co samples. The amount of phosphate formed on the Co surface was low and the presence of BSA in the solution did not change significantly the result. The surface was shown to be covered by  $\text{Co}^{2+}$  in all of the solutions, however, fitting revealed the

predominance of hydroxides in PBS, whereas oxides were mainly found in the BSA solution.

Elemental Mo in BSA was shown to be mostly composed of Mo in the metallic form and  $\text{Mo}^{6+}$ , with a high deposition of proteins, which was shown to react with BSA possibly forming molybdenum-nitrogen bonds at the surface.

Cr and CoCrMo showed a similar behaviour. In pure PBS, both showed large deposition of phosphates on the surface, however, when BSA was present, the amount of phosphate decreased drastically. Also, the passivating oxide layer on CoCrMo and Cr was seen to be present in the  $\text{Cr}^{3+}$  oxidation state in all solutions.

CoCrMo only showed  $\text{Co}^{2+}$  and  $\text{Co}^{3+}$  in the presence of PBS, whereas no Co was detected in BSA and BSA+PBS. CoCrMo immersed in BSA-containing solution showed low Mo oxidation and the surface was formed mostly of Mo metal, however, in PBS significant  $\text{Mo}^{4+}$  was found.

## **6.5 Analysis of the Electrolyte Following Anodic Polarization**

### **6.5.1 - Inductively Coupled Plasma Mass Spectrometry**

Figure 6.27 shows the Co, Cr and Mo ionic release from the elemental reference materials into the electrolyte as measured by ICP-MS using the sample preparation protocol described in Section 5.1, with 30 kDa MWCO ultrafilters. For all elements, high dissolution was observed in the presence of PBS, whereas low dissolution occurred when the electrolyte used included BSA. The proteins appear to have acted as a biolayer, coating the metal surface and effectively reducing the contact of the metal with  $\text{H}_2\text{O}$  and dispersed ions. This biolayer may have partially blocked the migration of metallic ions into the solution, however it could also complex with preferential metal species. In BSA+PBS solutions, the proteins adsorbed on the surface may have not covered the entire area, leading to sites which were more susceptible to localized corrosion.

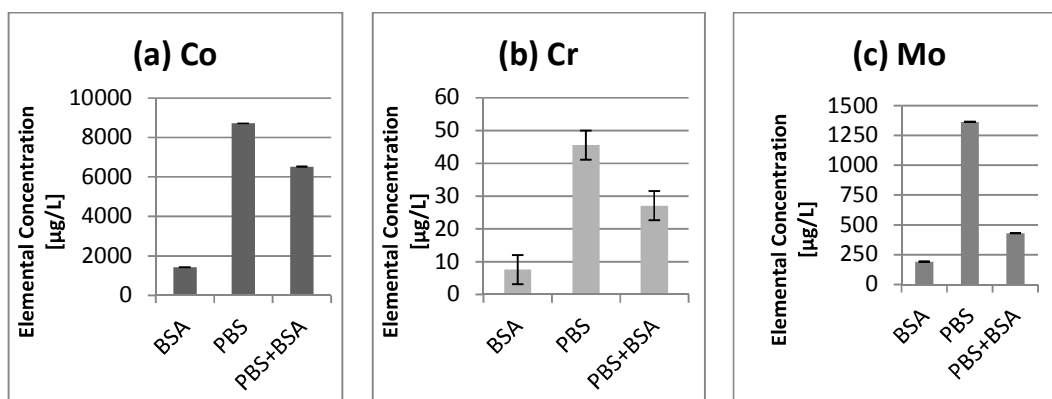


**Figure 6.27** - ICP-MS on (a) Co, (b) Cr and (c) Mo after anodic polarization of elemental reference materials.

In terms of absolute amounts, Co and Mo exhibited more ionic release than Cr (about 200x and 20x respectively). The relatively low Cr corrosion rate started to increase after disruption of the passivating layer in the transpassive region, where pits started to be formed [see Figure 6.5 (b) and Figure 6.10].

Figure 6.28 shows the ICP-MS measurement of ionic release from CoCrMo alloy after anodic polarization. The results shows some differences compared to the elemental metal reference samples (Figure 6.27). Co ionic release remained the highest in PBS and BSA+PBS solutions during the polarization tests. However, when BSA was added to the electrolyte, Co ions levels dropped to less than half. In addition, the presence of BSA in the solution increased the amount of Mo ions released and a selective preferential dissolution of Mo from the CoCrMo alloy was found in pure BSA.

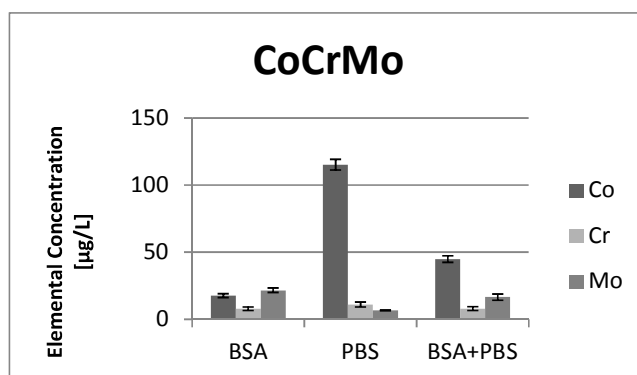
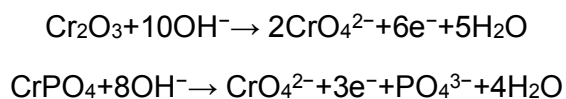


**Figure 6.28** - ICP-MS in different biological solutions following anodic polarization of CoCrMo low carbon alloy.

The dissolution behaviour of CoCrMo alloy after anodic polarization showed a similar trend to the particles studied in Chapter 5. In that, both Mo showed preferential release in the presence of BSA, while highly increased solubility of Co was evident in PBS-containing solution. In all situations, Cr shows no relevant significant amount of ionic release, unless the pH of the solution is altered to acidic conditions.

### 6.5.2 - Ultraviolet–visible Spectroscopy

UV-Vis analysis on the electrolyte following anodic polarization showed an absorption peak at around 370 nm indicating a possible transpassive dissolution of the Cr<sub>2</sub>O<sub>3</sub> layer on CoCrMo [Figure 6.29 (c)] and Cr [Figure 6.29 (f)] samples in PBS electrolyte via the formation of CrO<sub>4</sub><sup>2-</sup> [232]. Cr corrosion may be associated with transpassive dissolution of Cr<sub>2</sub>O<sub>3</sub>, and could increase in the presence of phosphates as described by Ouerd *et al.* (2008), where the concentration of CrO<sub>4</sub><sup>2-</sup> formed by the reaction in the solution depends on the amount of CrPO<sub>4</sub> formed during immersion of the alloy in PBS:



Anodic polarized Co and Mo samples presented no relevant data during UV-Vis spectral analysis, because the absorption peaks were only related to the biological media.

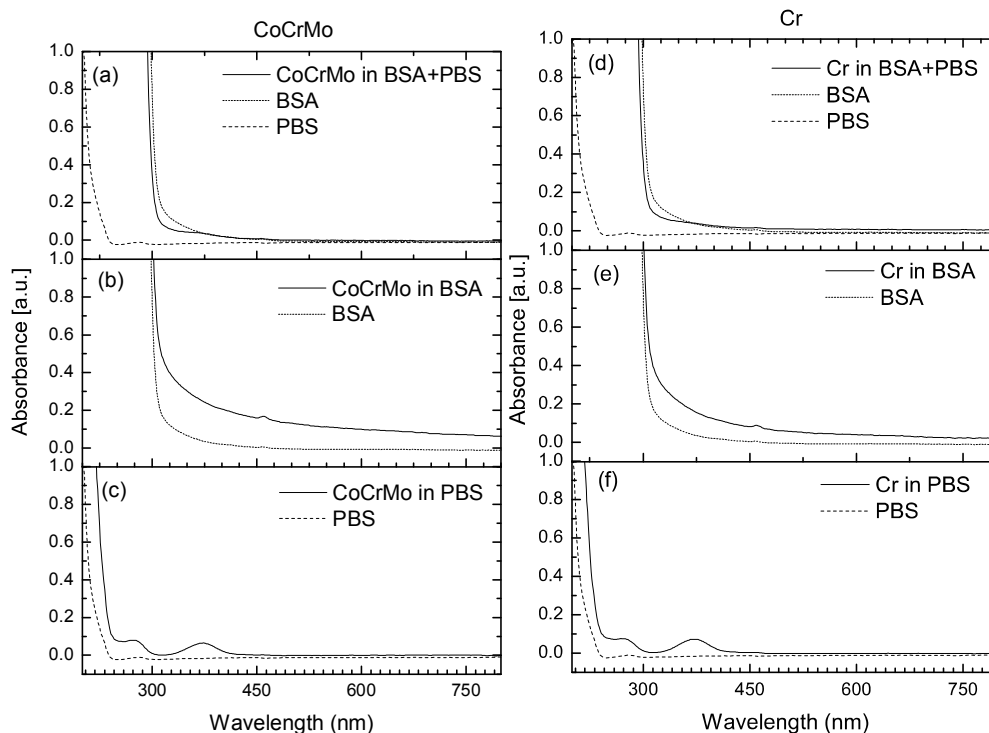


**Figure 6.29** - UV-VIS spectra of electrolyte following anodic polarization of CoCrMo and Cr samples in different biological media.

## 6.6 Discussion

Co metal surfaces after anodic polarization were found to be covered by a native passive film formed of cobalt(II) oxide and also hydroxide (Figure 6.21). This layer is generally stable in neutral alkaline solutions [212]. However, in the presence of PBS solution at 37°C, the integrity of the surface was highly affected by spontaneous active dissolution with an increase in the potential [Figure 6.5 (a)]. Metikos-Hukovic and Babic (2007) have shown that Co dissolution is significantly suppressed by alloying with Cr and Mo, which in this study showed a drop in the level of ionic release by a factor of 80x (Figure 6.27 and Figure 6.28). The biolayer formed by BSA on Co was shown to not be as thick as on Cr or Mo, however it protected the surface by decreasing the current density during anodic polarization (Table 6.1). The size of the pits in the presence of phosphate was found to be higher than in albumin, with a significant amount of Cl and Na found within the pits, probably as a result of an autocatalytic process (Figure 6.6 and Figure 6.9). The anodic reaction continues until intermetallic particles and corrosion products present in a pit

become suspended after the detachment of intermetallic particles from the pit. The corrosion products that contained Cl with intermetallic particles inside the pits highlighted the role of the chloride ion. The variations of anodic current density in PBS and BSA+PBS solutions showed that the chloride ion has a rate determining effect for anodic reactions (Table 6.1).

Cr and CoCrMo showed a similar behaviour during polarization that could be attributed to the passive chromium oxide layer dominating electrochemical reactions (Table 6.1 and Figure 6.5). PBS is known to improve the repassivation properties in steel alloys by limiting the acidity of the electrolyte to initiated pits [233]. However in both metals tested pitting dissolution occurred (Figure 6.10 and Figure 6.14), probably during transpassive dissolution of the  $\text{Cr}_2\text{O}_3$  oxide layer which formed soluble  $\text{CrO}_4^{2-}$ , which was evidenced by UV-vis (Figure 6.29). The breakdown of the passive film was associated with the presence of aggressive ions such as  $\text{Cl}^-$  and the growth of pitting depends on the change in pH of the solution. Cr in BSA was shown to delay the initiation of pitting by increasing the breakdown potential, but this was not observed in CoCrMo, which showed an identical breakdown potential (Table 6.1). Presumably, the presence of salts in PBS solutions (containing chlorides) in our experiments can attack and destroy the passive film more quickly than it can be repaired in a low oxygen environment. Not only CoCrMo and Cr, but also Co and Mo samples presented high metal dissolution according to ICP-MS.

The surface of Mo metal after anodic polarization in PBS showed severe degradation with high metal dissolution (Figure 6.11, Figure 6.12 and Figure 6.13). The surface was mainly composed of Mo(+4) oxidation state with some Mo(0) and negligible Mo (+6). The test in BSA containing-solution showed reduced dissolution and a different surface composition, which was richer in Mo (0) and Mo(+6). Martin *et al.* (2013) have suggested that Mo is essential for the formation of an organic film at the surface of Mo metal and CoCrMo alloys [56]. Mo metal oxidizes to Mo(+4), forming  $\text{MoO}_2$  according to the following spontaneous reaction with water above the potential ca.  $-0.8 E_{(\text{Ag}/\text{AgCl})}$ , pH 7.4 at 37°C and  $\text{MoO}_2$  then further oxidizes to Mo(+6):



This may indicate that during anodic polarization in PBS, Mo(6+) molybdate ions only partially remain on the surface, and are probably mostly released into solution consistent with the ICP-MS results (Figure 6.27 and Figure 6.28). However, in the presence of BSA, the Mo(+6) ions released are most likely to bond to the biolayer and are measured in a much lower quantity in the solution. XPS indicated the presence of Mo-N bonds at the surface of BSA solution sample (Figure 6.25), probably as a result of a secondary reaction between proteins and Mo ions.

CoCrMo anodic corrosion showed an interesting trend during corrosion in BSA solution, where preferential release of Mo occurred followed by Co (Figure 6.28). The species present at the surface was Mo(0), whereas in PBS it was Mo(+4). The biolayer may avoid further redox reactions in aqueous solutions creating a barrier, however Mo dissolution measured by ICP-MS may indicate the presence of another reaction between protein molecules and Mo metal that could also increase Mo dissolution. Espallargas *et al.* (2014) studied Mo dissolution during CoCrMo anodic polarization using PBS with 36 g/l albumin. Albumin was shown to drastically increase the Mo concentration in the electrolyte below the transpassive region of the alloy [150]. This implied that Mo was dissolving from the alloy even before high potentials could be applied.

Some researchers have found albumin acting as a cathodic inhibitor on CoCrMo and that it accelerates the anodic reaction in solution with and without phosphates [53,225]. These authors used 0.5 g/L of albumin diluted in the electrolyte (mostly composed of PBS) during their studies, which may not be a realistic approach in terms of the actual absolute amount of protein present *in-vivo*. Indeed, Brandt *et al.* (2010) have shown that for simulated synovial fluid the total protein constituents are measured at the levels of 15–25 g/L for healthy patients and  $31.8 \pm 1.9$  g/L to simulate patients with osteoarthritic hip diseases [132]. In addition, it is known that diseased joints can exhibit much higher protein concentrations in the range of 36–54 g/L [120].

## 6.7 Conclusion

The experimental technique used in this chapter involved anodic polarization of Co, Cr, Mo and CoCrMo alloy surfaces in the presence of BSA, PBS and BSA+PBS media. This creates electron depletion at the surface and hence a favourable environment for the adsorption of phosphate ions and albumin molecules. Thus, the BSA+PBS solution showed a competitive adsorption on the sample surfaces and influenced the electrochemical behaviour. In the presence of BSA SEM/EDX mainly showed the presence of a bilayer at the surface which was typically rich in carbon and nitrogen, supporting the hypothesis of an adsorbed protein bilayer.

The total metal ion release measured for elemental reference materials were much higher as compared to a CoCrMo alloy. Co and Mo samples showed active dissolution in all electrolyte solutions, whereas degradation of CoCrMo and Cr samples were controlled by a passivating oxide layer. The use of PBS accelerated the corrosion for all samples, increasing the metal ion concentration in the electrolyte and there was a high incidence and growth of pitting corrosion on Co samples. SEM images showed a clear difference in the pit morphology depending on the solution employed.

For electrochemical tests in the presence of BSA, at a realistic concentration, proteins were found to play an important role in Mo dissolution from CoCrMo. Mo presumably reacts with amino acid residues present in protein molecules, initiating preferential dissolution even at low potentials, where there is no disruption of the Cr passivation layer in CoCrMo alloys. Nevertheless, in order to understand the mechanism of Mo corrosion in proteins, it would be necessary to follow the dissolution state of the alloy over a range of different low potentials.

## Chapter 7 - Conclusions

The main aim of this research was to develop a method to produce significant amounts of representative synthetic CoCrMo wear debris. In this project, we have used the hitherto unexplored approach of mechanochemical milling to produce a large amount of mimetic CoCrMo wear debris nanoparticulates. In Chapter 4 it was demonstrated that this was a simple and efficient method to generate synthetic nanoparticles similar in size and shape to CoCrMo wear debris from hip implants observed in-vivo. A wide range of particle sizes were obtained by milling and these can then be size-separated by centrifugation, which also helps to remove trace levels of contamination from the milling process. The composition of synthetic wear debris was found to be close to real wear debris and similar to the raw starting material. This process was compared to the pin-on-plate technique, which takes a long time to generate much fewer particles, most of which were in a size range larger than that commonly found in-vivo (ca. 30 nm). The particle concentration generated for one milling run (about 2 h) was estimated to be equivalent to about 20 years of metal nanoparticles generated in vivo, assuming all hip wear debris remains in the joint.

The relatively large scale production of CoCrMo nanoparticles allowed corrosion studies to be undertaken in Chapter 5 as well as an investigation of protein binding properties in relevant media. However, dissolution studies are often based on solution spectrometry (mass or optical) that require the removal of all particles from tested solutions in order to avoid distortions in the final results. Nanoparticles produced by milling could easily be ionized during ICP analysis, if not correctly separated from the solution. The commonly reported and established techniques for separating nanoscale wear debris from lubricant fluids using only centrifugation or ultracentrifugation, and these processes were found to be sub-optimal not only for milled fluids but also to hip simulation, leading to residual wear nanoparticles suspended in the analyte fluid. The use of a centrifugation plus ultrafiltration step during ICP-MS sample preparation was shown to efficiently remove nanoparticulate wear debris that remained in the supernatant after just centrifugal sedimentation, by creating a physical barrier that efficiently retains all remaining particulates in the membrane. The addition of the ultrafiltration step in ICP-MS sample preparation after

tribocorrosion of CoCrMo alloys using a hip simulator decreased the overall level of metal ions by about 6 times compared to centrifugation alone and about 2 times when compared to ultracentrifugation alone. Importantly, there was observed to be a significant change in the relative elemental ratios in the solution (from the base alloy composition) following ultrafiltration, suggesting much higher levels of Mo (and to a lesser extent Co) dissolution together with a very low release of Cr during the walking cycle simulation. This two steps ICP-MS sample preparation is essential for the correct estimation of chemical/ electrochemical hip degradation under biotribocorrosion simulations.

This revised ICP-MS sample preparation method was employed after the production of CoCrMo nanoparticles by milling and allowed the identification of the dissolution of specific metallic elements in different biological media and pH environments. The corrosion studies in different media have revealed the preferential dissolution of Mo in the presence of serum proteins, and that, based on the pH dependence, it is likely that more significant Co and Cr solubility will only occur if particles are taken up by phagocytic cells and digested in lysosomes.

In Chapter 6, TEM analysis suggested the formation of a protein corona on synthetic CoCrMo wear debris particles incubated with BSA and the particles were found to be deficient in molybdenum by EDX presumably as a result of dissolution. An interaction with proteins was also seen for elemental reference oxide materials where ICP-MS showed that the reference materials underwent dissolution of predominantly molybdenum ions under static incubation in the presence of BSA. During zeta potential titration, CoCrMo and Molybdenum nanoparticles showed the highest affinity for BSA. The results provided a good indication of the importance of binding between albumin proteins and molybdenum, which may directly influence the strong dissolution of this element when CoCrMo alloy nanoparticles are produced as hip-implant wear debris *in vivo* in the presence of serum proteins. These findings are important as it highlighted the interaction of Mo rich surfaces with amide groups in serum which could modify biological molecules, altering their ability to function properly.

The compositional analysis of the surfaces (by XPS) of Co, Cr and Mo reference materials as well as a CoCrMo alloy following anodic polarization in

the presence of biological media showed the presence of a biolayer which was typically rich in carbon and nitrogen, supporting the hypothesis of an adsorbed protein layer seen in the nanoparticulate debris by TEM. BSA and PBS solutions showed competitive absorption of proteins and salts on the sample surface and this influenced the ultimate electrochemical behaviour. The total metal ion release measured for elemental reference materials was much higher as compared to a CoCrMo alloy. Co and Mo samples showed active dissolution in all electrolyte solutions, whereas the degradation of CoCrMo and Cr samples were controlled by a passivating oxide layer. The use of PBS accelerated the corrosion for all samples increasing the metal ion concentration in the electrolyte and there was a high incidence and growth of pitting corrosion on Co samples. SEM images showed a clear difference in the pit morphology depending on the solution employed.

For electrochemical tests in the presence of BSA, at a realistic serum concentration, proteins were found to play an important role in Mo dissolution from CoCrMo. Mo was thought to react with amino acid residues present in protein molecules, initiating preferential dissolution even at low potentials, where there is no disruption of the Cr passivation layer in CoCrMo alloys.

In summary, this study has highlighted some important findings with respect to:

- An alternative method to produce CoCrMo nanoparticulate wear debris in significant quantities;
- The development of an accurate sample preparation method prior to ICP-MS analysis, which can improve the quantification of tribocorrosion studies by attributing correctly the contribution of chemical degradation in failing hip implants;
- The high levels of Mo dissolution in CoCrMo alloy that have only recently been reported in literature, and that was linked in this work with the high affinity of this metal for residues of the proteins found in serum albumin;
- The formation of a metal complex between proteins and the metal ions released during tribocorrosion of micro-sized particles.

## 7.1 Limitations of this Study and Future Work

Despite the interesting results obtained, there are still a number of limitations or future work that needs to be addressed:

- After milling, centrifugal sedimentation of large particles effectively removed most of the Zr contamination, reducing it to trace levels. Ideally, the use of a vial/ balls made of the CoCrMo material would avoid any contamination of this nature, but may compromise the size reduction. Further tests using CoCrMo beads in combination with a Zr vial could in theory produce good results in terms of size reduction and contamination, potentially avoiding the centrifugation process. In addition, the use of a planetary ball mill could produce even larger amounts of nanoparticles in less time, by increasing the frictional forces during the process.
- The study suggested the formation of complexes between the metal ion and BSA proteins, however further investigation is required to identify the exact nature of the complex. Indeed, it is important to confirm the possibility of molybdenum carbonyl formation during CoCrMo hip implant wear, owing to the high toxicity of these species.
- This study focused on the interaction of metal particles with albumin serum, isolating the response for this specific protein. Albumin represent about 70% of total proteins present in the synovial fluid. Hence it would be interesting to study the synergistic effect of all the proteins during CoCrMo tribocorrosion.
- In order to understand the mechanism of CoCrMo alloy corrosion in the presence of proteins under anodic polarization, it would be necessary to follow the dissolution state of the alloy over a range of different low potentials.

- In a separate line of collaborative research, toxicological studies are currently being conducted to examine the toxicity and oxidative stress response toward the nano- and micro-sized milled CoCrMo particles produced in this research (see Appendix A). The hypothesis of this study was that nano- and micro-CoCrMo particles exert a cell-specific, time and dose-dependent toxicity and oxidative stress response in lung epithelial cells, osteoblasts and macrophages. So far, it was found that both nano- and micro-CoCrMo particles induced a time and dose-dependent toxicity in all three types of cells studied. At the same mass dose, nano-CoCrMo significantly reduced the viability of macrophages as compared to micro-particles and significantly improved the viability of lung epithelial cells and osteoblasts. This work is ongoing.

## References

- [1] H. Gray, *Gray's Anatomy of the Human Body*, (1918). <http://www.bartleby.com/107/>.
- [2] R.C. Lawrence, D.T. Felson, C.G. Helmick, L.M. Arnold, H. Choi, R.A. Deyo, et al., Estimates of the prevalence of arthritis and other rheumatic conditions in the United States. Part II., *Arthritis Rheum.* 58 (2008) 26–35. doi:10.1002/art.23176.
- [3] G.M. Swash M., *Hutchison's Clinical Methods*, Saunders Elsevier. (2007).
- [4] S. Pramanik, A.K. Agarwal, K. Rai, Chronology of Total Hip Joint Replacement and Materials Development, *Trends Biomater. Artif. Organs.* 19 (2005). <http://www.biomaterials.org.in/ojs/index.php/tibao/article/view/274> (accessed November 16, 2015).
- [5] C. Knight, The 1970s – A joint revolution, *J. Orthop. Nurs.* 13 (2009) 24–28. doi:10.1016/j.joon.2008.11.006.
- [6] NJR, PUBLIC AND PATIENT GUIDE TO THE NJR'S 11TH ANNUAL REPORT 2014, 2014. [www.njrcentre.org.uk](http://www.njrcentre.org.uk).
- [7] NJR, National Joint Registry for England and Wales 8th Annual Report, 2011. doi:ISSN 1745-1450.
- [8] A.J. Smith, P. Dieppe, K. Vernon, M. Porter, A.W. Blom, Failure rates of stemmed metal-on-metal hip replacements: analysis of data from the National Joint Registry of England and Wales, *Lancet.* 379 (2012) 1199–1204. doi:10.1016/S0140-6736(12)60353-5.
- [9] J.L. Howard, H.M. Kremers, Y.A. Loechler, C.D. Schleck, W.S. Harmsen, D.J. Berry, et al., Comparative Survival of Uncemented Acetabular Components Following Primary Total Hip Arthroplasty, *J. Bone Jt. Surg.* 93 (2011) 1597–1604. doi:10.2106/jbjs.j.00195.
- [10] A.S. Greenwald, J.P. Garino, Alternative bearing surfaces: the good, the bad, and the ugly., *J. Bone Joint Surg. Am.* 83-A Suppl (2001) 68–72. <http://www.ncbi.nlm.nih.gov/pubmed/11712837> (accessed April 23, 2015).

- [11] I.C. Clarke, M. Manaka, D.D. Green, P. Williams, G. Pezzotti, Y.-H. Kim, et al., Current status of zirconia used in total hip implants., *J. Bone Joint Surg. Am.* 85-A Suppl (2003) 73–84. [http://jbjs.org/content/85/suppl\\_4/73.abstract](http://jbjs.org/content/85/suppl_4/73.abstract) (accessed September 17, 2015).
- [12] S.R. Simon, *Orthopaedic Basic Science*, American Academy of Orthopaedic, 1994.
- [13] J. Walczak, F. Shahgaldi, F. Heatley, In vivo corrosion of 316L stainless-steel hip implants: morphology and elemental compositions of corrosion products., *Biomaterials.* 19 (1998) 229–37. <http://www.ncbi.nlm.nih.gov/pubmed/9678872> (accessed May 8, 2015).
- [14] T.P. Schmalzried, P.C. Peters, B.T. Maurer, C.R. Bragdon, W.H. Harris, Long-duration metal-on-metal total hip arthroplasties with low wear of the articulating surfaces., *J. Arthroplasty.* 11 (1996) 322–31. <http://www.ncbi.nlm.nih.gov/pubmed/8713913> (accessed May 6, 2015).
- [15] D. Dowson, C. Hardaker, M. Flett, G.H. Isaac, A hip joint simulator study of the performance of metal-on-metal joints: Part I: The role of materials, *J. Arthroplasty.* 19 (2004) 118–123. doi:10.1016/j.arth.2004.09.015.
- [16] A.J. Smith, P. Dieppe, P.W. Howard, A.W. Blom, Failure rates of metal-on-metal hip resurfacings: analysis of data from the National Joint Registry for England and Wales, *Lancet.* 380 (2012) 1759–1766. doi:10.1016/S0140-6736(12)60989-1.
- [17] D.J. Langton, R. Sidaginamale, J.K. Lord, A.V.F. Nargol, T.J. Joyce, Taper junction failure in large-diameter metal-on-metal bearings., *Bone Joint Res.* 1 (2012) 56–63. doi:10.1302/2046-3758.14.2000047.
- [18] A.E. Goode, J.M. Perkins, A. Sandison, C. Karunakaran, H. Cheng, D. Wall, et al., Chemical speciation of nanoparticles surrounding metal-on-metal hips., *Chem. Commun. (Camb).* 48 (2012) 8335–7. doi:10.1039/c2cc33016d.
- [19] M.B. Ward, A.P. Brown, A. Cox, A. Curry, J. Denton, Microscopical analysis of synovial fluid wear debris from failing CoCr hip prostheses, *J. Phys. Conf. Ser.* 241 (2010) 012022. doi:10.1088/1742-6596/241/1/012022.
- [20] H. G. Willert, G. H. Buchhorn, A. Fayyazi, R. Flury, M. Windler, G. Koster, et al., Metal-on-Metal Bearings and Hypersensitivity in Patients with Artificial Hip Joints. A Clinical and Histomorphological Study, *J. Bone Jt. Surg.* 87 (2005) 8.

doi:10.2106/JBJS.A.02039pp.

- [21] I. Catelas, J.B. Medley, P. a Campbell, O.L. Huk, J.D. Bobyn, Comparison of in vitro with in vivo characteristics of wear particles from metal-metal hip implants., *J. Biomed. Mater. Res. B. Appl. Biomater.* 70 (2004) 167–78. doi:10.1002/jbm.b.20036.
- [22] C. Brown, S. Williams, J.L. Tipper, J. Fisher, E. Ingham, Characterisation of wear particles produced by metal on metal and ceramic on metal hip prostheses under standard and microseparation simulation., *J. Mater. Sci. Mater. Med.* 18 (2007) 819–27. doi:10.1007/s10856-006-0015-z.
- [23] J.A. Williams, Wear and wear particles—some fundamentals, *Tribol. Int.* 38 (2005) 863–870. doi:10.1016/j.triboint.2005.03.007.
- [24] Y. Yan, A. Neville, D. Dowson, Understanding the role of corrosion in the degradation of metal-on-metal implants., *Proc. Inst. Mech. Eng. H.* 220 (2006) 173–181. doi:10.1243/095441105X63246.
- [25] I. Catelas, A. Petit, D.J. Zukor, J. Antoniou, O.L. Huk, TNF-alpha secretion and macrophage mortality induced by cobalt and chromium ions in vitro - Qualitative analysis of apoptosis, *Biomaterials.* 24 (2003) 383–391. doi:10.1016/S0142-9612(02)00351-4.
- [26] K. Magone, D. Luckenbill, T. Goswami, Metal ions as inflammatory initiators of osteolysis, *Arch. Orthop. Trauma Surg.* 135 (2015) 683–95. doi:10.1007/s00402-015-2196-8.
- [27] A. Massè, M. Bosetti, C. Buratti, O. Visentin, D. Bergadano, M. Cannas, Ion release and chromosomal damage from total hip prostheses with metal-on-metal articulation., *J. Biomed. Mater. Res. B. Appl. Biomater.* 67 (2003) 750–7. doi:10.1002/jbm.b.10070.
- [28] J.H. Dumbleton, M.T. Manley, Metal-on-Metal Total Hip Replacement, *J. Arthroplasty.* 20 (2005) 174–188. doi:10.1016/j.arth.2004.08.011.
- [29] M.C. Rizzetti, P. Liberini, G. Zarattini, S. Catalani, U. Pazzaglia, P. Apostoli, et al., Loss of sight and sound. Could it be the hip?, *Lancet.* 373 (2009) 1052. doi:10.1016/S0140-6736(09)60490-6.
- [30] D. Cohen, How safe are metal-on-metal hip implants?, *Br. Med. J.* 344 (2012) e1410–e1410. doi:10.1136/bmj.e1410.

- [31] J. Hesketh, Q. Meng, D. Dowson, A. Neville, Biotribocorrosion of metal-on-metal hip replacements: How surface degradation can influence metal ion formation, *Tribol. Int.* 65 (2013) 128–137. doi:10.1016/j.triboint.2013.02.025.
- [32] B. Alemón, M. Flores, W. Ramírez, J.C. Huegel, E. Broitman, Tribocorrosion behavior and ions release of CoCrMo alloy coated with a TiAlVCN/CNx multilayer in simulated body fluid plus bovine serum albumin, *Tribol. Int.* 81 (2015) 159–168. doi:10.1016/j.triboint.2014.08.011.
- [33] Y. Yan, A. Neville, D. Dowson, S. Williams, Tribocorrosion in implants-assessing high carbon and low carbon Co-Cr-Mo alloys by in situ electrochemical measurements, *Tribol. Int.* 39 (2006) 1509–1517. doi:10.1016/j.triboint.2006.01.016.
- [34] S.S. Jakobsen, CoCrMo Alloy in vitro and in vivo studies, University of Aarhus, 2008.
- [35] P.J. Firkins, J.L. Tipper, M.R. Saadatzadeh, E. Ingham, M.H. Stone, R. Farrar, et al., Quantitative analysis of wear and wear debris from metal-on-metal hip prostheses tested In a physiological hip joint simulator, *Biomed. Mater. Eng.* 11 (2001) 143–157. <Go to ISI>://WOS:000168645300007.
- [36] A.A. Goldsmith, D. Dowson, Development of a ten-station, multi-axis hip joint simulator., *Proc. Inst. Mech. Eng. H.* 213 (1999) 311–6. <http://www.ncbi.nlm.nih.gov/pubmed/10466362> (accessed May 5, 2015).
- [37] Y. Yan, D. Dowson, A. Neville, In-situ electrochemical study of interaction of tribology and corrosion in artificial hip prosthesis simulators., *J. Mech. Behav. Biomed. Mater.* 18 (2013) 191–9. doi:10.1016/j.jmbbm.2012.08.009.
- [38] Y. Yan, A. Neville, D. Dowson, S. Williams, J. Fisher, Effect of metallic nanoparticles on the biotribocorrosion behaviour of Metal-on-Metal hip prostheses, *Wear.* 267 (2009) 683–688. doi:10.1016/j.wear.2008.12.110.
- [39] J. Gallagher, Metal-on-metal hip replacements “high failure rate,” *Heal. Sci.* (2012). <http://www.bbc.co.uk/news/health-17337993>.
- [40] O.R. Network, Orthopedic Network News, (2011). <http://recon.orthopedicnetworknews.com>.

- [41] a G. Cobb, T.P. Schmalzreid, The clinical significance of metal ion release from cobalt-chromium metal-on-metal hip joint arthroplasty, *Proc. Inst. Mech. Eng. Part H J. Eng. Med.* 220 (2006) 385–398. doi:10.1243/09544119JEIM78.
- [42] I.D. Learmonth, C.P. Case, Metallic debris from orthopaedics implants, *Lancet.* 369 (2007) 4.
- [43] Abul K. Abbas, Andrew H. Lichtman, S. Pillai, *Cellular and Molecular Immunology*, 7th ed., Saunders, 2011.
- [44] P. Roach, D. Eglin, K. Rohde, P. CC, Modern biomaterials: a review-bulk properties and implications of surface modifications, *J. Mater. Sci. - Mater. Med.* 18 (2007) 14.
- [45] Kao WJ, Hubbell JA, A. JM, Protein-mediated macrophage adhesion and activation on biomaterials: a model for modulating cell behavior, *J. Mater. Sci. - Mater. Med.* 10 (1999) 4.
- [46] Ziats NP, Miller KM, In vitro and in vivo interactions of cells with biomaterials, *Biomaterials.* 9 (1999) 8.
- [47] Bi Y, Collier TO, Goldberg VM, Anderson JM, Adherent endotoxin mediates biological responses of titanium particles without stimulating their phagocytosis, *J. Orthop. Res.* 20 (1988) 7.
- [48] Fritz EA, Glant TT, Vermes C, Jacobs JJ, Chemokine gene activation in human bone marrow-derived osteoblasts following exposure to particulate wear debris, *J. Biomed. Mater. Res.* 77 (2006) 9.
- [49] K. Rajamäki, T. Nordström, K. Nurmi, K.E.O. Åkerman, P.T. Kovanen, K. Öörni, et al., Extracellular acidosis is a novel danger signal alerting innate immunity via the NLRP3 inflammasome., *J. Biol. Chem.* 288 (2013) 13410–9. doi:10.1074/jbc.M112.426254.
- [50] S.S. Jakobsen, A. Larsen, M. Stoltenberg, J.M. Bruun, K. Soballe, Effects of as-cast and wrought cobalt-chrome-molybdenum and titanium-aluminium-vanadium alloys on cytokine gene expression and protein secretion in j774a.1 macrophages, *Eur. Cells Mater.* 14 (2007) 10.
- [51] J. Black, G. Hastings, *Handbook of Biomaterial Properties*, Chapman&Hall, London, 1998.

- [52] A. Carek, J.Z. Babic, Z. Schauperl, T. Badel, Mechanical Properties of Co-Cr Alloys for Metal Base Framework, *Int. J. Prosthodont. Restor. Dent.* 1 (2011) 13–19.
- [53] C. Valero Vidal, A. Igual Muñoz, Electrochemical characterisation of biomedical alloys for surgical implants in simulated body fluids, *Corros. Sci.* 50 (2008) 1954–1961. doi:10.1016/j.corsci.2008.04.002.
- [54] E. Bettini, T. Eriksson, M. Boström, C. Leygraf, J. Pan, Influence of metal carbides on dissolution behavior of biomedical CoCrMo alloy: SEM, TEM and AFM studies, *Electrochim. Acta.* 56 (2011) 9413–9419. doi:10.1016/j.electacta.2011.08.028.
- [55] I. Milošev, H.-H. Strehblow, The composition of the surface passive film formed on CoCrMo alloy in simulated physiological solution, *Electrochim. Acta.* 48 (2003) 2767–2774. doi:10.1016/S0013-4686(03)00396-7.
- [56] E.J. Martin, R. Pourzal, M.T. Mathew, K.R. Shull, Dominant role of molybdenum in the electrochemical deposition of biological macromolecules on metallic surfaces., *Langmuir.* 29 (2013) 4813–22. doi:10.1021/la304046q.
- [57] ASTM, Standard Specification for Cobalt-28 Chromium-6 Molybdenum Alloy Castings and Casting Alloy for Surgical Implants (UNS R30075), F 75, 2002.
- [58] J. Alvarado, R. Maldonado, J. Marxuach, R. Otero, Biomechanics of hip and knee prostheses 1, (2003) 1–20.
- [59] W.D. Callister, *Materials Science and Engineering, An Introduction*, 2007.
- [60] Nolan FJ, Farrar R, Schmidt MB, Phillips H, T. JK, Effect of head size and diametrical clearance on wear production of a new metal-on-metal hip prosthesis, in: 42th Annu. Meet. Orthop. Res. Soc., 1997.
- [61] I. Timmerman, H. Amstutz, *Metal-on-Metal Articulation and Wear: frequently asked questions*, 2005.
- [62] J. Cawley, J.E.P. Metcalf, A.H. Jones, T.J. Band, D.S. Skupien, A tribological study of cobalt chromium molybdenum alloys used in metal-on-metal resurfacing hip arthroplasty, *Wear.* 255 (2003) 999–1006. doi:10.1016/S0043-1648(03)00046-2.
- [63] R. Liu, M.X. Yao, P.C. Patnaik, X. Wu, Effects of Heat Treatment on Mechanical

and Tribological Properties of Cobalt-Base Tribaloy Alloys, *J. Mater. Eng. Perform.* 14 (2005) 634–640. doi:10.1361/105994905X64567.

- [64] K.P. Gupta, The Co-Cr-Mo (Cobalt-Chromium-Molybdenum) System, *J. Phase Equilibria Diffus.* 26 (2005) 87–92. doi:10.1007/s11669-005-0071-y.
- [65] R. Turrubiates-Estrada, A. Salinas-Rodriguez, H.F. Lopez, FCC to HCP transformation kinetics in a Co–27Cr–5Mo–0.23C alloy, *J. Mater. Sci.* 46 (2010) 254–262. doi:10.1007/s10853-010-4969-3.
- [66] A. Mani, H.F. Lopez, Deformation induced FCC to HCP transformation in a Co–27Cr–5Mo–0.05C alloy, *Mater. Sci. Eng. A.* 528 (2011) 3037–3043. doi:10.1016/j.msea.2010.12.024.
- [67] R. Pourzal, R. Theissmann, M. Morlock, A. Fischer, Micro-structural alterations within different areas of articulating surfaces of a metal-on-metal hip resurfacing system, *Wear.* 267 (2009) 689–694. doi:10.1016/j.wear.2009.01.012.
- [68] J. Hesketh, X. Hu, Y. Yan, D. Dowson, A. Neville, Biotribocorrosion: Some electrochemical observations from an instrumented hip joint simulator, *Tribol. Int.* 59 (2013) 332–338. doi:10.1016/j.triboint.2012.05.028.
- [69] S.-H. Lee, N. Nomura, A. Chiba, Significant Improvement in Mechanical Properties of Biomedical Co-Cr-Mo Alloys with Combination of N Addition and Cr-Enrichment, *Mater. Trans.* 49 (2008) 260–264. doi:10.2320/matertrans.MRA2007220.
- [70] I.D. Learmonth, C. Young, C. Rorabeck, The operation of the century: total hip replacement., *Lancet.* 370 (2007) 1508–19. doi:10.1016/S0140-6736(07)60457-7.
- [71] P.M. Pellicci, E.A. Salvati, H.J. Robinson, Mechanical failures in total hip replacement requiring reoperation., *J. Bone Joint Surg. Am.* 61 (1979) 28–36. <http://www.ncbi.nlm.nih.gov/pubmed/759432> (accessed September 21, 2015).
- [72] D.H. Nawabi, N.A. Nassif, H.T. Do, K. Stoner, M. Elpers, E.P. Su, et al., What causes unexplained pain in patients with metal-on metal hip devices? A retrieval, histologic, and imaging analysis., *Clin. Orthop. Relat. Res.* 472 (2014) 543–54. doi:10.1007/s11999-013-3199-9.
- [73] A.J. Hart, S.A. Sabah, A.S. Bandi, P. Maggiore, P. Tarassoli, B. Sampson, et al.,

- Sensitivity and specificity of blood cobalt and chromium metal ions for predicting failure of metal-on-metal hip replacement., *J. Bone Joint Surg. Br.* 93 (2011) 1308–13. doi:10.1302/0301-620X.93B10.26249.
- [74] S.J. MacDonald, W. Brodner, J.J. Jacobs, A consensus paper on metal ions in metal-on-metal hip arthroplasties, *J. Arthroplasty.* 19 (2004) 12–16. doi:10.1016/j.arth.2004.09.009.
- [75] The London Implant Retrieval Centre, Measurement of Wear of Explanted Hip Joints, <http://www3.imperial.ac.uk/tribology/projects/currentprojects/measurementofwearofexplantedhipjoints>. (2015).
- [76] J. Appleby, E. Poteliakhoff, K. Shah, N. Devlin, Using patient-reported outcome measures to estimate cost-effectiveness of hip replacements in English hospitals., *J. R. Soc. Med.* 106 (2013) 323–31. doi:10.1177/0141076813489678.
- [77] Y. Yan, A. Neville, J. Hesketh, D. Dowson, Real-time corrosion measurements to assess biotribocorrosion mechanisms with a hip simulator, *Tribol. Int.* 63 (2013) 115–122. doi:10.1016/j.triboint.2012.08.006.
- [78] P. Ponthiaux, R. Bayon, F. Wenger, J.-P. Celis, *Bio-Tribocorrosion in Biomaterials and Medical Implants*, Elsevier, 2013. doi:10.1533/9780857098603.3.372.
- [79] M.T. Mathew, J.J. Jacobs, M.A. Wimmer, Wear-corrosion synergism in a CoCrMo hip bearing alloy is influenced by proteins., *Clin. Orthop. Relat. Res.* 470 (2012) 3109–17. doi:10.1007/s11999-012-2563-5.
- [80] A.H. Hosman, H.C. van der Mei, S.K. Bulstra, H.J. Busscher, D. Neut, Effects of metal-on-metal wear on the host immune system and infection in hip arthroplasty., *Acta Orthop.* 81 (2010) 526–34. doi:10.3109/17453674.2010.519169.
- [81] P. Damm, F. Graichen, A. Rohlmann, A. Bender, G. Bergmann, Total hip joint prosthesis for in vivo measurement of forces and moments, *Med. Eng. Phys.* 32 (2010) 95–100. doi:10.1016/j.medengphy.2009.10.003.
- [82] M.A. Wimmer, A. Fischer, R. Büscher, R. Pourzal, C. Sprecher, R. Hauert, et al., Wear mechanisms in metal-on-metal bearings: the importance of tribochemical reaction layers., *J. Orthop. Res.* 28 (2010) 436–43. doi:10.1002/jor.21020.
- [83] G. Bergmann, F. Graichen, A. Rohlmann, N. Verdonschot, G.H. van Lenthe,

Frictional heating of total hip implants, Part 1: measurements in patients, *J. Biomech.* 34 (2001) 421–428.  
<http://linkinghub.elsevier.com/retrieve/pii/S0021929000001883?showall=true>.

- [84] M.. Wimmer, J. Loos, R. Nassutt, M. Heitkemper, A. Fischer, The acting wear mechanisms on metal-on-metal hip joint bearings: in vitro results, *Wear.* 250 (2001) 129–139. doi:10.1016/S0043-1648(01)00654-8.
- [85] H.W. Pickering, *On the Roles of Corrosion Products in Local Cell Processes.*, (1986).  
<http://oai.dtic.mil/oai/oai?verb=getRecord&metadataPrefix=html&identifier=ADA162448> (accessed June 6, 2015).
- [86] N.J. Hallab, C. Messina, A. Skipor, J.J. Jacobs, Differences in the fretting corrosion of metal–metal and ceramic–metal modular junctions of total hip replacements, *J. Orthop. Res.* 22 (2004) 250–259. doi:10.1016/s0736-0266(03)00186-4.
- [87] M. Bryant, R. Farrar, R. Freeman, K. Brummitt, A. Neville, Fretting corrosion characteristics of polished collarless tapered stems in a simulated biological environment, *Tribol. Int.* 65 (2013) 105–112. doi:10.1016/j.triboint.2013.01.024.
- [88] M. Silva, E.F. Shepherd, W.O. Jackson, F.J. Dorey, T.P. Schmalzried, Average patient walking activity approaches 2 million cycles per year: pedometers under-record walking activity., *J. Arthroplasty.* 17 (2002) 693–7. <http://www.ncbi.nlm.nih.gov/pubmed/12216021> (accessed September 15, 2014).
- [89] P.F. Doorn, P.A. Campbell, J. Worrall, P.D. Benya, H.A. McKellop, H.C. Amstutz, Metal wear particle characterization from metal on metal total hip replacements: transmission electron microscopy study of periprosthetic tissues and isolated particles., *J. Biomed. Mater. Res.* 42 (1998) 103–11. <http://www.ncbi.nlm.nih.gov/pubmed/9740012> (accessed April 14, 2015).
- [90] A.P. Elfick, R.M. Hall, I.M. Pinder, A. Unsworth, Wear in retrieved acetabular components: effect of femoral head radius and patient parameters., *J. Arthroplasty.* 13 (1998) 291–5. <http://www.ncbi.nlm.nih.gov/pubmed/9590640> (accessed May 14, 2015).
- [91] G.C. Clark, D.F. Williams, The effects of proteins on metallic corrosion., *J. Biomed. Mater. Res.* 16 (1982) 125–34. doi:10.1002/jbm.820160205.

- [92] A. Kocijan, I. Milosev, B. Pihlar, Cobalt-based alloys for orthopaedic applications studied by electrochemical and XPS analysis., *J. Mater. Sci. Mater. Med.* 15 (2004) 643–50. <http://www.ncbi.nlm.nih.gov/pubmed/15346730> (accessed May 19, 2015).
- [93] J.J. Jacobs, J.L. Gilbert, R.M. Urban, Corrosion of metal orthopaedic implants., *J. Bone Joint Surg. Am.* 80 (1998) 268–82. <http://www.ncbi.nlm.nih.gov/pubmed/9486734> (accessed May 19, 2015).
- [94] J. Zhu, N. Xu, C. Zhang, Characteristics of copper corrosion in simulated uterine fluid in the presence of protein., *Adv. Contracept.* 15 (1999) 179–90. <http://www.ncbi.nlm.nih.gov/pubmed/11019949> (accessed March 24, 2015).
- [95] R.D. Shannon, Revised effective ionic radii and systematic studies of interatomic distances in halides and chalcogenides, *Acta Crystallogr. Sect. A.* 32 (1976) 751–767. doi:10.1107/S0567739476001551.
- [96] J.L. Gilbert, L. Zarka, E.B. Chang, C.H. Thomas, The reduction half cell in biomaterials corrosion: Oxygen diffusion profiles near and cell response to polarized titanium surfaces, *J. Biomed. Mater. Res.* 42 (1998) 321–330. doi:10.1002/(sici)1097-4636(199811)42:2<321::aid-jbm18>3.0.co;2-l.
- [97] Mu Y, Kobayashi T, Sumita M, Yamamoto A, T. Hanawa, Y. Mu, et al., Metal ion release from titanium with active oxygen species generated by rat macrophages in vitro, *J. Biomed. Mater. Res.* 49 (2000) 5. doi:10.1002/(sici)1097-4636(200002)49:2<238::aid-jbm12>3.0.co;2-j.
- [98] G. Danscher, In vivo liberation of gold ions from gold implants. Autometallographic tracing of gold in cells adjacent to metallic gold, *Histochem. Cell Biol.* 117 (2002) 447–452. doi:10.1007/s00418-002-0400-8.
- [99] T.A. Simoes, A.E. Goode, A.E. Porter, M.P. Ryan, S.J. Milne, A.P. Brown, et al., Microstructural characterization of low and high carbon CoCrMo alloy nanoparticles produced by mechanical milling, *J. Phys. Conf. Ser.* 522 (2014) 012059. doi:10.1088/1742-6596/522/1/012059.
- [100] I. Catelas, J.D. Bobyn, J.B. Medley, J.J. Krygier, D.J. Zukor, A. Petit, et al., Effects of digestion protocols on the isolation and characterization of metal-metal wear particles. I. Analysis of particle size and shape., *J. Biomed. Mater. Res.* 55 (2001) 320–9. <http://www.ncbi.nlm.nih.gov/pubmed/11255185> (accessed February 14, 2014).

- [101] A.J. Hart, P.D. Quinn, B. Sampson, A. Sandison, K.D. Atkinson, J.A. Skinner, et al., The chemical form of metallic debris in tissues surrounding metal-on-metal hips with unexplained failure, *Acta Biomater.* 6 (2010) 4439–4446. doi:10.1016/j.actbio.2010.06.006.
- [102] J. Zimmermann, L.C. Ciacchi, Origin of the Selective Cr Oxidation in CoCr Alloy Surfaces, *J. Phys. Chem. Lett.* 1 (2010) 2343–2348. doi:10.1021/jz1007164.
- [103] X. Zhang, Y. Li, N. Tang, E. Onodera, A. Chiba, Corrosion behaviour of CoCrMo alloys in 2 wt% sulphuric acid solution, *Electrochim. Acta.* 125 (2014) 543–555. doi:10.1016/j.electacta.2014.01.143.
- [104] M. Hasegawa, K. Yoshida, H. Wakabayashi, A. Sudo, Cobalt and chromium ion release after large-diameter metal-on-metal total hip arthroplasty., *J. Arthroplasty.* 27 (2012) 990–6. doi:10.1016/j.arth.2011.12.016.
- [105] L. Savarino, D. Granchi, G. Ciapetti, E. Cenni, A. Nardi Pantoli, R. Rotini, et al., Ion release in patients with metal-on-metal hip bearings in total joint replacement: a comparison with metal-on-polyethylene bearings., *J. Biomed. Mater. Res.* 63 (2002) 467–74. doi:10.1002/jbm.10299.
- [106] M.T. Clarke, P.T.H. Lee, A. Arora, R.N. Villar, Levels of metal ions after small- and large-diameter metal-on-metal hip arthroplasty., *J. Bone Joint Surg. Br.* 85 (2003) 913–917. doi:10.1302/0301-620X.85B6.14166.
- [107] R.P. Sidaginamale, T.J. Joyce, J.K. Lord, R. Jefferson, P.G. Blain, A.V.F. Nargol, et al., Blood metal ion testing is an effective screening tool to identify poorly performing metal-on-metal bearing surfaces., *Bone Joint Res.* 2 (2013) 84–95. doi:10.1302/2046-3758.25.2000148.
- [108] A.J. Hart, J.A. Skinner, P. Winship, N. Faria, E. Kulinskaya, D. Webster, et al., Circulating levels of cobalt and chromium from metal-on-metal hip replacement are associated with CD8+ T-cell lymphopenia., *J. Bone Joint Surg. Br.* 91 (2009) 835–42. doi:10.1302/0301-620X.91B6.21844.
- [109] J.P. Wise, S.S. Wise, J.E. Little, The cytotoxicity and genotoxicity of particulate and soluble hexavalent chromium in human lung cells., *Mutat. Res.* 517 (2002) 221–9. <http://www.ncbi.nlm.nih.gov/pubmed/12034323> (accessed June 8, 2015).
- [110] N.J. Hallab, K. Mikecz, C. Vermes, A. Skipor, J.J. Jacobs, Orthopaedic implant related metal toxicity in terms of human lymphocyte reactivity to metal-protein

complexes produced from cobalt-base and titanium-base implant alloy degradation., *Mol. Cell. Biochem.* 222 (2001) 127–36. <http://www.ncbi.nlm.nih.gov/pubmed/11678594> (accessed February 18, 2015).

- [111] J.M.H. Smolders, P. Bisseling, A. Hol, C. Van Der Straeten, B.W. Schreurs, J.L.C. van Susante, Metal ion interpretation in resurfacing versus conventional hip arthroplasty and in whole blood versus serum. How should we interpret metal ion data, *Hip Int.* 21 (2011) 587–595. doi:10.5301/HIP.2011.8643.
- [112] C. Jantzen, H.L. Jørgensen, B.R. Duus, S.L. Spørring, J.B. Lauritzen, Chromium and cobalt ion concentrations in blood and serum following various types of metal-on-metal hip arthroplasties: a literature overview., *Acta Orthop.* 84 (2013) 229–36. doi:10.3109/17453674.2013.792034.
- [113] S.T. Donell, C. Darrah, J.F. Nolan, J. Wimhurst, A. Toms, T.H.W. Barker, et al., Early failure of the Ultima metal-on-metal total hip replacement in the presence of normal plain radiographs, *J. Bone Jt. Surg. - Br. Vol.* 92-B (2010) 1501–1508. doi:10.1302/0301-620X.92B11.24504.
- [114] L. Savarino, M. Greco, E. Cenni, L. Cavasinni, R. Rotini, N. Baldini, et al., Differences in ion release after ceramic-on-ceramic and metal-on-metal total hip replacement. Medium-term follow-up., *J. Bone Joint Surg. Br.* 88 (2006) 472–6. doi:10.1302/0301-620X.88B4.17333.
- [115] R.M. Urban, J.J. Jacobs, M.J. Tomlinson, J. Gavrilovic, J. Black, M. Peoc'h, Dissemination of wear particles to the liver, spleen, and abdominal lymph nodes of patients with hip or knee replacement., *J. Bone Joint Surg. Am.* 82 (2000) 457–76. <http://www.ncbi.nlm.nih.gov/pubmed/10761937> (accessed May 20, 2015).
- [116] A.K. Matthies, J.A. Skinner, H. Osmani, J. Henckel, A.J. Hart, Pseudotumors are common in well-positioned low-wearing metal-on-metal hips., *Clin. Orthop. Relat. Res.* 470 (2012) 1895–906. doi:10.1007/s11999-011-2201-7.
- [117] A.J. Hart, P.D. Quinn, F. Lali, B. Sampson, J.A. Skinner, J.J. Powell, et al., Cobalt from metal-on-metal hip replacements may be the clinically relevant active agent responsible for periprosthetic tissue reactions., *Acta Biomater.* 8 (2012) 3865–73. doi:10.1016/j.actbio.2012.05.003.
- [118] O.D. Neikov, I.B. Murashova, N.A. Yefimov, S. Naboychenko, *Handbook of Non-Ferrous Metal Powders: Technologies and Applications*, Elsevier, 2009. <https://books.google.com/books?id=6aP3te2hGuQC&pgis=1> (accessed June 11, 2015).

- [119] C. Voegtlin, Toxicity of certain heavy metal carbonyls : Ni(CO)<sub>4</sub>, Mo(CO)<sub>6</sub>, W(CO)<sub>6</sub>, Cr(CO)<sub>6</sub>, Oak Ridge, Tenn.: Technical Information Division, Oak Ridge Directed Operation, 1947. <http://catalog.hathitrust.org/Record/005979744> (accessed June 11, 2015).
- [120] H. Yue, W. Wei, Z. Yue, P. Lv, L. Wang, G. Ma, et al., Particle size affects the cellular response in macrophages, *Eur. J. Pharm. Sci.* 41 (2010) 650–657. doi:10.1016/j.ejps.2010.09.006.
- [121] M.S. Caicedo, R. Desai, K. McAllister, A. Reddy, J.J. Jacobs, N.J. Hallab, Soluble and particulate Co-Cr-Mo alloy implant metals activate the inflammasome danger signaling pathway in human macrophages: a novel mechanism for implant debris reactivity., *J. Orthop. Res.* 27 (2009) 847–54. doi:10.1002/jor.20826.
- [122] I. Papageorgiou, C. Brown, R. Schins, S. Singh, R. Newson, S. Davis, et al., The effect of nano- and micron-sized particles of cobalt-chromium alloy on human fibroblasts in vitro., *Biomaterials.* 28 (2007) 2946–58. doi:10.1016/j.biomaterials.2007.02.034.
- [123] Y.-M. Kwon, Z. Xia, S. Glyn-Jones, D. Beard, H.S. Gill, D.W. Murray, Dose-dependent cytotoxicity of clinically relevant cobalt nanoparticles and ions on macrophages in vitro., *Biomed. Mater.* 4 (2009) 025018. doi:10.1088/1748-6041/4/2/025018.
- [124] K. Merritt, S.A. Brown, Release of hexavalent chromium from corrosion of stainless steel and cobalt-chromium alloys., *J. Biomed. Mater. Res.* 29 (1995) 627–33. doi:10.1002/jbm.820290510.
- [125] M.G. Shettlemore, K.J. Bundy, Examination of in vivo influences on bioluminescent microbial assessment of corrosion product toxicity., *Biomaterials.* 22 (2001) 2215–28. <http://www.ncbi.nlm.nih.gov/pubmed/11456061> (accessed September 22, 2014).
- [126] J. Guertin, Toxicity and Health Effects of Chromium (All Oxidation States), in: *Chromium(VI) Handb.*, CRC Press, 2004: pp. 215–234. doi:doi:10.1201/9780203487969.ch6.
- [127] H.S. Gill, G. Grammatopoulos, S. Adshead, E. Tsialogiannis, E. Tsiridis, Molecular and immune toxicity of CoCr nanoparticles in MoM hip arthroplasty., *Trends*

Mol. Med. 18 (2012) 145–55. doi:10.1016/j.molmed.2011.12.002.

- [128] M. Akbar, J.M. Brewer, M.H. Grant, Effect of chromium and cobalt ions on primary human lymphocytes in vitro, *J. Immunotoxicol.* 8 (2011) 140–149. doi:10.3109/1547691X.2011.553845.
- [129] C. Suryanarayana, Mechanical alloying and milling, *Prog. Mater. Sci.* 46 (2001) 1–184. doi:10.1016/S0079-6425(99)00010-9.
- [130] S.F. Lomayeva, E.P. Yelsukov, G.N. Konygin, G.A. Dorofeev, V.I. Povstugar \*, S.S. Mikhailova, et al., The influence of a surfactant on the characteristics of the iron powders obtained by mechanical milling in organic media, *Colloids and Surfaces.* 162 (1999) 279–284.
- [131] S. Karimi, T. Nickchi, A. Alfantazi, Long-term corrosion investigation of AISI 316L, Co–28Cr–6Mo, and Ti–6Al–4V alloys in simulated body solutions, *Appl. Surf. Sci.* 258 (2012) 6087–6096. doi:10.1016/j.apsusc.2012.03.008.
- [132] J.-M. Brandt, L.K. Brière, J. Marr, S.J. MacDonald, R.B. Bourne, J.B. Medley, Biochemical comparisons of osteoarthritic human synovial fluid with calf sera used in knee simulator wear testing., *J. Biomed. Mater. Res. A.* 94 (2010) 961–71. doi:10.1002/jbm.a.32728.
- [133] D. Mazzucco, R. Scott, M. Spector, Composition of joint fluid in patients undergoing total knee replacement and revision arthroplasty: correlation with flow properties., *Biomaterials.* 25 (2004) 4433–45. doi:10.1016/j.biomaterials.2003.11.023.
- [134] S. Ghosh, D. Choudhury, N.S. Das, B. Pingguan-Murphy, Tribological role of synovial fluid compositions on artificial joints - a systematic review of the last 10 years, *Lubr. Sci.* 26 (2014) 387–410. doi:10.1002/lis.1266.
- [135] C. Myant, P. Cann, On the matter of synovial fluid lubrication: implications for Metal-on-Metal hip tribology., *J. Mech. Behav. Biomed. Mater.* 34 (2014) 338–48. doi:10.1016/j.jmbbm.2013.12.016.
- [136] A. Wang, A. Essner, G. Schmidig, The effects of lubricant composition on in vitro wear testing of polymeric acetabular components., *J. Biomed. Mater. Res. B. Appl. Biomater.* 68 (2004) 45–52. doi:10.1002/jbm.b.10077.
- [137] A.-M. Trunfio-Sfarghiu, Y. Berthier, M.-H. Meurisse, J.-P. Rieu, Multiscale analysis of the tribological role of the molecular assemblies of synovial fluid.

Case of a healthy joint and implants, *Tribol. Int.* 40 (2007) 1500–1515.  
doi:10.1016/j.triboint.2007.02.008.

- [138] S. Guedes, R. Vitorino, R. Domingues, F. Amado, P. Domingues, Oxidation of bovine serum albumin: identification of oxidation products and structural modifications., *Rapid Commun. Mass Spectrom.* 23 (2009) 2307–15.  
doi:10.1002/rcm.4149.
- [139] X.M. He, D.C. Carter, Atomic structure and chemistry of human serum albumin., *Nature.* 358 (1992) 209–15. doi:10.1038/358209a0.
- [140] J.-M. Brandt, K. Charron, L. Zhao, S.J. MacDonald, J.B. Medley, Calf serum constituent fractions influence polyethylene wear and microbial growth in knee simulator testing, *Proc. Inst. Mech. Eng. Part H J. Eng. Med.* 226 (2012) 427–440. doi:10.1177/0954411912444248.
- [141] S. Kasai-Morita, T. Horie, S. Awazu, Influence of the N-B transition of human serum albumin on the structure of the warfarin-binding site., *Biochim. Biophys. Acta.* 915 (1987) 277–83. <http://www.ncbi.nlm.nih.gov/pubmed/3651475> (accessed June 12, 2015).
- [142] G. Sudlow, D.J. Birkett, D.N. Wade, The characterization of two specific drug binding sites on human serum albumin., *Mol. Pharmacol.* 11 (1975) 824–32. <http://www.ncbi.nlm.nih.gov/pubmed/1207674> (accessed June 12, 2015).
- [143] U. Böhme, U. Scheler, Effective charge of bovine serum albumin determined by electrophoresis NMR, *Chem. Phys. Lett.* 435 (2007) 342–345.  
doi:10.1016/j.cplett.2006.12.068.
- [144] K. Rezwan, L.P. Meier, L.J. Gauckler, Lysozyme and bovine serum albumin adsorption on uncoated silica and AlOOH-coated silica particles: the influence of positively and negatively charged oxide surface coatings., *Biomaterials.* 26 (2005) 4351–7. doi:10.1016/j.biomaterials.2004.11.017.
- [145] P.F. Spahr, J.T. Edsall, Amino acid composition of human and bovine serum mercaptalbumins, *J. Biol. Chem.* 239 (1964) 850–4.  
<http://www.ncbi.nlm.nih.gov/pubmed/14154465> (accessed June 13, 2015).
- [146] D.R. Lide, *CRC Handbook of Chemistry and Physics*, 85th Edition, CRC Press, 2004.  
[https://books.google.co.uk/books/about/CRC\\_handbook\\_of\\_chemistry\\_and\\_physics.html?id=WDI8hA006AC&pgis=1](https://books.google.co.uk/books/about/CRC_handbook_of_chemistry_and_physics.html?id=WDI8hA006AC&pgis=1) (accessed June 13, 2015).

- [147] C. Valero Vidal, A. Olmo Juan, A. Igual Muñoz, Adsorption of bovine serum albumin on CoCrMo surface: effect of temperature and protein concentration., *Colloids Surf. B. Biointerfaces.* 80 (2010) 1–11. doi:10.1016/j.colsurfb.2010.05.005.
- [148] S. Karimi, T. Nickchi, A. Alfantazi, Effects of bovine serum albumin on the corrosion behaviour of AISI 316L, Co-28Cr-6Mo, and Ti-6Al-4V alloys in phosphate buffered saline solutions, *Corros. Sci.* 53 (2011) 3262–3272. doi:10.1016/j.corsci.2011.06.009.
- [149] C.-T. Duong, J.-H. Lee, Y. Cho, J.-S. Nam, H.-N. Kim, S.-S. Lee, et al., Effect of protein concentrations of bovine serum albumin and  $\gamma$ -globulin on the frictional response of a cobalt-chromium femoral head., *J. Mater. Sci. Mater. Med.* 23 (2012) 1323–30. doi:10.1007/s10856-012-4603-9.
- [150] N. Espallargas, C. Torres, A.I. Muñoz, A metal ion release study of CoCrMo exposed to corrosion and tribocorrosion conditions in simulated body fluids, *Wear.* (2014). doi:10.1016/j.wear.2014.12.030.
- [151] M. Metikoš-Huković, Z. Pilić, R. Babić, D. Omanović, Influence of alloying elements on the corrosion stability of CoCrMo implant alloy in Hank's solution, *Acta Biomater.* 2 (2006) 693–700. <http://www.sciencedirect.com/science/article/pii/S1742706106000705> (accessed January 21, 2014).
- [152] I. Catelas, J.D. Bobyn, J.B. Medley, J.J. Krygier, D.J. Zukor, O.L. Huk, Size, shape, and composition of wear particles from metal-metal hip simulator testing: effects of alloy and number of loading cycles., *J. Biomed. Mater. Res. A.* 67 (2003) 312–27. doi:10.1002/jbm.a.10088.
- [153] I. Leslie, S. Williams, C. Brown, G. Isaac, Z. Jin, E. Ingham, et al., Effect of bearing size on the long-term wear, wear debris, and ion levels of large diameter metal-on-metal hip replacements-An in vitro study., *J. Biomed. Mater. Res. B. Appl. Biomater.* 87 (2008) 163–72. doi:10.1002/jbm.b.31087.
- [154] J. Fisher, D. Dowson, Tribology of total artificial joints, *Arch. Proc. Inst. Mech. Eng. Part H J. Eng. Med.* 1989-1996 (vols 203-210). 205 (1991) 73–79. doi:10.1243/PIME\_PROC\_1991\_205\_271\_02.
- [155] Y. Chen, Y. Li, S. Kurosu, K. Yamanaka, N. Tang, Y. Koizumi, et al., Effects of sigma phase and carbide on the wear behavior of CoCrMo alloys in Hanks'

solution, *Wear.* 310 (2014) 51–62.  
<http://www.sciencedirect.com/science/article/pii/S0043164813006066>  
(accessed January 21, 2014).

- [156] J. Benjamin, Dispersion strengthened superalloys by mechanical alloying, *Metall. Mater. Trans. B.* 1 (1970) 2943–2951. doi:10.1007/bf03037835.
- [157] P. Baláz, *Mechanochemistry in Nanoscience and Minerals Engineering*, Springer Berlin Heidelberg, Berlin, Heidelberg, 2008. doi:10.1007/978-3-540-74855-7.
- [158] C.C. Koch, The synthesis and structure of nanocrystalline materials produced by mechanical attrition: A review, *Nanostructured Mater.* 2 (1993) 109–129. doi:10.1016/0965-9773(93)90016-5.
- [159] T. Raghu, R. Sundaresan, P. Ramakrishnan, T.R. Mohan, Synthesis of Nanocrystalline Copper Tungsten Alloys by Mechanical Alloying, *Mater. Sci. Eng.* 304-306 (2001) 3.
- [160] A.P. Smith, J.S. Shay, R.J. Spontak, C.M. Balik, H. Ade, S.D. Smith, et al., High-energy mechanical milling of poly(methyl methacrylate), polyisoprene and poly(ethylene-alt-propylene), *Polymer (Guildf.)* 41 (2000) 6271–6283. doi:10.1016/S0032-3861(99)00830-7.
- [161] V.M. Chakka, B. Altuncevahir, Z.Q. Jin, Y. Li, J.P. Liu, Magnetic nanoparticles produced by surfactant-assisted ball milling, *J. Appl. Phys.* 99 (2006) 08E912. doi:10.1063/1.2170593.
- [162] P.P. Chin, J. Ding, J.B. Yi, B.H. Liu, Synthesis of FeS<sub>2</sub> and FeS nanoparticles by high-energy mechanical milling and mechanochemical processing, *J. Alloys Compd.* 390 (2005) 255–260. doi:10.1016/j.jallcom.2004.07.053.
- [163] SPEX SamplePrep, *Handbook of Sample Preparation*, (2015). [http://www.spexsampleprep.com/#download\\_handbook](http://www.spexsampleprep.com/#download_handbook).
- [164] C.L. De Castro, B.S. Mitchell, Nanoparticles from Mechanical Attrition, in: M.-I. Baraton (Ed.), *Synth. Funct. Surf. Treat. Nanoparticles*, New Orleans, Louisiana, USA, 2002.
- [165] P. López-Mahía, S. Muniategui, D. Prada-Rodríguez, M.C. Prieto-Blanco, SURFACTANTS AND DETERGENTS, in: W. Editors-in-Chief: Paul, T. Alan, P. Colin (Eds.), *Encycl. Anal. Sci. (Second Ed., Elsevier, Oxford, 2005: pp. 554–561*. doi:10.1016/b0-12-369397-7/00608-7.

- [166] J. Dutta, H. Hofmann, Self-organization of colloidal nanoparticles, *Encycl. Nanosci. .... X* (2004). [http://www.researchgate.net/publication/52000696\\_Self-organization\\_of\\_colloidal\\_nanoparticles/file/79e41505894bd0d532.pdf](http://www.researchgate.net/publication/52000696_Self-organization_of_colloidal_nanoparticles/file/79e41505894bd0d532.pdf) (accessed March 10, 2014).
- [167] Y. Liao, E. Hoffman, M. Wimmer, A. Fischer, J. Jacobs, L. Marks, CoCrMo metal-on-metal hip replacements., *Phys. Chem. Chem. Phys.* 15 (2013) 746–56. doi:10.1039/c2cp42968c.
- [168] R.W. Revie, H.H. Uhlig, *Corrosion and Corrosion Control*, John Wiley & Sons, Inc., Hoboken, NJ, USA, 2008. doi:10.1002/9780470277270.
- [169] E. McCafferty, Validation of corrosion rates measured by the Tafel extrapolation method, *Corros. Sci.* 47 (2005) 3202–3215. doi:10.1016/j.corsci.2005.05.046.
- [170] E. Poorqasemi, O. Abootalebi, M. Peikari, F. Haqdar, Investigating accuracy of the Tafel extrapolation method in HCl solutions, *Corros. Sci.* 51 (2009) 1043–1054. doi:10.1016/j.corsci.2009.03.001.
- [171] E. Bettini, C. Leygraf, J. Pan, Nature of current increase for a CoCrMo alloy : “transpassive” dissolution vs. water oxidation, *Int. J. Electrochem. Sci.* 8 (2013) 11791–11804. <http://www.diva-portal.org/smash/record.jsf?pid=diva2:651791&dsid=-1551> (accessed June 16, 2015).
- [172] M. Yang, Y. Dai, C. Song, Q. Zhai, Microstructure evolution of grey cast iron powder by high pressure gas atomization, *J. Mater. Process. Technol.* 210 (2010) 351–355. doi:10.1016/j.jmatprotec.2009.09.023.
- [173] H. Yuexiang, Z. Hong, Characteristics of a low-cobalt AB5-type hydrogen storage alloy obtained by a gas-atomization processing, *J. Alloys Compd.* 305 (2000) 76–81. doi:10.1016/S0925-8388(00)00702-7.
- [174] L. Reimer, *Scanning Electron Microscopy: Physics of Image Formation and Microanalysis*, Springer Science & Business Media, 1998. [http://books.google.co.uk/books/about/Scanning\\_Electron\\_Microscopy.html?id=0Fm3T6F6\\_LEC&pgis=1](http://books.google.co.uk/books/about/Scanning_Electron_Microscopy.html?id=0Fm3T6F6_LEC&pgis=1) (accessed April 21, 2015).
- [175] D.B. Williams, C.B. Carter, *Transmission Electron Microscopy: A Textbook for Materials Science*, Plenum Press, 1996. <http://books.google.co.uk/books?id=edQ87ObsRtwC>.

- [176] A. Montaser, *Inductively Coupled Plasma Mass Spectrometry*, John Wiley & Sons, 1998.  
[http://books.google.co.uk/books/about/Inductively\\_Coupled\\_Plasma\\_Mass\\_Spectrom.html?id=-c9nIF\\_gc30C&pgis=1](http://books.google.co.uk/books/about/Inductively_Coupled_Plasma_Mass_Spectrom.html?id=-c9nIF_gc30C&pgis=1) (accessed April 21, 2015).
- [177] S.H. Tan, G. Horlick, Matrix-effect observations in inductively coupled plasma mass spectrometry, *J. Anal. At. Spectrom.* 2 (1987) 745. doi:10.1039/ja9870200745.
- [178] C. Vandecasteele, H. Vanhoe, R. Dams, *Inductively Coupled Plasma Mass Spectrometry of Biological Samples\* Invited Lecture*, *J. Anal. At. Spectrom.* 8 (1993).
- [179] L. Guo, P.H. Santschi, Ultrafiltration and its Applications to Sampling and Characterisation of Aquatic Colloids, in: *Environ. Colloids Part.*, John Wiley & Sons, Ltd, 2006: pp. 159–221. doi:10.1002/9780470024539.ch4.
- [180] J.F. Moulder, W.F. Stickle, P. E. Sobol, K. Bomben, *Handbook of X-ray Photoelectron Spectroscopy: A Reference Book of Standard Spectra for Identification and Interpretation of XPS Data*, 2nd ed., Physical Electronics Division, Perkin-Elmer Corporation, 1992.  
[http://books.google.co.uk/books/about/Handbook\\_of\\_X\\_ray\\_Photoelectron\\_Spectros.html?id=A\\_XGQgAACAAJ&pgis=1](http://books.google.co.uk/books/about/Handbook_of_X_ray_Photoelectron_Spectros.html?id=A_XGQgAACAAJ&pgis=1) (accessed April 16, 2015).
- [181] J. Baltrusaitis, P.M. Jayaweera, V.H. Grassian, XPS study of nitrogen dioxide adsorption on metal oxide particle surfaces under different environmental conditions., *Phys. Chem. Chem. Phys.* 11 (2009) 8295–305. doi:10.1039/b907584d.
- [182] M.C. Biesinger, B.P. Payne, A.P. Grosvenor, L.W.M. Lau, A.R. Gerson, R.S.C. Smart, Resolving surface chemical states in XPS analysis of first row transition metals, oxides and hydroxides: Cr, Mn, Fe, Co and Ni, *Appl. Surf. Sci.* 257 (2011) 2717–2730. doi:10.1016/j.apsusc.2010.10.051.
- [183] M.C. Biesinger, C. Brown, J.R. Mycroft, R.D. Davidson, N.S. McIntyre, X-ray photoelectron spectroscopy studies of chromium compounds, *Surf. Interface Anal.* 36 (2004) 1550–1563. doi:10.1002/sia.1983.
- [184] J. Baltrusaitis, B. Mendoza-Sanchez, V. Fernandez, R. Veenstra, N. Dukstiene, A. Roberts, et al., Generalized molybdenum oxide surface chemical state XPS determination via informed amorphous sample model, *Appl. Surf. Sci.* 326

(2015) 151–161. doi:10.1016/j.apsusc.2014.11.077.

- [185] D.O. Scanlon, G.W. Watson, D.J. Payne, G.R. Atkinson, R.G. Egdell, D.S.L. Law, Theoretical and Experimental Study of the Electronic Structures of MoO<sub>3</sub> and MoO<sub>2</sub>, *J. Phys. Chem. C* 114 (2010) 4636–4645. doi:10.1021/jp9093172.
- [186] B.J. Berne, R. Pecora, *Dynamic Light Scattering: With Applications to Chemistry, Biology, and Physics*, Courier Corporation, 2000. [http://books.google.co.uk/books/about/Dynamic\\_Light\\_Scattering.html?id=vB54ABhmuEC&pgis=1](http://books.google.co.uk/books/about/Dynamic_Light_Scattering.html?id=vB54ABhmuEC&pgis=1) (accessed April 21, 2015).
- [187] V.K. Raghunathan, S. Hawkins, C.P. Case, S. Mann, S. Davis, J. Lane, et al., Factors that may affect the nanotoxicology of hard materials for surgical applications, University of Bristol, Bristol, 2010. <http://www.defra.gov.uk>.
- [188] R.C. Weast, *Handbook of Chemistry and Physics*, 66th editi, CRC Press, 1985.
- [189] Malvern, Zeta Potential theory, in: *Zeta Sizer Nano Ser. - Man.*, n.d.
- [190] B.C. Smith, *Fundamentals of Fourier Transform Infrared Spectroscopy*, CRC Press, 1995. [http://books.google.co.uk/books/about/Fundamentals\\_of\\_Fourier\\_Transform\\_Infrar.html?id=cL\\_cvNCoEmkC&pgis=1](http://books.google.co.uk/books/about/Fundamentals_of_Fourier_Transform_Infrar.html?id=cL_cvNCoEmkC&pgis=1) (accessed April 20, 2015).
- [191] A. Neumann, W. Hoyer, M.W. Wolff, U. Reichl, A. Pfitzner, B. Roth, New method for density determination of nanoparticles using a CPS disc centrifuge™., *Colloids Surf. B. Biointerfaces* 104 (2013) 27–31. doi:10.1016/j.colsurfb.2012.11.014.
- [192] W. Anderson, D. Kozak, V.A. Coleman, Å.K. Jämting, M. Trau, A comparative study of submicron particle sizing platforms: accuracy, precision and resolution analysis of polydisperse particle size distributions., *J. Colloid Interface Sci.* 405 (2013) 322–30. doi:10.1016/j.jcis.2013.02.030.
- [193] O.M. Posada, D. Gilmour, R.J. Tate, M.H. Grant, CoCr wear particles generated from CoCr alloy metal-on-metal hip replacements, and cobalt ions stimulate apoptosis and expression of general toxicology-related genes in monocyte-like U937 cells., *Toxicol. Appl. Pharmacol.* 281 (2014) 125–135. doi:10.1016/j.taap.2014.09.010.
- [194] A.W. Hayes, *Principles and Methods of Toxicology*, Fifth Edit, CRC Press, 2007. <https://books.google.com/books?id=vgHXTId8rnYC&pgis=1> (accessed August

31, 2015).

- [195] J. Cohen, Multiple regression as a general data-analytic system, *Psychol. Bull.* (1968). <http://citeseerx.ist.psu.edu/viewdoc/summary?doi=10.1.1.476.6180> (accessed September 4, 2015).
- [196] R. Gohar, H. Rahnejat, *Fundamentals of Tribology*, 2008. <http://www.worldscientific.com/worldscibooks/10.1142/p553> (accessed September 14, 2015).
- [197] F. Billi, P. Benya, E. Ebrahimzadeh, P. Campbell, F. Chan, H.A. McKellop, Metal wear particles: What we know, what we do not know, and why., *SAS J.* 3 (2009) 133–42. doi:10.1016/j.esas.2009.11.006.
- [198] W.R. Hagen, Cellular uptake of molybdenum and tungsten, *Coord. Chem. Rev.* 255 (2011) 1117–1128. doi:10.1016/j.ccr.2011.02.009.
- [199] a Salinas-Rodriguez, J.L. Rodriguez-Galicia, A. Salinas Rodriguez, J.L. Rodriguez Galicia, Deformation behavior of low-carbon Co-Cr-Mo alloys for low-friction implant applications, *J. Biomed. Mater. Res.* 31 (1996) 409–419. doi:10.1002/(sici)1097-4636(199607)31:3<409::aid-jbm16>3.0.co;2-d.
- [200] J.V. Giacchi, C.N. Morando, O. Fornaro, H.A. Palacio, Microstructural characterization of as-cast biocompatible Co–Cr–Mo alloys, *Mater. Charact.* 62 (2011) 53–61. doi:10.1016/j.matchar.2010.10.011.
- [201] J.A. Muñoz-Tabares, E. Jiménez-Piqué, M. Anglada, Subsurface evaluation of hydrothermal degradation of zirconia, *Acta Mater.* 59 (2011) 473–484. doi:10.1016/j.actamat.2010.09.047.
- [202] P. Huang, Z. Li, H. Hu, D. Cui, Synthesis and Characterization of Bovine Serum Albumin-Conjugated Copper Sulfide Nanocomposites, *J. Nanomater.* 2010 (2010) 1–6. doi:10.1155/2010/641545.
- [203] S. Karimi, A. Alfantazi, Ion release and surface oxide composition of AISI 316L, Co-28Cr-6Mo, and Ti-6Al-4V alloys immersed in human serum albumin solutions., *Mater. Sci. Eng. C. Mater. Biol. Appl.* 40 (2014) 435–44. doi:10.1016/j.msec.2014.04.007.
- [204] Y. Hedberg, X. Wang, J. Hedberg, M. Lundin, E. Blomberg, I.O. Wallinder, Surface-protein interactions on different stainless steel grades: effects of protein adsorption, surface changes and metal release., *J. Mater. Sci. Mater.*

Med. 24 (2013) 1015–33. doi:10.1007/s10856-013-4859-8.

- [205] P. Maffre, S. Brandholt, K. Nienhaus, L. Shang, W.J. Parak, G.U. Nienhaus, Effects of surface functionalization on the adsorption of human serum albumin onto nanoparticles - a fluorescence correlation spectroscopy study., *Beilstein J. Nanotechnol.* 5 (2014) 2036–47. doi:10.3762/bjnano.5.212.
- [206] J.H. Shannahan, X. Lai, P.C. Ke, R. Podila, J.M. Brown, F.A. Witzmann, Silver nanoparticle protein corona composition in cell culture media., *PLoS One.* 8 (2013) e74001. doi:10.1371/journal.pone.0074001.
- [207] Y. Yan, A. Neville, D. Dowson, Biotribocorrosion of CoCrMo orthopaedic implant materials—Assessing the formation and effect of the biofilm, *Tribol. Int.* 40 (2007) 1492–1499. doi:10.1016/j.triboint.2007.02.019.
- [208] J.P. Kretzer, M. Krachler, J. Reinders, E. Jakubowitz, M. Thomsen, C. Heisel, Determination of Low Wear Rates in Metal-On-Metal Hip Joint Replacements Based on Ultra Trace Element Analysis in Simulator Studies, *Tribol. Lett.* 37 (2009) 23–29. doi:10.1007/s11249-009-9486-7.
- [209] C. Heisel, N. Streich, M. Krachler, E. Jakubowitz, J.P. Kretzer, Characterization of the running-in period in total hip resurfacing arthroplasty: an in vivo and in vitro metal ion analysis., *J. Bone Joint Surg. Am.* 90 Suppl 3 (2008) 125–33. doi:10.2106/JBJS.H.00437.
- [210] B. Patel, G. Favaro, F. Inam, M.J. Reece, A. Angadji, W. Bonfield, et al., Cobalt-based orthopaedic alloys: Relationship between forming route, microstructure and tribological performance, *Mater. Sci. Eng. C.* 32 (2012) 1222–1229. doi:10.1016/j.msec.2012.03.012.
- [211] J.R. Goldberg, J.L. Gilbert, Electrochemical response of CoCrMo to high-speed fracture of its metal oxide using an electrochemical scratch test method., *J. Biomed. Mater. Res.* 37 (1997) 421–31. <http://www.ncbi.nlm.nih.gov/pubmed/9368147> (accessed January 27, 2015).
- [212] M. Pourbaix, J. Burbank, Atlas D-Equilibres Electrochimiques, *J. Electrochem. Soc.* 111 (1964) 14C. doi:10.1149/1.2426051.
- [213] Y.L. Chou, J.W. Yeh, H.C. Shih, The effect of molybdenum on the corrosion behaviour of the high-entropy alloys Co<sub>1.5</sub>CrFeNi<sub>1.5</sub>Ti<sub>0.5</sub>Mox in aqueous environments, *Corros. Sci.* 52 (2010) 2571–2581. doi:10.1016/j.corsci.2010.04.004.

- [214] J.L. Tipper, P.J. Firkins, E. Ingham, J. Fisher, M.H. Stone, R. Farrar, Quantitative analysis of the wear and wear debris from low and high carbon content cobalt chrome alloys used in metal on metal total hip replacements., *J. Mater. Sci. Mater. Med.* 10 (1999) 353–62. <http://www.ncbi.nlm.nih.gov/pubmed/15348136> (accessed August 3, 2015).
- [215] K. Ilo, K. Aboelmagd, H. Hothi, R. Whittaker, A. Asaad, G. Blunn, et al., Modularity of Metal-on-Metal Hip Implants Increases Cobalt:Chromium Ratio, (2015). <http://prgmobileapps.com/AppUpdates/ors2015/Abstracts/abs963.html>.
- [216] J.-M. Brandt, K.D.J. Charron, L. Zhao, S.J. MacDonald, J.B. Medley, Commissioning of a displacement-controlled knee wear simulator and exploration of some issues related to the lubricant., *Proc. Inst. Mech. Eng. H.* 225 (2011) 736–52. <http://www.ncbi.nlm.nih.gov/pubmed/21922951> (accessed September 12, 2014).
- [217] W. Gresham, J.V.E. Hardy, *Synthesis of metal carbonyls*, (1949). <https://www.google.com/patents/US2473993>.
- [218] I. Dolamic, T. Bürgi, In Situ ATR-IR Study on the Photocatalytic Decomposition of Amino Acids over Au/TiO<sub>2</sub> and TiO<sub>2</sub>, *J. Phys. Chem. C.* 115 (2011) 2228–2234. doi:10.1021/jp1102753.
- [219] R.A. Goyer, T.W. Clarkson, *Toxic Effects of Metals*, 5th editio, McGraw-Hill, New York, 1996.
- [220] M. Ardon, P.D. Hayes, G. Hogarth, Microwave-Assisted Reflux in Organometallic Chemistry: Synthesis and Structural Determination of Molybdenum Carbonyl Complexes. An Intermediate-Level Organometallic-Inorganic Experiment, *J. Chem. Educ.* 79 (2002) 1249. doi:10.1021/ed079p1249.
- [221] A.K. Mishra, D.W. Shoesmith, Effect of Alloying Elements on Crevice Corrosion Inhibition of Nickel-Chromium-Molybdenum-Tungsten Alloys Under Aggressive Conditions: An Electrochemical Study, *Corrosion.* 70 (2014) 721–730. doi:10.5006/1170.
- [222] Outotec, HSC chemistry, (n.d.). <http://www.outotec.com/en/Products--services/HSC-Chemistry/>.
- [223] V.M. Salinas-Bravo, R.C. Newman, An alternative method to determine critical

pitting temperature of stainless steels in ferric chloride solution, *Corros. Sci.* 36 (1994) 67–77. doi:10.1016/0010-938X(94)90109-0.

- [224] J.R. Scully, N.D. Budiansky, Y. Tiwary, A.S. Mikhailov, J.L. Hudson, An alternate explanation for the abrupt current increase at the pitting potential, *Corros. Sci.* 50 (2008) 316–324. doi:10.1016/j.corsci.2007.08.002.
- [225] A.I. Muñoz, S. Mischler, Interactive Effects of Albumin and Phosphate Ions on the Corrosion of CoCrMo Implant Alloy, *J. Electrochem. Soc.* 154 (2007) C562. doi:10.1149/1.2764238.
- [226] M.T. Mathew, C. Nagelli, R. Pourzal, A. Fischer, M.P. Laurent, J.J. Jacobs, et al., Tribolayer formation in a metal-on-metal (MoM) hip joint: An electrochemical investigation, *J. Mech. Behav. Biomed. Mater.* 29 (2014) 199–212. <http://www.sciencedirect.com/science/article/pii/S1751616113002750> (accessed December 2, 2013).
- [227] S. Ray, A.G. Shard, Quantitative analysis of adsorbed proteins by X-ray photoelectron spectroscopy., *Anal. Chem.* 83 (2011) 8659–66. doi:10.1021/ac202110x.
- [228] T. Nakajima, Chemical Vapor Deposition of Tungsten Carbide, Molybdenum Carbide Nitride, and Molybdenum Nitride Films, *J. Electrochem. Soc.* 144 (1997) 2096. doi:10.1149/1.1837747.
- [229] F. Peng, L. Cai, H. Yu, H. Wang, J. Yang, Synthesis and characterization of substitutional and interstitial nitrogen-doped titanium dioxides with visible light photocatalytic activity, *J. Solid State Chem.* 181 (2008) 130–136. doi:10.1016/j.jssc.2007.11.012.
- [230] F. Werfel, E. Minni, Photoemission study of the electronic structure of Mo and Mo oxides, *J. Phys. C Solid State Phys.* 16 (1983) 6091–6100. doi:10.1088/0022-3719/16/31/022.
- [231] J.-G. Choi, L.T. Thompson, XPS study of as-prepared and reduced molybdenum oxides, *Appl. Surf. Sci.* 93 (1996) 143–149. doi:10.1016/0169-4332(95)00317-7.
- [232] A. Ouerd, C. Alemany-Dumont, B. Normand, S. Szunerits, Reactivity of CoCrMo alloy in physiological medium: Electrochemical characterization of the metal/protein interface, *Electrochim. Acta.* 53 (2008) 4461–4469. doi:10.1016/j.electacta.2008.01.025.

- [233] M. Lakatos-Varsányi, F. Falkenberg, I. Olefjord, The influence of phosphate on repassivation of 304 stainless steel in neutral chloride solution, *Electrochim. Acta.* 43 (1998) 187–197. doi:10.1016/S0013-4686(97)00224-7.

## Appendix A

### DRAFT PAPER

#### **Toxicity and oxidative stress response induced by nano- and micro-CoCrMo particles in human cells are cell specific**

Andrea L. Armstead,<sup>a,b</sup> Thiago A. Simoes,<sup>c</sup> Xianfeng Wang,<sup>a,d</sup> Rik Brydson,<sup>c</sup> Bing-Hua Jiang,<sup>e</sup> Yon Rojanasakul<sup>b,f</sup> and Bingyun Li<sup>a,b,f,\*</sup>

<sup>a</sup>*Biomaterials, Bioengineering & Nanotechnology Laboratory, Department of Orthopaedics, School of Medicine, West Virginia University, Morgantown, WV 26506, USA*

<sup>b</sup>*Department of Basic Pharmaceutical Sciences, School of Pharmacy, West Virginia University, Morgantown, WV 26506, USA*

<sup>c</sup>*Institute for Materials Research, SCAPE, University of Leeds, LS2 9JT, UK*

<sup>d</sup>*State Key Laboratory for Modification of Chemical Fibers and Polymer Materials, College of Materials Science and Engineering, and Key Laboratory of Textile Science and Technology, Ministry of Education, College of Textiles, Donghua University, Shanghai 201620, China*

<sup>e</sup>*Department of Pathology, Anatomy and Cell Biology, Thomas Jefferson University, Philadelphia, PA 19107, USA*

<sup>f</sup>*Mary Babb Randolph Cancer Center, Morgantown, WV 26506, USA*

*\*Correspondence to:*

Bingyun Li, PhD, Associate Professor

Director, Biomaterials, Bioengineering & Nanotechnology Laboratory

Department of Orthopaedics

School of Medicine, West Virginia University

1 Medical Center Drive

Morgantown, WV 26506-9196, USA

Tel: 1-304-293-1075, Fax: 1-304-293-7070, Email: [bili@hsc.wvu.edu](mailto:bili@hsc.wvu.edu)

URL: <http://medicine.hsc.wvu.edu/ortho-bli/>

**Short Title:** Toxicity of CoCrMo nanoparticles and microparticles

**Keywords:** Nanoparticle, microparticle, orthopaedic implant wear, toxicity, oxidative stress, cobalt chromium molybdenum

## ABSTRACT

Metal-on-metal (MoM) joint implants are used routinely during total hip and knee replacements and are typically composed of cobalt chromium molybdenum (CoCrMo) alloys. CoCrMo “wear particles”, in the nano- and micro-size ranges, are generated *in situ*. Meanwhile, occupational exposure to CoCrMo particles may be associated with the development of industrial dental worker’s pneumoconiosis and pulmonary exposure to CoCrMo particles is therefore a relevant concern in the manufacturing of MoM implants. The *objective* of this study was to examine the toxicity and oxidative stress response toward nano- and micro-sized CoCrMo particles *in vitro*. We *hypothesized* that nano- and micro-CoCrMo particles would exert cell-specific, time and dose-dependent toxicity and oxidative stress response in lung epithelial cells, osteoblasts and macrophages. We found that both nano- and micro-CoCrMo particles induced a time and dose-dependent toxicity in all three types of cells studied. Both nano- and micro-CoCrMo particles led to significant decreases in viability of lung epithelial cells and osteoblasts at doses of 100 and 1000  $\mu\text{g/mL}$  and macrophages at doses of 10, 100 and 1000  $\mu\text{g/mL}$ . The effect of particle size on cell viability was interesting and cell specific; compared to micro-CoCrMo, nano-CoCrMo significantly increased the viability of lung epithelial cells at doses of 100 and 1000  $\mu\text{g/mL}$  and of osteoblasts at 1000  $\mu\text{g/mL}$  and, by contrast, significantly reduced the viability of macrophages at 1000  $\mu\text{g/mL}$ . Similarly, the oxidative responses, represented by 2',7'-dichlorofluorescein diacetate (DCF) and dihydroethidium (DHE) fluorescences against nano- and micro-CoCrMo exposures were found to be cell specific. Nano-CoCrMo significantly increased the DCF levels in lung epithelial cells at 100 and 1000  $\mu\text{g/mL}$ , in osteoblasts at 0.1, 100 and 1000  $\mu\text{g/mL}$  and in macrophages at all doses studied (0.1-1000  $\mu\text{g/mL}$ ). Nano-CoCrMo significantly increased the DHE levels in osteoblasts and macrophages at all doses studied while no significant differences in DHE levels were seen in lung epithelial cells. Meanwhile, micro-CoCrMo significantly increased the DCF levels in lung epithelial cells at 10, 100 and 1000  $\mu\text{g/mL}$ , in osteoblasts at 0.1, 10, 100 and 1000  $\mu\text{g/mL}$  and in macrophages at all doses studied. It also significantly increased the DHE levels in osteoblasts and macrophages at all doses studied while no significant differences in DHE levels were observed in lung epithelial cells. Compared to micro-CoCrMo, nano-CoCrMo significantly increased the DCF levels in all cells studied at 100 and 1000  $\mu\text{g/mL}$  and significantly reduced the DCF levels in macrophages at 0.1, 1 and 10  $\mu\text{g/mL}$ . Compared to micro-CoCrMo, nano-CoCrMo significantly decreased the DHE levels at 0.1, 1, 10 and 100  $\mu\text{g/mL}$ , significantly increased the DHE levels at 1000  $\mu\text{g/mL}$  in osteoblasts and significantly increased the DHE levels in macrophages at all doses examined; no significant differences in DHE levels were observed in lung epithelial cells. Our findings highlight the potential roles that nano- and micro-CoCrMo particles, whether exposure is due to inhalation or implant wear, and associated oxidative stress may play in the increasingly reported implant loosening, osteolysis and systemic complications in orthopaedic patients, and may explain the risk of lung diseases in dental workers.

## INTRODUCTION

Over a million total hip replacement procedures are performed each year; one-third of these surgeries use metal-on-metal (MoM) implant devices composed of cobalt chromium molybdenum (CoCrMo) alloys [1-3]. While MoM implant devices offer advantages, such as increased strength and resistance to wear, over previous implant technology employing polymeric and/or ceramic articulating surfaces, they are not

without their faults and risks [4, 5]. In particular, new evidence is emerging that MoM CoCrMo implants generate wear particles *in situ*, within the micro- and nano-size range, as a result of implant breakdown between the articulating joint surfaces [4-11]. The generation of wear particles increases when the implant is improperly aligned, causing aseptic loosening of the joint, uneven wear and damage within the implant area [5, 9]. The current literature suggests that CoCrMo wear particles released locally within the joint area and surrounding tissues may cause cellular toxicity and a subsequent inflammatory response [4, 5, 9, 11].

Given this evidence and emerging concerns regarding the long term effects of CoCrMo particle exposure in joint replacement patients, the toxicity of CoCrMo wear particles has recently been explored *in vitro* [1, 4, 6, 8, 10-26] and *in vivo* [27-29]. To date, CoCrMo particle toxicity has been reported in cell types such as osteoblasts, osteoclasts, fibroblasts, leukocytes and macrophages and CoCrMo particle exposure has been found to cause reproductive toxicity [30, 31], genotoxicity and inflammatory immune reactions in exposed mice [7, 27, 28].

In addition to “internal” and localized CoCrMo particle exposure due to MoM implant wear, alternative routes of exposure such as inhalation or secondary exposure(s) due to particle translocation or migration from the initial site must be considered. For instance, CoCrMo particle inhalation may occur during the manufacturing and production of MoM implants in the medical device industry, thereby presenting an occupational exposure hazard. Although occupational exposure to CoCrMo particles has not been directly reported to date in orthopaedic implant manufacturing settings, pulmonary exposure to CoCrMo “dusts” with a similar composition to MoM orthopaedic implant material have been reported previously in dental implant manufacturing settings [32]. Inhalation of CoCrMo particles might have been associated with the “dental technician’s pneumoconiosis” (DTP) in a number of cases [32-38]. In other industrial and manufacturing settings, inhalation of cobalt-containing metal “dusts”, such as tungsten carbide cobalt (WC-Co), have been well-associated with the development of pneumoconiosis, occupational asthma and lung disease with increased risk of lung cancer [39-52]. For DTP resulting from exposure to CoCrMo particles, patients develop lung disease with a similar clinical presentation to hard metal lung disease (HMLD) resulting from occupational inhalation of WC-Co particles [9, 38, 53]; therefore, we believe it is pertinent to examine the effects of CoCrMo particle exposure in a relevant *in vitro* pulmonary model.

Additionally, there is an emerging body of literature which demonstrates that particles within the nano-size range are capable of tissue translocation and migration to other organs, such as the liver, spleen or lungs [54-69], where tissue deposition occurs and a secondary particle exposure is generated. This phenomenon may occur for CoCrMo particles generated internally at orthopaedic implant sites and the potential for secondary CoCrMo toxicity at sites distant from the initial exposure cannot be excluded. Therefore, it is critically important to understand the full range of effects of CoCrMo particle exposure on a variety of cell types which are potential targets for CoCrMo particle exposure, whether the initial exposure was due to internal particle generation from orthopaedic implants or from external sources such as inhalation in occupational settings. The goal of the current study was to examine the toxicity and oxidative stress response toward nano- and micro-sized CoCrMo particles, for the first time, in an *in vitro* pulmonary model using lung epithelial cells and compare the outcomes with other implant site relevant cells such as human osteoblasts and macrophages using a nanotoxicity model recently developed in our lab [70]. Based on our current understanding of CoCrMo particle toxicity, we *hypothesized* that nano- and

micro-CoCrMo particles would exert cell-specific, time and dose-dependent toxicity and oxidative stress response in lung epithelial cells, osteoblasts and macrophages.

## **MATERIALS and METHODS**

**Materials and Reagents:** CoCrMo microparticles (micro-CoCrMo) in the form of gas atomized powders from ASTM75 implants were used as received from Sandvik Osprey (Sandviken, Sweden); the chemical composition was  $63.3 \pm 1.1$  wt.% Co,  $30.2 \pm 0.7$  wt.% Cr and  $6.5 \pm 1.2$  wt.% Mo. Human lung bronchial epithelial BEAS-2B cells [70], THP-1 (TIB-202) human monocyte/macrophage [71] and h.FOB1.19 (CRL-11372) human osteoblast cells [72-75] from our previous studies were from American Type Tissue Collection (ATCC; Manassas, VA). Dulbecco's Modified Eagle Media (DMEM), Ham's F12 Medium, sterile phosphate buffered saline (PBS), 0.25% trypsin/ethylenediaminetetraacetic acid (EDTA), fetal bovine serum (FBS), G418 sulfate (geneticin) cell selection agent and penicillin/streptomycin were purchased from Lonza (Allendale, NJ). RPMI-1640 culture medium was purchased from ATCC. Isopropanol, hydrochloric acid, Triton-X-100, thiazolyl blue tetrazolium bromide (MTT reagent), 2',7'-dichlorofluorescein diacetate (DCF), dihydroethidium (DHE) and phorbol-12-myristate-13-acetate (PMA) were purchased from Sigma-Aldrich (St. Louis, MO).

**Particle Preparation:** CoCrMo nanoparticles (nano-CoCrMo) were obtained via mechanical milling of the micro-CoCrMo particles. In brief, micro-CoCrMo particles were milled in 20 g/L of a heat shocked fetal bovine serum (FBS) solution (pH 7.0). The powders were ball milled for 2.5 hr at a ball-to-powder weight ratio of 3:2 in a high energy Spex 8000M mill (Metuchen, NJ) using zirconium oxide ceramic vials and balls. Before milling, the vial was fully filled with an inert gas (Argon) to avoid atmospheric contamination. After collection, samples were centrifuged in a Heraeus Megafuge at 25°C for 10 min with a centrifugal force of 8000G to remove most of the FBS and coarse particles. Fine particles in the dispersion were collected for this study. For cell culture studies, both nano- and micro-CoCrMo particles were prepared using our previous protocol [76] in a phosphate buffered saline (PBS) solution containing 10% FBS as a stabilization agent and sonicated using an Omni International Sonic Ruptor 250 Ultrasonic Homogenizer (Kennesaw, GA). A stock concentration of 5 mg/mL CoCrMo particles was prepared by sonication (2 min, 120 watts power output, frequency 20 kHz) in an ice bath, to minimize heating of the sample during particle dispersion. Dilute particle suspensions, ranging from 0.1 to 1000  $\mu\text{g/mL}$ , were prepared in DMEM containing 10% FBS and used immediately on the day of each experiment. Note that from an occupational standpoint, exposure limits have been set for cobalt particles alone, but limits have yet to be defined for cobalt-containing alloys such as CoCrMo or WC-Co, which have been reported to cause similar types of pneumoconiosis following pulmonary exposure [32-36, 38-53]. Further, it is difficult to define an exact *in vitro* dosage parameter due to the variability and extent of MoM orthopaedic implant wear on an individual patient basis. Therefore, in this study, we intentionally encompassed a range of particle exposures, from 0.1 to 1000  $\mu\text{g/mL}$ , to represent the potential range in CoCrMo exposure which may occur in occupational implant manufacturing settings and in orthopaedic patient implant wear particle exposures.

**Particle Characterization:** The particle size of nano-CoCrMo was analyzed using transmission electron microscopy (TEM) with a FEI Tecnai F20 field emission gun TEM operated at 200 kV and fitted with an Oxford Instruments ultrathin window ISIS

energy dispersive X-ray (EDX) system. A 3.5  $\mu\text{L}$  droplet of particle dispersion was placed on a glow discharge-treated carbon support film (R1.2/1.3 Quantifoil MicroTools GmbH; measured hole diameter of 1.65  $\mu\text{m}$ ), blotted and plunge frozen in liquid ethane [77]. Average particle size was achieved by measuring Feret diameter of ca. 300 particles, which is defined as the distance between the most widely spaced nanoparticles in an agglomerate [77]. The particle size of micro-CoCrMo particles was characterized using scanning electron microscope (SEM). Secondary electron images were taken using a Hitachi SU8230 Ultimate Cold Field Emission operated at 2 keV, 8.2 mm working distance and employing an in-lens electron detector. Elemental composition was determined via EDX. In addition, the average sizes of nano- and micro-CoCrMo particles in suspension were determined using dynamic light scattering (DLS, Malvern Zetasizer version 7.01, Malvern Instruments).

**CoCrMo Particle Assay Interference:** Prior to execution of the cell viability and oxidative stress assays, the potential interference of CoCrMo particles was examined under the experimental conditions. To test compatibility with the MTT-based cell viability assay, 200  $\mu\text{L}$  of CoCrMo suspensions (0.1 to 1000  $\mu\text{g}/\text{mL}$  in DMEM) was added to duplicate wells in a 96-well plate. The plate was briefly centrifuged ( $500 \times g$ , 5 min) to pellet the particles at the bottom of the wells. The supernatant was then aspirated and 100  $\mu\text{L}$  of plain (un-supplemented) DMEM was added to each well containing CoCrMo particles, along with 10  $\mu\text{L}$  of MTT reagent. After 2 hr incubation at 37°C, 100  $\mu\text{L}$  of solubilization solution was added to each well and the absorbance was determined at 570 nm. Any auto-reduction of the MTT dye reagent to formazan by the CoCrMo particles themselves would have been detected as an increase in absorbance compared to the blank wells, containing only media, MTT dye reagent and solubilization solution. Similarly, for the oxidative stress assay, we tested whether the CoCrMo particles caused increased fluorescence of either DCF or DHE under our assay conditions. CoCrMo particle suspensions were plated and centrifuged in duplicate wells of a 96-well plate as described above. The supernatant was then aspirated and replaced with 100  $\mu\text{L}$  of 10  $\mu\text{M}$  DCF or DHE working solution prepared in PBS. Plates were incubated for 15 min in the dark and then the fluorescence intensity of each well was quantified every 5 min, up to one hour, at 520 nm for DCF or 620 nm for DHE, to identify any potential particle/dye interference compared to the blank (dye solution only) wells.

**Cell Culture and THP-1 Macrophage Differentiation:** BEAS-2B lung epithelial cells were cultured in DMEM supplemented with 10% FBS and 1% penicillin-streptomycin and maintained at 37°C and 5%  $\text{CO}_2$ . Human osteoblasts (h.FOB 1.19) were cultured in 1:1 Ham's F12/DMEM supplemented with 10% FBS, 1% penicillin-streptomycin and 0.3 mg/mL G418 and maintained at 37°C and 5%  $\text{CO}_2$ . Upon confluency, BEAS-2B and osteoblasts (OB) were rinsed with PBS and trypsinized, transferred to 15 mL tubes and centrifuged at 1200 rpm for 7 min to pellet. Cell pellets were re-suspended in appropriate media at the desired plating density of  $1.5 \times 10^5$  cells/mL, transferred to a 96-well tissue culture plate and allowed to adhere overnight prior to the assay(s).

THP-1 monocytes were maintained in suspension culture in RPMI-1640 supplemented with 10% FBS, 1% penicillin-streptomycin and 0.05 mM beta-mercaptoethanol and maintained at 37°C and 5%  $\text{CO}_2$ . Upon confluency, THP-1 cells were transferred to 15 mL tubes and centrifuged at  $125 \times g$  for 5 min to pellet. The cell pellet was re-suspended in RPMI-1640 containing 10 ng/mL PMA, which induces THP-1 monocytes to undergo macrophage (M0) differentiation, and plated in a 96-well culture plate at the desired density of  $1.5 \times 10^5$  cells/mL. After 24 hr, THP-1 to M0

differentiation was confirmed via examination of cell morphology using a light microscope [78, 79], where M0 cells underwent a signature change in morphology and became adherent to the culture dish.

**CoCrMo Particle Exposure:** Exposure to nano- and micro-CoCrMo particles was achieved by aspirating the media from each well and immediately replacing it with an equivalent volume of CoCrMo particle suspension at a concentration of 0.1-1000  $\mu\text{g}/\text{mL}$ . Cell plates were then incubated at 37° C and 5% CO<sub>2</sub> for exposure periods of 6, 12, 24 and 48 hr.

**Cell Viability Assay:** For the viability assay, cells were exposed to either nano- or micro-CoCrMo particles at concentrations of 0.1, 1, 10, 100 and 1000  $\mu\text{g}/\text{mL}$  for exposure periods of 6, 12, 24 and 48 hr. Following particle treatment, cells were rinsed once with sterile PBS to remove traces of media and excess particles. Then, 100  $\mu\text{L}$  of un-supplemented DMEM was added to each well, followed by the addition of 10  $\mu\text{L}$  MTT reagent to achieve a final concentration of 0.5 mg/mL MTT reagent per well. Cells were incubated for 2 hr at 37° C and 5% CO<sub>2</sub> to allow conversion of the soluble salt (yellow) to formazan crystals (purple). Crystal formation was confirmed using light microscopy. 100  $\mu\text{L}$  of solubilization solution (0.1 M HCl in isopropanol with 10% Triton-X) was then added to each well to dissolve the formazan crystals and the absorbance of each well was recorded at 570 nm using a Bio-Tek  $\mu\text{Quant}$  microplate reader (Winooski, VT). Blank values were subtracted from absorbance readings. Cell viability was calculated by dividing the absorbance of particle treated cells by the absorbance of control cells receiving media treatment only and converted to percentage; control cells represented 100% viability.

**Oxidative Stress Assay:** Oxidative stress was examined at the same CoCrMo particle concentrations and exposure range described for the viability assay (above). Following particle treatment, cells were rinsed once with sterile PBS to remove traces of media and excess particles. Oxidative stress was then determined by the addition of 10  $\mu\text{M}$  DCF or DHE in PBS following particle treatment. Plates were incubated for 15 min in the dark and then fluorescence intensity of each well was quantified at 520 nm for DCF or 620 nm for DHE using a Bio-Tek Synergy H4 plate reader (Winooski, VT). The relative fluorescence of particle-treated cells was calculated as fold over control.

**Statistical Analyses:** All experiments were performed in triplicate and data are presented as mean  $\pm$  standard deviation. Statistical analysis was carried out by two-way analysis of variance (ANOVA) using GraphPad Prism 6 software (La Jolla, CA). P values < 0.05 were considered significant.

## RESULTS

**CoCrMo Particle Characterization and Assay Interference:** TEM and SEM examinations showed that the nano- and micro-CoCrMo particles had average sizes of 35.4 nm (**Figures 1A and C**) and 4.8  $\mu\text{m}$  (**Figures 1B and D**), respectively. DLS analysis indicated that nano-CoCrMo averaged 54 nm and micro-CoCrMo particles averaged 5.0  $\mu\text{m}$  in suspensions. EDX confirmed that the composition of nano- and micro-CoCrMo particles were largely Co, Cr and Mo (**Figure S1**). We did not find any significant CoCrMo particle interference in our assays; no significant auto-reduction of the MTT dye was identified in the viability assay (**Figure S2**) and no significant changes in DCF/DHE fluorescence were observed due to CoCrMo particles under the assay conditions tested (**Figure S3**).

**CoCrMo Effects on Cell Viability:** BEAS-2B, OB and M0 were exposed to nano- and micro-CoCrMo particles at concentrations of 0.1, 1, 10, 100 and 1000  $\mu\text{g/mL}$  for durations of 6, 12, 24 and 48 hr. For BEAS-2B, the average cell viability was about 90-98% (vs. control of 100%) for cells exposed to nano- and micro-CoCrMo particles at concentrations of 0.1, 1 and 10  $\mu\text{g/mL}$  for durations of 6-48 hr; the cell viability tended to decrease with increasing particle exposure time from 6 hr to 48 hr at concentrations of both 100 and 1000  $\mu\text{g/mL}$  (**Figure 2**). In cells exposed to nano-CoCrMo particles (**Figure 2A**), a significant reduction in viability (compared to control) was observed at 100  $\mu\text{g/mL}$  after 12, 24 and 48 hr of exposure and at the highest concentration of 1000  $\mu\text{g/mL}$  after 6-48 hr of exposure. Similarly, in BEAS-2B cells exposed to micro-CoCrMo particles (**Figure 2B**), a significant reduction in viability (compared to control) was observed at 100  $\mu\text{g/mL}$  after 12, 24 and 48 hr of exposure and at the highest concentration of 1000  $\mu\text{g/mL}$  after 6-48 hr of exposure. When comparing the toxicity of nano- and micro-CoCrMo under identical conditions, nano-CoCrMo caused significantly less toxicity than micro-CoCrMo in BEAS-2B cells at 100  $\mu\text{g/mL}$  after 24 and 48 hr of exposure and at 1000  $\mu\text{g/mL}$  after 6 and 12 hr of exposure; toxicity was similar for 1000  $\mu\text{g/mL}$  nano- and micro-CoCrMo after 24 and 48 hr of exposure.

For OB, cell viability remained high ( $> 90\%$ ) over the exposure periods tested (6-48 hr) for 0.1-10  $\mu\text{g/mL}$  nano- and micro-CoCrMo particles (**Figure 3**). At 100 and 1000  $\mu\text{g/mL}$ , a significant decrease in cell viability (compared to control) was observed after 6-48 hr exposure of nano- (**Figure 3A**) and micro-CoCrMo (**Figure 3B**) particles and the cell viability decreased with increasing exposure time. There were no significant differences in the toxicity of nano- and micro-CoCrMo particles over the concentration and exposure range studied, with the exception of 1000  $\mu\text{g/mL}$ , where nano-CoCrMo caused significantly less toxicity than micro-CoCrMo in OB after 24 hr of exposure ( $\sim 70\%$  vs.  $\sim 60\%$  remaining cell viability, respectively).

In M0, cell viability remained  $> 90\%$  for the lowest concentrations of 0.1 and 1  $\mu\text{g/mL}$  over the 6-48 hr exposure period for both nano- and micro-CoCrMo (**Figure 4**). M0 exposed to nano-CoCrMo had significantly reduced viability (compared to control) after 24 and 48 hr exposure to 10  $\mu\text{g/mL}$  (**Figure 4A**); no significant toxicity was observed between CoCrMo particles and controls at this concentration in either BEAS-2B or OB under these conditions. Significantly reduced cell viability was also observed for the micro-CoCrMo particles at 10  $\mu\text{g/mL}$  after 48 hr of exposure (**Figure 4B**). Moreover, at 100 and 1000  $\mu\text{g/mL}$ , a significant decrease in cell viability (compared to control) was observed for both nano- and micro-CoCrMo particles at the time exposures studied except at 6 hr of 100  $\mu\text{g/mL}$  of micro-CoCrMo particles. When compared directly, M0 viability after exposure to 1000  $\mu\text{g/mL}$  nano-CoCrMo for 24 and 48 hr was significantly lower than M0 exposed to micro-CoCrMo particles under identical conditions.

**CoCrMo Effects on Oxidative Stress:** Oxidative stress was measured in the form of DCF/DHE fluorescence after exposure to nano- and micro-CoCrMo particles under identical exposure conditions tested in the viability assay. Compared to control, there was a significant increase in DCF fluorescence in BEAS-2B cells exposed to 100  $\mu\text{g/mL}$  nano-CoCrMo after 6, 12 and 24 hr of exposure and at 1000  $\mu\text{g/mL}$  after 6, 12, 24 and 48 hr of exposure; a maximum 3.5 fold increase in DCF fluorescence was observed in BEAS-2B cells exposed to 1000  $\mu\text{g/mL}$  nano-CoCrMo after 6 hr of exposure, after which DCF fluorescence decreased with increasing exposure time (**Figure 5A**). In BEAS-2B cells exposed to micro-CoCrMo particles, a significant increase in DCF fluorescence was observed after 6 hr exposure to 10 and 100  $\mu\text{g/mL}$

and after 6, 12, 24 and 48 hr exposure to 1000 µg/mL micro-CoCrMo; a maximum 2.3 fold increase in DCF fluorescence was observed in cells exposed to 1000 µg/mL micro-CoCrMo after 6 hr of exposure (**Figure 5B**). At 1000 µg/mL of both nano- and micro-CoCrMo particles, the DCF fluorescence decreased with increasing exposure time (**Figure 5**). In addition, nano-CoCrMo particles caused a significantly greater change in DCF fluorescence compared to micro-CoCrMo particles after 6, 12 and 24 hr exposure to 100 µg/mL and after 6, 12, 24 and 48 hr at 1000 µg/mL (**Figure 5**).

For DHE, no significant differences, compared to control, were observed in BEAS-2B fluorescence after exposure to nano-CoCrMo (**Figure 6A**) or micro-CoCrMo (**Figure 6B**) particles. The observed DHE fluorescence in BEAS-2B cells exposed to both nano- and micro-CoCrMo particles was about the same as the control cells at all concentrations (0.1-1000 µg/mL) and exposure times (6-48 hr) studied.

In OB, nano-CoCrMo caused a significant increase in DCF fluorescence, compared to control, at 0.1 µg/mL after 12 hr, at 100 µg/mL after 12 and 24 hr and a maximum increase in DCF fluorescence at 1000 µg/mL after 24 hr of exposure, about 1.5-fold higher than control (**Figure 7A**). Exposure to micro-CoCrMo caused significantly increased DCF fluorescence, compared to control, after 12 hr exposure to 0.1, 10, 100 and 1000 µg/mL and after 24 hr exposure to 1000 µg/mL (**Figure 7B**). Overall, nano-CoCrMo caused significantly higher DCF fluorescence than micro-CoCrMo in OB after 24 hr exposure to 100 and 1000 µg/mL (**Figure 7**).

A varied effect on DHE fluorescence was observed in OB exposed to nano- and micro-CoCrMo particles (**Figure 8**). Compared to control, a significant increase in DHE fluorescence was observed in OB exposed to nano-CoCrMo at 0.1 µg/mL after 48 hr, at 1 µg/mL after 6, 24 and 48 hr, at 10 µg/mL after 12, 24 and 48 hr, at 100 µg/mL after 6 and 12 hr and at 1000 µg/mL after 6, 12, 24, and 48 hr of exposure (**Figure 8A**). For micro-CoCrMo particles, a significant increase in DHE, compared to control, was observed for 0.1-1000 µg/mL after 6 hr of exposure and for 1, 10, 100 and 1000 µg/mL after 12 hr of exposure (**Figure 8B**). Compared to micro-CoCrMo, nano-CoCrMo caused significantly less DHE fluorescence at 0.1 and 1 µg/mL after 6 hr and at 1, 10 and 100 µg/mL after 12 hr; however, at 1000 µg/mL, nano-CoCrMo caused significantly higher DHE fluorescence than micro-CoCrMo after 6, 24 and 48 hr of exposure (**Figure 8A**).

In M0, nano- and micro-CoCrMo particles caused significant increases in DCF fluorescence, compared to control, at all concentrations (0.1-1000 µg/mL) and exposure times tested (**Figure 9**). The maximum increase in DCF was observed at 1000 µg/mL after 6 and 12 hr exposure (**Figure 9**) for both nano- and micro-CoCrMo particles. Compared directly, nano-CoCrMo caused significantly less DCF fluorescence than micro-CoCrMo particles after 12 hr exposure to 0.1, 10 and 100 µg/mL; however, nano-CoCrMo caused significantly higher DCF fluorescence than micro-CoCrMo after 6 and 12 hr exposure to 100 µg/mL and after 24 and 48 hr exposure to 1000 µg/mL (**Figure 9**).

Significantly increased DHE fluorescence, compared to control, was observed in M0 exposed to nano-CoCrMo at all concentrations tested (0.1-1000 µg/mL) after 6, 12 and 24 hr of exposure; no changes in DHE were observed after 48 hr of exposure at any concentration (**Figure 10A**). In M0 exposed to micro-CoCrMo, a significant increase in DHE fluorescence was observed after 6 and 12 hr exposure to 0.1-1000 µg/mL; DHE levels were similar to control at all concentrations after 24 and 48 hr of exposure to micro-CoCrMo (**Figure 10B**). Compared to micro-CoCrMo, nano-CoCrMo caused significantly higher DHE levels in M0 at all concentrations (0.1-1000 µg/mL) after 12 and 24 hr of exposure (**Figure 10**).

## DISCUSSION

Nanoparticles, due to their smaller size, have a higher capacity (compared to microparticles) to enter the circulatory system and deposit in tissues and organs such as liver, spleen, kidney, lymph node and lung [9, 56, 57, 80, 81], and the potential systemic effects of nanoparticle exposure could be of importance [37, 82, 83]. However, the role of nanoparticles and microparticles from orthopaedic implant wear in systemic responses is unknown although patients who undergo MoM joint replacements have presented translocation and deposition of CoCrMo wear particles in lymph nodes, liver and spleen [7-9, 84]. Meanwhile, inhalation of cobalt-containing metal particles may be associated with dental technician's pneumoconiosis [32-34, 36, 38, 53], and CoCrMo wear particles have also been a major concern of local toxicity and inflammation. Therefore, the goal of this study was to examine the toxic effects of nano- and micro-sized CoCrMo particles, originating from ASTM F75 orthopaedic implant materials, in a range of relevant cell types representing the potential routes of exposures, including lung epithelial cells, osteoblasts and macrophages.

Our studies suggest that both nano- and micro-CoCrMo particles can induce toxicity in all cell types studied and the responses of cell viability and oxidative stress are dose, exposure time and cell type specific. Across the three cell types tested, at low concentrations (i.e. 0.1 and 1  $\mu\text{g}/\text{mL}$ ), nano- and micro-CoCrMo particles did not cause significant toxicity in our viability assay. Typically, in the presence of small amounts of foreign particles, cells may isolate the particles in internal phagolysosomal compartments, which could prohibit them from further interacting with other cellular components thereby preventing extensive cellular toxicity [19, 85-88]. The similarity in low toxicity between the nano- and micro-CoCrMo particles reported here in lung epithelial cells, osteoblasts and macrophages at concentrations less than 10  $\mu\text{g}/\text{mL}$  seems to support the high biocompatibility of CoCrMo alloys in orthopaedic settings [89]; CoCrMo has been used prevalently in orthopaedic surgeries [9]. At high concentrations (i.e. 100 and 1000  $\mu\text{g}/\text{mL}$  for BEAS-2B and OB cells, and 10, 100 and 1000  $\mu\text{g}/\text{mL}$  for M0 cells), both nano- and micro-CoCrMo particles could lead to significant decreases in viability in all cell types tested. It was reported that significant toxicity was observed in osteoblast-like cells exposed to  $\geq 100 \mu\text{g}/\text{mL}$  micro-CoCr alloy particles after 24 and 48 hr exposure [12]. The current study provides direct evidence that nano- and micro-CoCrMo particles cause toxicity toward lung epithelial cells *in vitro*, which may help explain the risk of lung disease in dental workers [32, 33, 35, 36, 38, 53] and highlights the need for further examination of pulmonary toxicity caused by CoCrMo particles, whether exposure is due to inhalation (in the case of DTP) or local implant wear particles.

One would normally expect that nanoparticles exert greater toxic effects than microparticles of the same chemical composition due to their smaller size and increased surface area [37, 57, 81, 90-94]. However, in this study, no significant differences in cell viability were observed between nano- and micro-CoCrMo particle exposures in most of the concentrations and exposure times studied. Interestingly, compared to micro-CoCrMo particles, nano-CoCrMo particles led to significantly lower viability of macrophages and significantly higher viability of lung epithelial cells and osteoblasts at 1000  $\mu\text{g}/\text{mL}$ . In macrophages, it was believed that nanoparticles, due to their smaller size and thereby faster degradation, could lead to more impairment in phagocytosis and be more toxic to macrophages compared to microparticles [91, 95-97]. It is not clear

why nano-CoCrMo was less toxic, compared to micro-CoCrMo, to lung epithelial cells and osteoblasts in this study and further investigations are much needed.

Oxidative stress has been implicated in age-related bone resorption and osteoporosis [98, 99] and in toxicity of CoCrMo particles in fibroblasts [6, 18, 20, 22, 100], and may also play a role in the progression of lung diseases [101], such as those caused by cobalt-containing metal exposures [102]. Therefore, it is important to examine the capacity of nano- and micro-CoCrMo particles in causing oxidative stress in our cell models. In this case, we used a two-fold approach to assess the induction of oxidative stress using DCF, which serves as a ‘generalized’ marker for reactive oxygen species [103], and DHE, which serves as a specific marker of superoxide anion [104]. It seems that the oxidative responses against nano- and micro-CoCrMo particles were cell specific: both nano- and micro-CoCrMo particles resulted in significantly higher DCF levels and DHE levels in OB and M0 cells; significantly higher DCF and DHE levels were observed in macrophages at all concentrations studied (0.1-1000  $\mu\text{g/mL}$ ). It seems that the OB cells behaved like the M0 immune cells, which are known to exhibit a “respiratory burst” upon phagocytosis of microbes, marked by significant increases in the production of hydrogen peroxide and superoxide anion via enzymatic pathways that are critical for initiating anti-microbial response and infection clearance [105]. The significantly increased oxidative stress of OB and M0 cells may have contributed to the increased risks of implant loosening and osteolysis in orthopaedic implant patients. By contrast, BEAS-2B cells had no significant DHE changes but had significantly increased DCF levels at relatively high particle concentrations (e.g. 100 and 1000  $\mu\text{g/mL}$ ). Moreover, nano-CoCrMo caused significantly higher levels of oxidative stress in lung epithelial cells compared to micro-CoCrMo particles at concentrations of 100 and 1000  $\mu\text{g/mL}$ , which was consistent with the expected size-dependent effect due to the increased reactive surface area of nano-CoCrMo compared to micro-CoCrMo. No significant differences were found in the DHE assay, which suggests that CoCrMo particles cause oxidative stress via other species than superoxide anion. Additionally, we found these results were consistent with the fibroblast studies in the literature [18, 22], which found high levels of oxidative stress, marked by increased levels of DCF fluorescence, after as little as 2 hr of exposure [22] and increased levels of 8-OHdG staining, a marker of oxidative stress induced DNA damage, after 24 hr of exposure to CoCrMo particles [18]. Increased levels of oxidative stress in lung epithelial cells could ultimately lead to downstream effects such as DNA damage and genotoxicity upon long term exposure [16, 18-20] and may therefore be a contributing factor in the development of lung disease from pulmonary CoCrMo particle exposure in occupational settings.

## CONCLUSION

This study examined the toxicity of nano- and micro-CoCrMo particles and determined whether their exposure induced oxidative stress in human lung epithelial cells, osteoblasts and macrophages. We found that both nano- and micro-CoCrMo particles can induce toxicity to osteoblasts and lung epithelial cells at doses of 100  $\mu\text{g/mL}$  or higher and to macrophages at doses of 10  $\mu\text{g/mL}$  or higher, and the toxicity and oxidative responses are cell specific. Compared to micro-CoCrMo particles, nano-CoCrMo particles resulted in significantly lower viability of macrophages at 1000  $\mu\text{g/mL}$  and significantly higher viability of lung epithelial cells at 100 and 1000  $\mu\text{g/mL}$  and osteoblasts at 1000  $\mu\text{g/mL}$ . At the same dose, significantly reduced viability of macrophages was also seen at shorter exposure times (e.g. 24 hr at 10  $\mu\text{g/mL}$  and 6 hr at 100  $\mu\text{g/mL}$ ) exposed to nano-CoCrMo compared to micro-CoCrMo. Meanwhile,

compared to control, both nano- and micro-CoCrMo may lead to significantly increased DCF levels in the cell types tested. Compared to control, no significant differences in DHE levels were observed in lung epithelial cells while significantly higher DHE levels were found in both osteoblasts and macrophages at 0.1-1000  $\mu\text{g/mL}$ . Compared to micro-CoCrMo, nano-CoCrMo particle treatment also caused significantly higher DCF levels in all three types of cells at high particle concentrations (i.e. 100 and 1000  $\mu\text{g/mL}$ ) and significantly lower DCF levels at 0.1, 1 and 10  $\mu\text{g/mL}$  in macrophages. Nano-CoCrMo, compared to micro-CoCrMo, also resulted in significantly lower DHE levels at 0.1, 1, 10 and 100  $\mu\text{g/mL}$  and significantly higher DHE levels at 1000  $\mu\text{g/mL}$  in osteoblasts; there were also significantly higher DHE levels in macrophages at all doses studied. Therefore, these *in vitro* findings suggest that both nano- and micro-CoCrMo particles can induce toxicity and the responses of cell viability and oxidative stress are dose, exposure time and cell type specific.

#### **ACKNOWLEDGEMENT**

We acknowledge financial support from the AO Foundation (Project S-13-15 L was supported by the AO Foundation) and the West Virginia National Aeronautics and Space Administration Experimental Program to Stimulate Competitive Research (WV NASA EPSCoR). AA thanks the American Foundation for Pharmaceutical Education for her Pre-Doctoral Fellowship in Pharmaceutical Sciences award 2012-14. We acknowledge use of the WVU Shared Research Facilities. The authors thank Dale Porter for assistance with dynamic light scattering analysis and Suzanne Danley for proofreading.

## FIGURE AND TABLE LEGEND

**Figure 1.** A,B) Images and C,D) particle size distribution of A,C) nano- and B, D) micro-CoCrMo particles.

**Figure 2.** Viability of BEAS-2B lung epithelial cells after exposure to A) nano- and B) micro-CoCrMo particles. (\*P < 0.05, †P < 0.01 compared to control; ‡P < 0.05 vs. micro-CoCrMo)

**Figure 3.** Viability of osteoblasts after exposure to A) nano- and B) micro-CoCrMo particles. (\*P < 0.05, †P < 0.01 compared to control; ‡P < 0.05 vs. micro-CoCrMo)

**Figure 4.** Viability of macrophages after exposure to A) nano- and B) micro-CoCrMo particles. (\*P < 0.05, †P < 0.01 compared to control; ‡P < 0.05 vs. micro-CoCrMo)

**Figure 5.** BEAS-2B oxidative stress measured via fluorescence intensity of DCF after exposure to A) nano- and B) micro-CoCrMo particles. (\*P < 0.05, †P < 0.01 compared to control; ‡P < 0.05 vs. micro-CoCrMo)

**Figure 6.** BEAS-2B oxidative stress measured via fluorescence intensity of DHE after exposure to A) nano- and B) micro-CoCrMo particles. (\*P < 0.05, †P < 0.01 compared to control; ‡P < 0.05 vs. micro-CoCrMo)

**Figure 7.** Osteoblast oxidative stress measured via fluorescence intensity of DCF after exposure to A) nano- and B) micro-CoCrMo particles. (\*P < 0.05, †P < 0.01 compared to control; ‡P < 0.05 vs. micro-CoCrMo)

**Figure 8.** Osteoblast oxidative stress measured via fluorescence intensity of DHE after exposure to A) nano- and B) micro-CoCrMo particles. (\*P < 0.05, †P < 0.01 compared to control; ‡P < 0.05 vs. micro-CoCrMo)

**Figure 9.** Macrophage oxidative stress measured via fluorescence intensity of DCF after exposure to A) nano- and B) micro-CoCrMo particles. (\*P < 0.05, †P < 0.01 compared to control; ‡P < 0.05 vs. micro-CoCrMo)

**Figure 10.** Macrophage oxidative stress measured via fluorescence intensity of DHE after exposure to A) nano- and B) micro-CoCrMo particles. (\*P < 0.05, †P < 0.01 compared to control; ‡P < 0.05 vs. micro-CoCrMo)

## REFERENCES

1. Goode, A.E., et al., *Chemical speciation of nanoparticles surrounding metal-on-metal hips*. Chemical Communications, 2012. **48**(67): p. 8335-8337.
2. Varma, A., B.Y. Li, and A. Mukasyan, *Novel synthesis of orthopaedic implant materials*. Advanced Engineering Materials, 2002. **4**(7): p. 482-487.
3. Li, B.Y., A. Mukasyan, and A. Varma, *Combustion synthesis of CoCrMo orthopedic implant alloys: microstructure and properties*. Materials Research Innovations, 2003. **7**(4): p. 245-252.
4. Ingham, E. and J. Fisher, *Biological reactions to wear debris in total joint replacement*. Proceedings of the Institution of Mechanical Engineers Part H-Journal of Engineering in Medicine, 2000. **214**(H1): p. 21-37.
5. Pourzal, R., et al., *Characterization of Wear Particles Generated from CoCrMo Alloy under Sliding Wear Conditions*. Wear, 2011. **271**(9-10): p. 1658-1666.
6. Germain, M.A., et al., *Comparison of the cytotoxicity of clinically relevant cobalt-chromium and alumina ceramic wear particles in vitro*. Biomaterials, 2003. **24**(3): p. 469-479.
7. Gill, H.S., et al., *Molecular and immune toxicity of CoCr nanoparticles in MoM hip arthroplasty*. Trends Mol Med, 2012. **18**(3): p. 145-55.
8. Hosman, A.H., et al., *Effects of metal-on-metal wear on the host immune system and infection in hip arthroplasty*. Acta Orthop, 2010. **81**(5): p. 526-34.
9. Keegan, G.M., I.D. Learmonth, and C.P. Case, *A systematic comparison of the actual, potential, and theoretical health effects of cobalt and chromium exposures from industry and surgical implants*. Crit Rev Toxicol, 2008. **38**(8): p. 645-74.
10. Sansone, V., D. Pagani, and M. Melato, *The effects on bone cells of metal ions released from orthopaedic implants. A review*. Clin Cases Miner Bone Metab, 2013. **10**(1): p. 34-40.
11. Ogunwale, B., et al., *Investigating the immunologic effects of CoCr nanoparticles*. Clin Orthop Relat Res, 2009. **467**(11): p. 3010-6.
12. Allen, M.J., et al., *The effects of particulate cobalt, chromium and cobalt-chromium alloy on human osteoblast-like cells in vitro*. Journal of Bone and Joint Surgery-British Volume, 1997. **79B**(3): p. 475-482.
13. Behl, B., et al., *Biological effects of cobalt-chromium nanoparticles and ions on dural fibroblasts and dural epithelial cells*. Biomaterials, 2013. **34**(14): p. 3547-58.
14. Bhabra, G., et al., *Nanoparticles can cause DNA damage across a cellular barrier*. Nature Nanotechnology, 2009. **4**(12): p. 876-883.
15. Christian, W.V., et al., *Toxicology-based cancer causation analysis of CoCr-containing hip implants: a quantitative assessment of genotoxicity and tumorigenicity studies*. Journal of Applied Toxicology, 2014. **34**(9): p. 939-967.
16. Figgitt, M., et al., *The genotoxicity of physiological concentrations of chromium (Cr(III) and Cr(VI)) and cobalt (Co(II)): An in vitro study*. Mutation Research-Fundamental and Molecular Mechanisms of Mutagenesis, 2010. **688**(1-2): p. 53-61.
17. Landsiedel, R., et al., *Genotoxicity investigations on nanomaterials: Methods, preparation and characterization of test material, potential artifacts and limitations-Many questions, some answers*. Mutation Research-Reviews in Mutation Research, 2009. **681**(2-3): p. 241-258.
18. Papageorgiou, I., et al., *The effect of nano- and micron-sized particles of cobalt-chromium alloy on human fibroblasts in vitro*. Biomaterials, 2007. **28**(19): p. 2946-2958.
19. Papageorgiou, I., et al., *Macrophages detoxify the genotoxic and cytotoxic effects of surgical cobalt chrome alloy particles but not quartz particles on human cells in vitro*. Mutat Res, 2008. **643**(1-2): p. 11-9.

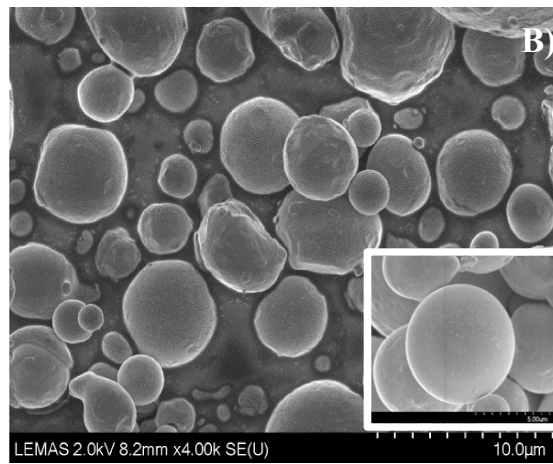
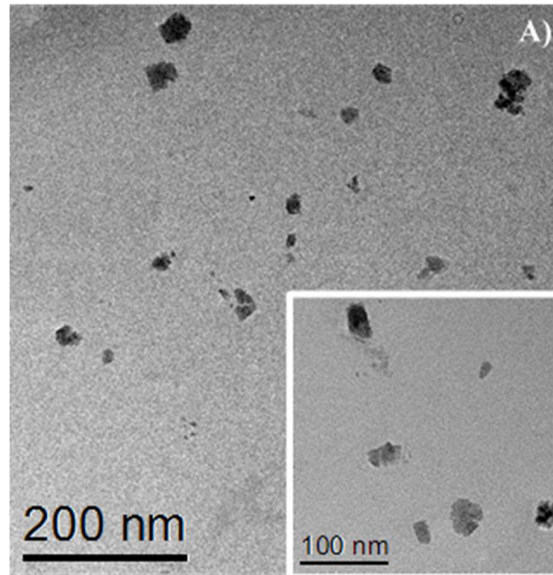
20. Papageorgiou, I., et al., *Genotoxic effects of particles of surgical cobalt chrome alloy on human cells of different age in vitro*. *Mutat Res*, 2007. **619**(1-2): p. 45-58.
21. Potnis, P.A., D.K. Dutta, and S.C. Wood, *Toll-like receptor 4 signaling pathway mediates proinflammatory immune response to cobalt-alloy particles*. *Cellular Immunology*, 2013. **282**(1): p. 53-65.
22. Raghunathan, V.K., et al., *Influence of particle size and reactive oxygen species on cobalt chrome nanoparticle-mediated genotoxicity*. *Biomaterials*, 2013. **34**(14): p. 3559-3570.
23. Sood, A., et al., *Signalling of DNA damage and cytokines across cell barriers exposed to nanoparticles depends on barrier thickness*. *Nature Nanotechnology*, 2011. **6**(12): p. 824-833.
24. Tan, H.C., et al., *Covalently grafted BMP-7 peptide to reduce macrophage/monocyte activity: An in vitro study on cobalt chromium alloy*. *Biotechnology and Bioengineering*, 2013. **110**(3): p. 969-979.
25. Tan, H.C., et al., *Anti-fibrosis effect of BMP-7 peptide functionalization on cobalt chromium alloy*. *Journal of Orthopaedic Research*, 2013. **31**(6): p. 983-990.
26. Thomas, I.T. and E.J. Evans, *The Effect of Cobalt Chromium Molybdenum Powder on Collagen Formation by Fibroblasts Invitro*. *Biomaterials*, 1986. **7**(4): p. 301-304.
27. Brown, C., et al., *Consequences of exposure to peri-articular injections of micro- and nano-particulate cobalt-chromium alloy*. *Biomaterials*, 2013. **34**(34): p. 8564-80.
28. Hosman, A.H., et al., *The influence of Co-Cr and UHMWPE particles on infection persistence: an in vivo study in mice*. *J Orthop Res*, 2012. **30**(3): p. 341-7.
29. Scharf, B., et al., *Molecular analysis of chromium and cobalt-related toxicity*. *Sci Rep*, 2014. **4**: p. 5729.
30. Taylor, U., et al., *Impact of Metal Nanoparticles on Germ Cell Viability and Functionality*. *Reproduction in Domestic Animals*, 2012. **47**: p. 359-368.
31. Wang, Z., et al., *Reproductive toxicity in adult male rats following intra-articular injection of cobalt-chromium nanoparticles*. *Journal of Orthopaedic Science*, 2013. **18**(6): p. 1020-1026.
32. Morgenroth, K., et al., *Morphology and pathogenesis of pneumoconiosis in dental technicians*. *Pathol Res Pract*, 1985. **179**(4-5): p. 528-36.
33. Rom, W.N., et al., *Pneumoconiosis and exposures of dental laboratory technicians*. *Am J Public Health*, 1984. **74**(11): p. 1252-7.
34. Sherson, D., N. Maltbaek, and O. Olsen, *Small Opacities among Dental Laboratory Technicians in Copenhagen*. *British Journal of Industrial Medicine*, 1988. **45**(5): p. 320-324.
35. Sherson, D., N. Maltbaek, and K. Heydorn, *A dental technician with pulmonary fibrosis: a case of chromium-cobalt alloy pneumoconiosis?* *Eur Respir J*, 1990. **3**(10): p. 1227-9.
36. Choudat, D., *Occupational lung diseases among dental technicians*. *Tuber Lung Dis*, 1994. **75**(2): p. 99-104.
37. Oberdorster, G., J. Ferin, and B.E. Lehnert, *Correlation between particle size, in vivo particle persistence, and lung injury*. *Environ Health Perspect*, 1994. **102 Suppl 5**: p. 173-9.
38. Selden, A., et al., *Three cases of dental technician's pneumoconiosis related to cobalt-chromium-molybdenum dust exposure*. *Chest*, 1996. **109**(3): p. 837-42.
39. Nielsen, J., J.R. Jepsen, and F. Egede, *The hard-metal lung. Cobalt-induced pneumoconiosis*. *Ugeskr Laeger*, 1986. **148**(21): p. 1311-2.
40. Kusaka, Y., et al., *Effect of hard metal dust on ventilatory function*. *Br J Ind Med*, 1986. **43**(7): p. 486-9.
41. Demedts, M., *Cobalt and hard metal*. *Chest*, 1986. **89**(2): p. 316.

42. Cullen, M.R., *Respiratory diseases from hard metal exposure. A continuing enigma*. Chest, 1984. **86**(4): p. 513-4.
43. Rystedt, I. and T. Fischer, *Relationship between nickel and cobalt sensitization in hard metal workers*. Contact Dermatitis, 1983. **9**(3): p. 195-200.
44. Perdrix, A., et al., *Cobalt and sintered metal carbides. Value of the determination of cobalt as a tracer of exposure to hard metals*. Toxicol Eur Res, 1983. **5**(5): p. 233-40.
45. Hillerdal, G. and M. Hartung, *On cobalt in tissues from hard metal workers*. Int Arch Occup Environ Health, 1983. **53**(1): p. 89-90.
46. Fischer, T. and I. Rystedt, *Cobalt allergy in hard metal workers*. Contact Dermatitis, 1983. **9**(2): p. 115-21.
47. Kusaka, Y., et al., *Bronchopulmonary diseases due to the hard metal dust*. Sangyo Igaku, 1982. **24**(6): p. 636-48.
48. Galy, P., et al., *Pulmonary disorders in the hard metal industry*. Rev Inst Hyg Mines (Hasselt), 1974. **29**(3): p. 130-7.
49. Joseph, M., *Hard metal pneumoconiosis*. Australas Radiol, 1968. **12**(2): p. 92-5.
50. Beritic, T., et al., *Pneumoconiosis Caused by Hard Metal Dust*. Arh Hig Rada Toksikol, 1963. **14**: p. 261-8.
51. Trautmann, H., *Pneumoconiosis due to inhalation of hard metal dusts*. Hefte Unfallheilkd, 1958. **56**: p. 99-103.
52. Lundgren, K.D. and H. Ohman, *Pneumoconiosis in hard metal industry; technical and medical problems*. Virchows Arch, 1954. **325**(3): p. 259-84.
53. Selden, A.I., et al., *Exposure to cobalt chromium dust and lung disorders in dental technicians*. Thorax, 1995. **50**(7): p. 769-72.
54. Borm, P.J., R.P. Schins, and C. Albrecht, *Inhaled particles and lung cancer, part B: paradigms and risk assessment*. Int J Cancer, 2004. **110**(1): p. 3-14.
55. Cassee, F.R., et al., *Exposure, health and ecological effects review of engineered nanoscale cerium and cerium oxide associated with its use as a fuel additive*. Crit Rev Toxicol, 2011. **41**(3): p. 213-29.
56. Castranova, V., *Overview of current toxicological knowledge of engineered nanoparticles*. J Occup Environ Med, 2011. **53**(6 Suppl): p. S14-7.
57. Cattaneo, A.G., et al., *Nanotechnology and human health: risks and benefits*. J Appl Toxicol, 2010. **30**(8): p. 730-44.
58. Choi, M., et al., *Chitosan nanoparticles show rapid extrapulmonary tissue distribution and excretion with mild pulmonary inflammation to mice*. Toxicol Lett, 2010. **199**(2): p. 144-52.
59. Du, Z., et al., *Cardiovascular toxicity of different sizes amorphous silica nanoparticles in rats after intratracheal instillation*. Cardiovasc Toxicol, 2013. **13**(3): p. 194-207.
60. Geraets, L., et al., *Tissue distribution of inhaled micro- and nano-sized cerium oxide particles in rats: results from a 28-day exposure study*. Toxicol Sci, 2012. **127**(2): p. 463-73.
61. He, X., et al., *Lung deposition and extrapulmonary translocation of nano-ceria after intratracheal instillation*. Nanotechnology, 2010. **21**(28): p. 285103.
62. Knuckles, T.L., et al., *Nanoparticle inhalation alters systemic arteriolar vasoreactivity through sympathetic and cyclooxygenase-mediated pathways*. Nanotoxicology, 2012. **6**(7): p. 724-35.
63. LeBlanc, A.J., et al., *Nanoparticle inhalation impairs coronary microvascular reactivity via a local reactive oxygen species-dependent mechanism*. Cardiovasc Toxicol, 2010. **10**(1): p. 27-36.
64. Minarchick, V.C., et al., *Pulmonary cerium dioxide nanoparticle exposure differentially impairs coronary and mesenteric arteriolar reactivity*. Cardiovasc Toxicol, 2013. **13**(4): p. 323-37.

65. Nurkiewicz, T.R., et al., *Particulate matter exposure impairs systemic microvascular endothelium-dependent dilation*. Environ Health Perspect, 2004. **112**(13): p. 1299-306.
66. Nurkiewicz, T.R., et al., *Systemic microvascular dysfunction and inflammation after pulmonary particulate matter exposure*. Environ Health Perspect, 2006. **114**(3): p. 412-9.
67. Song, Y., et al., *Nanomaterials in humans: identification, characteristics, and potential damage*. Toxicol Pathol, 2011. **39**(5): p. 841-9.
68. Stapleton, P.A., et al., *Xenobiotic particle exposure and microvascular endpoints: a call to arms*. Microcirculation, 2012. **19**(2): p. 126-42.
69. Zhu, M.T., et al., *Particokinetics and extrapulmonary translocation of intratracheally instilled ferric oxide nanoparticles in rats and the potential health risk assessment*. Toxicol Sci, 2009. **107**(2): p. 342-51.
70. Armstead, A.L., C.B. Arena, and B. Li, *Exploring the potential role of tungsten carbide cobalt (WC-Co) nanoparticle internalization in observed toxicity toward lung epithelial cells in vitro*. Toxicol Appl Pharmacol, 2014. **278**(1): p. 1-8.
71. Hamza, T. and B.Y. Li, *Differential responses of osteoblasts and macrophages upon Staphylococcus aureus infection*. BMC Microbiology, 2014. **14**.
72. Hamza, T., et al., *Intra-cellular Staphylococcus aureus alone causes infection in vivo*. Eur Cell Mater, 2013. **25**: p. 341-50; discussion 350.
73. Noore, J., A. Noore, and B. Li, *Cationic antimicrobial peptide LL-37 is effective against both extra- and intracellular Staphylococcus aureus*. Antimicrob Agents Chemother, 2013. **57**(3): p. 1283-90.
74. Li, H.S., et al., *Cefazolin Embedded Biodegradable Polypeptide Nanofilms Promising for Infection Prevention: A Preliminary Study on Cell Responses*. Journal of Orthopaedic Research, 2010. **28**(8): p. 992-999.
75. Likibi, F., B.B. Jiang, and B.Y. Li, *Biomimetic nanocoating promotes osteoblast cell adhesion on biomedical implants*. J Mater Res, 2008. **23**(12): p. 3222-3228.
76. Armstead, A.L., et al., *Acute inflammatory responses of nanoparticles in an intra-tracheal instillation rat model*. PLoS One, 2015. **10**(3): p. e0118778.
77. Hondow, N., et al., *Quantitative characterization of nanoparticle agglomeration within biological media*. Journal of Nanoparticle Research, 2012. **14**(7).
78. Daigneault, M., et al., *The identification of markers of macrophage differentiation in PMA-stimulated THP-1 cells and monocyte-derived macrophages*. PLoS One, 2010. **5**(1): p. e8668.
79. Takashiba, S., et al., *Differentiation of monocytes to macrophages primes cells for lipopolysaccharide stimulation via accumulation of cytoplasmic nuclear factor kappaB*. Infect Immun, 1999. **67**(11): p. 5573-8.
80. Parry, M.C., et al., *Blood levels of cobalt and chromium are inversely correlated to head size after metal-on-metal resurfacing arthroplasty*. Hip International, 2013. **23**(6): p. 529-534.
81. Albanese, A., P.S. Tang, and W.C. Chan, *The effect of nanoparticle size, shape, and surface chemistry on biological systems*. Annu Rev Biomed Eng, 2012. **14**: p. 1-16.
82. Oberdorster, G., *Lung particle overload: implications for occupational exposures to particles*. Regul Toxicol Pharmacol, 1995. **21**(1): p. 123-35.
83. Oberdorster, G., *Pulmonary effects of inhaled ultrafine particles*. Int Arch Occup Environ Health, 2001. **74**(1): p. 1-8.
84. Gatti, A.M. and F. Rivasi, *Biocompatibility of micro- and nanoparticles. Part I: in liver and kidney*. Biomaterials, 2002. **23**(11): p. 2381-7.
85. Mosser, D.M., *The many faces of macrophage activation*. J Leukoc Biol, 2003. **73**(2): p. 209-12.
86. Miyata, R. and S.F. van Eeden, *The innate and adaptive immune response induced by alveolar macrophages exposed to ambient particulate matter*. Toxicol Appl Pharmacol, 2011. **257**(2): p. 209-26.

87. Sica, A. and A. Mantovani, *Macrophage plasticity and polarization: in vivo veritas*. J Clin Invest, 2012. **122**(3): p. 787-95.
88. Antonios, J.K., et al., *Macrophage polarization in response to wear particles in vitro*. Cell Mol Immunol, 2013. **10**(6): p. 471-82.
89. Hinuber, C., et al., *Biocompatibility and mechanical properties of diamond-like coatings on cobalt-chromium-molybdenum steel and titanium-aluminum-vanadium biomedical alloys*. J Biomed Mater Res A, 2010. **95**(2): p. 388-400.
90. Buzea, C., I.I. Pacheco, and K. Robbie, *Nanomaterials and nanoparticles: Sources and toxicity*. Biointerphases, 2007. **2**(4): p. Mr17-Mr71.
91. Canton, I. and G. Battaglia, *Endocytosis at the nanoscale*. Chem Soc Rev, 2012. **41**(7): p. 2718-39.
92. Fischer, H.C. and W.C.W. Chan, *Nanotoxicity: the growing need for in vivo study*. Current Opinion in Biotechnology, 2007. **18**(6): p. 565-571.
93. Oberdorster, G., E. Oberdorster, and J. Oberdorster, *Nanotoxicology: an emerging discipline evolving from studies of ultrafine particles*. Environ Health Perspect, 2005. **113**(7): p. 823-39.
94. Nel, A.E., et al., *Understanding biophysicochemical interactions at the nano-bio interface*. Nat Mater, 2009. **8**(7): p. 543-57.
95. Wagner, A.J., et al., *Cellular Interaction of Different Forms of Aluminum Nanoparticles in Rat Alveolar Macrophages*. The Journal of Physical Chemistry B, 2007. **111**(25): p. 7353-7359.
96. Wottrich, R., S. Diabate, and H.F. Krug, *Biological effects of ultrafine model particles in human macrophages and epithelial cells in mono- and co-culture*. Int J Hyg Environ Health, 2004. **207**(4): p. 353-61.
97. Geiser, M., *Morphological aspects of particle uptake by lung phagocytes*. Microsc Res Tech, 2002. **57**(6): p. 512-22.
98. Cervellati, C., et al., *Oxidative stress and bone resorption interplay as a possible trigger for postmenopausal osteoporosis*. Biomed Res Int, 2014. **2014**: p. 569563.
99. Nathan, F.M., et al., *Oxidative stress and antioxidant status in primary bone and soft tissue sarcoma*. BMC Cancer, 2011. **11**: p. 382.
100. Tsaousi, A., E. Jones, and C.P. Case, *The in vitro genotoxicity of orthopaedic ceramic (Al<sub>2</sub>O<sub>3</sub>) and metal (CoCr alloy) particles*. Mutat Res, 2010. **697**(1-2): p. 1-9.
101. Brody, J.S. and A. Spira, *State of the art. Chronic obstructive pulmonary disease, inflammation, and lung cancer*. Proc Am Thorac Soc, 2006. **3**(6): p. 535-7.
102. Lison, D., *Human toxicity of cobalt-containing dust and experimental studies on the mechanism of interstitial lung disease (hard metal disease)*. Crit Rev Toxicol, 1996. **26**(6): p. 585-616.
103. Chen, X., et al., *2',7'-Dichlorodihydrofluorescein as a fluorescent probe for reactive oxygen species measurement: Forty years of application and controversy*. Free Radic Res, 2010. **44**(6): p. 587-604.
104. Chen, X., et al., *Fluorescent and luminescent probes for detection of reactive oxygen and nitrogen species*. Chem Soc Rev, 2011. **40**(9): p. 4783-804.
105. Iles, K.E. and H.J. Forman, *Macrophage signaling and respiratory burst*. Immunol Res, 2002. **26**(1-3): p. 95-105.

**FIGURES**



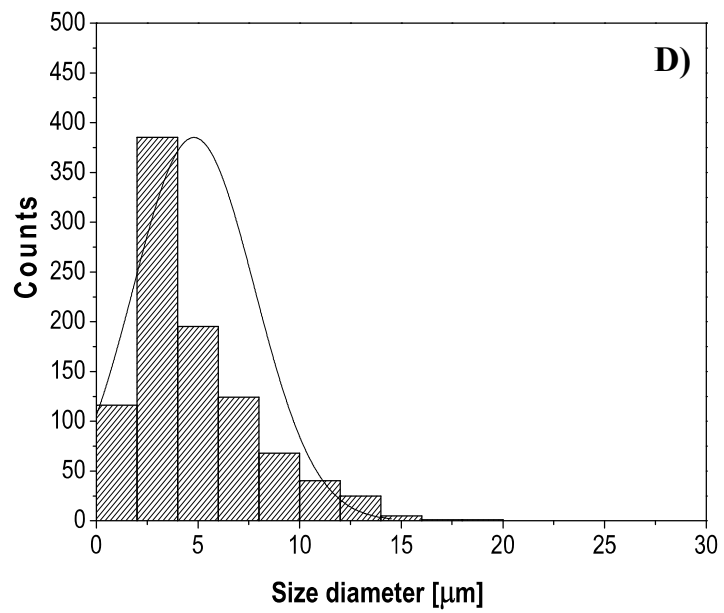
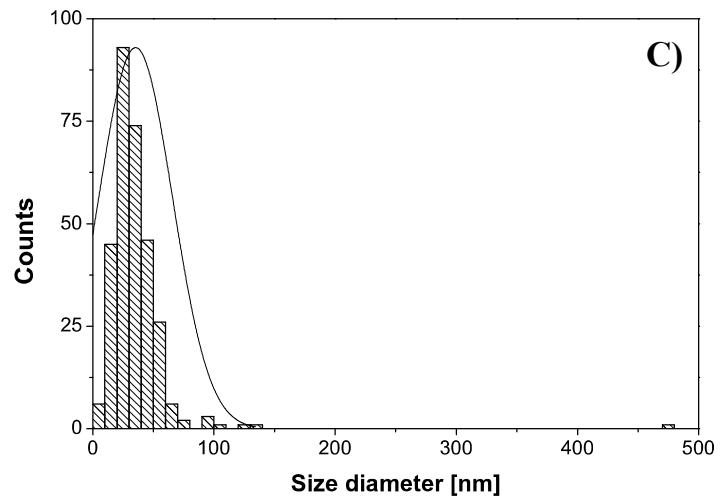


**Figure 1.**

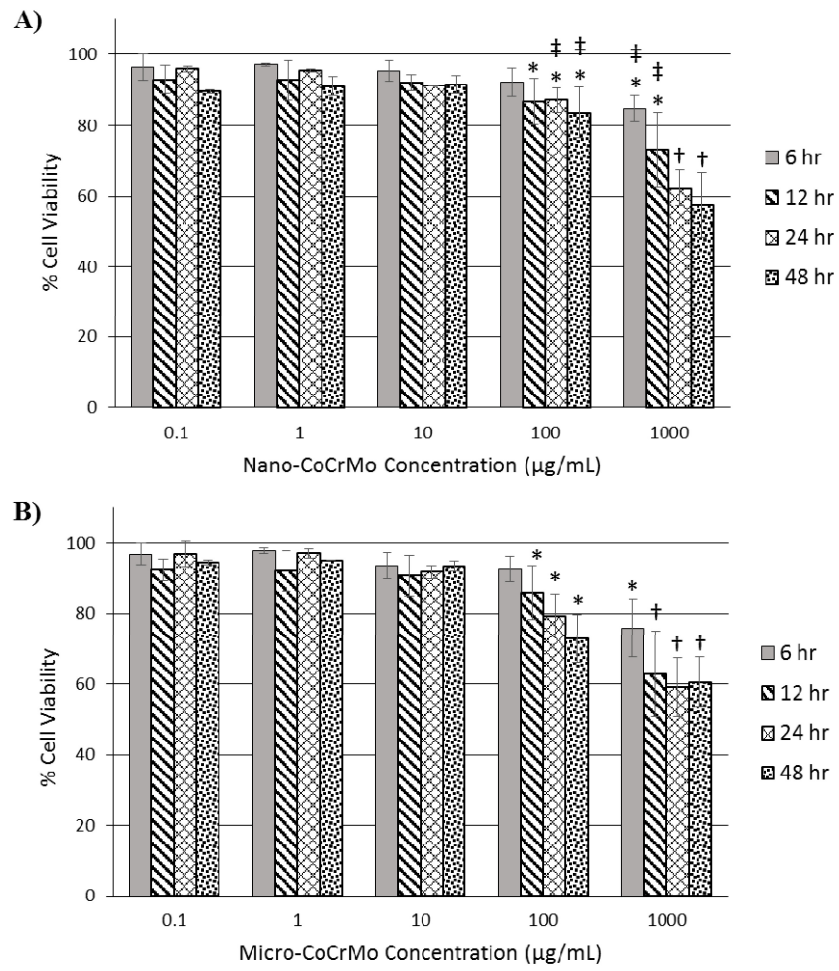


**Figure 2.**

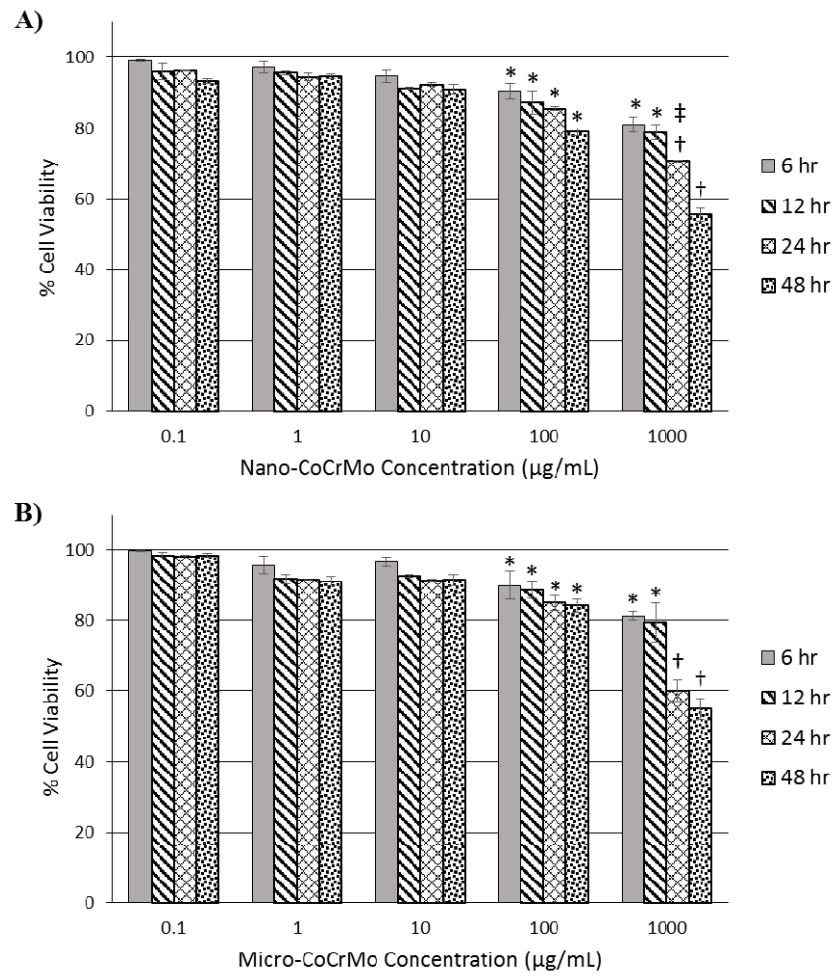


**Figure 3.**

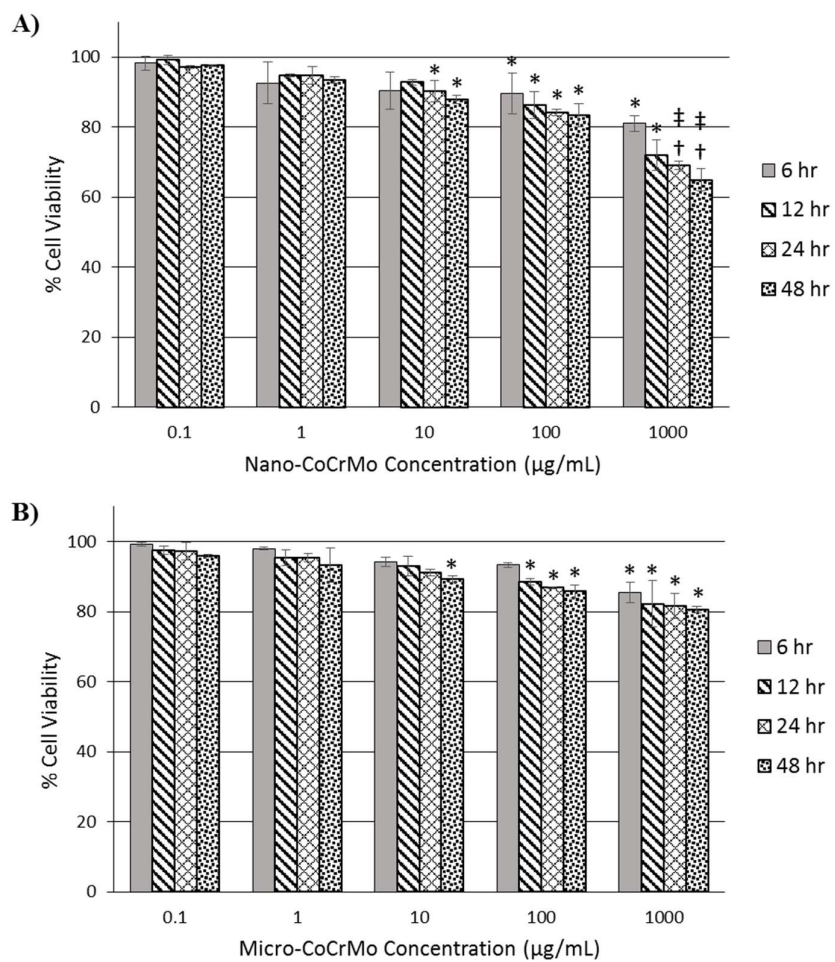


**Figure 4.**

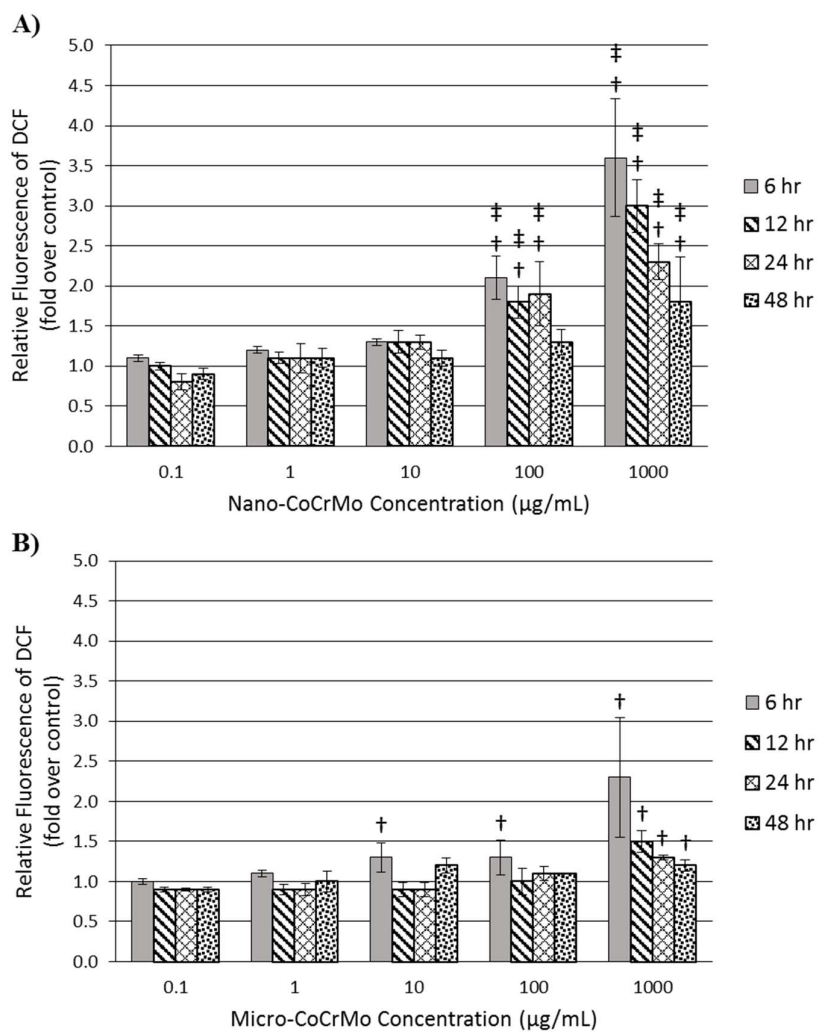


**Figure 5.**

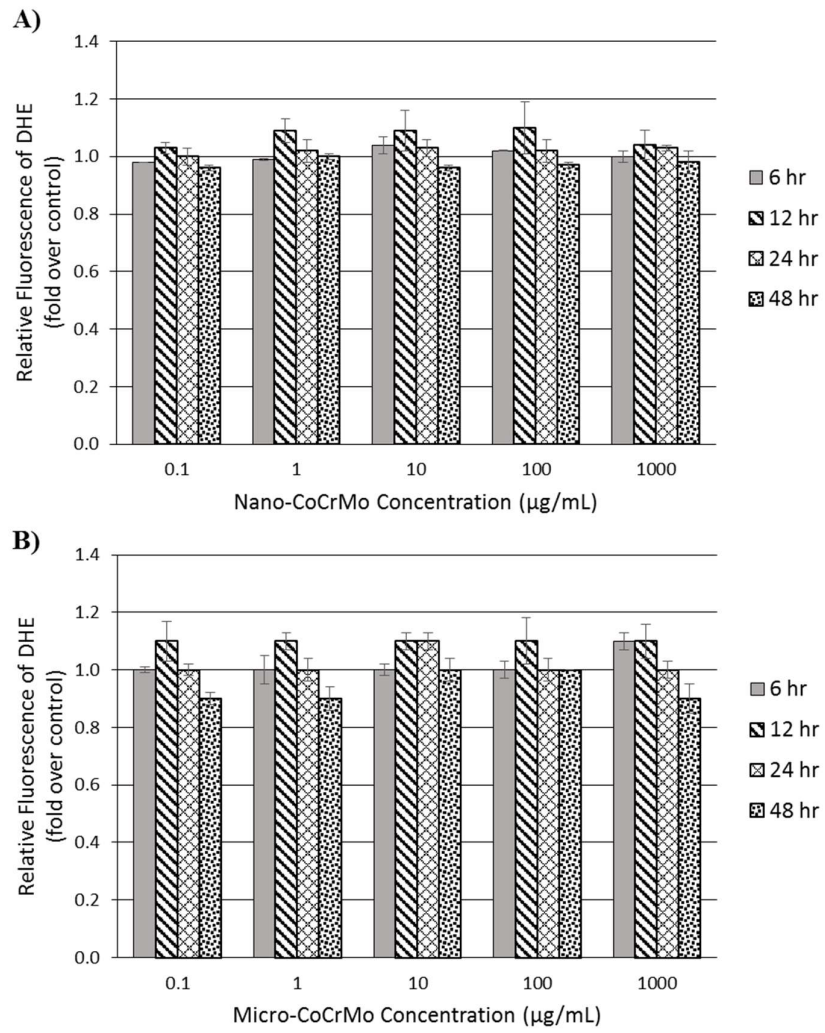


**Figure 6.**

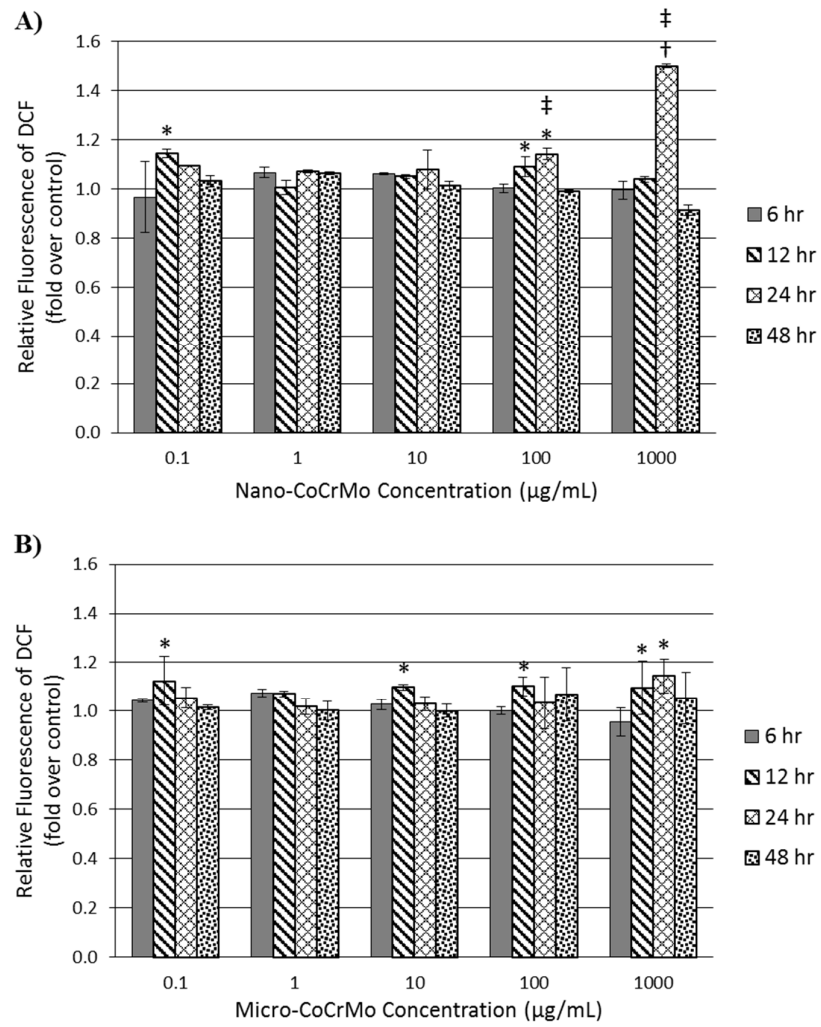


**Figure 7.**

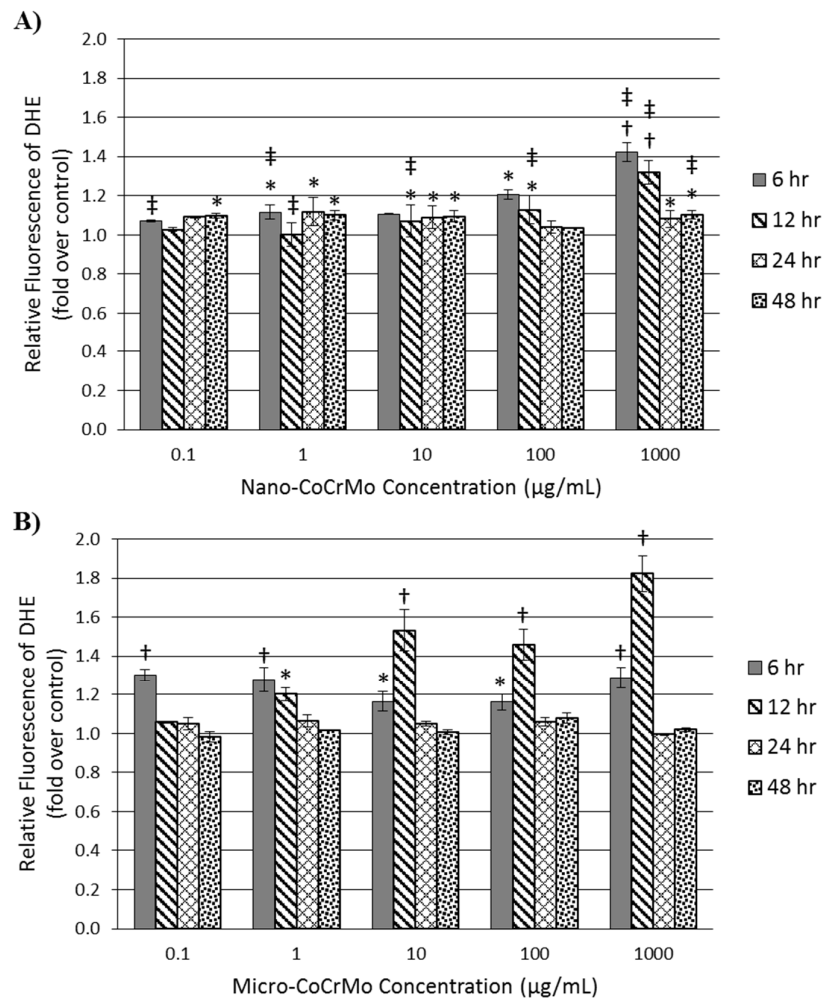


**Figure 8.**

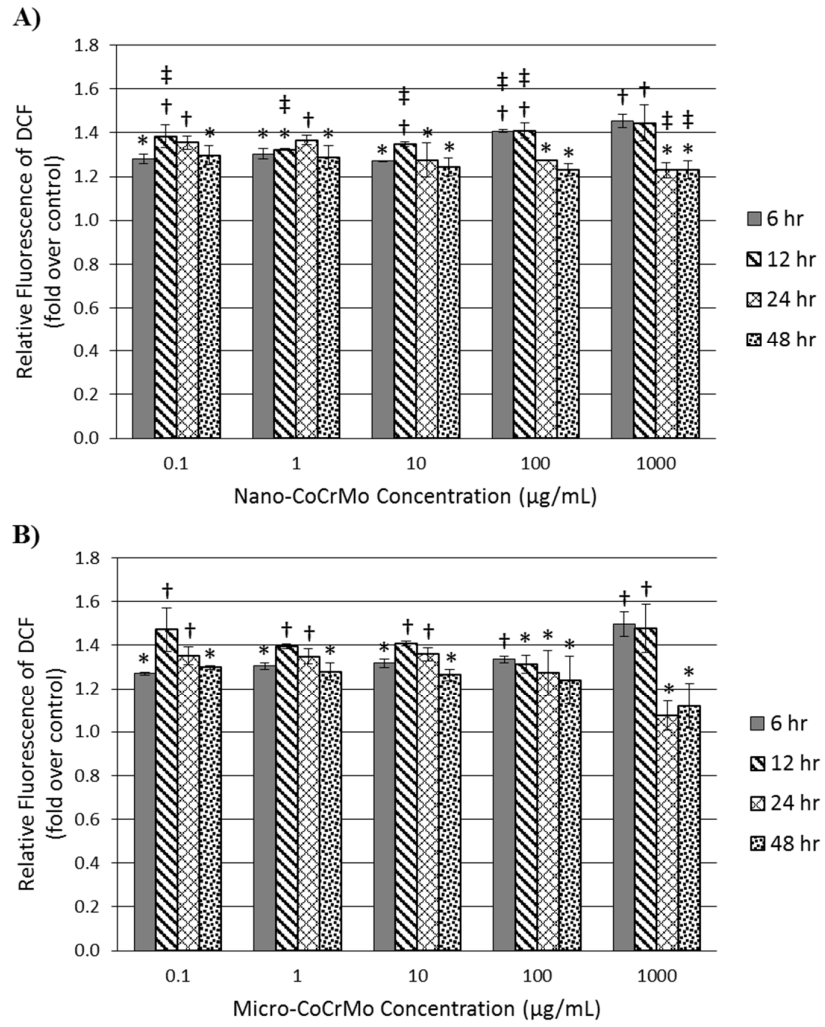


**Figure 9.**

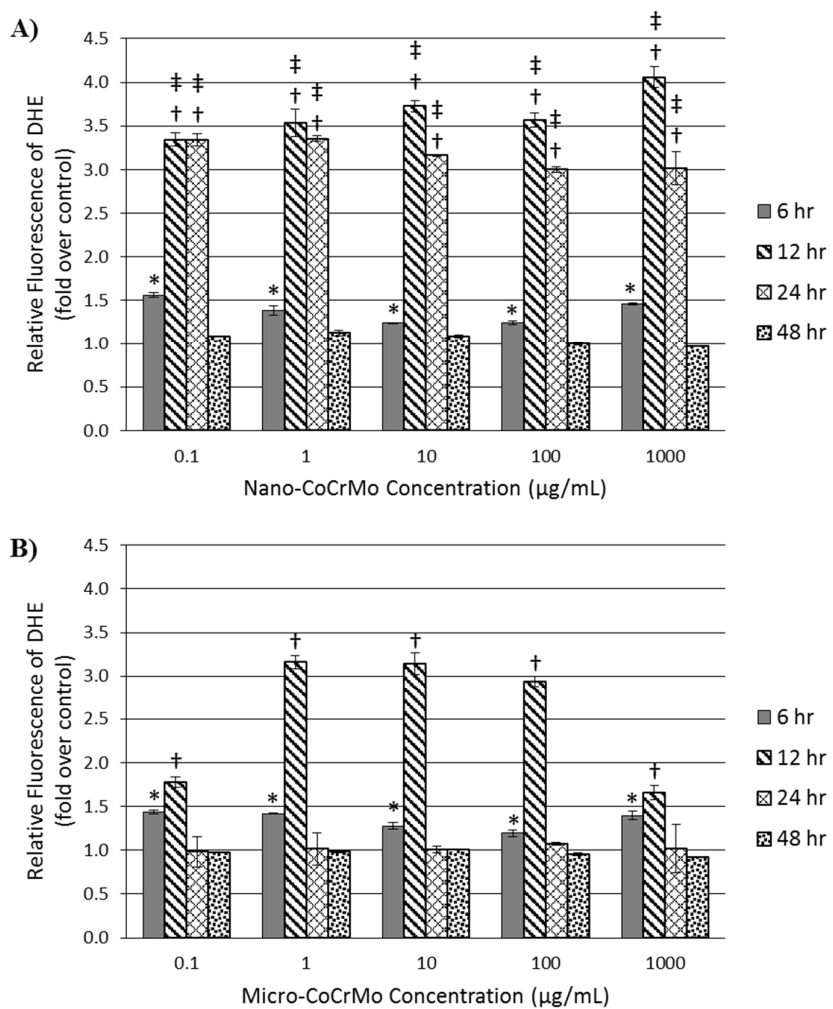


**Figure 10.**